Universitat Autònoma de Barcelona

PhD Thesis

Synthesis and Characterisation of Ferrite Nanoparticles for $YBa_2Cu_3O_7$ - Nanocomposite Superconducting Layers: a Neutron and Synchrotron Study

Author: Eduardo Solano Minuesa

Supervised by:

Prof. Josep Ros Badosa

Dr. Susagna Ricart Miro

PhD program in Chemistry

Chemistry department - Science faculty

ICMAB

2013

CSIC

Universitat Autònoma de Barcelona

PhD Thesis

Synthesis and Characterisation of Ferrite Nanoparticles for $YBa_2Cu_3O_7$ - Nanocomposite Superconducting Layers: a Neutron and Synchrotron Study

Author: Eduardo Solano Minuesa

Supervised by:

Prof. Josep Ros Badosa

Dr. Susagna Ricart Miro

PhD program in Chemistry

Chemistry department - Science faculty

ICMAB

2013

CSIC

Report submitted to aspire to the Doctor degree by:

Eduardo Solano Minuesa

Checked and accepted:

Prof. Josep Ros Badosa

Dr. Susagna Ricart Miro

Bellaterra. Tuesday, September 3, 2013

Time's up...

Acknowledgements

Esta es, curiosamente, la última página escrita de este manuscrito, y es a su vez, la más complicada de redactar. Aquí expreso por escrito el sentimiento de agradecimiento hacia aquellas personas que han participado de una u otra forma en la producción de todo este trabajo:

A mis directores de tesis, el Profesor Josep Ros y la Dra. Susagna Ricart, los cuales me han aconsejado y guiado durante este arduo trabajo. Igualmente al Dr. Ramón Yáñez, por abrirme las puertas de entrada.

Existen también otros científicos sin los cuales la elaboración de esta tesis no hubiese sido posible. Ellos son el Dr. Manuel Valvidares et al., guía también del "máster de radiación de sincrotrón y aceleradores de partículas" y mentor en la técnica de XAS-XMCD de sincrotrón; el Dr. Cristian Mocuta et al., quien fue mi director durante la estada pre-doctoral realizando estudios con difracción de rayos-X de sincrotrón; también el Dr. Carlos Frontera, porque sin sus explicaciones y ayuda con la difracción de neutrones y refinamiento de Rietveld, una parte de este trabajo no hubiese podido ser realizado. Al Profesor Xavier Granados, el Dr. Albert Calleja, la Dra. Teresa Puig y el Profesor Xavier Obradors, juntamente con otros científicos del equipo, han sido un gran apoyo por permitirme colaborar con ellos y vislumbrar una pequeña parte de su gran conocimiento científico.

No he de olvidar a (la Dra.) Marta Vilardell, piedra angular de parte de los estudios realizados con superconductores. También el personal experto en las diferentes técnicas y servicios recurridos que han ido poniendo su parte según progresaba este trabajo: (HR)TEM, RX, SQUID, TGA-DCS, Sala Blanca... han sido de gran ayuda.

A aquellos compañeros de viaje del laboratorio, unidad y/o departamento de la UAB, al grupo de Superconductores del ICMAB, y a todas aquellas personas que

he conocido durante esta tesis doctoral, porque me han ayudado científicamente, y porque me han regalado inolvidables momentos, y aunque la vida es constante cambio, nunca los olvidaré. Y por supuesto, a aquellas personas (tanto de dentro como de fuera del ámbito academico) con las que he compartido los momentos de descanso, de alegría y también de desesperación, personas que finalmente no es que sean un pilar de la tesis, si no que son algo más.

Y a falta de parecer desconsiderado, espero que cada uno/a que lea estas líneas y no encuentre su nombre entre ellas, sea capaz de identificarse en uno u otro lugar, porque puedo asegurar que, durante la escritura de estos agradecimentos me he acordado de todos y cada uno de vosotros/as.

Por lo que fue, por lo que es, y por lo que será, a todos y todas, gracias.

Motivation & Overview

"There's plenty room at the bottom" was the title of a conference imparted by the physicist Richard Phillips Feynman[1] on 29^{th} December 1959 at the annual meeting of the American Physical Society. Feynman explained "the problem of manipulating and controlling things on a small scale", laying the foundation of actual nanoscience and nanotechnology ways. Feynman ventured the huge potential of manipulating the matter at the nanoscale, where the quantum and macroscopic laws converge, giving as result materials with interesting properties which it will be discussed during this lecture.

Challenges in develop new materials with improved and/or added properties make the nanoscience and nanotechnology leading the actual research. Different scientific fields are forced to merge, leaving behind the scientific isolation with the finality to collaborate, and as consequence, develop new optimised nanostructured systems. Chemists, physicists, engineers, biologist..., work together with a common end point: science for the society.

This thesis deserves to be started with the Feynman's phrase due to the main motivation of the present project is to develop new nanostrucures and apply them into new systems that improve the quality of life of the actual and future society. Since is not possible to cover all the scientific fields, this work is focused on a specific scientific part: the synthesis and characterisation of magnetic ferrite nanoparticles (MFe_2O_4) and, in addition, the characterisation of the nanoparticles and the new generated nanocomposite $YBa_2Cu_3O_{7-\delta}$ superconducting thin layers with MFe_2O_4 nanoparticles embedded, using neutron and synchrotron radiation as powerful techniques.

---

[1] R. P. Feynman, "There's plenty room at the bottom," *Engineerind and Science*, vol. 23, pp. 22–36, 1960.

These new nanocomposites are promising in applications concerning electrical transport, high power motors, intense magnetic fields, etc. The work that is developed here will provide a part to carry out the main objective: generate more efficient superconducting tapes and wires.

Contents

Abbreviations

acac	Acetylacotenate
BM	Bending Magnet
BYTO	Ba_2YTaO_6
BZO	$BaZrO_3$
CSD	Chemical Solution Deposition
DSC	Differential Scanning Calorimetry
GIXRD	Grazing Incidence XRD
H_c	Critical Magnetic Field
HR-TEM	High Resolution TEM
HTS	High Temperature Superconductor
ID	Insertion Device
J_c	Critical Current
LAO	$LaAlO_3$
NPD	Neutron Powder Diffraction
NPs	Nanoparticles
Oh	Octahedral
Oleyl	Oleylamine
SC	SuperConducting
SQUID	Superconductor QUantum Interference Device
STSI	Scientific-Technical Singular Infrastructures
T_c	Critical Temperature
Td	Tetrahedral
TEM	Transmission Electron Microscopy
TGA	ThermoGravimetric Analysis
TREG	Triethylene Glycol
XAS	X-ray Absorption Spectroscopy

XMCD	X-ray Magnetic Circular Dichroism
XPS	X-ray Photoemission Spectroscopy
XRD	X-ray Diffraction
XRPD	X-ray Powder Diffraction
YBCO	$YBa_2Cu_3O_{7-\delta}$

Abstract

In this PhD work the synthesis of MFe_2O_4 nanoparticles and the development of new $YBa_2Cu_3O_{7-\delta}$ superconducting layers with those magnetic nanoparticles embedded has been studied:

First, a new one-pot synthetic methodology via two approaches, thermal and microwave, was optimised. Then, the obtained MFe_2O_4 (M = Mn, Fe, Co, Ni, Cu, Zn) ferrites were characterised with common laboratory techniques to demonstrate that both heating methods produce similar high quality nanoparticles in high concentration. Thus, $MnFe_2O_4$ nanoparticles were embedded inside $YBa_2Cu_3O_{7-\delta}$ superconducting layers in order to improve their intrinsic properties via *ex-situ* approach, using ink-jet printing deposition.

Neutron and synchrotron radiation were profited as powerful techniques to accomplish a deep study of the structure and properties of the nanoparticles and different nanocomposite superconducting layers. X-ray Magnetic Circular Dichroism (XMCD), X-ray and Neutron Diffraction (XRD, ND) analyses have been exploited to obtain information about the structure, composition and behaviour of the new generated $YBa_2Cu_3O_{7-\delta}$-Nanoparticles nanocomposite.

Objectives

The main objective of this PhD study is to generate new nanocomposite superconducting layers with magnetic ferrite nanoparticles embedded within the structure.

With this aim, it a new synthetic methodology to produce ferrite magnetic nanoparticles (MFe_2O_4) has been developed, following the results obtained by characterising the nanocrystals generated. In addition, it is interesting to optimise a one-pot synthetic route which reduces the reactant consummation, the temperature needed and the time employed; in other words, to implement a more efficient eco-friendly technique. The optimised procedure must to produce nanoparticles with specific properties: size below 10 nm, low diameter deviation, high stability in polar media (for future applications with the superconductor chemical solution), superparamagnetic behaviour, etc.

After the formation, identification and characterisation of the different ferrite nanoparticles, a system to introduce the ferrite nanoparticles nanoparticles in the superconducting $YBa_2Cu_3O_{7-\delta}$ (YBCO) matrix is required. Once it was optimised, the results will be characterised to study the influence of include magnetic regions in the superconducting structure.

In this vein, *Large Scientific Facilities* will be profited, like neutron reactors and synchrotrons to perform an accurate characterisation of all the (nano)materials studied, because they provide the necessary tools via different and complementary high resolution powerful techniques. These facilities allow to obtain deep chemical and physical information that can not be achieved with common laboratory techniques.

After this work, a better understanding about the synthesis of MFe_2O_4 nanoparticles and new YBCO superconducting nanocomposites, and their characterisation with different techniques in singular facilities should have been attained.

Part I

General Introduction

Chapter 1

General Introduction

Contents

1.1 Nanoscience & nanotechnology

"Nano" comes from the Greek and means *dwarf*. Nowadays "Nano" is a prefix which refers to an order of magnitude 10^{-9} units. Then, a nanomaterial is defined as a material which has at least one spatial dimension under the range of 100 nm. Lasts years, big efforts have been applied to understand and control these materials whose properties between the macroscopic and quantum world make them very useful systems.

Nanoscience is the field whose research is focused on the study of the physic, chemistry, biology, etc. of a nanoscopic system. By its part, the nanotechnology designs, produces and applies these kind of nanostructures.

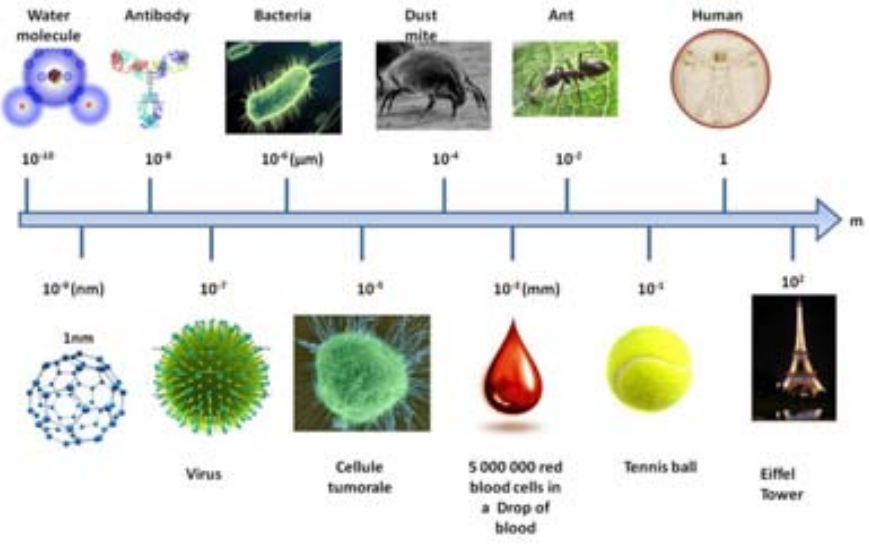

Figure 1.1: Comparison of the nanoscale in relation to the macroscopic world.

Current technology and knowledge have allowed to develop new nanometric structures which have different properties when comparing with the common bulk materials. This research develops the synthesis, generation and application of MFe_2O_4 magnetic nanoparticles into nanostructured YBCO superconducting thin layers, in order to generate new more efficient nanocomposite nanostructured superconducting systems.

1.2 Nanoparticles

Since now, several sorts of nanoparticles have been synthesised, characterised and applied in different fields. A general classification (among others) can be done depending on their composition:

1. Metallic: Formed by a cluster of metal atoms with an oxidation state equal to zero. Different properties are present in these variety of nanoparticles, such as plasmon resonance,[1] electronic current transport,[2] etc.

2. Quantum dots: Nanoparticles composed generally by two elements, being one of them a metal whose electronic configuration gives a gap between the conduction and valence band characteristic of a semiconductor. Some examples of quantum dots are PbS, Ag_2S, $TiO_2 \ldots$[3] One of the most known property is the photoluminescence under ultraviolet light or other energy sources. The wavelength emitted by these nanoparticles depends on their size and shape, because a quantum confinement of the pair electron - hole is produced.[4]

3. Metallic oxides: As their name indicates, this type of nanoparticles belong to a subclass composed by a metallic oxide. Even they could be enclosed in the quantum dots category, the differentiation comes from their special mechanical properties:[5] low elasticity, low hardness, high plasticity, etc. It is in this subcategory to which the magnetic ferrite nanoparticles belongs, but due to their intrinsic properties they can be also classified as *magnetic nanoparticles*.

4. Magnetic: Nanoparticles whose composition and structure confer them magnetic properties, specially *ferro-*, *ferri-*, and *superparamagnetism*. Due to the research developed in this work is based on magnetic nanoparticles, a short explanation about magnetism and magnetic behaviour has been introduced below in the point 1.2.1 section ii.

1.2.1 Properties

Nanostructured systems present properties between the bulk and atomic systems, showing new capabilities that can be profited to produce new materials with new potential applications. These new characteristics come from the fact that their small

size affect to the electronic configuration of the system, that is between discrete energetic levels and continuous band configuration.[6] Most significant characteristics for the case presented here is the size and the magnetism of the MFe_2O_4 nanoparticles, properties that will be explained below.

i Surface-volume ratio

When a material decreases in size, the ratio between their surface and total volume increase. The augmentation of the surface brings a gain of the superficial atoms, which are more reactive because they are in the interphase containing free atomic orbitals. This particularity makes nanoparticles interesting to surface process, because the surface by unit of mass is larger and their electronic configuration is different (when comparing with a microscopic material). Applications in catalysis are being carried out with nanostructured compounds in order to decrease the catalyst amount or to develop new catalysts.[7, 8] Counterpart, the surface-volume ratio is linked with the surface tension, which is higher for smaller systems (more interphase area). This unfavourable energetic state produces the aggregation and/or coalescence of the nanostructured system in order to reduce the superficial energy by reducing the surface-volume ratio.[9]

In order to avoid their aggregation and/or coalescence, and maintain their nanosize, several physico-chemical methods are used to stabilise the nanoparticles:[10]

1. Electrostatic: Produced by an electric bilayer on the surface of the nanoparticles, generating a Culombic repulsion between two individual particles and avoiding their approximation to produce the aggregation. This electric bilayer is achieved by the adsorption of ions on the surface.

2. Steric: Process that consist of surrounding the nanoparticles by molecules that, by a steric hindrance and geometric constrains, prevent the system aggregation.

3. Ionic liquid: Stabilisation system which can be considered as a mixture of electrostatic and steric. An ionic liquid is a liquid formed by cations and anions that electrostatically isolated the nanoparticles, but because the ionic liquid molecules should be large structures, they can coordinate with the nanoparticle surface, generating a shell of molecules which produce steric stabilisation.

The class of stabilisation can determine the dispersion media of the nanoparticles, because the interaction between the dispersant and the nanoparticle is carried out by the stabiliser. While a electrostatic stabilisation is adequate to polar dispersant due to their interactions, steric stabilised nanoparticles can be dispersed in polar or non-polars solvents depending on the nature of the coordinate molecule: for a polar ligand, polar solvent is needed, while nanoparticles with non-polar surrounding molecules are dispersible in non-polar media. Ionic liquids by its part are adequate to stabilise nanoparticles with application in polar systems.

ii Magnetism

Due to the nanoparticles studied in this research work are magnetic nanoparticles, a brief explanation about magnetism[11] deserves to be developed:

A magnetic field is produced as consequence of the movement of a charged particle (generating an electric current). In the case of magnetic atoms, the magnetism is originated by the unpaired electrons (charged particle) of the last atomic orbital in the fundamental state. In other words, the atomic magnetism is produced by paramagnetic atoms as consequence of their electronic configuration.

The magnetic moment of the electron (spin magnetic moment), jointly with their movement (orbital magnetic moment) produces an associated magnetic field that, for paramagnetic atoms, the resultant of the sum of the different magnetic vectors inside the atom is not null. The contribution of each electron to the global magnetic moment of the atom can be defined as one Bohr magneton μ_B.

$$\mu_B = \frac{e\hbar}{2m_e} = 9.27 \cdot 10^{-24} J \cdot T^{-1}$$

Depending on the number of unpaired electrons, one atom can contribute to the global magnetic moment with several μ_B. For the $3d^n$ atoms, the maximum contribution is for a spin up configuration with 5 unpaired electrons ($Mn^{2+}, Fe^{3+} \dots$), while the less contribution is for non magnetic atoms where all the electrons are paired. If a crystal structure is considered, where the atoms are repeated in the space, the atomic magnetic moment of one atom can interact with other magnetic atoms close to the first one, and as consequence, generate a constructive or destructive result. Then, in spite of a material is composed by magnetic atoms, the global magnetism could be zero (as in the case of the antiferromagnetic substances). Following this line,

di erent class of materials can be classi ed in function of their magnetic macroscopic behaviour as it can be seen below.

1. No magnetic: Material that is not a ected by an external magnetic eld.
2. Diamagnetic: Material which is repelled by the magnetic ux lines. In these materials all the electrons are paired, and the opposition to the external magnetic eld comes from the orbital magnetic moment of the electrons.
3. Paramagnetic: Material containing unpaired electrons whose magnetic vector is randomly oriented (giving as result a zero global magnetic moment) and can be oriented by the action of an external magnetic eld. Some materials becomes paramagnetic when the thermal energy can disorient the magnetic dipoles.
4. Ferromagnetic: Material formed by paramagnetic atoms which disposed in the same direction and sense, generating a total magnetic moment which is the sum of the di erent magnetic atoms that conform the material (hard magnet).
5. Ferrimagnetic: Like a ferromagnetic material but some magnetic atoms counteracts the magnetic moment of others because they have the same direction but opposite sense (soft magnet).
6. Antiferromagnetic: Material with zero magnetic moment due to the sum of the di erent magnetic atoms is null.
7. Superparamagnetic: Magnetic behaviour which can be classi ed as paramagnetism with a high magnetic sensitivity. In other words, the magnetic material is completely magnetised under a low intensity external magnetic eld (fast magnetisation response).

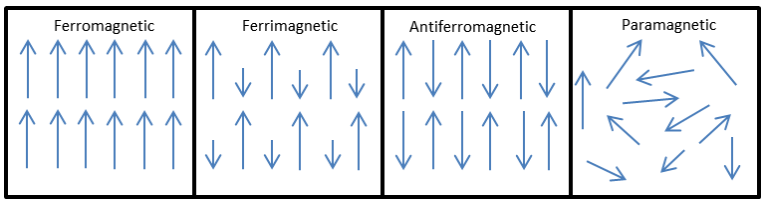

Figure 1.2: Schematic representation of the atomic spin orientation of the magnetic atoms in a crystal cell depending on their magnetic behaviour.

A magnetic material can be formed by di erent magnetic domains which have

an independent magnetic behaviour. For a multidomain material the magnetism can be modi ed by the orientation of these regions, because the global net magnetism depends on the global sum of the parts. If domains are randomly oriented or counteracts each other, the global magnetism of the sample is zero, while if an external magnetic eld is applied, the magnetic force of the material can be controlled.

If a multidomain material is subdue to an external magnetic eld H, and if H is strong enough, the magnetisation direction of the domains can be changed in order to be oriented respect to the external magnetic eld. In this vein, the magnetic strength of a material under an external magnetic eld H, is the magnetisation $M(H)$. The following gure 1.3 shows graphically the magnetisation degree in function of the intensity of the external magnetic eld H (hysteresis loop). Di erent sections can be di erence and will be explained below:

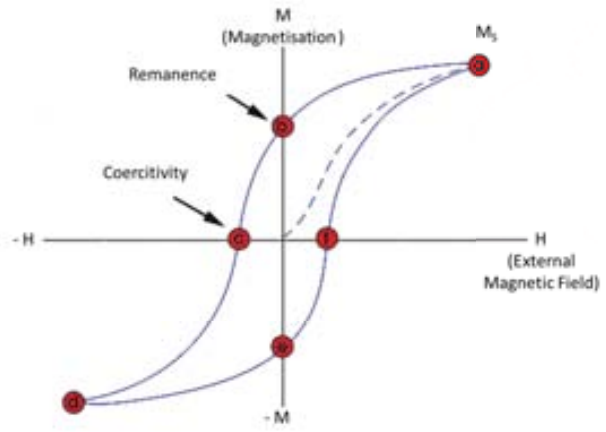

Figure 1.3: Hysteresis loop of a magnetic material.[12] The start point of the measurement is the origin of coordinates, and the magnetisation of the sample in function of the applied external magnetic eld is analysed.

As it can be seen in the hysteresis loop, there are di erent points in the graph that provides magnetic information about the material. *a* (M_S) is the magnetisation of saturation, which is the maximum magnetisation that the material can achieve and can not increase even increasing H; *b (e)* is the remanence or magnetic eld resultant after saturate the sample and remove H (measurement of the force of the generated permanent magnet); *c (f)* is the coercitivity, or measure of H needed to demagnetise the material after have been magnetised.

A hard permanent magnet (ferromagnetic) has a large coercitivity field (open cycle), while a paramagnetic material has a small coercitivity field. In the case of diamagnetic samples, it does not exist a cycle because no answer to the magnetic field H is produced. But for the case of interest (as it will be seen) the superparamagnetic substances has a quick response and it saturates under a low intensity magnetic field and has a magnetic coercitivity and remanence close to zero, giving the typical cycle with a S shape.

1.2.2 Applications

Nanostructured systems are investigated in order to apply them in a scientific or social field with the purpose to improve the technology and resources available. Because the nanoscience and nanotechnology are recent fields in research, nowadays the direct applications come to be spread.

Here, several actual and potential applications of nanostructured materials are presented[13] with the finality to show the actual efforts and the importance to research in this kind of materials:

1. Drug delivery: Nanoparticles can be functionalised (with a recognition system and a determinate molecule) in order to concentrate the drug or the nanoparticles into a specific cell or part of the body. The release of the drug or the manipulation of the nanoparticles can be controlled by different techniques, such as ultrasounds, magnetic fields, pH, etc. Even more, the nanoparticles could be recovered when they are excreted by the body for to be re-used.

2. Materials: Graphene & carbon nanotubes consist of a carbon monolayer in two configurations: as monolayer (graphene) or tube (Carbon nanotube). Their physico-chemical properties make them very useful in different fields, specially in materials science where new and more efficient materials are being developed.

3. Catalysis: Principally due to they large surface / volume ratio, nanoparticles are very promising in the field of heterogeneous catalysis. Also, the electronic atomic configuration of these nanostructures makes that some process only could be carried out thanks to new nanostructured catalyst.

4. Magnetic recording: Magnetic nanostructured systems are promising in order

to develop faster writing-reading systems with high density of information storage due to the reduction of the bit size.

Promising uses of nanotechnology can be achieved thanks to the new efforts applied in research and development of new nanostructures and application of these novel materials.

1.3 Superconductors

Superconductivity was discovered by K. Onnes studying mercury in 1911.[14] In 1987, high temperature superconductors (HTS) based on metal oxides such as the $YBa_2Cu_3O_{7-\delta}$ were discovered,[15] which has a critical temperature of 92 K. A superconductor is a material whose properties allow to transport the electrical current without energy loss. This property is limited by three critical conditions: temperature (T_c), external magnetic field (H_c) and current (J_c). These parameters limited the working conditions of the superconductor, and if one of them is exceeded, the superconductivity is broken, passing the material to be a normal conductor (see figure (a)) .

Complementarily to the current capabilities, is worth mentioning the Meissner effect, that consist of the expulsion of the external magnetic field by the superconducting material (fact that allows the superconductor to "levitate" on a magnetic field). Once a H_c is achieved, the magnetic flux lines penetrates into the material breaking down the superconductivity.

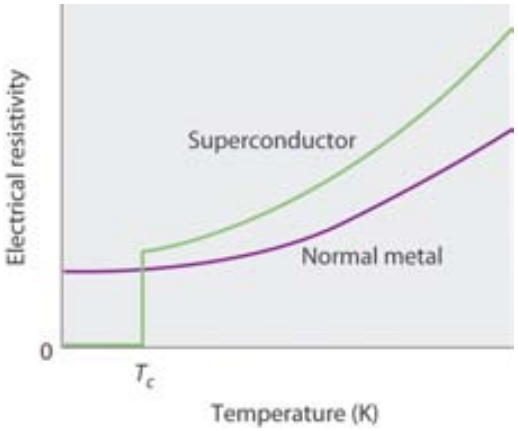

Figure 1.4: Diagram comparing the resistance in function of the temperature of a normal and superconducting metal.

Two species of superconductors can be differentiated: type I and type II. The main difference among them is that when the critical conditions are achieved, the first one becomes a normal conductor, where the external magnetic field can penetrate into the material, while the denominated

II pass through a mixed state (denominated Meissner state) between the normal and the superconducting one (gure (b)). In this state, the external magnetic eld penetrates into the material (without break the superconductivity) forming magnetic vortex: quantum cylindrical magnetic ux lines. As a result, the range of working of the type II SC is increased, but because the energy dissipation by the movement of these vortex, their superconducting capabilities are also gradually loss.

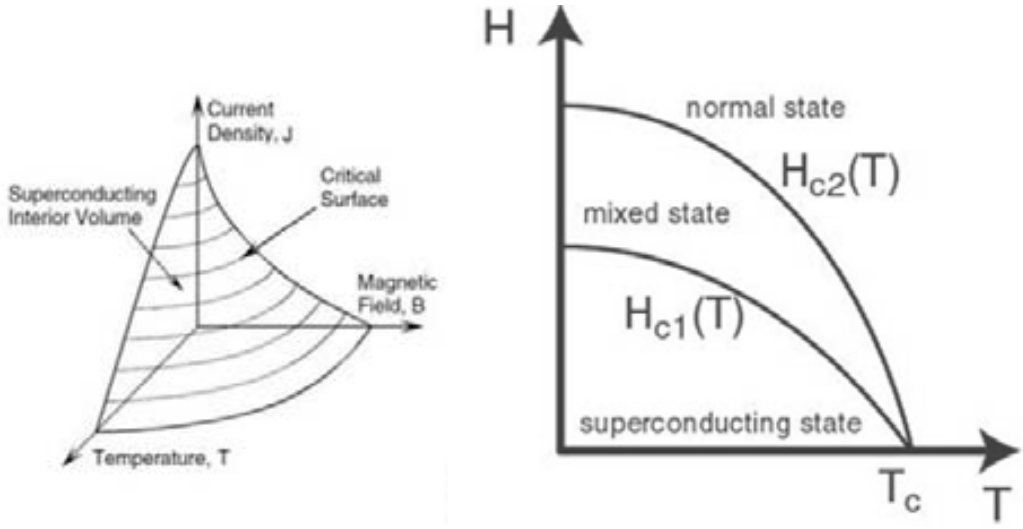

(a) Working limits of a superconductor (b) States of a type II HTS

Figure 1.5: Critical limits of a superconductor (a)[16] and states of a type II superconductor (b)[17] where the Meissner (mixed) state can be di erentiated.

When the penetration of the external magnetic eld H increase, more and more magnetic vortex are generated until reach the H_c, point where the superconductivity properties are lost. In order to increase the H_c value, new proposes to limit the movement of these vortex is being studied. knowing that their apparition cannot be avoided, it is possible to reduce their displacement to limit their energy dissipation by the use of non-superconducting regions inside the structure which will produce a vortex anchorage (pinning). In a short view, the decay of the superconducting properties can be belated by the pinning of the magnetic vortex, increasing as consequence the superconducting capabilities.

1.3.1 Vortex pinning

Vortex pinning is the phenomenon trough the magnetic vortex are anchored inside the superconducting structure, avoiding their movement and as consequence their energy dissipation.[14]

Vortex anchorage capability depends on the shape, size and distribution of the structural defects present in the superconducting material matrix. Image 1.6, shows the main defects present for the case of YBCO, the superconducting structure studied in this work.

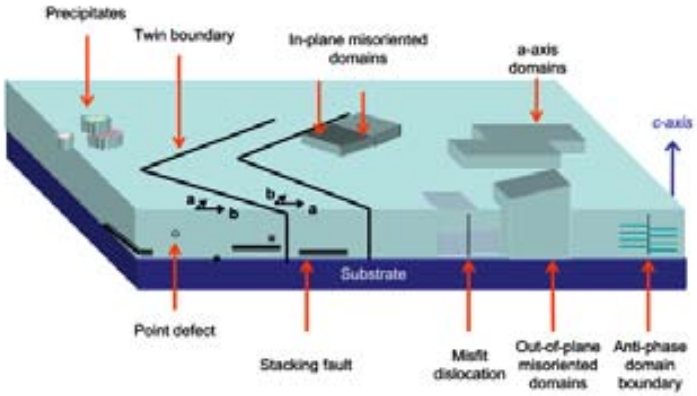

Figure 1.6: Structural defects present in YBCO epitaxial thin lms.[18]

These natural defects can act themselves as vortex pinning, but if some of them are present in large quantities (such as: precipitates, a-axis domains, dislocations, anti-phase domains, etc.) the superconductivity properties can be decreased because large non-superconductivity regions are generated. With the aim to control these structural defects (that act as pinning centres), a research eld in superconductivity is focused on the generation of arti cial no superconducting regions inside the structure with the main objective to control their quantity, distribution, shape, etc. In the chapter 2, section 2.3, an explanation of the methodology to produce $YBa_2Cu_3O_7$ nanostructured layers with nanoparticles embedded is developed.

1.3.2 Applications

Applications of the superconducting materials occupy a spread scienti c and practical eld.[19] Here, a pair of the actual applications are brie y explained:

1. Electronics: Based generally on the Josephson junctions, different applications can be found in this field, such as SQUID (*Superconducting QUantum Interference Device*). This device contains two Josephson junctions which works with superconducting materials and it is used to the measure of low magnetic fields (even 10^{-6} emu); Bolometer, system to detect all electromagnetic radiations coming from an object, founded on the temperature variation of the superconductor by the radiation (changing their resistance); digital components profiting the currents circulating inside the Josephson junction, generating 0 and 1 bits, etc.

2. Power: From cable conductors with high efficiency to magnets for Magnetic Resonance Imaging, passing through magnets for high energy physics and magnetic levitation. Also, new motors with higher power can be developed due to the high current transport capabilities of the superconducting materials.

For all of these applications and more, studies in the improvement of superconducting materials are being carried out by several groups of research. In this work, the efforts have been focused in to generate new nanocomposite YBCO superconducting layers with magnetic MFe_2O_4 nanoparticles embedded, whose properties have been deeply studied as synthesised and when embedded inside the superconducting nanostructured layer.

Bibliography Chapter 1

[1] L. M. Liz-Marzan, "Nanometals: formation and color," *Materials Today*, pp. 26–31, 2004. (cited on page(s) 31)

[2] Y. A. Koksharov, *Magnetism of nanoparticles : Effects of size, shape, and interactions*. wiley-vch ed., 2009. (cited on page(s) 31)

[3] A. Alivisatos, "Semiconductor clusters, canocrystals, and Quantum Dots," *Science*, vol. 271, no. 5251, pp. 933–937, 1996. (cited on page(s) 31)

[4] T. Takagahara, "Effects of dielectric confinement and electron-hole exchange interaction on excitronic states in semiconductor quantum dots," *Physical Review B*, vol. 47, no. 8, pp. 4569–4584, 1993. (cited on page(s) 31)

[5] J. Kruenate, R. Tongpool, T. Panyathanmaporn, and P. Kongrat, "Optical and mechanical properties of polypropylene modified by metal oxides," *Surface and Interface Analysis*, vol. 36, no. 8, pp. 1044–1047, 2004. (cited on page(s) 31)

[6] R. Banerjee, R. Jayakrishnan, and P. Ayyub, "Effect of the size-induced structural transformation on the band gap in CdS nanoparticles effect of the size-induced structural transformation on the band gap in CdS nanoparticles," *Journal of physics. Condensed matter*, vol. 12, pp. 10647–10654, 2000. (cited on page(s) 32)

[7] J. E. Tasca, A. Ponzinibbio, G. Diaz, R. D. Bravo, A. Lavat, and M. G. Gonzalez, "$CuFe_2O_4$ nanoparticles: A magnetically recoverable catalyst for selective deacetylation of carbohydrate derivatives," *Topics in Catalysis*, vol. 53, no. 15-18, pp. 1087–1090, 2010. (cited on page(s) 32)

[8] L. He, Y. Yu, C. Zhang, and H. He, "Complete catalytic oxidation of o-xylene over CeO_2 nanocubes," *Journal of Environmental Sciences*, vol. 23, no. 1, pp. 160–165, 2011. (cited on page(s) 32)

[9] B. Ingham, T. H. Lim, C. J. Dotzler, A. Henning, M. F. Toney, and R. D. Tilley, "How nanoparticles coalesce: An in situ study of Au nanoparticle aggregation and grain growth," *Chemistry of Materials*, vol. 23, no. 14, pp. 3312–3317, 2011. (cited on page(s) 32)

[10] S. Laurent, D. Forge, M. Port, A. Roch, C. Robic, L. Vander Elst, and R. N. Muller, "Magnetic iron oxide nanoparticles: synthesis, stabilization, vectorization, physicochemical characterizations, and biological applications," *Chemical reviews*, vol. 108, no. 6, pp. 2064–110, 2008. (cited on page(s) 32)

[11] J. Stöhr and H. C. Siegmann, *Magnetism: from fundamentals to nanoscale dynamics*. Springer, 2006. (cited on page(s) 33, 146)

[12] Image modified from `http://goo.gl/m61NP`. Access Jan. 2013. (cited on page(s) 35)

[13] H. Goesmann and C. Feldmann, "Nanoparticulate functional materials," *Angewandte Chemie*, vol. 49, no. 8, pp. 1362–1395, 2010. (cited on page(s) 36)

[14] A. Llordes, K. Zalamova, S. Ricart, A. Palau, A. Pomar, T. Puig, A. Hardy, M. K. Van Bael, and X. Obradors, "Evolution of metal-trifluoroacetate precursors in the thermal decomposition toward high-performance $YBa_2Cu_3O_7$ superconducting films," *Chemistry of Materials*, vol. 22, no. 5, pp. 1686–1694, 2010. (cited on page(s) 37, 39, 55)

[15] M. K. Wu, J. R. Ashburn, C. J. Torng, P. H. Hor, R. L. Meng, L. Gao, Z. J. Huang, Y. Q. Wang, and C. W. Chu, "Superconductivity at 93 K in a new mixed-phase Y-Ba-Cu-O compound system at ambient pressure," *Physical Review Letters*, vol. 58, no. 9, pp. 908–910, 1987. (cited on page(s) 37, 53)

[16] Image taken from `http://goo.gl/ud7id`. Access Jan. 2013. (cited on page(s) 38)

[17] Image taken from `http://goo.gl/Gl9sL`. Access Dec. 2012. (cited on page(s) 38, 53)

[18] A. Llordes i Gil, *Superconducting nanocomposite films grown by chemical solution deposition: Synthesis, microstructure and properties.* PhD thesis, ICMAB-UAB, 2010. (cited on page(s) 39, 54, 94, 95)

[19] V. Z. Kresin and S. A. Wold, *Fundamentals of superconductivity.* plenum press ed., 1990. (cited on page(s) 39)

Part II

Nanostructured Materials

Chapter 2

Introduction

Contents

Research in nanostructured materials is currently a high impact scientific field due to their present and potential future applications. For this research, among the different field in nanomaterials research, two principal kinds of nanostructured systems have been studied with the aim to combine them to generate new improved materials. These materials are magnetic ferrite nanoparticles (MFe_2O_4) and high temperature superconductors (HTS). The intrinsic properties of both nanostructured systems can be mixed to generate new superconducting materials with better current transport capabilities.

In this chapter, a brief introduction concerning the generation and properties of MFe_2O_4 and HTS (specifically $YBa_2Cu_3O_{7-\delta}$, abbreviated as $YBCO$) are discussed, taking into account the generation of nanocomposite nanostructured YBCO thin layers with MFe_2O_4 nanoparticles embedded inside the crystal structure.

2.1 Ferrite magnetic nanoparticles

Ferrite magnetic nanoparticles are a subclass of magnetic nanoparticles based on an iron oxide structure: the magnetite.

Magnetite is an iron (II) and iron (III) oxide (Fe_3O_4), and by substituting the iron (II) by another divalent cation, a new family of compounds is presented: the ferrites (MFe_2O_4). These compounds have been structurally and magnetically studied for ages due to their magnetic applications, and nowadays, new future perspectives to use these compound in a nanoscale size are being developed (as in this report). Here, the synthesis, characterisation and applications of a family of ferrites MFe_2O_4 (M= Mn, Fe, Co, Ni, Cu, Zn) is treated. Below, a description of the structure, properties and synthetic methodologies are resumed with the aim to better understanding the ferrites, which are a fundamental part of this work.

2.1.1 Structure and magnetism

i Crystal structure

Ferrite structure (MFe_2O_4) is a face-centred cubic close packing of O^{2-} anions where the divalent cation M^{2+} and the Fe^{3+} occupy 1/2 of the octahedral (B) and 1/8 of

the tetrahedral (A) interstitial holes of the structure (AB_2O_4). Eight molecules of MFe_2O_4 generate the unit cell with a $Fd3m$ symmetry.

Two di erent types of spinels can be di erentiated: normal and inverse. Normal spinel consists of a AB_2O_4 structure (like $MgAl_2O_4$) where the divalent cation occupies the tetrahedral sites while the trivalent cation occupies the octahedral ones. In some cases, as it will be discussed, an inversion of the crystallographic position can occur, and the divalent cations displaces the half of Fe^{3+}, generating a structure where the divalent cation occupies the half of the octahedral sites, while the Fe^{3+} is located in both, the tetrahedral (A) and octahedral (B) crystallographic occupied positions. A general formula to di erentiate normal and inverse spinel can be writing as:

$$\text{Normal spinel: } (A^{II})^A(B^{III})_2^BO_4$$
$$\text{Inverse spinel: } (B^{III})^A(A^{II}B^{III})^BO_4$$

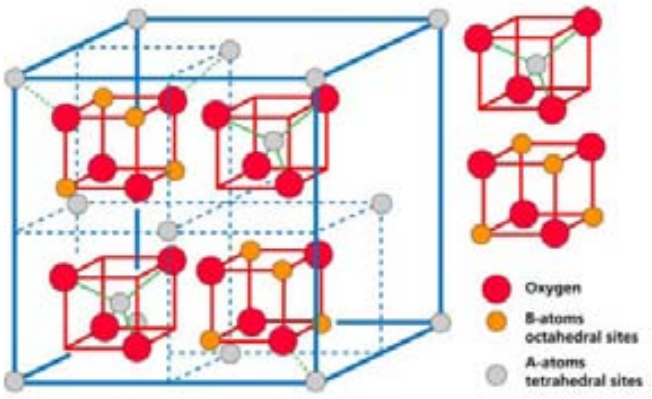

Figure 2.1: Graphic representation of the spinel structure.[1] Note the two (octahedral and tetrahedral) subunits, which are repeated four times in one unit cell.

Properties of the spinel can be adapted by changing the cations nature, and for this case, by changing the nature of the divalent cation. One of the most important e ects of change this ion is that the structure can vary between the normal and inverse spinel, modifying subsequently their physicochemical characteristics. For example, at bulk scale, magnetite (Fe_3O_4), cobalt ferrite ($CoFe_2O_4$)... are an inverse spinel structure, while zinc ferrite ($ZnFe_2O_4$) is a normal one. Normal or inverse structure comes de ned generally by crystal eld energy, but in some cases, when the generation of the crystal has been produced at low temperature and/or short time, atomic mobility is not enough to produce a perfect cationic distribution in

the spinel structure, giving as a result a crystal with a certain inversion degree i (0 i 1). Following this, a general formula (and speci c for ferrite structures) taking into account the inversion degree can be wrote:

$$(M^{2+})_1^A{}_i(Fe^{3+})_i^A(M^{2+})_i^B(Fe^{3+})_2^B{}_iO_4$$

Properties of ferrite spinel structures can be also controlled and selected by changing this inversion degree, because the physicochemical characteristics are correlated with this parameter. One of the most remarkable characteristics that can be tuned by the inversion degree is the magnetism.

ii Magnetism and spinel structure

Spinel structure at bulk scale presents a ferrimagnetic behaviour, where the orientation of the magnetic spin of the cations situated in the octahedral (Oh) sites are antiparallel with which ones of the tetrahedral (Td).[2] The spin magnetic moment is directioned in the diagonal of the crystallographic cube (direction [1 1 1]).

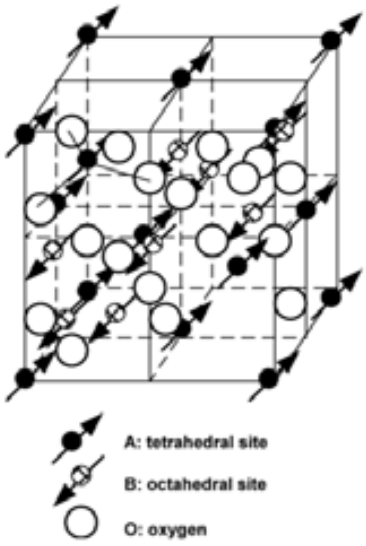

Figure 2.2: Partial representation of the magnetic cell of the spinel.[2] Note that the magnetic moment vectors are oriented in the diagonal of the cube and are antiparallel between the A and B sublattices

Global net magnetism comes determined by the di erence in the contribution of the Oh and Td sites, and then, by selecting the metallic cation (maintaining constant

Fe^{3+}) and the distribution among the different crystallographic sites, it is possible to generate a tunable magnetic system. This modifiable parameter comes from the electronic configuration of each atom, because it gives different magnetic properties depending on their electronic configuration.

Magnetic properties of spinel ferrite has been studied to control, adapt, and apply their behaviour to new systems in different scientific-technical fields, such as: informatics,[3, 4] chemistry,[5, 6] medicine,[7] food science,[8] etc. Nowadays, the development of new nanostructured systems generates a new vision of applications, because ferrites present a superparamagnetic behaviour. Interest in these nanostructured magnets have been increase exponentially last years due to the new generation techniques[9, 10] and applications.[11, 12]

2.1.2 Synthetic routes

Since now, different procedures to generate magnetic ferrite nanoparticles have been reported. The methodology classifies several synthetic routes, which depending on the final application, have to be selected. Sonochemical,[13, 14] microemulsions,[15, 16] metal-organic decomposition,[17, 18] coprecipitation,[19, 20] solvothermal,[21, 22] etc. In the case that is presented here, a thermal chemical decompositon methodology based on the polyol and oleylamine route have been optimised.

1. Polyol route: This is a synthetic methodology to generate nanocrystals using a short chain glycol,[23] such as ethyleneglycol, diethyleneglycol, etc. It has been demonstrated previously that the use of these glycols to prepare magnetic ferrite nanoparticles is an adequate methodology.[24]

   Functions of the glycol are principally two: as solvent of the reaction mixture and capping ligand of the nanocrystals formed. In addition, the high boiling point of the glycol makes the reaction mixture capable to achieve temperatures of hundreds of degrees (depending of the kind of glycol), increasing the crystallinity of the NPs.[25] In the case presented here, which continues previous presented works,[17, 24] a new one-pot synthetic route using TREG as capping ligand has been developped and optimised.

   In a short view, the polyol route consists of the releasing of metal cations by

the thermal decomposition of metal-organic molecules. Thermal conditions and chemical properties of the solvent cause the formation of the more stable structure: the spinel. The growth of the resulting nanoparticles is controlled by the presence of the capping ligand (TREG), molecule which coordinated on the surface and avoids the incorporation of new atoms to the nanostructure and/or their coalescence.

2. Oleylamine route: By changing only the solvent of the reaction mixture (TREG) by Oleylamine (Oleyl)[17, 26] and following the same procedure, similar ferrites are synthesised with this new capping ligand.[27]

The dispersibility of the nanoparticles is determined by the interaction of the stabilising system (capping ligand) with the solvent. Due to TREG is a polar molecule, the nanoparticles generated are dispersibles in polar solvents (such as water, alcohols, chloroform, etc.), while nanocrystals synthesised with Oleyl as capping ligand are dispersibles in non-polar solvents (hexane, toluene, etc.) due to their non-polar properties.

In the chapter 3, section 3.1, a detailed explanation of the synthetic methodology will be presented.

2.2 $YBa_2Cu_3O_{7-\delta}$ superconducting layers

$YBa_2Cu_3O_{7-\delta}$ is a type II superconducting material that is presently investigated to improve their superconducting properties and to generate more efficient superconducting layers and wires. This research is based on the preparation of thin films (∼200 nm up to 1000 nm) of epitaxial YBCO supported on a $LaAlO_3$ (LAO) (1 0 0) oriented single crystal. The results obtained are extrapolated to the fabrication of multilayer coated conductors to produce long (hundreds of meters) of high efficient superconducting wires.

2.2.1 Structure and properties

YBCO can be considered as a triple perovskite structure ABO_3, formed by two $BaCuO_3$ cubes and a central $YCuO_3$ cube with anion deficiency in the plane (z=1/2)

(See gure 2.3). The crystallographic structure of the YBCO depends on the anion (oxygen) de ciency[28] which is correlated with χ. For high anion vacancies ($\chi > 0\ 5$), YBCO has a tetragonal structure which is not superconducting. But, in the case that $1 > \chi > 0\ 5$, a phase transition occurs until an orthorhombic structure, which is the superconducting one. By controlling the anion de ciency, improved YBCO superconducting crystal can be generated, demonstrating that for a χ 0 06, the better current capabilities could be achieved ($YBa_2Cu_3O_{6\ 94}$).[29]

YBCO was discovered in 1987[30] with a T_c $92K$, being classi ed as a High Temperature Superconductor (HTS). This new category of HTS is de ned by the existence of a mixed state between the normal state and the superconducting one. In this mixed state, when a external magnetic eld is applied, the magnetic ux lines penetrates into the superconductor, generating magnetic quantum vortex which produces energy dissipation. In spite of this disadvantage, it implies the possibility to work under high intense external magnetic eld without loss completely their superconducting properties, fact that is really interesting for most eld, remarking engineering with new electric motors with high power.

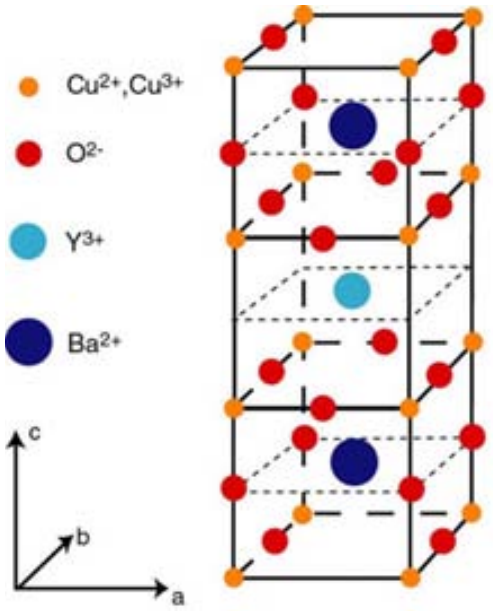

Figure 2.3: YBCO crystal structure.[31] The crystal orientation is also identi ed.

Superconducting properties of YBCO are present along their single crystal structure, making that crystal defects (grain boundaries, dislocations, misoriented domains, etc.) decrease or break the superconducting continuity. With the aim

to produce a continuous superconducting wire, long tapes are fabricated through chemical solution deposition (CSD) route on an epitaxial substrate. At laboratory scale, this substrate is a (1 0 0) oriented $LaAlO_3$ (LAO) single crystal, where the YBCO crystal is grown epitaxial with the z-axis perpendicular to the surface. The selection of this substrate is due to their similar cell parameters with the YBCO a and b directions. The following table 2.1 compares the cell parameters of YBCO and LAO:[32]

	Cell parameters (Å)	
YBCO ($\delta \approx 0.1$)	a	3.823
	b	3.886
	c	11.684
LAO	a=b=c	3.792

Table 2.1: Comparison of crystal cell parameters between YBCO and LAO

As it can be seen, the mismatching between the LAO and the YBCO a and b directions is less than 2.5 %, making the LAO as an adequate substrate to growth YBCO epitaxially on it.

Generation of YBCO superconducting layers on LAO substrate can carried out by different techniques through CSD, and among them, two have been selected: spin-coating and ink-jet printing, as they will be explained at the point 2.2.3.

2.2.2 Chemical precursors

Manufacturing of YBCO on LAO single crystals is carried out by a CSD route. It consists of the deposition on a substrate a chemical solution with the desired composition that after a thermal procedure, the required compound will be formed. In the case of YBCO, a precursors of different cations are needed, and among different possibilities, the metal trifluoroacetates $[M(CF_3COO)_n]$ in anhydrous methanol is one of the most adequate chemical precursor.[33, 34]

Importance of the fluoride precursors is due to the chemistry reactions of the different steps in the process.[35] To generate YBCO from the trifluoroacetates solution,[33, 36] it is needed a first thermal treatment (from room temperature up to

310^{o}C) called *Pyrolysis*, where the solvent is evaporated and the organic precursors decomposed. Here, di erent chemical phases are formed,[37] such as Y_2O_3 CuO and BaF_2. The last compound is crucial to avoid the formation of $BaCO_3$, which can produce deleterious e ects on the nal superconducting properties due to the presence of the residual carbon on the nal layer. After this rst step, a *Growth* of the YBCO on the LAO single crystal is carried out until 810^{o}C with a controlled temperature ramp and atmosphere. All of this thermal process has been optimised in order to obtain the better results in YBCO crystal structure, and then, performance.

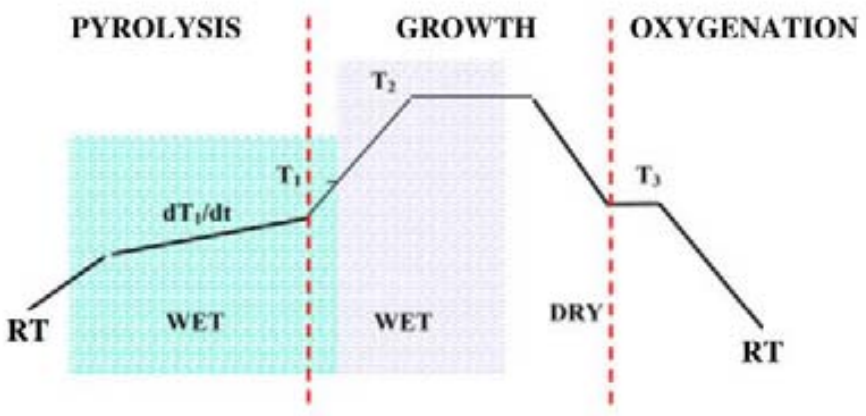

Figure 2.4: General scheme of the thermal process to generate YBCO layers.[33] Note the two main parts: Pyrolysis and Growth jointly with oxygenation with dry or wet atmosphere.

After the thermal process, epitaxial YBCO, that has been grown on the LAO substrate, has been produced. This process can be repeated in order to obtain a thicker lm of YBCO until 2 microns.[35]

2.2.3 Synthetic methodology

Two principal methodologies are used to generate YBCO superconducting layers by CSD: spin-coating and ink-jet printing (see gure 2.5). Both manufacturing routes generates similar thin lms of YBCO layers, being ink-jet printing the adequate one to generate long superconducting tapes. Below, a short explanation of these systems is presented:

i Spin-coating

Technique which is based on a deposition of a drop (15 µl) on a substrate and spinned at high revolutions (for example 6000 r.p.m.) during several seconds ($\sim$ 30 s). With this procedure, a thin layer of solution wet the surface homogeneously. Afterwards, the substrate with the thin liquid film deposited is thermally treated to evaporate the solvent, generating a layer of solid compounds on the surface.

Spin coating conditions such as the acceleration, spin rotation, time, etc. determinate the amount of the liquid deposited on the substrate, and as consequence, the final thickness of the layer generated.[38]

ii Ink-jet printing

Methodology consisting of the continuous deposition, drop by drop, of a chemical solution on a substrate. The drops formation rate, jointly with the coordinated movement of the substrate, make a controlled deposition of drops (volume, frequency, pattern shape...), allowing the formation of a pattern with the desired chemical composition.

The drop formation occurs because the vibration of a piezoelectric governed by an electrical current. Single or multinozzle headprinters can be used and coordinated with the substrate movement to make a faster printing of the chemical solution, allowing to produce a printing with a controlled spacing and quantity of the YBCO chemical solution on the LAO substrate. After the printing process, a thermal treatment is needed to generate a continuous thin film. This optimised process generates similar thin film layers than the laboratory spin coating technique with the advantage to exactly control the amount of the solution deposited.

Using ink-jet printing systems, the volume of the drop, their space, the rheological parameters, etc. make the conditions to generate a layer with a specific thickness, shape, etc.[39, 40]

These methodologies have been applied in order to generate YBCO superconducting layers and nanocomposite YBCO-NPs nanocomposites. However, ink-jet printing, by its part, is one of the most promising techniques to manufacture long superconducting tapes because spin coating is limited to laboratory scale. With

the proper ink-jet system (multi injection, continuous solution...), coupled with the adequate control temperature (furnace) and atmosphere, it is possible to produce a continuous long YBCO superconducting tapes.

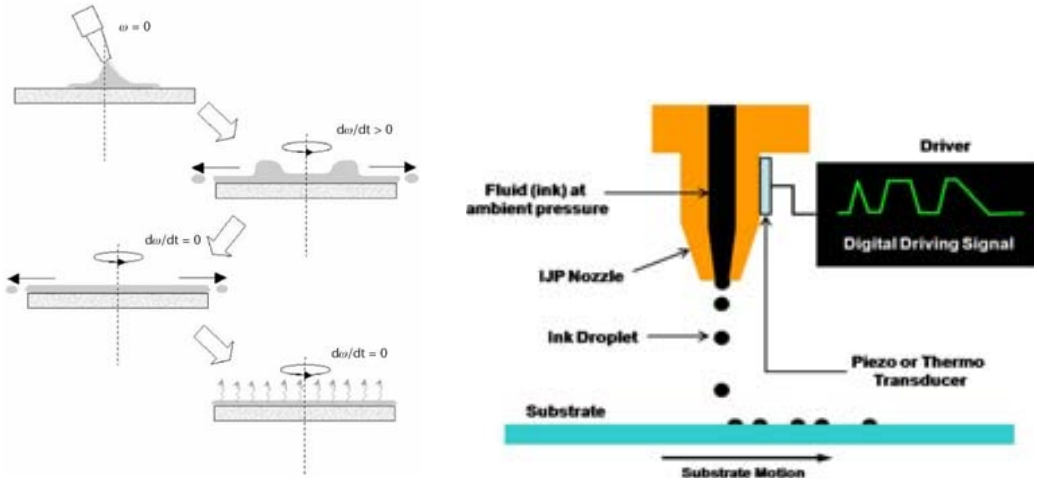

(a) Spin coating (b) Ink-jet printing scheme

Figure 2.5: Graphical comparison of spin-coating (a)[41] and ink-jet printing (b)[42] technologies.

2.3 $YBa_2Cu_3O_7$ nanocomposite superconducting layers

YBCO nanostructured layers have been demonstrated to be high e cient systems with high current capabilities. Magnetic vortex motion along the YBCO structure generates energy dissipation, decreasing the current transport properties of the superconductor. The generation of controlled crystal defects inside the YBCO crystal matrix can control the displacement of these vortex, avoiding energy loss and in consequence, improving their sperconducting parameters.

2.3.1 Improvement of superconducting capabilities

Focusing in to produce more e cient superconducting long tapes or coated conductors of YBCO, new nanocomposite nanocomposites are being developed. Because the

generation of controlled crystal defects in the YBCO can improve the superconducting properties,[43] the inclusion of other structural and compositional phases inside the structure can do it.[44] Non-superconducting nanostructured regions can act as vortex pinning centres due to principally two phenomena that are actually under discussion: by to be non-superconducting regions by themselves, and by generating a distortion of the YBCO matrix, producing internal crystallographic microstrain that acts as vortex pinning centres.[45, 46]

Pinning centres work as long as the crystallographic distortions reach, so many of them are needed to produce an efficient pinning global effect. But, as drawback, the generation of too much non-superconducting regions can break the global superconductivity performance. In order to fix this, a new concept of vortex pinning has been developed and studied: magnetic vortex pinning.[47] This new concept develops the idea that the magnetic field produced by the magnetic nanostructures embedded inside the YBCO have larger interaction volume, doing that less structures can reach larger pinning distances, improving the superconducting properties even more than normal pinning. Under this concept, it has been investigated the inclusion of magnetic ferrite nanoparticles inside the YBCO matrix and study their properties.

2.3.2 Generation of controlled defects

Previous research in superconducting materials has been showed that the generation of crystal defects by including nanostructured materials (as for example nanoparticles), is a promising way to improve the current transport capabilities.[45] The approach to generate these nanoparticles inside the superconducting structure can be taken by two ways: *in-situ* or *ex-situ*:

1. *In-situ*: It is based on the addition of the napoparticles chemical precursors to the YBCO chemical solution and follow the same procedure as it was a pure YBCO layer. Because YBCO is formed, the other precursors will form the stablest crystal structure inside the YBCO matrix (always if both structures are compatibles, if not they will segregate). By the deficiency of localised precursor, the structure formed will have a limited size in nanoscale range (around tens of nanometers or less).

2. *Ex-situ*: This approach uses nanoparticles preformed and characterised pre-

viously to incorporate them into the superconducting layer before growing. Basically the procedure is to mix the YBCO precursor solution with the nanostructured preformed material and deposit the solution on the substrate, or even modify the substrate at the nanoscale and to make growth the YBCO on it.

Although *in-situ* methodology seems to be more complicated to perform (because the need of control the crystallisation temperatures of the chemical precursors after the decomposition and the coalescence of the secondary phase nanoparticles) to generate non-superconducting defects of the adequate size in the material, is the *ex-situ* methodology that requires also high efforts. First of all, the generation and control of the nanostructure synthesised externally; second, the structural compatibility of the YBCO and the external phase, because if not, a segregation of the nanocrystals outside the superconducting layer occurs;[48] finally, and not less important, it is the methodology to embedded these nanostructured crystals inside the superconducting matrix without break the continuous superconductivity capabilities.

In this research, the development of new nanocomposite superconducting layers nanostructured with ferrite magnetic nanoparticles MFe_2O_4 prepared by *ex-situ* methodology has been studied. In addition, the structure and properties of YBCO with NPs embedded by *in-situ* procedure containing different kinds of nanostructures has been investigated.

Bibliography Chapter 2

[1] C. Degueldre, G. Kuri, C. N. Borca, and D. Grolimund, "X-ray micro- fluorescence, diffraction and absorption spectroscopy for local structure investigation of a radioactive zinc ferrite deposit," *Corrosion Science*, vol. 51, no. 8, pp. 1690–1695, 2009. (cited on page(s) 49)

[2] D. S. Mathew and R.-S. Juang, "An overview of the structure and magnetism of spinel ferrite nanoparticles and their synthesis in microemulsions," *Chemical Engineering Journal*, vol. 129, no. 1-3, pp. 51–65, 2007. (cited on page(s) 50)

[3] W. Hu, N. Qin, G. Wu, Y. Lin, S. Li, and D. Bao, "Opportunity of spinel ferrite materials in nonvolatile memory device applications based on their resistive switching performances," *Journal of the American Chemical Society*, vol. 134, no. 36, pp. 14658–14661, 2012. (cited on page(s) 51)

[4] V. Kumbhar, A. Jagadale, N. Shinde, and C. Lokhande, "Chemical synthesis of spinel cobalt ferrite ($CoFe_2O_4$) nano-flakes for supercapacitor application," *Applied Surface Science*, vol. 259, pp. 39–43, 2012. (cited on page(s) 51)

[5] R. Benrabaa, H. Boukhlouf, A. Löfberg, A. Rubbens, R.-N. Vannier, E. Bordes-Richard, and A. Barama, "Nickel ferrite spinel as catalyst precursor in the dry reforming of methane: Synthesis, characterization and catalytic properties," *Journal of Natural Gas Chemistry*, vol. 21, no. 5, pp. 595–604, 2012. (cited on page(s) 51)

[6] D. Hong, Y. Yamada, T. Nagatomi, Y. Takai, and S. Fukuzumi, "Catalysis of nickel ferrite for photocatalytic water oxidation using $[Ru(bpy)_3]^{2+}$ and $S_2O_8^{2-}$," *Journal of the American Chemical Society*, vol. 134, no. 48, pp. 19572–19575, 2012. (cited on page(s) 51)

[7] S. Amiri and H. Shokrollahi, "The role of cobalt ferrite magnetic nanoparticles in medical science," *Materials Science and Engineering: C*, vol. 33, no. 1, pp. 1–8, 2013. (cited on page(s) 51)

[8] M. Cao, Z. Li, J. Wang, W. Ge, T. Yue, R. Li, V. L. Colvin, and W. W. Yu, "Food related applications of magnetic iron oxide nanoparticles: Enzyme immobilization, protein purification, and food analysis," *Trends in Food Science & Technology*, vol. 27, no. 1, pp. 47–56, 2012. (cited on page(s) 51, 160)

[9] W. Feng, L.-D. Sun, Y.-W. Zhang, and C.-H. Yan, "Synthesis and assembly of rare earth nanostructures directed by the principle of coordination chemistry in solution-based process," *Coordination Chemistry Reviews*, vol. 254, no. 9-10, pp. 1038–1053, 2010. (cited on page(s) 51, 71, 72)

[10] R. Hao, R. Xing, Z. Xu, Y. Hou, S. Gao, and S. Sun, "Synthesis, functionalization, and biomedical applications of multifunctional magnetic nanoparticles," *Advanced Materials*, vol. 22, no. 25, pp. 2729–42, 2010. (cited on page(s) 51)

[11] M. Sugimoto, "The past, present, and future of ferrites," *Journal of American Ceramic Society*, vol. 83, no. 2, pp. 269–280, 1999. (cited on page(s) 51)

[12] R. Valenzuela, "Novel Applications of Ferrites," *Physics Research International*, vol. 2012, pp. 1–9, 2012. (cited on page(s) 51)

[13] D. Chen, H. Liu, and L. Li, "One-step synthesis of manganese ferrite nanoparticles by ultrasonic wave-assisted ball milling technology," *Materials Chemistry and Physics*, vol. 134, no. 2-3, pp. 921–924, 2012. (cited on page(s) 51)

[14] H. A. Choudhury, A. Choudhary, M. Sivakumar, and V. S. Moholkar, "Ultrasonics sonochemistry mechanistic investigation of the sonochemical synthesis of zinc ferrite," *Ultrasonics - Sonochemistry*, vol. 20, no. 1, pp. 294–302, 2013. (cited on page(s) 51)

[15] K. Wongwailikhit and S. Horwongsakul, "The preparation of iron (III) oxide nanoparticles using W/O microemulsion," *Materials Letters*, vol. 65, no. 17-18, pp. 2820–2822, 2011. (cited on page(s) 51)

[16] M. A. Malik, M. Younus, and M. A. Hashim, "Microemulsion method: A novel route to synthesize organic and inorganic nanomaterials," *Arabian Journal of Chemistry*, vol. 5, no. 4, pp. 397–417, 2012. (cited on page(s) 51)

[17] S. Sun, H. Zeng, D. B. Robinson, S. Raoux, P. M. Rice, S. X. Wang, and G. Li, "Monodisperse MFe_2O_4 (M = Fe, Co, Mn) nanoparticles," *Journal of the American Chemical Society*, vol. 126, no. 1, pp. 273–279, 2004. (cited on page(s) 51, 52)

[18] P. Guardia, J. Perez-Juste, A. Labarta, X. Batlle, and L. M. Liz-Marzan, "Heating rate influence on the synthesis of iron oxide nanoparticles: the case of decanoic acid," *Chemical Communications*, vol. 46, no. 33, pp. 6108–6110, 2010. (cited on page(s) 51)

[19] X. Wang, J. Zhuang, Q. Peng, and Y. Li, "A general strategy for nanocrystal synthesis," *Nature*, vol. 437, no. 7055, pp. 121–124, 2005. (cited on page(s) 51)

[20] T. Hosono, H. Takahashi, A. Fujita, R. J. Joseyphus, K. Tohji, and B. Jeyadevan, "Synthesis of magnetite nanoparticles for AC magnetic heating," *Journal of Magnetism and Magnetic Materials*, vol. 321, no. 19, pp. 3019–3023, 2009. (cited on page(s) 51)

[21] X.-M. Liu and J.-K. Kim, "Solvothermal synthesis and magnetic properties of magnetite nanoplatelets," *Materials Letters*, vol. 63, no. 3-4, pp. 428–430, 2009. (cited on page(s) 51)

[22] J. Ma, J. Zhao, W. Li, S. Zhang, Z. Tian, and S. Basov, "Preparation of cobalt ferrite nanoparticles via a novel solvothermal approach using divalent iron salt as precursors," *Materials Research Bulletin*, vol. 48, no. 2, pp. 214–217, 2013. (cited on page(s) 51)

[23] C. Feldmann, "Polyol-Mediated Synthesis of Nanoscale Functional Materials," *Advanced Functional Materials*, vol. 13, no. 2, pp. 101–107, 2003. (cited on page(s) 51)

[24] W. Cai and J. Wan, "Facile synthesis of superparamagnetic magnetite nanoparticles in liquid polyols," *Journal of Colloid and Interface Science*, vol. 305, no. 2, pp. 366–370, 2007. (cited on page(s) 51, 68, 71)

[25] Y. Il, D. Kim, and C. Sub, "Synthesis and characterization of $CoFe_2O_4$ magnetic nanoparticles prepared by temperature-controlled coprecipitation method," *Physica B: Condensed Matter*, vol. 337, pp. 42–51, 2003. (cited on page(s) 51)

[26] Z. Xu, C. Shen, Y. Hou, H. Gao, and S. Sun, "Oleylamine as both reducing agent and stabilizer in a facile synthesis of magnetite nanoparticles," *Journal of Chemical Matter*, vol. 21, no. 9, pp. 1778–1780, 2009. (cited on page(s) 52)

[27] L. Perez-Mirabet, E. Solano, F. Martinez-Julian, R. Guzman, J. Arbiol, T. Puig, X. Obradors, A. Pomar, R. Yañez, J. Ros, and S. Ricart, "One-pot synthesis of stable colloidal solutions of MFe_2O_4 nanoparticles using oleylamine as solvent and stabilizer," *Materials Research Bulletin*, vol. 48, no. 3, pp. 966–972, 2013. (cited on page(s) 52, 85, 184)

[28] M. A. Beno, L. Soderholm, D. W. Capone, D. G. Hinks, and J. D. Jorgensen, "Structure of the single phase high temperature superconductor $YBa_2Cu_3O_{7-\delta}$," *Applied Physical Letters*, vol. 51, pp. 57–59, 1987. (cited on page(s) 53)

[29] V. R. Vlad, *Growth and characterization of chemical solution based nanostructured coated conductors with CeO_2 cap layers.* PhD thesis, ICMAB-UAB, 2011. (cited on page(s) 53)

[30] M. K. Wu, J. R. Ashburn, C. J. Torng, P. H. Hor, R. L. Meng, L. Gao, Z. J. Huang, Y. Q. Wang, and C. W. Chu, "Superconductivity at 93 K in a new mixed-phase Y-Ba-Cu-O compound system at ambient pressure," *Physical Review Letters*, vol. 58, no. 9, pp. 908–910, 1987. (cited on page(s) 37, 53)

[31] Image taken from `http://goo.gl/Gl9sL`. Access Dec. 2012. (cited on page(s) 38, 53)

[32] A. Llordes i Gil, *Superconducting nanocomposite films grown by chemical solution deposition: Synthesis, microstructure and properties.* PhD thesis, ICMAB-UAB, 2010. (cited on page(s) 39, 54, 94, 95)

[33] X. Obradors, T. Puig, A. Pomar, F. Sandiumenge, S. Piñol, N. Mestres, O. Castaño, M. Coll, A. Cavallaro, A. Palau, J. Gazquez, J. C. Gonzalez, J. Gutierrez, N. Roma, S. Ricart, J. M. Moreto, M. D. Rossell, and G. V. Tendeloo, "Chemical solution deposition: a path towards low cost coated conductors," *Superconductor Science and Technology*, vol. 17, no. 8, pp. 1055–1064, 2004. (cited on page(s) 54, 55)

[34] B. Rousseau, A. Canizares, E. Veron, R. Ramy-Ratiarison, A. Blin, D. De Sousa Meneses, P. Simon, F. Berberich, H. Graafsma, A. Pomar, N. Mestres,

T. Puig, and X. Obradors, "Characterisation of $YBa_2Cu_3O_{6+x}$ films grown by the trifluoro-acetate metal organic decomposition route by infrared spectroscopy," *Thin Solid Films*, vol. 515, no. 4, pp. 1607–1611, 2006. (cited on page(s) 54, 94)

[35] X. Obradors, T. Puig, S. Ricart, M. Coll, J. Gazquez, A. Palau, and X. Granados, "Growth, nanostructure and vortex pinning in superconducting $YBa_2Cu_3O_7$ thin films based on trifluoroacetate solutions," *Superconductor Science and Technology*, vol. 25, no. 12, p. 123001, 2012. (cited on page(s) 54, 55)

[36] H. Chen, K. Zalamova, A. Pomar, X. Granados, T. Puig, and X. Obradors, "Nucleation and growth rate influence on microstructure and critical currents of TFA-$YBa_2Cu_3O_7$ under low-pressure conditions," *Journal of Materials Research*, vol. 25, no. 12, pp. 2371–2379, 2010. (cited on page(s) 54)

[37] A. Llordes, K. Zalamova, S. Ricart, A. Palau, A. Pomar, T. Puig, A. Hardy, M. K. Van Bael, and X. Obradors, "Evolution of metal-trifluoroacetate precursors in the thermal decomposition toward high-performance $YBa_2Cu_3O_7$ superconducting films," *Chemistry of Materials*, vol. 22, no. 5, pp. 1686–1694, 2010. (cited on page(s) 37, 39, 55)

[38] T. Araki, H. Kurosaki, and Y. Yamada, "Coating processes for $YBa_2Cu_3O_{7-x}$ superconductor by metalorganic deposition method using trifluoroacetates," *Superconductor Science and Technology*, vol. 783, no. 14, pp. 783–786, 2001. (cited on page(s) 56)

[39] M. Vilardell, X. Granados, S. Ricart, R. Cobas, M. Arjona, T. Puig, X. Obradors, S. C. Hopkins, B. A. Glowacki, J. Bennewitz, M. Falter, and M. Bà̀cker, "Ink jet printing for functional ceramic coatings," *Journal of Imaging Science and Technology*, vol. 55, no. 4, p. 040304, 2011. (cited on page(s) 56, 98)

[40] I. Van Driessche, J. Feys, S. C. Hopkins, P. Lommens, X. Granados, B. A. Glowacki, S. Ricart, B. Holzapfel, M. Vilardell, A. Kirchner, and M. Bäcker, "Chemical solution deposition using ink-jet printing for YBCO coated conductors," *Superconductor Science and Technology*, vol. 25, no. 6, p. 065017, 2012. (cited on page(s) 56, 98)

[41] Image taken from `http://goo.gl/CkgGG`. Access Dec. 2012. (cited on page(s) 57)

[42] Image taken from `http://goo.gl/NiFHi`. Access Dec. 2012. (cited on page(s) 57)

[43] K. Matsumoto and P. Mele, "Artificial pinning center technology to enhance vortex pinning in YBCO coated conductors," *Superconductor Science and Technology*, vol. 23, no. 1, p. 14001, 2010. (cited on page(s) 58)

[44] A. Pomar, V. R. Vlad, A. Llordes, J. Gutierrez, S. Ricart, T. Puig, X. Obradors, A. Usoskin, and Y. S. Z. Ss, "Enhanced vortex pinning in YBCO coated conductors with BZO nanoparticles from chemical solution deposition," *IEEE Transactions on Applied Superconductivity*, vol. 19, no. 3, pp. 3258–3261, 2009. (cited on page(s) 58)

[45] J. Gutierrez, A. Llordes, J. Gazquez, M. Gibert, N. Roma, S. Ricart, A. Pomar, F. Sandiumenge, N. Mestres, T. Puig, and X. Obradors, "Strong isotropic flux pinning in solution-derived $YBa_2Cu_3O_{7-x}$ nanocomposite superconductor films," *Nature Materials*, vol. 6, no. 5, pp. 367–73, 2007. (cited on page(s) 58, 99)

[46] A. Llordes, A. Palau, J. Gazquez, M. Coll, R. Vlad, A. Pomar, J. Arbiol, R. Guzman, S. Ye, V. Rouco, F. Sandiumenge, S. Ricart, T. Puig, M. Varela, D. Chateigner, J. Vanacken, J. Gutierrez, V. Moshchalkov, G. Deutscher, C. Magen, and X. Obradors, "Nanoscale strain-induced pair suppression as a vortex-pinning mechanism in high-temperature superconductors," *Nature Materials*, 2012. (cited on page(s) 58)

[47] M. Velez, J. Martin, J. Villegas, A. Hoffmann, E. Gonzalez, J. Vicent, and I. K. Schuller, "Superconducting vortex pinning with artificial magnetic nanostructures," *Journal of Magnetism and Magnetic Materials*, vol. 320, no. 21, pp. 2547–2562, 2008. (cited on page(s) 58)

[48] F. Martinez-Julian, S. Ricart, A. Pomar, M. Coll, P. Abellan, F. Sandiumenge, M. J. Casanove, X. Obradors, T. Puig, I. Partoriza-Santos, and L. M. Liz-Marzan, "Chemical solution approaches to $YBa_2Cu_3O_{7-\delta}$-Au nanocomposite superconducting thin films," *Journal of Nanoscience and Nanotechnology*, vol. 11, no. 4, pp. 3245–3255, 2011. (cited on page(s) 59)

Chapter 3

Ferrite Magnetic Nanoparticles

Contents

In this chapter, the synthesis of the magnetic ferrite nanoparticles developed during this work is discussed. It starts with the experimental procedure, continuing with the methodology and precursors, and finishing with the characterisation: structure, composition and behaviour of the materials obtained with this procedure.

3.1 Synthesis

As commented before, the thermal procedure to prepare nanostructured ferrite nanocrystals is based on the polyol synthetic route,[1] where a metalorganic precursor is thermally decomposed in the glycolic solvent. In this study, a new optimised route to synthesise MFe_2O_4 magnetic ferrite nanoparticles through the decomposition of the corresponding metal acetylacetonates in triethylene glycol is presented via two procedures: thermal and microwave assisted methodology.[2]

3.1.1 Experimental procedure

Fabrication of ferrite nanoparticles is carried out via thermal and microwave[3] procedures, which generate similar nanostructures, as it will be discussed later. Next, the detailed experimental procedure is explained to obtain a 13 mM dispersion of free MFe_2O_4 NPs:

1. Thermal:

   0.64 mmol of $Fe(acac)_3$ with 0.32 mmol of $M(acac)_2$ for MFe_2O_4, or only 0.96 mmol of $Fe(acac)_3$ for Fe_3O_4, are mixed with 12.5 ml of triethylene glycol (TREG) in a 50 ml round-bottom flask. The initial red solution is introduced in an ultrasonic bath during 10 minutes to favour the dissolution of the precursors. Then, the mixture is heated under stirring with a controlled ramp of 1 ^oC/min until 280 ^oC, where the temperature is maintained during 150 minutes. Finally, the sample is naturally cooled down until room temperature.

2. Microwave radiation:

   0.64 mmol of $Fe(acac)_3$ with 0.32 mmol of $M(acac)_2$ for MFe_2O_4, or only 0.96 mmol of $Fe(acac)_3$ for Fe_3O_4, are mixed with 12.5 ml of triethylene glycol (TREG) in a 35 ml adapted microwave vial. The initial solution is introduced in

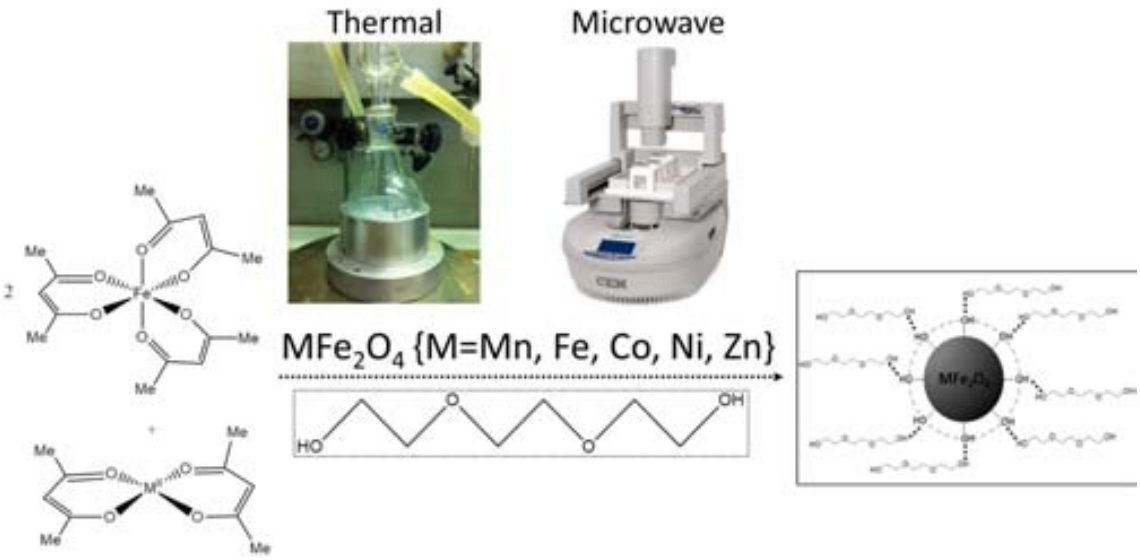

Figure 3.1: Scheme of the synthetic procedure to generate MFe_2O_4 magnetic nanoparticles via the two synthetic methodologies, thermal and microwave radiation assistance.

an ultrasonic bath during 10 minutes to favour the dissolution. Then, the initial reaction mixture is heated under stirring at 300 W of microwave power until 220 ^oC (for Fe, Co and Zn ferrites) or 280 ^oC (for Mn and Ni ferrites), where the temperature is maintained during only 10 minutes. Finally, the sample is cooled down until room temperature by an external room temperature nitrogen gas flow.

For both methodologies, the nanoparticles (MFe_2O_4) dispersed in TREG are separated and washed through magnetic precipitation by adding 12.5 ml of 1:4 ethanol:ethyl acetate solution. Obtained magnetic ferrite nanocrystals are then dispersed in the proper polar solvent, in this case, 25 ml of ethanol 96 %. For some applications, the NPs can be used as synthesised in TREG, because no byproducts are expected during the chemical process.

The reaction can be done to obtain different concentrations of nanoparticles up to 260 mM of final free MFe_2O_4. The scalability of the process makes the synthetic methodology more adaptable to the final use of the nanoparticles, where different concentration for the final applications could be needed. Moreover, final concentration of the NPs can be obtained by adding the proper volume of the desired solvent after the initial cleaning of the NPs.

The main di erence between both methodologies (thermal and microwave) used is mainly the heating method. While thermal is a continuous heating of the solution by thermal conduction, microwave is a radiation heating system. This e ect in uences in the fact that for thermal, a heating of the solution occurs from the external part to the inner one with stirring help, while microwave radiation heats more uniformly the media because is a radiative process. Radiative heating is more e ective to synthesise homogeneous nanoparticles, because this methodology avoids the generation of thermal gradients that can in uence in the nal size distribution and properties of the nanoparticles formed.[4]

This di erence in the activation method makes microwave radiation route an optimal process to produce similar nanoparticles than thermal method, which needs 20 times more time and higher temperature. Figure 3.2, shows graphically this di erence in the reaction conditions.

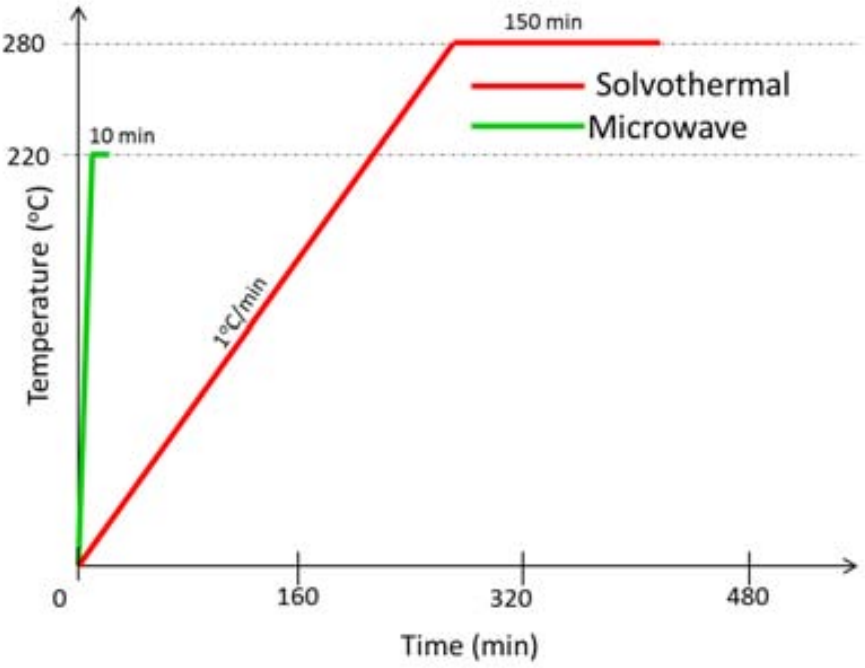

Figure 3.2: Graphical representation of the time and temperature needed to generate the nanoparticles via both methodologies: thermal and microwave.

Di erences of the obtained nal product generated by microwave and thermal route will be discussed below at the section 3.2, where the characterisation of these nanoparticles are discussed.

3.1.2 Chemical precursors

The optimised synthetic methodology starts from the selection of the metal precursors for the reaction. In this section the chemical precursors are described and justi ed as the adequate compounds to perform the synthetic study.

i Metal precursors

Metal acetylacetonates ($M(acac)_x$) have proved, by Cai et al.,[1] to be good metalorganic precursors due to their physicochemical properties. Cai studied the decomposition of the iron (III) acetylacetonate to generate magnetite with favourable results. These compounds are coordination complexes where the ligand, the acetylacetonate, is a bidentate system that coordinates with the metallic centre through an interaction ϕ-donor.

$M(acac)_x$coordination complexes have the property to decompose thermally releasing the centre metallic to the solvent medium, and by controlling this decomposition, it is possible to control the quantity of free metal in the reaction. One strong point of using acetylacetonate as precursor is that during their decomposition it generates CO_2 and acetone[5] as byproducts, both volatiles molecules which do not contaminate the nal solution.

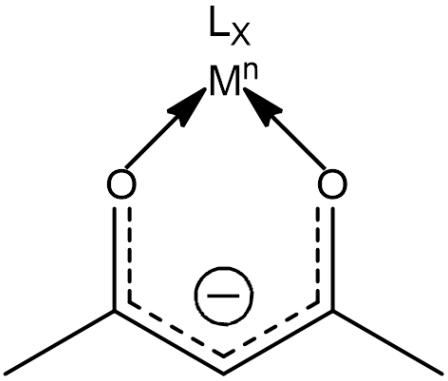

Figure 3.3: Acetylacetonate ligand coordinating a metallic centre with n oxidation state

The releasing of the metal precursors in the reaction media is a critical factor to take into account. Following the LaMer curve[6] (gure 3.4), it can be deduced that the free precursor is concentrated in the solvent until a critical point where the nucleation (formation of the rst crystalline nucleus) occurs, and then these nanoparticles grow until the point of solubility is reached. If the releasing of the metallic precursors occurs slowly, then a few nucleus will be formed, nucleus which will grow by incorporating new atoms in the structure until the solubility point. By counterpart, if the releasing is quick, a lot of nucleus will be formed, and they will grow later. Studying this fact, for the same quantity of initial matter, less nucleation crystals implies bigger

nanoparticles, while if more nucleus are formed in the first stage, then their size will be limited by the absence of material.

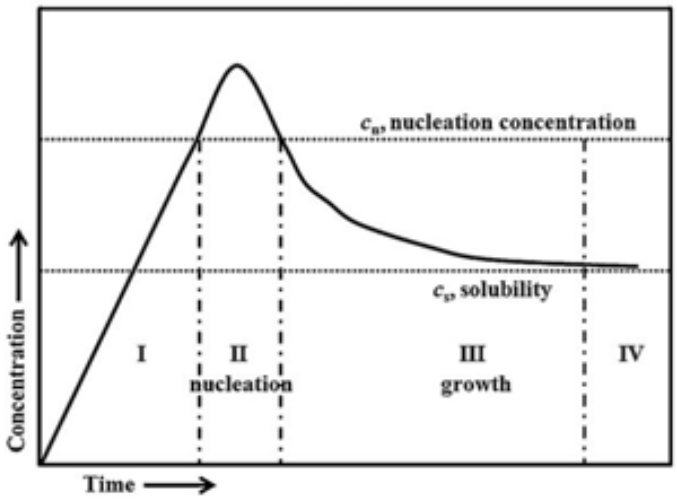

Figure 3.4: LaMer curve,[6] where the different stages of the nucleation and growth can be related.

For the synthesis presented here, the temperature ramp of the thermal route has been studied in order to optimise this parameter. A faster temperature ramp implies more uncontrolled decomposition of the metal precursors, generating bigger nanoparticles with higher size distribution that are unstable in dispersion, while a slower ramp does not implies any advantage in the final size, shape or behaviour obtained.

It has to be commented that for MFe_2O_4 synthesis, the corresponding $M(acac)_2$ is mixed with the $Fe(acac)_3$ to generate the proper MFe_2O_4, except for the case of the magnetite (Fe_3O_4), where only $Fe(acac)_3$ is needed. This absence of the divalent cation is justified by the fact that it is generated *in-situ* in the reaction media. The partial reduction of the Fe^{3+} to Fe^{2+} is produced by the solvent, fact explained below at the section ii.

ii Solvent and capping ligand

Solvent and capping ligand of the nanoparticles are determinant points to study when the final applications of the structures generated are considered. While the solvent seems to be harmless, it is an important factor because if a simple and

efficient process is looked for, the solvent has to be directly compatible with the application or easily removable from the nanoparticles. By its part, the capping ligand depends also on the application, because it can affect to the size and shape of the nanoparticles, and can determinate the final dispersant.[7]

With the aim to simplify the synthetic route as much as possible, the solvent of the reaction and the capping ligand is the same compound, the triethylene glycol (TREG). This polar compound grants the nanoparticles to be dispersible in a huge range of polar solvents (water, alcohols, chloroform...), amplifying their potential applications. The same solvent has been used in both synthetic routes, microwave and thermal, giving similar results.

Concerning to control the size and shape of the nanoparticles through the ratio metal/capping ligand/solvent,[8] for this methodology the solvent (and capping ligand) is infinitely in excess respect to the metal precursors and then, it is not possible to perform control shape and size when the reaction is carried out following the optimised one-pot process by controlling this ratio.

TREG plays also a third important role in the synthesis of the magnetite (Fe_3O_4), because it acts as reducing agent. When Fe_3O_4 is synthesised, only iron (III) acetylacetonate is added to the reaction media. The *in-situ* generation of the iron (II) is produced by the partial reduction of the iron (III) by the aldehyde groups present in the glycol media, groups which have been formed during the thermal treatment.[9] In the case of ferrites, before produce the reduction, the spinel structure is already formed, avoiding the reduction process as demonstrated by Neutron Powder Diffraction in the chapter 8.

3.1.3 Dispersion media: stabilisation

The phenomenon that allows to suspend the nanoparticles in a liquid, forming a colloidal dispersion, is the interaction between the capping ligand (or electrostatic charge) and the solvent. This interaction has to overcome the gravity force to maintain the nanocrystals suspended into the liquid. For the nanocrystals generated with the studied procedure, the capping ligand (TREG) is who interacts with the dispersant by principally hydrogen bonds.

With the aim to use these nanoparticles generated in different application fields, it is needed to swap the capping ligand to change the dispersant media, or change this ligand to another functional molecule, etc.[10–12] Then, a study to exchange the TREG by other capping molecule has been realised. The selected molecules were Oleylamine and Oleic Acid because they are non-polar molecules that allow to disperse the NPs in non-polar solvents, such as hexane, toluene... In the section 3.3, this procedure is detailed.

It is remarkable that even the nanoparticles capped with TREG are more stable when dispersed in water, they are generally suspended in ethanol or methanol absolute due to their future applications in the superconductor tapes generation.

3.2 Characterization

In this part, the characterisation of the different ferrite nanoparticles synthesised is discussed. Common laboratory techniques have been applied in order to know the principal properties of the nanocrystals generated, techniques as (High-Resolution) Transmission Electron Microscopy (HR-TEM), X-ray Powder Diffraction (XRPD), ThermoGravimetric and Calorimetry Analysis (TGA & DSC), magnetism via Superconductor QUantum Interference Device (SQUID), etc.

Below, a brief explanation of the technique used, together with the results obtained are exposed:

3.2.1 Transmission electron microscopy

Transmission Electron Microscopy[13] is a microscopic technique where electrons are used as a source of light because they have a wavelength shorter than the visible range of the electromagnetic spectra, allowing to observe an image with a resolution around the nanometer. Among the different electron microscopy techniques, electron transmission microscopy has been used, where in order to form an image the electrons which have gone through the specimen are analysed, detecting them with a digital CCD camera. Results presented here have been obtained using a *Jeol 2011* microscope.

When a dispersion of nanoparticles is obtained in their corresponding solvent, a drop of the colloidal solution (3 l) is deposited on a Cu TEM grid coated with a carbon thin lm, and then the liquid is evaporated. As consequence, the nanoparticles are deposited on the carbon, and the grid is ready to introduce it in the TEM to generate the images required. Principally, TEM images are analysed in order to study the size distribution and dispersion of the di erent MFe_2O_4 colloidal dispersion generated.

A resume of the obtained images is presented in the following gure 3.5:

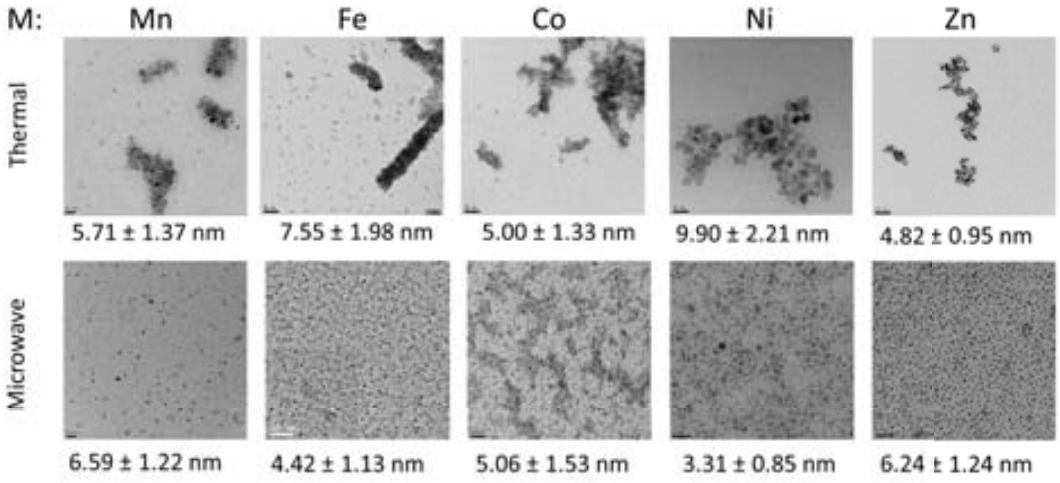

Figure 3.5: TEM images of the di erent MFe_2O_4 obtained through thermal and microwave route, together with their measured mean size and deviation.

In the TEM images, it can be seen clearly how microwave generates more dispersed nanoparticles, while the thermal method present some aggregates. This main di erence can be justify by the di erences in the annealing time and temperature. It is well known that glycols polymerise at high temperatures, and in this case, the TREG can polymerise at the synthesis temperature, which is higher for the thermal methodology and that is maintained during more time. Thus, the TREG polymerise forming a polyglycol, which aggregates the nanoparticles, and because a higher polymerisation degree is achieved in the thermal route, more aggregates of nanoparticles can be found in this methodology.

A fact parallel to the formation of these cumulus of nanoparticles is the stability of the nanoparticles. In despite of both methodologies generate long-time stable nanoparticles, after some time, in the thermal systems some macroscopic particles

can be found in the bottom of the container. Probably, these macroscopic systems are a grouping of aggregates where the gravity overcomes the lift force. In the case of microwave colloidal solutions, any macroscopic material is found even stored at room temperature during months.

i High resolution TEM

High Resolution TEM is an improved microscopic technique where the power of the microscopy is higher and the electronic aberration is corrected as much as possible. This technique, with a resolution up to 1 A, can be coupled with an electron analyser in order to capture and analyse the electrons ejected by the sample, obtaining chemical information about the atoms present in the compost. HR-TEM used for these analyses is *Jeol 2010F* with eld emission gun which operates at 200 kV with a point to point resolution of 0.19 nm and a Cs value of 0.5. Electron Energy Loss Spectroscopy (EELS) analyses were performed in a *Gatan GIF 2000* detector coupled to the *Jeol 2010F* microscope, giving chemical composition of the sample.

Figure 3.6 shows an example of the images obtained with this technique for the di erent kinds of ferrites obtained by both methodologies.

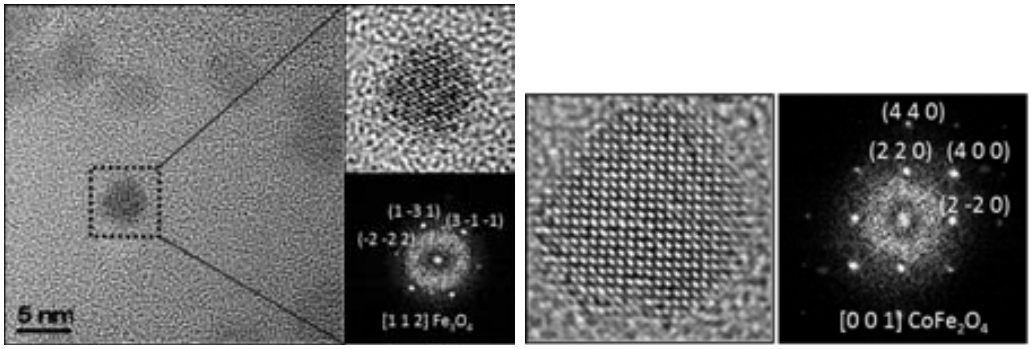

(a) HRTEM of Fe_3O_4 (b) HRTEM of $CoFe_2O_4$

Figure 3.6: HRTEM of the Fe_3O_4 (a) and the $CoFe_2O_4$ (b). In the FFT images, di raction spots of di erent planes of the spinel structure can be observed.

By analysing the direct image and the Fourier Fast Transform image, the nanoparticles present the expected spinel structure with their corresponding atomic distribution: Fe:O 3:4 for Fe_3O_4, and Co:Fe:O 1:2:4 in the case of $CoFe_2O_4$; relation obtained by EELS technique. Results are in agreement with the ratio (only for

metals) measured with Inductively Coupled Plasma (ICP). Trough HRTEM, any difference can be observed in the structure of the nanoparticles, being all of them spinel with the proper atomic distribution. In order to know and study deeply the structure and microstructure of these nanoparticles, in the chapter 8, results coming from neutron powder diffraction together with Rietveld refinement are detailed.

3.2.2 X-ray diffraction

X-ray powder diffraction (XRPD) is a technique which gives structural information about the sample, focusing in the diffracting crystallographic planes. This technique is deeply explained in the part III, section 7.1.1. Here, only the basic characterisation of the samples with common laboratory X-ray is presented. Analyses were performed with a *Rigaku D* diffractometer equipped with a rotating anode and Cu K_α source (λ=0.154056 nm).

As result of the measurements it can be confirmed through the indexed Bragg planes, that all the ferrite nanoparticles generated have the expected spinel structure with spatial group $Fd\bar{3}m$. XRPD patterns obtained for the NPs synthesised by thermal and microwave routes are indistinguishable due to all the ferrites have the same spinel structure with the same structure factor and similar form factor, as it can be seen in the figure 3.7.

Data calculated through the X-ray diffraction pattern demonstrated that the cell parameter is around the expected 8.4 Å, with a crystalline coherent size calculated by the *Debye-Scherrer* formula[14] (equation 3.1) in agreement with the obtained via TEM analyses.

$$D = \frac{K \cdot \lambda}{\beta \cdot cos\theta} \tag{3.1}$$

where D is the coherent crystal domain size, K the shape factor (value ~ 0.9), β is the full width high maximum (FWHM) of the Bragg peak, and θ the Bragg angle.

Because the form factor for the different spinel ferrites is similar, there is no possible identification of the different ferrites through the X-ray diffraction pattern, and no possible contamination of maghemite ($\gamma{-}Fe_2O_3$) inside the magnetite (Fe_3O_4) can be detected as byproduct of the reaction. To study deeper the composition and

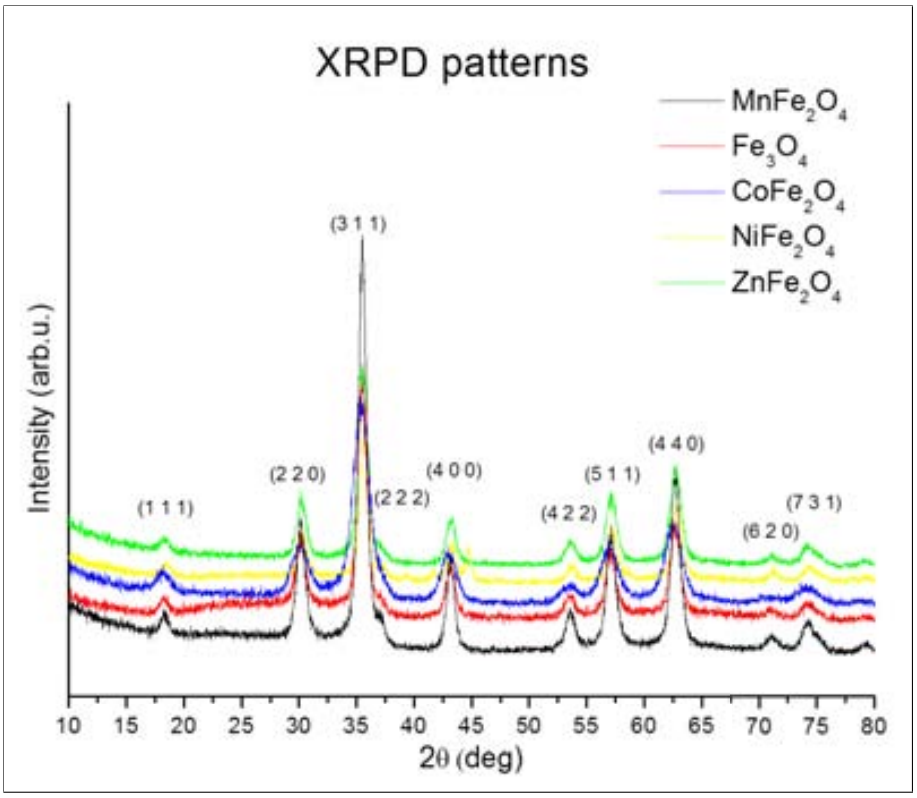

Figure 3.7: X-ray powder di raction patterns obtained for the di erent kinds of ferrites. The Bragg di raction planes are signalled with the corresponding Miller index.

structure of the nanoparticles synthesised, in the part III, chapter 8, a deeper study of the structure via Rietveld re nement of neutron powder di raction is treated.

i The case of the $CuFe_2O_4$

In the special case of $CuFe_2O_4$, similar synthesis is carried out using as precursors $Cu(acac)_2$ and $Fe(acac)_3$ in TREG. For both synthetic routes, an extra Bragg peak appears, corresponding to metallic copper as it can be shown in the following di ractogram 3.8.

Generation of metallic copper in the synthetic route could be justi ed by the fact that the two metal acetylacetonates decompose at di erent temperatures: while $Fe(acac)_3$ does it at $160\,^oC$, the copper one decomposes at $260\,^oC$. This di erence in the temperature makes that rst of all Fe_3O_4 nanoparticles are generated in the reaction conditions, because there is no free metallic copper for to be incorporated

into the spinel structure when it is being formed. Finally, after the formation of the magnetite, copper is released by the decomposition of the copper acetylacetonate, and the reaction more favoured is to be reduced to Cu^0 by action of the aldehyde groups present in the glycolic media formed at high temperature.[9] This metallic copper is less stabilised by TREG as the spinel, and due to there is not other adequate capping ligand in the medium, the Cu systems grow until a macroscopic structure.

If the last hypothesis is correct, it means that changing the copper precursor by one which release the Cu^{2+} when the spinel is being formed, the copper will incorporate inside the structure and finally no free Cu^{2+} is present to produce the reduction to Cu^o. Then, selecting an ionic compound of Cu^{2+}, it can be assured that in the reaction medium the Cu^{2+} ions can combine with the released Fe^{3+} forming the spinel structure. The ionic compound used to check this hypothesis was the copper (II) chloride ($CuCl_2$).

Following the synthetic route, but changing the $Cu(acac)_2$ by $CuCl_2$, it is possible to obtain magnetic ferrite nanoparticles without visible and deducible presence of copper metallic. To prove this absence, XRPD (figure 3.8) was performed, obtaining a diffraction patter typical for the spinel without secondary phases as Cu^o, CuO...

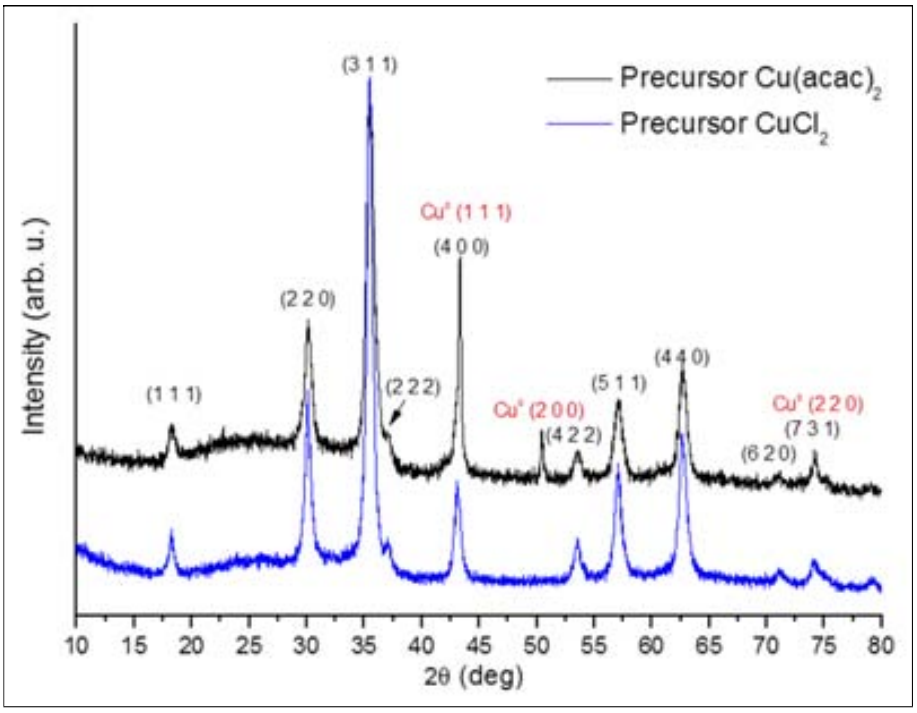

Figure 3.8: X-ray powder di raction of $CuFe_2O_4$ NPs generated with two di erent precursors. Note the presence of Cu^o when $Cu(acac)_2$ is used.

3.2.3 Thermogravimetric & di erential scanning calorimetry

Thermogravimetric Analyses (TGA), together with Di erential Scanning Calorimetry (DSC), have been performed in order to evaluate the amount of capping ligand adsorbed on the nanoparticles and the possible phase transitions with the temperature. While TGA measures the di erence in weight in function of the temperature, DSC detects the heat variation of the sample also in function of the temperature, observing possible decomposition, oxidation steps, exo- or endo- thermal process etc. These measurements were performed under air at a heating rate ramp of 5 ^oC/min going from room temperature up to 800 ^oC using a *NETZSCH STA 449 C* analyser. Graphic 3.9 shows an example of the curves obtained.

As it can be shown in the examples, di erent signals in the TGA can be di erentiated: the rst one, which occurs below 100 ^oC, is due to the evaporation of residual water adsorbed in the sample. The signal comprised between 200 and 300 ^oC can be assigned to the ligand decomposition, in this case the TREG. After these signals,

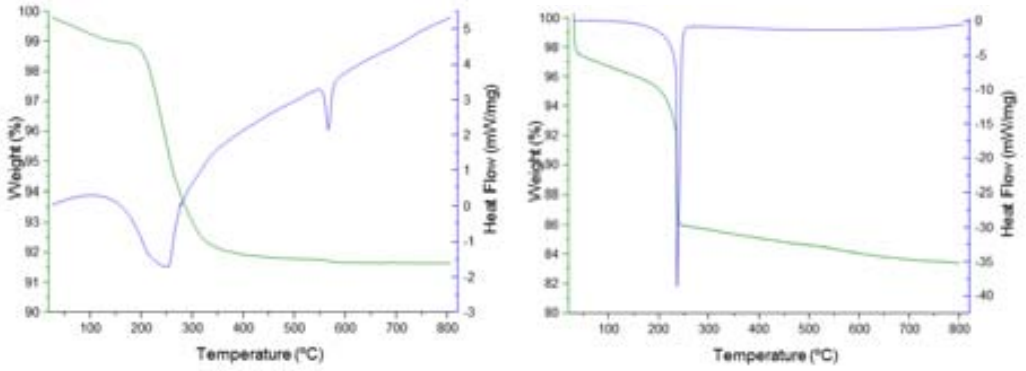

(a) TGA-DSC Fe_3O_4 (b) TGA-DSC $CoFe_2O_4$

Figure 3.9: TGA and DSC curves obtained when analysing the nanoparticles powder. Figures show an example of (a) magnetite, and (b) cobalt ferrite.

no remarkable weight loss occurs. By its part, DSC signal displays an exothermic process which occurs when the TREG decomposes, probably due to their oxidation in the oxidising atmosphere. Also DSC shows, only in the case of the magnetite an exothermic process at temperatures upper 600 ^oC with any mass change, fact that correspond to the oxidation of the Fe^{2+} to Fe^{3+}, changing the structure of the compound from the spinel to an hexagonal structure of the hematite (Fe_2O_3). This last DSC signal is not observed in the other ferrite cases, because no possible oxidation can happens.

TGA analyses allows to know exactly the quantity of organic ligand which remain on the surface of the nanoparticles to realise the di erent physicochemical analysis required. The percentage of organic ligand varies in function of the cleaning process of the nanoparticles, but for a typical case where the nanoparticles are washed three times with the ethyl acetate and ethanol mixture, around of 20 % of the matter is organic, being the rest (80 %) the inorganic magnetic material. It is crucial to know this value because the magnetic analyses performed with the SQUID magnetometer (below at point 3.2.4) needs to know exactly the quantity of magnetic material in order to calculate their magnetic moments quantitatively.

3.2.4 Magnetometry

Magnetometry analyses have been performed through Superconductor Quantum Interference Device (abbreviated as SQUID) that is a quantitative magnetometer based on superconducting loops containing Josephson junctions.[15] Exactly, measurements have been obtained with a *Quantum design MPMS XL-7T* with a maximum magnetic field of 7 Tesla. Data from SQUID is an hysteresis loop (explained in the chapter 1, section ii), where the magnetic moment of the nanoparticles is measured in function of the external magnetic field at constant temperature of 10 K.

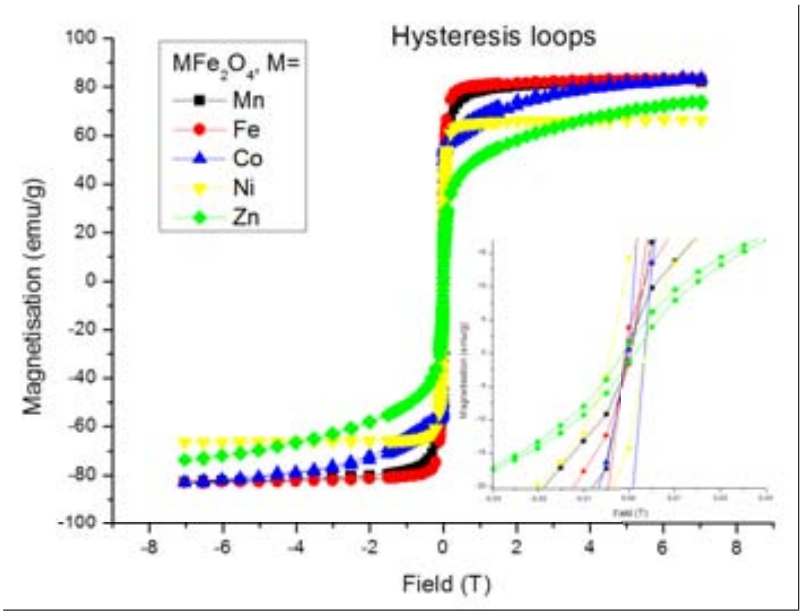

Figure 3.10: Hysteresis loops of synthesised ferrite magnetic nanoparticles by thermal methodology.

Hysteresis loops obtained (gure 3.10), demonstrate the superparamagnetic behaviour of the magnetic ferrite nanoparticles. The inset shows the low coercitive values of the nanoparticles, proving the low magnetic remanence. Below, the table 3.1 resumes the typical values obtained when the hysteresis loops are analysed. It is remarkable that in all the cases the magnetic saturation value (M_s) has been corrected with the residual mass at 600 ^oC extracted from the TGA analyses.

Results have shown a lower magnetic saturation values and higher coercitive eld for the case of the microwave synthesised nanoparticles. Even this performance belows to a soft ferrimagnetic material, it is notable that this phenomenon has proved

Magnetic properties				
Composition	M_s (emu/g)		$\mu_0 H_c$ (mT)	
	Thermal	Microwave	Thermal	Microwave
$MnFe_2O_4$	79.6	70.5	1	4.7
Fe_3O_4	81.7	75.8	1.8	3.5
$CoFe_2O_4$	74.4	63.8	2.6	14.7
$NiFe_2O_4$	65.6	23.3	7.4	11.2
$ZnFe_2O_4$	57.9	55.1	2.8	3.4

Table 3.1: Magnetic saturation (M_s) and coercitive field ($\mu_0 H_c$) of the magnetic ferrites generated.

that the microwave nanoparticles present a higher internal atomic disorder, because a higher value of the coercitive field means higher internal anisotropy, decreasing the M_s values. These anisotropy could be understood if the nanoparticles are compared with a core-shell structure, where there are some differences between the magnetic behaviour of the surface and the internal structure of the spinel ferrites.[16, 17]

Precisely, when $CoFe_2O_4$ is fabricated via thermal route, it occurs that sometimes the SQUID magnetometry gives a higher coercitive field with superparamagnetic and ferromagnetic mixed performance. This indicates the presence of two compounds inside the structure, a cobalt oxide and magnetite. But because only the spinel structure is found in the XRPD pattern, the presence of a strong magnetic compound can come from the anisotropic distribution of the cobalt inside the NP.

Copper ferrite, which is synthesised via $CuCl_2$ precursor, and compared with the standard $Cu(acac)_2$ (reaction which produce metallic copper) is analysed via SQUID magnetometry. As the hysteresis loops shows, when the precursor is the ionic salt, the expected behaviour of the superparamagnetic $CuFe_2O_4$, while if metallic copper is produced, a mixture of ferrimagnetism (coming from the Fe_3O_4) and diamagnetism (from Cu^o) can be deduced (figure 3.11).

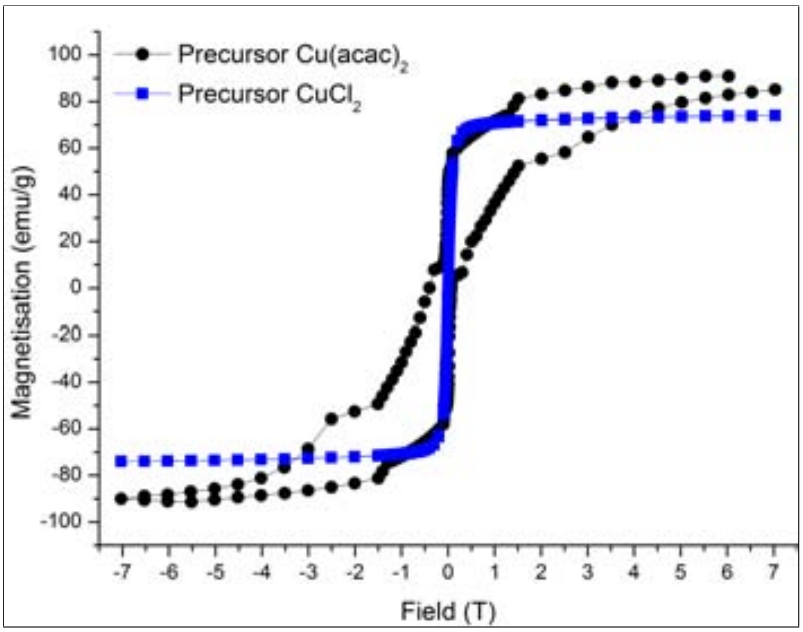

Figure 3.11: Hysteresis loops of $CuFe_2O_4$ ferrite NPs for the two different precursors. Note the correct superparamagnetic behaviour for the case of $CuCl_2$ precursor.

3.3 Ligand exchange

As it has been already stated, sometimes it is needed to change the capping ligand for the possible applications when a synthetic route is known and optimised. In this case, it has been developed a ligand exchange between the TREG (polar) by the Oleylamine or Oleic Acid (non-polar), in order to synthesise the nanoparticles through the polyol route, but dispersing the final obtained nanoparticles in hexane (among others).

The ligand exchange procedure is performed by two different methodologies as explained here: a dispersion of MFe_2O_4 nanoparticles in ethanol is evaporated and cleaned 3 times with an ethyl acetate:ethanol mixture with magnetic precipitation, in order to extract as much TREG as possible without aggregate the nanocrystals. After the last magnetic decanting, two ways can be followed to the ligand exchange:

1. One phase procedure: NPs are redispersed in 10 ml of $CHCl_3$, and 2 ml of Oleylamine are added (infinite excess). Then, after 4 hours of stirring at room temperature, the chloroform is evaporated, and 25 ml of hexane are added to the nanoparticles, achieving a final dispersion in the non-polar media stable during months.

2. Two phases procedure: NPs are dispersed in 5 ml of basic $H_2O : NH_3$ 97.5:2.5. Next, 40 mg of Oleylamine or Oleic Acid and 20 ml of $CHCl_3$ are added, and the system is carried to re ux during 10 minutes. After this time, the organic phase is decanted and the chloroform evaporated in order to add 25 ml of hexane to disperse the nanocrystals.

In the gure 3.12 it can be seen the resultant TEM image before and after the ligand exchange. It is indistinguishable from those images obtained directly through the Oleylamine route.[18] The dispersion similar, but the system has partially coalesced giving a more size dispersion, fact that also occurs in the Oleylamine original synthesised NPs.

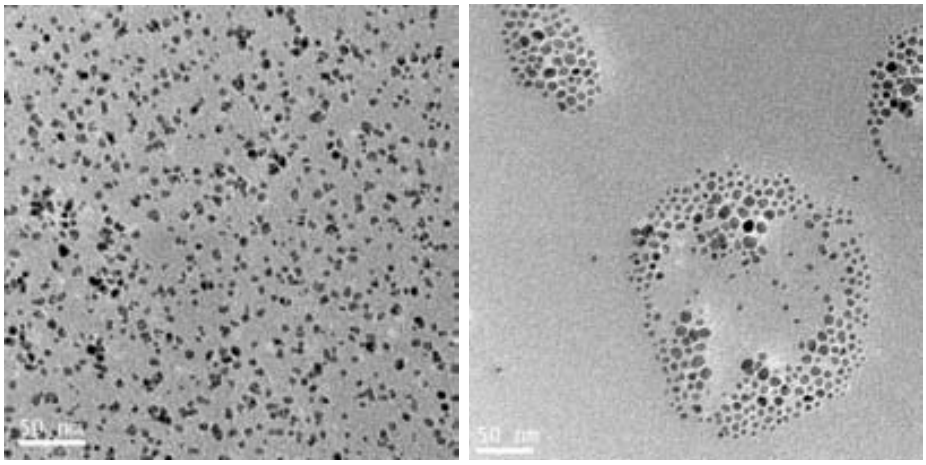

(a) NPs before ligand exchange (b) NPs after ligand exchange

Figure 3.12: Comparison of TEM images of Fe_3O_4 nanoparticles before (a) and after (b) the ligand exchange of TREG with Oleylamine

3.4 Plasma cleaning for capping ligand elimination

Complementarily to this study, it wants to be shown that the elimination of the capping ligand of the nanoparticles can be also carried out by physical methodologies, as it can be by *plasma cleaning*. This technique consists of a combustion of the organic matter (in this case the ligand) by action of a total ionised gas, (called

plasma) or a mixture of gases. Typically, Ar and O_2 are used for this purpose, as it has been done in this case.

Several experiments with di erent conditions were performed, obtaining the better results for the action of the plasma on the already prepared Cu TEM grid with nanoparticles with the following conditions: Pressure 100 mmHg of Ar; power 50 W; time 30 s.

Figure 3.13 shows the di erence between before and after the plasma cleaning treatment of the same sample. It can be deduced from this gure that the procedure to eliminate the organic compounds is clearly e ective, because the aggregated formed by the action of the organic capping ligand disappear. Instead of this, an homogeneous distribution of nanoparticles along all the copper grid is presented. The explanation of this change on the distribution comes from the fact that the plasma can charge electrostatically the nanoparticles, creating a repulsive e ect which maintains the nanoparticles separated.

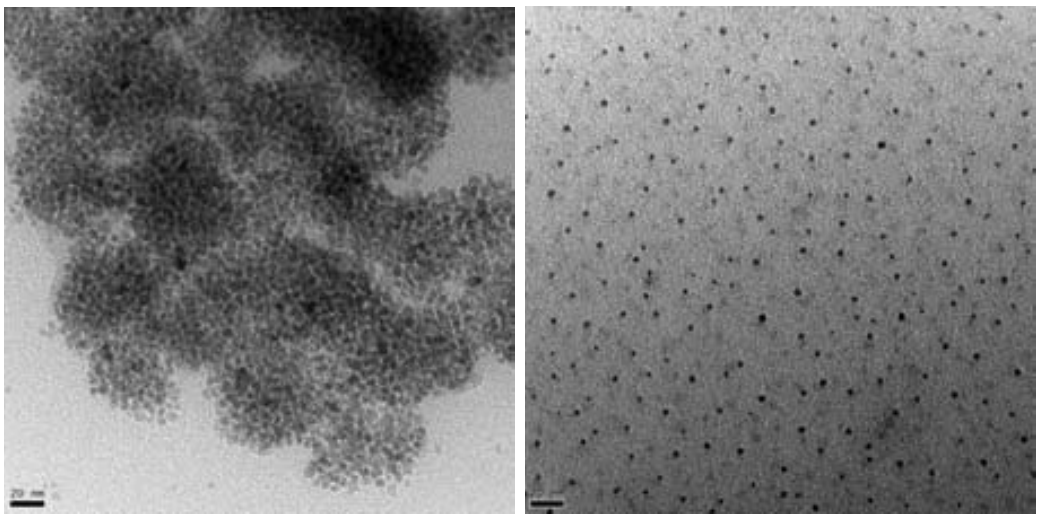

(a) Fe_3O_4 before plasma cleaning (b) Fe_3O_4 after plasma cleaning

Figure 3.13: Sub gure (a) shows a Cu TEM grid with nanoparticles with high quantity of organic matter. After the plasma cleaning procedure, the nanoparticles are more separated and homogeneously distributed on the grid as it can be shown in the sub gure (b).

E ectively, if the nanoparticles are needed without any capping ligand for possible applications, plasma cleaning can be an e ective methodology to achieve a high

dispersion degree with an electrostatic stabilisation and no aggregation.

3.5 Chapter summary

In this chapter, the synthesis of magnetic ferrite nanoparticles below 10 nm through thermo-chemical decomposition and microwave assistance route has been presented. Nanoparticles, dispersible in polar solvents, have been synthesised in a wide range of concentrations, up to 256 mM in free MFe_2O_4, and they have been characterised via common laboratory techniques.

Results show a high degree of dispersability, being better in the case of microwave methodology. X-ray diffraction shows the expected spinel structure, while SQUID measurements demonstrates the superparamagnetic behaviour of the nanostructures.

Complementary studies concerning the ligand exchange and elimination of the TREG have been developed. Data demonstrate that it is possible to eliminate completely the capping ligand or change it for other molecule more adequate for the final applications.

Bibliography Chapter 3

[1] W. Cai and J. Wan, "Facile synthesis of superparamagnetic magnetite nanoparticles in liquid polyols," *Journal of Colloid and Interface Science*, vol. 305, no. 2, pp. 366–370, 2007. (cited on page(s) 51, 68, 71)

[2] E. Solano, L. Perez-Mirabet, F. Martinez-Julian, R. Guzman, J. Arbiol, T. Puig, X. Obradors, R. Yañez, A. Pomar, S. Ricart, and J. Ros, "Facile and efficient one-pot solvothermal and microwave-assisted synthesis of stable colloidal solutions of MFe_2O_4 spinel magnetic nanoparticles," *Journal of Nanoparticle Research*, vol. 14, no. 8, pp. 1034–1048, 2012. (cited on page(s) 68)

[3] M. Nüchter, B. Ondruschka, W. Bonrath, A. Gum, and D. Jena, "Microwave assisted synthesis: a critical technology overview," *Green Chemistry*, vol. 6, pp. 128–141, 2004. (cited on page(s) 68)

[4] J. A. Gerbec, D. Magana, A. Washington, and G. F. Strouse, "Microwave-enhanced reaction rates for nanoparticle synthesis," *Journal of the American Chemical Society*, vol. 127, no. 45, pp. 15791–800, 2005. (cited on page(s) 70, 178)

[5] J. V. Hoene, R. G. Charles, and W. M. Hickam, "Thermal decomposition of metal acetylacetonates mass spectrometer studies," *Journal of Physical Chemistry*, vol. 62, no. 9, pp. 1098–1101, 1958. (cited on page(s) 71)

[6] W. Feng, L.-D. Sun, Y.-W. Zhang, and C.-H. Yan, "Synthesis and assembly of rare earth nanostructures directed by the principle of coordination chemistry in solution-based process," *Coordination Chemistry Reviews*, vol. 254, no. 9-10, pp. 1038–1053, 2010. (cited on page(s) 51, 71, 72)

[7] Y. Xia, Y. Xiong, B. Lim, and S. E. Skrabalak, "Shape-controlled synthesis of metal nanocrystals: simple chemistry meets complex physics?," *Angewandte Chemie*, vol. 48, no. 1, pp. 60–103, 2009. (cited on page(s) 73)

[8] P. Guardia, N. Perez, A. Labarta, and X. Batlle, "Controlled synthesis of iron oxide nanoparticles over a wide size range," *Langmuir : the ACS journal of surfaces and colloids*, vol. 26, no. 8, pp. 5843–7, 2010. (cited on page(s) 73)

[9] N. Miguel-Sancho, O. Bomati-Miguel, A. G. Roca, G. Martinez, M. Arruebo, and J. Santamaria, "Synthesis of magnetic nanocrystals by thermal decomposition in glycol media: Effect of process variables and mechanistic study," *Industrial & Engineering Chemistry Research*, vol. 51, no. 25, pp. 8348–8357, 2012. (cited on page(s) 73, 79, 184)

[10] M. G. Warner, S. M. Reed, J. E. Hutchison, and R. W. J. A. Chem, "Nanoparticles synthesized by interfacial ligand exchange reactions," no. 9, pp. 3316–3320, 2000. (cited on page(s) 74)

[11] M. S. Nikolic, M. Krack, V. Aleksandrovic, A. Kornowski, S. Förster, and H. Weller, "Tailor-made ligands for biocompatible nanoparticles," *Angewandte Chemie*, vol. 45, no. 39, pp. 6577–80, 2006. (cited on page(s) 74)

[12] A. Caragheorgheopol and V. Chechik (cited on page(s) 74)

[13] D. Williamsand and C. Carter, *Transmission Electron Microscopy*. 2009. (cited on page(s) 74)

[14] K. H. P. and A. L. E., *X-ray diffraction procedures for polycrystalline and amorphous materials*. 2nd ed., 1974. (cited on page(s) 77)

[15] J. Clarke and A. Braginski, *The SQUID handbook. Vol. II. Applications of SQUIDs and SQUID system*. 2nd ed., 2006. (cited on page(s) 82)

[16] S. Xie, J. Cheng, B. W. Wessels, and V. P. Dravid, "Interfacial structure and chemistry of epitaxial $CoFe_2O_4$ thin films on $SrTiO_3$ and MgO substrates," *Applied Physics Letters*, vol. 93, no. 18, p. 181901, 2008. (cited on page(s) 83)

[17] F. Rigato, J. Geshev, V. Skumryev, and J. Fontcuberta, "The magnetization of epitaxial nanometric $CoFe_2O_4$ (001) layers," *Journal of Applied Physics*, vol. 106, no. 11, p. 113924, 2009. (cited on page(s) 83)

[18] L. Perez-Mirabet, E. Solano, F. Martinez-Julian, R. Guzman, J. Arbiol, T. Puig, X. Obradors, A. Pomar, R. Yañez, J. Ros, and S. Ricart, "One-pot synthesis of stable colloidal solutions of MFe_2O_4 nanoparticles using oleylamine as solvent and stabilizer," *Materials Research Bulletin*, vol. 48, no. 3, pp. 966–972, 2013. (cited on page(s) 52, 85, 184)

Chapter 4

$YBa_2Cu_3O_{7-\delta}$ Superconducting Layers

Contents

This chapter describes the generation of YBCO superconducting (SC) thin film layers and their modification via *in-situ* and *ex-situ* approaches. This last procedure is interesting to control the properties of the preformed nanostructures that will be embedded into the YBCO thin layer.

4.1 Generation

$YBa_2Cu_3O_{7-\delta}$ (YBCO) superconducting thin layers are generated by an optimised Chemical Solution Deposition (CSD) technique,[1, 2] which consists of the deposition of a solution containing the YBCO metallic precursors on a substrate (in this case $LaAlO_3$ (LAO)). These chemical precursors are metal-organic compounds, specifically metal-trifluoroacetate (M(TFA)) salts: $Y(TFA)_3$, $Ba(TFA_2)$ and $Cu(TFA_2)$ with the stoichiometry 1:2:3 in methanol.[3] Because the thickness of the sample depends on the concentration of precursors and the rheological parameters,[4] the solution has been optimised to generate thin films around 300 nm of thickness, which is achieved with a concentration of precursors corresponding to 0.25M, 0.50M, 0.75M (1.5 M in total metal amount) respectively in methanol absolute. Water contamination ($\geq$2 %) must to be avoided because if not, undesired hydroxides are formed in the solution, unbalancing the molar ratio. Then, precautionary measures need to be taken into account when generating and manipulating the YBCO chemical precursors solution, such as dry atmosphere and anhydrous chemical precursors.

This solution is deposited by spin-coating or ink-jet printing on a LAO surface, as it has been explained in the section 2.2.3. Single crystal LAO is crucial because on it the YBCO will grow with an epitaxial orientation, being the long axis c of the crystal cell perpendicular to the LAO surface (0 0 1)//(0 0 1).

The procedure to fabricate the YBCO layer after the deposition is carried out following the next procedure:

1. Pyrolysis: The objective of this step is to eliminate the excess of the organic matter present in the solution (i.e. methanol, TFA and additives). Pyrolysis conditions influence have been studied previously and optimised in order to generate an homogeneous and smooth layer (instead, SC properties can be reduced by the presence of cracked regions and inhomogeneities). The

conditions of this procedure are resumed in the diagram 4.1.

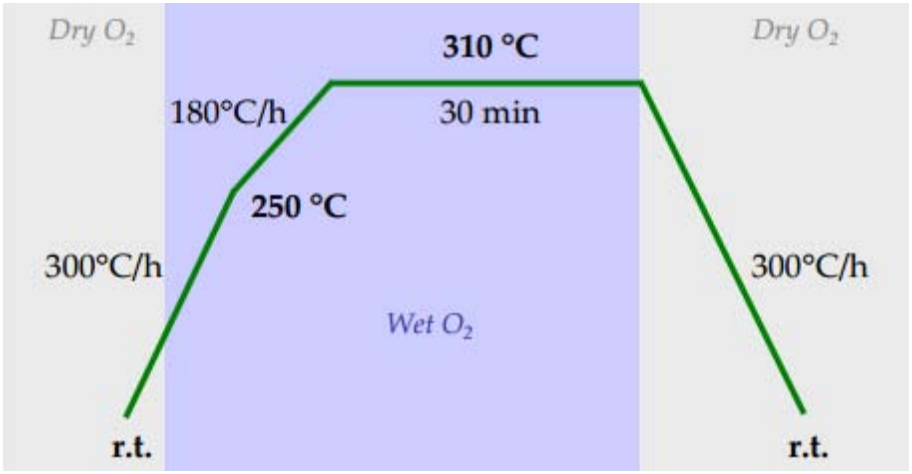

Figure 4.1: Diagram resuming the conditions and steps to perform the pyrolysis.[2] The water pressure is 22 mbar, and the oxygen ow rate 0.5 l/min.

2. Growth: The goal of this procedure is to generate the YBCO thin lm in a controlled form in order to generate an epitaxial growth on the LAO. The procedure is also resumed in the following gure 4.2.

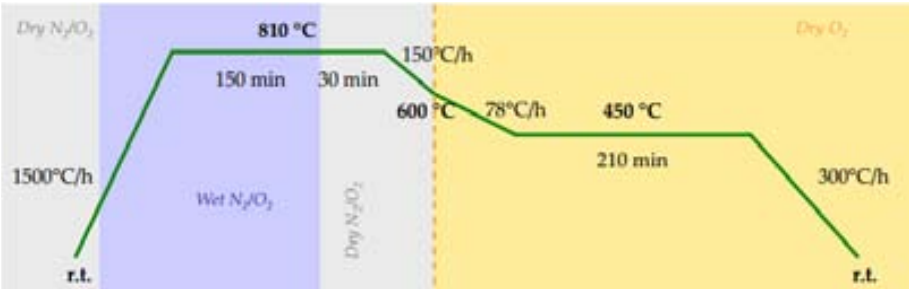

Figure 4.2: Conditions to $YBa_2Cu_3O_7$ growth.[2] The water pressure is 22 mbar, and the oxygen ow rate 0.6 l/min.

After this synthetic methodology, YBCO thin lm layers of 300 nm of thickness have been epitaxially growth on the LAO surface. Then, this layer is characterised in order to know their superconducting properties, such as: Critical temperature, current transport capability, etc.[a]

[a] Analyses of SC properties of the YBCO layers generated are not an objective of this work, but some data will be given to have a reference value on the quality of the generated layers.

4.2 Nanocomposite nanostructured layers

If nanocomposite HTS layers want to be synthesised by *in-situ* or *ex-situ* methodology, the same thermal process to standard YBCO has to be carried out. The only difference is that for the *in-situ* generation, the chemical precursors of the nanoparticles (that will be formed inside the YBCO when it grows) are added into metal trifluoroacetate chemical solution. By its part, the *ex-situ* methodology consists of mixing the YBCO chemical solution with a dispersion of preformed nanostructures that will be incorporated inside the YBCO crystal structure. The main difficulty of the first approach is to add chemical precursors that do no react with any YBCO component, because otherwise the layer will not be correctly generated. While the *a priori* disadvantage of the second method is the stabilisation of the nanoparticles in the chemical solution (with high ionic force) in order to maintain their size and properties and an homogeneous distribution along the YBCO thin film. In addition, for both methodologies, solid state reactions have to be avoided to eliminate possible formation of secondary phases that could decrease (or even destroy) the SC properties.

During this work, the study, development, and characterisation of a new nanocomposite YBCO by ex-situ methodology have been carried out. Then, the generation of YBCO superconducting layer with $MnFe_2O_4$ nanoparticles embedded is explained together with their common laboratory characterisation.[b]

4.2.1 $MnFe_2O_4$ nanoparticles embedded in $YBa_2Cu_3O_{7-\delta}$

The goal of this section is to describe step by step the procedure to generate YBCO SC layer with $MnFe_2O_4$ nanoparticles embedded inside the crystal structure. After that, the characterisation with common laboratory techniques of this nanocomposite is detailed.

[b] In spite of during this thesis other YBCO nanocomposite SC layers have been studied, their synthesis is out of our aim. In the part III, chapter 9 and 10, synchrotron radiation has been used to carried out the structural characterisation of different *in-situ* and *ex-situ* nanocomposite YBCO thin layers.

i Stabilisation of nanoparticles

The first step to embedded the preformed nanoparticles in the YBCO thin layer is to stabilise them into the high ionic force solution of YBCO chemical precursors. In the section 1.2.1, it has been explained the necessity of stabilise the nanoparticles in the dispersion media. In this case the nanoparticles are capped with TREG which stabilise the nanoparticles in polar media. Then, because it is interesting to maintain the nanoparticles as stable as possible, they are used without cleaning process to maintain as much as capping ligand as possible, in other words, as synthesised in TREG.

The objective is to generate SC layers with a 6 % of nanoparticles (counted as free molecules of MFe_2O_4) respect to the 1.5M of YBCO in sum of metals. But remembering the high influence of rheological parameters of the initial solution either in the deposition step (ink-jet printing) and also in the properties of the resulting layer, it is necessary to minimise the amount of TREG present. This fact is due to their high viscosity. Then, if the proportion of nanoparticles wants to be maintained constant, and the amount of TREG reduced to the minimum, one plausible solution achieved with the developed synthetic route of the NPs is to produce the nanoparticles in high concentration and dilute them with the proper solvent, mixing this new solution with that of the YBCO precursors. In other words:

For 1 ml of YBCO 0.75 M in sum of metals with 6 % of nanoparticles, 0.5 ml of YBCO 1.5 M is mixed with 0.5 ml of 90 mM solution of $MnFe_2O_4$ microwave synthesised nanoparticles. This last dispersion is achieved by diluting a concentrate 260 mM solution of nanoparticles in methanol. As result, the desired proportion of YBCO:NPs with the minimum quantity of TREG is obtained.

The mixture of both solutions is stable during months, which is remarkable because in general, nanoparticles are unstable in high ionic force solutions. To demonstrate it, a TEM image of the dispersion of the nanoparticles in the YBCO solution is taken after the process of generation of the thin layer. TEM image 4.3 demonstrates that the dispersion of the nanoparticles keeps constant without aggregates and coalescence.

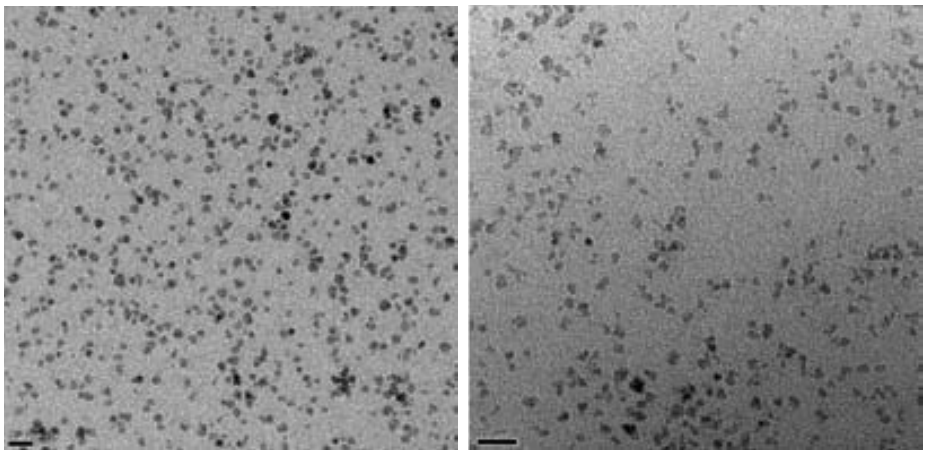

(a) $MnFe_2O_4$ as synthesised (b) $MnFe_2O_4$ in YBCO solution

Figure 4.3: $MnFe_2O_4$ nanoparticles synthesised via microwave as synthesised (a) and dispersed in the chemical solution of YBCO after more than 1 day (b). Note the no aggregation of the nanoparticles even in the high ionic force medium.

ii Ink-jet printing for nanocomposite $YBa_2Cu_3O_7$

The procedure to deposit the solution on the LAO single crystal has been the ink-jet printing technology.[5] The reason to utilise this technique and not spin-coating is because ink-jet allows to deposit the solution in a more controlled form. It occurs in the spin-coating that increasing the viscosity of the solution due to the presence of the TREG, wettability problems occur in the spinning stage, and then when the layer is pyrolysed it is cracked, avoiding the formation of a continuous single crystal layer. Ink-jet printing solves these problems by the deposition of multiple solution drops[6] on the LAO surface. Then, when the pyrolysis is performed, a continuous thin lm is generated. To clearly show the procedure, the formation of the drop which will be deposited on the LAO surface, can be studied following their evolution at di erent times (gure 4.4).

Notwithstanding the objective is to generate layers with 6 % of $MnFe_2O_4$, in order to know and control the new solution (with di erent viscosity and density), it has been started by layers with a lower content of NPs (and also TREG), starting by 1.5 % and 3 % of content of NPs respect to the YBCO.[c]

[c]At the time of writing this PhD. work, only 1.5 and 3 % of $MnFe_2O_4$ NPs embedded has been achieved, and only the 1.5 sample has been deeply analysed. In addition, the new investigation for produce *ex-situ* thin layers with spin coating technique seems to be e ective. Results will be noti ed by posterior works of the research group.

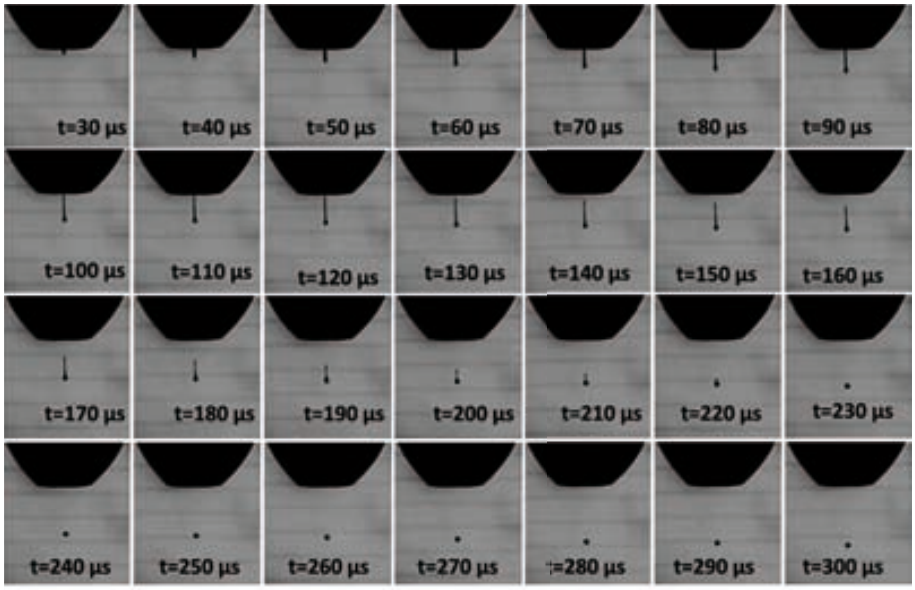

Figure 4.4: Image showing the evolution of the drop generated by the piezoelectric print-head at di erent times.

Several parameters must to be controlled when depositing the drop on the substrate, as it can be the concentration of the solution, the rheological parameters, and the spacing between drops. The thickness of the nal lm depends of these parameters, which have been optimised to obtain a YBCO thin lm between 150 to 200 nm. After the solution deposition on the LAO substrate, the sample is thermally treated with the standard procedure for YBCO generation, obtaining nanocomposite thin lms composed of YBCO with the corresponding $MnFe_2O_4$ ferrite magnetic nanoparticles.

iii Spin coating for nanocomposites

During this work, some *in-situ* YBCO nanocomposite layers have been studied. These new materials has not been prepared in this work, they only have been characterised. In spite of it, a brief explanation about the experimental procedure to generate this new *in-situ* nanocomposite YBCO layers is presented.

The *in-situ* generation of nanoparticles is carried out by mixing the metalorganic precursors of the nanoparticles jointly with the YBCO chemical solution and then, the standard YBCO growth process is carried out. Here, two nanoparticles generated *in-situ* in the YBCO have been studied: $BaZrO_3$ (BZO)[7] and Ba_2YTaO_6[8]

(BYTO). Complementarily, spin coating *ex-situ* YBCO thin layer with $BaCeO_3$ (BCO) NPs embedded have been also studied. These thin layers have been studied with synchrotron X-ray diffraction (chapter 10) in order to know the structure and microstructure of these new compounds, and try to understand how the structure and the correlated defects affect to the superconducting properties.

4.3 Results of *ex-situ* $MnFe_2O_4$-$YBa_2Cu_3O_{7-\delta}$

Due to that during this project $MnFe_2O_4$ -$YBa_2Cu_3O_{7-\delta}$ nanocomposite SC layers have been generated as a new system, the laboratory characterisation of this thin film with 1.5 % of nanoparticles embedded is presented.

4.3.1 X-ray diffraction

First analysis realised was the X-ray diffraction (XRD) where the Bragg peaks are observed for planes parallels to the surface only if the epitaxy growth has been correct. Diffraction pattern obtained from the *Rigaku D* diffractometer is present in the figure 4.5, showing the correct epitaxial growth of the thin layer.

It can be observed the Bragg peaks of the (0 0 l) planes (c planes) jointly to the LAO cubic planes, which are detected due to the penetration deep of the X-rays. With this pattern, it has been demonstrated the generation of YBCO epitaxially growth on the LAO single crystal substrate generated by ink-jet printing technology.

The diffractometer resolution is not the adequate to difference Bragg peaks coming from the spinel structure of the ferrite, because the main peak of the spinel (3 1 1) at 35.5^o is overlapped with the tail of the YBCO (0 0 5) peak. To achieve the necessary resolution it is needed to use synchrotron radiation in grazing incidence mode, as it will be explained in the chapter 10, where a deep analysis of the diffraction pattern is presented jointly with the cell parameter and microstrain calculations performed.

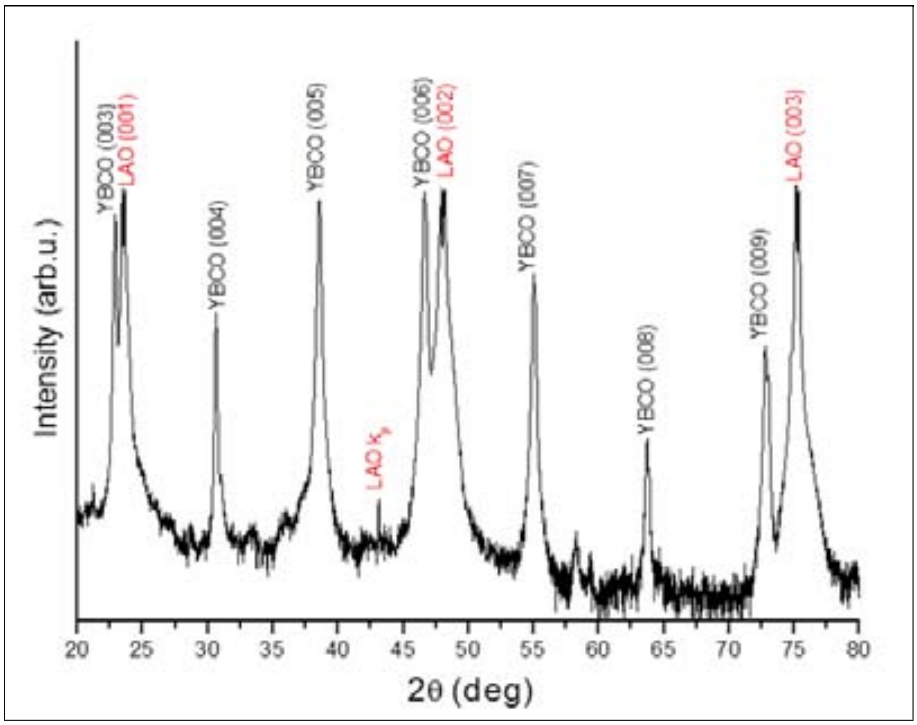

Figure 4.5: Out of plane X-ray di raction obtained for nanocomposite superconducting layer. The Bragg di raction signals the of planes parallels to the LAO surface are observed. The resolution is not enough to detect the spinel phase.

4.3.2 X-ray photoemission spectroscopy

X-ray photoemission spectroscopy (XPS) is a physical technique to obtain chemical information about a sample by pro ting the electronic con guration of the atoms. The sample is irradiated with photons with the wavelength adequate to excite the electrons of the 2p orbital. When these electrons absorb photons with a determinate energy they are excited until a higher energetic level (3d), and when the atom relaxes uorescence phenomenon occurs. Then, by detecting the uorescence signal, chemical information about the atoms composing the sample can be extracted.

As consequence of the analysis, selective information about the atomic composition of the sample can be obtained, because di erent wavelength excites di erent atoms. This methodology has been used in order to detect if in the YBCO SC layer there are Mn and Fe atoms, to check if these metals coming from the nanoparticles are distributed along the thin layer. Because the low energy needed to excite the 2p level of the atoms, the penetration deep of the analysis is minimum, being only a

super cial technique. With the nality to analyse deeper inside the layer, the sample is bombed with ions to scrape the surface and penetrate to the inner part of the YBCO (etching procedure).

XPS measurements performed to the YBCO layer with 1.5 % of $MnFe_2O_4$ have been done in an area of 700 by 300 m^2, with an etching speed of 1.5 nm/min. The energetic area analysed is the $2p$ $3d$ transition of the studied metals, whose absorption edge is around 640 an 710 eV respectively for the Mn and Fe atoms. The results obtained for each analysis for each deep (until a maximum of 60 nm) are detailed in the gure 4.6.

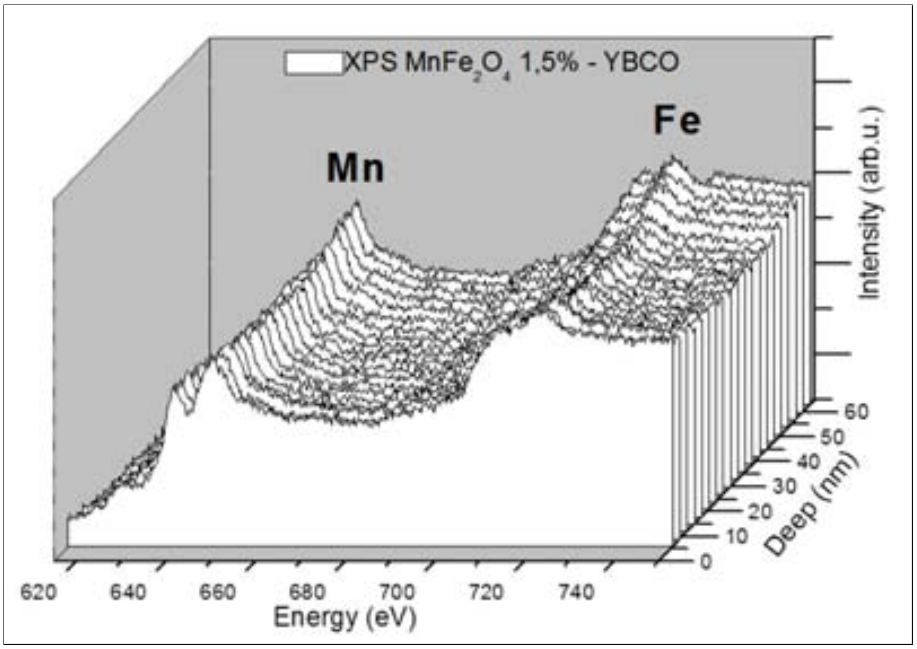

Figure 4.6: XPS of the YBCO thin layer with 1.5 % of $MnFe_2O_4$. The intensity is proportional to the quantity of atoms, and then, a constant ratio of metals is distributed in deep along the layer.

XPS shows clearly the distribution of the Mn and Fe metals along the rst 60 nm in deep of the YBCO SC layer. Because the intensity of the absorption edge for both metals is constant when the etching is performed, it means that the metals are distributed homogeneously along the sample. However, it is no possible to know if the metals are forming part of the spinel structure, or if the cations have spread along the crystal structure forming a solid solution, or if they are as iron and manganese oxide respectively. More studies concerning this objective are needed.

4.3.3 High resolution TEM

HR TEM has been performed to make a local research to probe the existence of the ferrite spinel nanoparticles inside the YBCO. Remembering that there are 1.5 % of nanoparticles inside the layer with an expected dimension between 7-10 nm, it is not easy found with TEM microscopy these structures. Otherwise, HR TEM analysis have been performed, founding results resumed in the following images 4.7 & 4.8 :

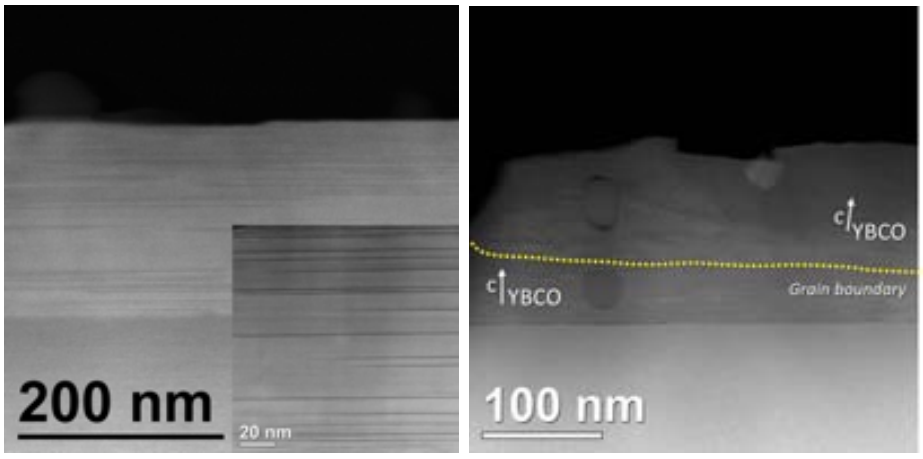

(a) Staking faults (b) Misaligned grains

Figure 4.7: High resolution TEM of the YBCO layer, where a staking faults (a) and misaligned grains (b) can be observed.

HR TEM shows how the YBCO layer with magnetic manganese ferrite nanoparticles has grown. In general trends, the image 4.7 demonstrates the correct growth of the YBCO layer, with some staking faults,[9] which are disorders in the staking of the di erent layers of YBCO crystal cells, generating interstitial planes in the structure. In addition, some disoriented grains of YBCO with some degrees out respect to the of the epitaxial direction can be observed. Grain boundaries present can a ect to the SC capabilities, because it breaks the continuity of the superconductor crystal.

Observing image 4.8, an elongated particle of $MnFe_2O_4$ embedded inside the YBCO structure has been found. This nanoparticle seems to be larger than the original manganese ferrite nanoparticles, and it could be thought that is due to coalescence phenomenon when the ensemble is thermally treated at 810 ^oC to grow the SC layer. In addition, the nanoparticle found present an epitaxial order respect to the LAO (as in the inset containing the FFT of the di raction can be observed).

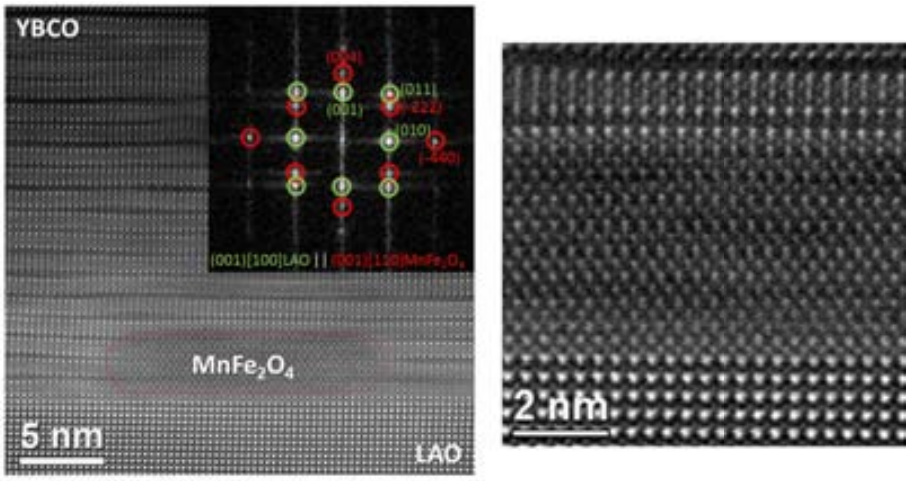

Figure 4.8: HR TEM of the YBCO containing 1.5 % of $MnFe_2O_4$. A $MnFe_2O_4$ nanoparticle can be observed in the remarked area with epitaxial growth orientation.

The fact that the HRTEM is optimised to an epitaxial view makes that random nanoparticles have less contrast, and they cannot be easily identi ed.

Despite this, it is a favourable result to found the spinel structure of the ferrite with the expected cationic ratio analysed by EELS (Electron Energy Loss Spectroscopy). This is the rst direct evidence obtained of the presence of $MnFe_2O_4$ nanoparticles in the YBCO structure.

4.3.4 Superconducting properties

In this section, the SC properties of the YBCO nanocomposite layer are evaluated. It is crucial to know the critical parameters of the layer in order to discern if the inclusion of the external structures inside the continuous crystal of YBCO a ect negatively or positively to their behaviour. Data refers always to the value at 77 K, that is the working temperature. This temperature has been selected because is the temperature of the liquid nitrogen, which is used as refrigerant in the most common applications.

Inclusion of nanostructured defects in YBCO has been demonstrated as a useful technique to improve the SC properties. Taken into account that one of the rst publications[10] about this research reports, an improvement of the J_c about the 150 % when Y_2O_3 nanoisland are present in the YBCO epitaxial layer (from 2.8 to 4.2

$MA\ cm^2$ at 77 K), it is expected at least, do not decrease the standard value of 2.8 $MA\ cm^2$.

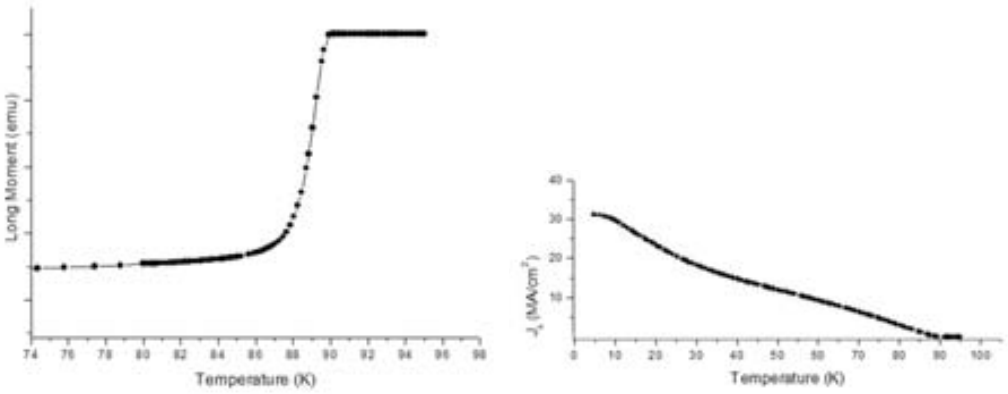

(a) M(T) (b) H(T)

Figure 4.9: M(T) (a) and H(T) already transformed to J_c (b) curves obtained via SQUID magnetometry to calculate the T_c and J_c parameters of the nanocomposite SC layer.

Obtained values for this new nanocomposite is a T_c of 89.2 K and a J_c of 4 $MA\ cm^2$ at 77 K, with only 1.5 % of $MnFe_2O_4$ embedded inside. These values have been obtained from the graphs of the gure 4.9 by interpolation at 77 K, for the case of J_c, while the T_c value has been obtained from the derived of the M(T) curve to obtain the in exion point. The transformation from the original data which contain the value of the eld H into J_c in function of the temperature (T) is carried out with the Bean model for a squared shape superconductor[11] (equation 4.1)

$$J_c(MA\ cm^2) = \frac{3\ \ m}{a^3 t} \tag{4.1}$$

where, J_c is the value of the critical current for a squared layer with thickness t and a as lateral dimension. m is the width of the hysteresis cycle when the sample is saturated.

In fact, it has been achieved a good quality HTS layer with $MnFe_2O_4$ nanoparticles embedded. Properties of the new nanocomposite have been improved respect to the reference previously published sample. The point is that the introduction of nanoparticles by the *ex-situ* methodology in YBCO is a big step in superconductors functionalisation with preformed nanostructures. The study of the structure of this

SC layer and the presence of the spinel ferrite structure inside the YBCO thin layer is studied and proved in the chapter 10.

4.4 Chapter summary

Different parameters concerning the generation of nanocomposite superconducting layers by *ex-situ* methodology have been studied in this chapter. Starting from the stabilisation of the nanoparticles in the high ionic force of the YBCO chemical solution precursors, until the use of the ink-jet printing conditions to generate thin films of YBCO with magnetic manganese ferrites embedded inside the structure.

The characterisation of this new nanocomposite SC layer, with 1.5 % of $MnFe_2O_4$ NPs embedded in the YBCO matrix, has led as a result a good superconducting properties, improving their critical current respect to the YBCO reference without structural modifications. In contrast, even some proves demonstrate the distribution of the metals which form the spinel along all the layer (XPS), and some TEM images shows the spinel structure, no direct determination of the distribution of the spinel ferrite structure has been obtained with the common laboratory techniques used.

Bibliography Chapter 4

[1] A. Pomar, A. Llordes, M. Gibert, S. Ricart, T. Puig, and X. Obradors, "Tuning the superconducting properties of $YBa_2Cu_3O_7$ tapes grown by chemical methods," *Physica C: Superconductivity*, vol. 460-462, pp. 1401–1404, 2007. (cited on page(s) 94)

[2] A. Llordes i Gil, *Superconducting nanocomposite films grown by chemical solution deposition: Synthesis, microstructure and properties.* PhD thesis, ICMAB-UAB, 2010. (cited on page(s) 39, 54, 94, 95)

[3] B. Rousseau, A. Canizares, E. Veron, R. Ramy-Ratiarison, A. Blin, D. De Sousa Meneses, P. Simon, F. Berberich, H. Graafsma, A. Pomar, N. Mestres, T. Puig, and X. Obradors, "Characterisation of $YBa_2Cu_3O_{6+x}$ films grown by the trifluoro-acetate metal organic decomposition route by infrared spectroscopy," *Thin Solid Films*, vol. 515, no. 4, pp. 1607–1611, 2006. (cited on page(s) 54, 94)

[4] S. Morlens, N. Roma, S. Ricart, A. Pomar, T. Puig, and X. Obradors, "Thickness control of solution deposited YBCO superconducting films by use of organic polymeric additives," *Journal of Materials Research*, 2007. (cited on page(s) 94)

[5] I. Van Driessche, J. Feys, S. C. Hopkins, P. Lommens, X. Granados, B. A. Glowacki, S. Ricart, B. Holzapfel, M. Vilardell, A. Kirchner, and M. Bäcker, "Chemical solution deposition using ink-jet printing for YBCO coated conductors," *Superconductor Science and Technology*, vol. 25, no. 6, p. 065017, 2012. (cited on page(s) 56, 98)

[6] M. Vilardell, X. Granados, S. Ricart, R. Cobas, M. Arjona, T. Puig, X. Obradors, S. C. Hopkins, B. A. Glowacki, J. Bennewitz, M. Falter, and M. Bà̀cker, "Ink jet printing for functional ceramic coatings," *Journal of Imaging Science and Technology*, vol. 55, no. 4, p. 040304, 2011. (cited on page(s) 56, 98)

[7] J. Gutierrez, A. Llordes, J. Gazquez, M. Gibert, N. Roma, S. Ricart, A. Pomar, F. Sandiumenge, N. Mestres, T. Puig, and X. Obradors, "Strong isotropic flux pinning in solution-derived $YBa_2Cu_3O_{7-x}$ nanocomposite superconductor films," *Nature Materials*, vol. 6, no. 5, pp. 367–73, 2007. (cited on page(s) 58, 99)

[8] M. Coll, S. Ye, V. Rouco, A. Palau, R. Guzman, J. Gazquez, J. Arbiol, H. Suo, T. Puig, and X. Obradors, "Solution-derived $YBa_2Cu_3O_7$ nanocomposite films with a Ba_2YTaO_6 secondary phase for improved superconducting properties," *Superconductor Science and Technology*, vol. 26, no. 1, p. 015001, 2013. (cited on page(s) 99)

[9] E. D. Specht, A. Goyal, J. Li, P. M. Martin, X. Li, and M. W. Rupich, "Stacking faults in $YBa_2Cu_3O_{7-x}$: Measurement using x-ray diffraction and effects on critical current," *Applied Physics Letters*, vol. 89, no. 16, p. 162510, 2006. (cited on page(s) 103)

[10] K. Matsumoto, T. Horide, K. Osamura, M. Mukaida, Y. Yoshida, A. Ichinose, and S. Horii, "Enhancement of critical current density of YBCO films by introduction of artificial pinning centers due to the distributed nano-scaled Y_2O_3 islands on substrates," *Physica C: Superconductivity*, vol. 412-414, pp. 1267–1271, 2004. (cited on page(s) 104)

[11] D.-X. Chen and R. Goldfarb, "Kim model for magnetization of type ii superconductors," *Journal of Applied Physics*, vol. 66, no. 6, pp. 2489–2500, 1989. (cited on page(s) 105)

Chapter 5

Conclusions Part II

Here, the conclusions concerning the synthesis and common laboratory characterisation of MFe_2O_4 nanoparticles and nanocomposite $YBa_2Cu_3O_{7-\delta}$ superconducting layers are presented.

Thermal and microwave synthetic routes have been optimised in order to obtain nanoparticles with a diameter below the 10 nm with a lower dispersion in size. Both procedures consist of the thermal decomposition of metal acetylacetonates via convective heating or microwave radiation heating in a TREG media, generating dispersible nanoparticles in polar media. The dispersion obtained is more homogeneous in the case of MW, because the lower temperature and shorter time produces lower polimerisation degree of the TREG, avoiding the formation of networks which trapping the nanoparticles which aggregate them.

The common laboratory techniques demonstrates in all the cases the similarities between two equal nanoparticles generated by the two procedures. XRD and SQUID magnetometry have been applied in order to check the expected spinel structure and their corresponding superparamagnetic behaviour.

Then, the interesting conclusion comes from the fact that both synthetic routes generate similar nanoparticles in size, shape and properties, even the decreasing of temperature in 60 degrees and reaction time in a factor of 20 for microwave procedure. This classifies the MW as an efficient and more eco-friendly synthetic route when compared with the common thermal one, because similar results are obtained using less temperature and shorter reaction times.

In the second part of this first section, the generation of nanocomposite superconducting layers via ink-jet printing with $MnFe_2O_4$ magnetic nanoparticles embedded has been studied. Starting from the stabilisation of the nanoparticles in high ionic force medium (YBCO chemical solution precursors), until the characterisation of the YBCO nanocomposite layer.

First of all, the stabilisation of the nanoparticles was a critical point to consider in order to avoid the formation of aggregates in the solution that later will be incorporated into the SC layer. The final developed process consist of disperse the obtained NPs (as synthesised in TREG) in the YBCO chemical solution. This new mixture will be deposited properly with ink-jet printing technology to generate the nanocomposite YBCO superconducting layers.

After the deposition of the mixture of NPs and YBCO solution, and after the growth of the layer by their corresponding thermal treatment, the new generated nanocomposite YBCO layer has been characterised with laboratory techniques, demonstrating that there can be $MnFe_2O_4$ NPs inside the YBCO layer (HR-TEM) and that the Fe and Mn are distributed along the thickness of the layer (XPS). Respect to the superconducting properties, even their are not the best result achieved for YBCO nanocomposites, results seems to be promising, because only 1.5 % in molar ratio of nanoparticles respect to the total amount of YBCO have been introduced into the YBCO matrix.

Part III

Large Scientific Facilities

Chapter 6

Introduction

Contents

6.1 Scientific-Technical Singular Infrastructures

"Scientific-Technical Singular Infrastructures" (STSI) is the denomination to a particular facility whose importance and strategic nature research, justify their availability to the scientific community and the high economic investment to their build and maintenance.

Several facilities are enclosed in this category. Focusing in the European Union,[1] the European Space Agency (ESA), European Organisation for Nuclear Research (CERN), Pulsed Neutron and Muon Source (ISIS), European Synchrotron Radiation Facility (ESRF), Institut Laue-Langevin (ILL), X-ray Free Electron Laser (XFEL) among others, are the larger scientific European facilities. Two main classes of STSI could be differentiated: The first class are those facilities which realise scientific research by themselves due to their specialisation (ESA, CERN...) while the second one corresponds to those that provide the tools and conditions to public researchers to perform analyses inside their specialised installations (such as generally synchrotron and neutron facilities). These second centres provide the last technology and resources to generate a high quality research in some key scientific fields for society development.

The access to these large facilities for public research groups is carried out by a public call, where a specialised scientific committee prioritises the time of analysis available depending on the scientific excellence of the proposal submitted. This prioritisation is based on the scientific potential or social impact obtained through the experiment requested. Private companies or research centres can access to these services by renting the equipment and the time of use.

Synchrotron and neutron facilities are a subset of the second group of STSI. Their practical applications cover a wide range of physicochemical techniques based on the particle-particle or radiation-particle interactions: spectroscopy, scattering, imaging and time-resolved measurements are the main four categories:

1. Spectroscopy: Subclass which involves radiation-particle interaction in function of the radiation energy.[2] Absorption or emission of light can be produced by the atoms of the material, providing structural or atomic information: Infrared spectroscopy (from 1.24 meV to 1.7 eV) gives information about vibrational modes of the molecules;[3] moreover, X-ray absorption spectroscopy[4] (from 120

eV to 120 keV) electronic atomic transition is revealed, obtaining as consequence, information about atomic specificity,[5] oxidation states,[6] coordination sphere,[7] magnetic properties[8]... By its part, γ-rays, ultraviolet or visible spectroscopy can be also used if they are needed for the respective cases.

2. Scattering: Analyses substantiated on the fact that a beam of particles or radiation can be modified in direction (and in some case also in energy) by the atoms or inhomogeneities present in the sample.[9] Elastic interaction (such as diffraction[10]) occurs when the direction of the incident beam changes maintaining constant their energy after interact with the sample. In case that the energy and direction were modified, an inelastic scattering is produced (as in the case of inelastic X-ray resonance[11]).

3. Imaging: Methodology based on the combination of light-matter interactions and advanced detection systems and computing.[12] Through this system, spatial distribution of sample inhomogeneities can be obtained, even in three dimensions, to investigate the internal structure with a non-destructive technique. Computed tomography,[13] fluorescence atomic selectivity,[14] or spatial irradiation to medical therapy[15] are three of the most important techniques used.

4. Time-resolved: These techniques (which can be combined with the previous ones) are based in the fact that the radiation or particle beam can be in pulses (not continuous). These beam pulsations can be exploited to make experiments with each pulse, obtaining distinct analysis at different times.[16] Time resolved techniques are very useful in investigating high speed chemical reactions,[17] electronic transitions,[18] etc.

Via the above mentioned techniques, the scientific potential of STSI have been previously demonstrated by several important discoveries. One of the most known examples is the 1997 Nobel price John Walker, who discovered the ATPase structure using Daresbury synchrotron light source.[19] The research in high technological facilities opens the doors to a new stage of knowledge and the corresponding social impact in a wide range of fields.

For magnetic ferrite nanoparticles and nanocomposite superconducting layers it is interesting to know their structure and magnetic behaviour. Two research techniques have been used: neutron and X-ray diffraction (ND & XRD) and X-ray Magnetic

Circular Dichroism (XMCD) through X-ray Absorption Spectroscopy (XAS).

In the continuation of this chapter, neutron and synchrotron large scientific facilities will be discussed as powerful techniques to characterise and study the properties of the mater.

6.2 Neutron reactors

Neutron reactors are installations to supply, control and apply the byproducts (neutrons, heat, radiation...) produced by a controlled nuclear chain reaction.[20] The two main purposes to build nuclear reactors are energy supply and research. The energy neutron reactors (commonly known as nuclear electric central) are aimed to transform the energy (heat) produced by the nuclear fission to electric energy through heat exchangers and turbines. The second group of nuclear reactors are developed and optimised to use neutrons produced to scientific research, field which is actually in expansion due to their actual and promising properties.

6.2.1 Neutron properties

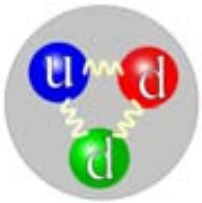

Figure 6.1: Neutron structure formed by two quarks down and one up.[21]

A neutron is one of the three particles which conform the atom. Formed by 3 quarks (2 down, 1 up; figure 6.1), it can be found at the nucleus of the atoms jointly with the other nucleon, the proton (2 quarks up, 1 down), linked each other by the *strong nuclear force*. Because their size, it can be described as a particle and wave at the same time, explaining their properties and behaviour through the quantum mechanics. Below, the principal physical properties of the neutron are showed[22–24] (table 6.1):

The average lifetime of the free neutrons is around 888 s before disintegrate into a proton (p^+), electron (e^-) and anti-neutrino ($\overline{\nu}$). Hence, neutrons have to be produced shortly before use them to the final objective.[25]

$$\mathrm{n} \rightarrow p^+ + e^- + \overline{\nu}$$

Neutron Properties	
Mass (m_n)	$1.675 \cdot 10^{-27} kg$
Charge	0
Confinement radius	0.7 fm
Spin	1/2
Magnetic moment	-1.913 μ_B
Nuclear magneton	$5.051 \cdot 10^{-27} JT^{-1}$
Average life time	887.6±3 s

Table 6.1: Principal physic neutron properties

Despite the zero charge of the neutron, an interaction with the atomic nucleus can occur and it can be described by the scattering length[a], differentiating lighter atoms from heavy ones, two similar Z atomic number atoms or even two isotopes, etc. The quasi-randomly dependence between the scattering length in function of the Z atomic number, as well as high cross sections from some light elements, make neutrons an adequate tool to distinguish two close Z atomic nucleus, detect lighter atoms or even difference among two different isotopes.

Their magnetic moment makes neutron sensitive to interact with unpaired electrons from magnetic samples[26] or radical molecules,[27] being interesting to analyse magnetic samples. Other property to mention is that their wavelength (from 0.1Å to 1000Å) is well adapted to probe atomic and molecular structures, study phonons[28, 29] and magnons,[30] etc.

6.2.2 Neutron generation and control

With the aim to use neutron beam for scientific research purposes, the generation and control of neutrons have to be understood. A simplified view about the neutron beam facilities and their applications are explained below:[20]

[a] Measure of the character and intensity of the interaction of a neutron with an atomic nucleus.

i Neutron reactor

As it have been presented in section 6.2, a fission reactor is a device where a controlled fission chain reaction of heavy atoms occurs. Typically U^{235} (nucleus whose number of neutrons exceeds the number of protons by around $\sim$40%), principally obtained from UO_2, UO_3 or U_3O_8, is used as principal fuel to produce the chain reaction and as consequence to generate neutrons.

The neutron reactor (figure 6.2) is contained into a physical space that has been protected in order to avoid the emission of radiation or radioactive materials outside, fact that can produce biological damage. Commonly, the reactor is surrounded by a neutron absorbing material (principally D_2O) and by a construction material (lead and/or metal enriched concrete) which involves all the nuclear reactor and the working complex including the beamlines.

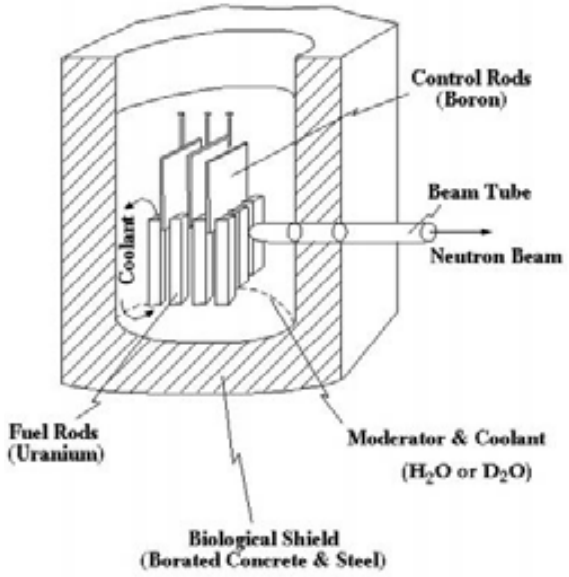

Figure 6.2: Schematic view of a neutron reaction core.[23]

Fission reaction can be explained as a continual breakage of heavy atomic nucleus following an impact of a neutron, producing two less heavy atoms, heat and three neutrons which restart this procedure. In more specific words, when initially a neutron is spontaneously emitted by a U^{235} nucleus and absorbed by other U^{235}, an unstable U^{236} is produced. Then, a rupture (fission) of the nucleus into less heavy atoms happens (such as Ba^{141} and Kr^{92}), generating energy and 3 new neutrons valuables to contribute to the chain reaction. Part of the neutrons are used to

maintain the nuclear reaction ratio, while the rest can be extracted from the reactor and used for experiments (see figure 6.3).

Different classes of neutrons are generated in the reactor, and they can be classified according to their energy: fast neutrons ($E_n > 1MeV$), intermediate energy ($1MeV > E_n > 1eV$) or slow ($E_n < 1eV$). The natural relationship of the three complementary neutrons fluxes generated is governed by a Maxwell-Boltzmann distribution, and it is a consequence of the first selection of neutrons that occurs naturally, since some nuclear fuels produces more or less fast neutrons depending on their atomic cross section[b]. In addition, other speed moderators can be interposed in the neutrons way in order to reduce their energy, or alternative techniques as gravitational or magnetic techniques can be also used to produce the desired energetic neutrons.

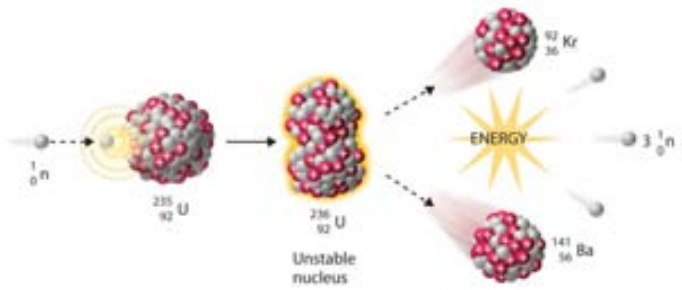

Figure 6.3: Atomic nuclear fission chain reaction.[31] Neutrons produced by the fission feed the chain reaction. In some cases a part of these neutrons are extracted from the core and profited to perform neutron experiments.

To avoid an uncontrolled fission reaction, neutron-absorbing materials (Cadmium, Boron ...) can be introduced into the high-protected reactor to produce the reaction slowdown. The importance of this control systems is high, because an uncontrolled reaction can produce an excess of heat, which can derived in the fission of the reaction container (nucleus fission) and produce severe consequences (Chernobyl disaster in 1986[32] or more recently Fukushima in 2011[33]).

[b] In this specific case, there is also the probability that a neutron is slowed by the interaction with the atoms of the fuel itself.

ii Neutron beam properties

Below, the most remarkable characteristics that make the neutron beam more relevant compared to other techniques are briefly explained:

1. Particle beam: Neutrons are particles that can interact with matter in a different way than electromagnetic radiation, and more information can be achieved. While photons interact with the electronic wave of the atoms, neutrons can interact with the atomic nucleus and/or unpaired e^-.

2. Energy: Nuclear reactors produce variable energetic neutrons that can be selected to perform the adequate analysis. The wavelength, variable from 0.1Å to 1000Å, makes possible to perform several analyses, as it can be atomic physics investigations with high energy neutrons or composition and structure determination using thermal or cold neutrons.

3. Spin: Neutron has a magnetic spin of 1/2. This property can be used to study radical or paramagnetic systems where an interaction between the neutron and unpaired e^- can occur.

4. Polarisation: Magnetic spin of neutrons can be oriented in order to produced a magnetic polarised neutron beam. Magnetic studies of materials can be carried out specifically by this characteristic.

iii Beamlines

Once neutrons have been produced, it is necessary to extract and transport them from the nuclear reactor until the experimental station. Wave-guides, which are metal conductions specifically designed to this purpose, are the responsible for carrying out this task. The denominated experimental stations are called beamlines; they are composed by a set of instrumentation to provide the tools and conditions required to perform the experiment. These conditions can come from the neutron beam (energy, flux, collimation, etc.) or from the sample (temperature, pressure, etc.).

Beamlines are commonly formed by four sectors that below briefly detailed:

1. Optics: Control the properties of the neutron beam coming from the reactor through the wave-guides. The final aim of the optical sector is to produce a

neutron beam with the characteristics required to perform the analysis. Here, enter and exit slits, monochromator, filters, etc. can be found.

2. Experimental section: Is in this part where the sample is mounted and oriented, and there the experimental conditions are applied through the corresponding system (such as: furnace, cryocooler, press, etc.).

3. Detector: The detection system is the last physical part of the beamline. It consists of the proper detector (depending on the kind of measure and neutron characteristics) which generate an electric signal proportional to the neutrons detected in the measurement. This analogical signal is transformed to a digital one and recorded by a computer system.

4. Control and acquisition system: Computing resource capable to control and supervise the different components which conform the beamline, and also used for acquisition and storage of data collected. It is in this remote part where the scientist works the most of the time in order to define all the conditions of the measurements, avoiding to be irradiated by the direct or scattered neutron beam of the experimental station.

6.2.3 Applications

Neutron scattering experiments can be useful to answer scientific questions that with another technique would be complicate or impossible. Few examples of use these neutron beams in some scientific fields are presented:

1. Engineering: Because neutron analysis is a non-destructive technique with high penetration deep, the study of structural tensions,[34] deformations,[35] impurities,[36] etc. in different materials is interesting.

2. Bioscience: Due to the high sensitivity of the neutrons to lighter atoms, biological systems can be deeply studied with neutron radiation.[37]

3. Particle physics: Study the properties of the matter at nuclear scale[38] can be crucial to understand and control the behaviour of the materials.

4. Physics, chemistry and materials science: To clarify the structure and properties of novel materials can help to develop new optimised products that can produce

a high positive impact in the actual society.[39, 40] Specially, questions related to magnetism were (and still are) widely addressed using neutrons.

The phenomenon which governs the most of the analyses performed with the neutron beam obtained at the nuclear reactors is the neutron scattering, and among the subclasses, neutron powder di raction deserves to be highlighted. Next chapters de nes this technique (section 7.1) and their application to the magnetic ferrite nanostructures (chapter 8).

6.3 Synchrotron lightsources

X-rays generation and control is a critical point to consider when a high ux (or brilliance) and high resolution is needed to perform detailed analysis of a sample. Cathodic X-ray tube was the rst X-ray source (which is actually the most common one) based on the photoelectric e ect, following by optimised techniques such as rotating anode and others more sophisticated[16] like synchrotron and the novel one, free electron lasers (FELs).[41] Figure 6.4 represents the evolution of the X-rays brilliance (see equation 6.8) since the cathodic tube technique until the FELs.

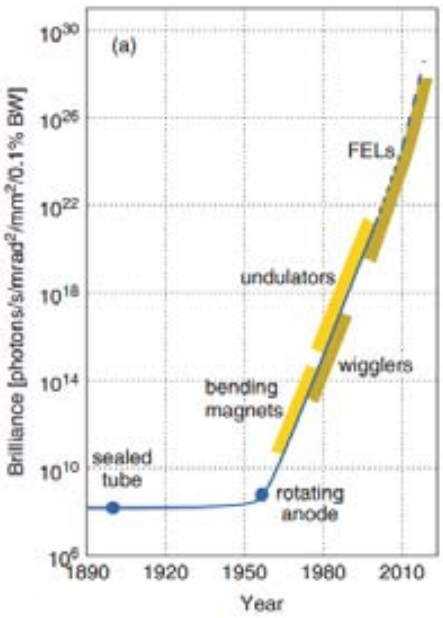

Figure 6.4: Brilliance of X-ray sources.[16] Bending magnets, wigglers and undulators are three components which can be used to produce synchrotron radiation

Development of this technology has allowed to generate and control high brilliance and focused X-ray beams which are very useful in fundamental research of the mater and its structure. In this work, it will be explained the 3^{th} generation lightsources that use Insertion Devices to produced a high flux of high brilliance X-ray beam: the synchrotron. It consists of a particle accelerator that is used in some particular cases (as in this) as source of electromagnetic radiation.

6.3.1 From classic to relativistic world

In order to understand the generation of X-rays by a synchrotron, a shallow explanation of the physics which governed this phenomenon is needed, a explanation which implies a little introduction to relativistic mechanics.[16, 42]

The energy of a rest particle is defined by the famous Einstein's equation 6.1:

$$E = mc^2 \tag{6.1}$$

where m is the mass of the particle and c the speed of light. When the particle is in motion, its energy is the sum of the rest energy and the kinetic energy (E_K) (equation 6.2):

$$E = mc^2 + E_K \tag{6.2}$$

When a charged particles is decelerated, it looses kinetic energy which is transform in emitted electromagnetic radiation. The radiation power emitted can be described[43] with Lamor formula when the speed of the particle is far from speed of light, a formula based on classical electrodynamics (formula 6.3):

$$P = \frac{2e^2a^2}{3c^3} \tag{6.3}$$

where P is the power irradiated, e the charge of the particle, a the acceleration, and c the speed of light; all in CSG units.

In the case of the synchrotron, a charged particle is accelerated (generally electrons) until a speed close of the speed of light in a circular trajectory. Then, considering the circular trajectory and the relativistic factor γ, and through a Lorenz

transformation, the emission of electromagnetic radiation by the charged particle each circular lap is given by (equation 6.4):

$$P = \frac{2}{3} c e^2 \frac{\beta^4 \gamma^4}{r^2} \tag{6.4}$$

being r the radius of the curvature and β and γ defined as:

$$\beta = \frac{v}{c} \quad \gamma = \frac{E}{mc^2} = \frac{1}{\sqrt{1-\beta^2}} \tag{6.5}$$

with v the speed of the charged particle, c the speed of light, E its energy and m its mass. γ is defined also as the relativistic factor (significant for v close to c), and changes between 0 for a particle without movement, and tends to 1 for a particle which travels to the speed of light.

It can be deduced from these equations the energy dependence in front of the γ factor, which is dependent from the speed of the e^-: higher speed entails higher e^- energy. Equation 6.6 relates the speed that it is possible to achieve in a circular trajectory with other limiting parameters:

$$v = \frac{qBr}{m} \tag{6.6}$$

where v is the speed of the e^-, q its charge, B the applied magnetic field to accelerate the e^-, r the radius of curvature and m the e^- mass. Following this equation, if higher speed wants to be achieved (higher power emitted), it is necessary to increase the magnetic field (B) or the curvature radius (r), explanation of why bigger facilities are being building to get higher energies. Large infrastructure investment is needed for build higher energy systems.

In the specific case of a synchrotron, an e^- is moved with a circular trajectory where the accelerating force is perpendicular to the direction of motion which is tangential to the circular orbit. When this relativistic electron is decelerated by a change of direction (to complete the circular trajectory), it emits an electromagnetic field tangentially to the curvature. The fact that the electrons travel at relativistic speed makes that the emission is produced tangentially to the curvature with lower divergence than in the case of non relativistic particles, figure 6.5.

The energy emitted by an e^- each circular lap can be calculated and simplified to depends on the energy of the e^- and the radius of the curvature. The formula 6.7

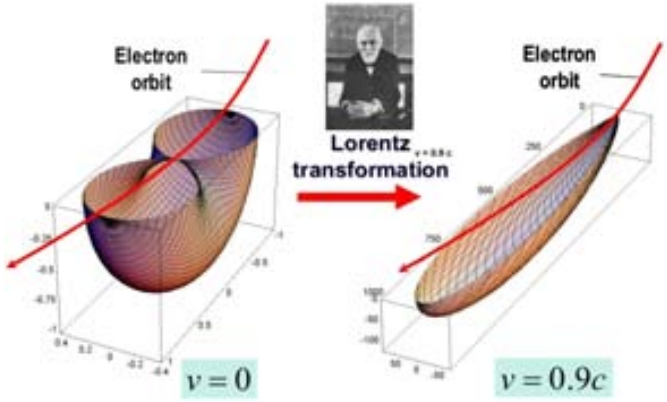

Figure 6.5: Emission field of a non relativistic electron (left) and another relativistic (right) which travels at speed close of the speed of light.[44] The emission field of the second one in less divergent and more addressed, effect with produces a higher radiation brilliance.

resumes the relationship between the energy of the accelerated electrons (E), the curvature radius (r) and the energy loss through radiation emitted (ΔE).

$$\Delta E(KeV) = 88.5 \frac{E^4(GeV^4)}{r(m)} \tag{6.7}$$

As it can be seen, the energy loss of the electron each lap (in form of radiation) is related by a 4^{th} power of its energy. Thus, the synchrotron radiation is significant for an energy higher than 1 GeV, like the most of the actual synchrotrons have.

Since this point, only one charged particle has taken into account, but in a synchrotron, millions of electrons are accelerated in bunches, and each electron produces electromagnetic radiation. This is the main cause of the high brilliance of the synchrotrons, because millions of electrons produce millions of photons when they decelerate at the same time. Generally, the electrical current carried by a synchrotron to produce electromagnetic radiation varies form 10 to 500 mA for the most of the cases.

6.3.2 Light generation and control

Synchrotron lightsources are designed to produce electromagnetic radiation (focused in X-ray, but considering the visible and infrared light) to be used in materials and structure research. As it has been explained, this radiation is produced when a

charged particle that moves close to the speed of light is decelerated by changing their direction in order to complete their circular trajectory. So that be possible, electrons have to be produced, then accelerated and finally maintained at the final speed into a close ring to produce a practically continuous radiation emission. In this point, the main parts which conform a synchrotron will be explained.[16]

i Instrumentation

LinAc, Booster and Storage Ring are the three principal sections that are needed to produce, accelerate and control the electrons which generate the electromagnetic radiation that will be profited in the beamlines to perform the desired experiment.

1. LinAc: (or linear accelerator). In this section the electrons are produced and accelerated until an energy of hundreds of MeV by action of an electric field. LinAc is generally formed by a thermoionic gun that produces electrons with a low divergence under a high electric field. A good performance of this section is crucial, because the divergence of the source affects to the final divergence of the radiation produced. When the electrons are accelerated by the LinAc, their are injected into the Booster.

2. Booster: Circular segment formed by straight and curved sections where the electrons injected by the LinAc are accelerated until the nominal energy. This is made by action of the radiofrequency system, which is synchronised with the pass of the electrons through the resonance cavity. When electrons go inside a radiofrequency cavity, an electromagnetic wave gives energy to these electrons, and also produces a distribution of them in bunches due to the interaction between the electromagnetic wave in the resonance cavity an the electrons. The repetitive and synchronised frequency interaction of this wave and the electrons does that the electron bunches increases their speed more than the 99.9999 % of the speed of light and until their final energy (around some GeV generally).

   Once the electrons have been accelerated until a the final speed and distributed into bunches, they are injected into the Storage Ring to maintain constant their energy and profit the synchrotron radiation produced when their trajectory is changed.

3. Storage Ring: The storage ring is the nal component of a synchrotron where the electrons accelerated by the Booster are maintained at their nal speed (by other radiofrequency system) and where their electromagnetic radiation is pro ted.

   It has similar constitution than the Booster, and it consists of a resonance cavity, bending magnets (BM) which are used to curve the trajectory of the electrons and produce as consequence electromagnetic radiation, quadrupoles and sextupoles to focus and defocus the electron beam to control their divergence and position into the vacuum tube, beam positioning control, etc. and nally, in case of 3^{th} generation sources, insertion devices, systems dedicated to produce electromagnetic radiation with speci c characteristics that will be pro ted at the end stations (see point ii).

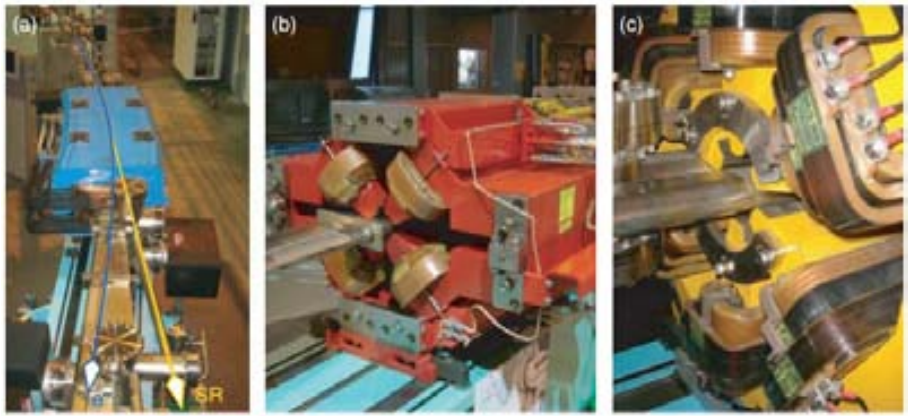

Figure 6.6: Main parts of a synchrotron storage ring:[16] (a) Bending magnet used to curve the trajectory of the electron beam. (b) and (c), quadrupole and sextupole to focus and defocus the electron beam.

Figure 6.7 shows an scheme of a typical synchrotron. The three main parts can be di erentiated. It can be seen that the Booster and Storage Ring are formed by linear and curved sections. Also, the beamline hutches that will be discussed later (part iv of this section) are showed.

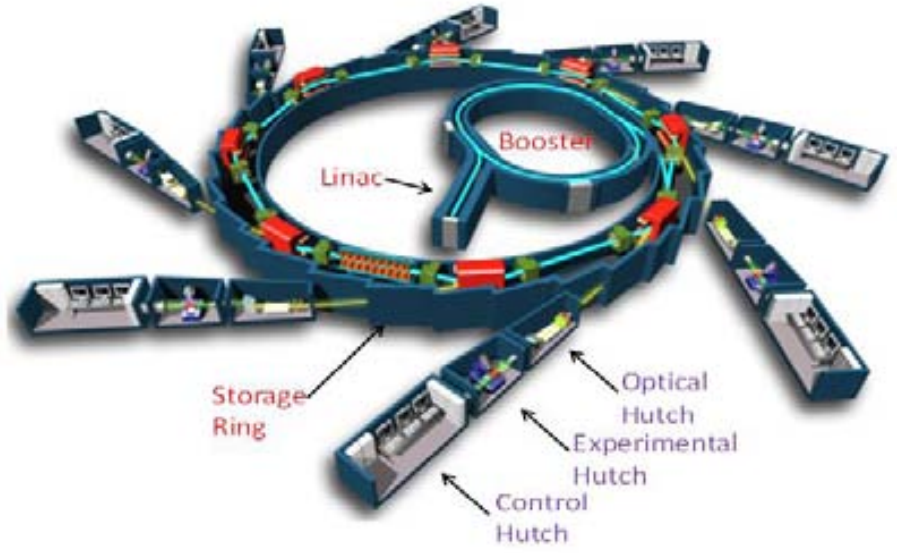

Figure 6.7: Synchrotron general scheme composed by LinAc, Booster and Storage Ring.[45] The beamline experimental hutches will be discussed later.

ii Insertion devices

Since this point, electromagnetic radiation generation has been explained as consequence of the deceleration of the electrons when their trajectory is changed, principally by the bending magnets of the synchrotron. If this concept is amplified, it exists the possibility to curve repetitively the trajectory of the electrons in a short space in order to generate an amplified electromagnetic radiation beam. As it has been demonstrated in the equation 6.4, the power (or energy) depends on the speed and the curvature radius. Then, for a constant speed, the energy of the emitted radiation can be controlled by modifying the curvature radius.

Bending magnets produce a contiguous spectra of electromagnetic radiation due to their variable curvature radius. Because of that, the radiation spectra is wide in energy but lower in flux for a precise energy. Profiting this effect, it is possible to generate a repetitive and controlled curvature of the electrons in a straight section of the storage ring to produce a controlled energy spectra, which is sharper and intenser than in the case of the bending magnets. This effect can be achieved by implementing insertion devices (ID) into the storage ring, devices which consist of a sequence of permanent magnets that curve repetitively the trajectory of the electrons.

Next, a brief explanation of the different systems of radiation generation will be discussed:

1. Bending magnet: It is a curved permanent magnet which is used to bend the trajectory of the electrons. Because of its variable curvature radius, a continuous electromagnetic spectra is produced tangentially to the trajectory of the electron bunch that pass through its magnetic field.

2. Wiggler: A wiggler is an insertion device that is formed by two sets of separated and alternate oriented permanent magnets. Between their two rows of permanent magnets the electron bunches pass through. The electrons describes a repetitive curved trajectory that can be controlled by the gap between these two sets of permanent magnets, because a variation of the magnetic field is generated. By an ID, a higher collimated and intenser beam is achieved than with a bending magnet.

3. Undulator: An undulator is based on the same properties than wigglers. This other ID profits the relative disposition between both sets of variable permanent magnets in order to produce interference effects with the radiation produced with the finality to obtain more collimated and sharper spectrum than in the case of wigglers.

Figure 6.8 represents a scheme of the bending magnet and ID (wiggler and undulator) to generate the synchrotron radiation. The brightness of the commented ID can be seen in the previous figure 6.4.

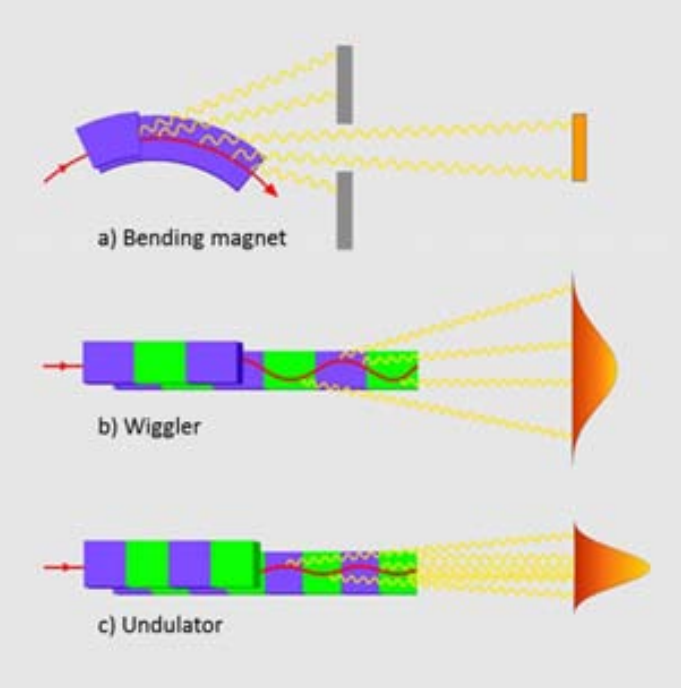

Figure 6.8: Scheme of the radiation produced by a bending magnet and the two kinds of Insertion Devices.[46]

iii Synchrotron radiation properties

Electromagnetic radiation produced by a synchrotron is very useful due to their properties that cannot be achieved with other common techniques. These principal properties are enumerated below:

1. Tunable energy: By monochromating or selecting the gap of an ID, it is possible to modify the energy of the light beam. The bending magnets produce a wide radiation spectra while the IDs generate a sharper energy peak, both of them have to be monochromated in order to achieve high energy resolution $\frac{E}{E}<10^{\ 4}$.

2. High ux: De ned as photons each second, the synchrotron radiation produces a ux that can be several orders bigger than a common X-ray cathodic tube.

3. High brilliance: It is the ux per area and per solid angle:

$$B = \frac{ph\ \ s}{mrad^2\ \ mm^2 source\ area\ \ 0\ 1\ \%\ of\ bandwith} \tag{6.8}$$

As it has been explained, the 3^{th} generation sources produces a high brilliance as it can be seen in gure 6.4. This high brilliance can be achieved due to the

low divergence and high flux of the light beam.

4. High stability: Synchrotron radiation produces a light beam with a high stability which allows to control the beam position by the optics with high micrometer, even nanometer precision.

5. Planar or selectable polarisation: Due to the planar circular orbit of the electrons, the light produced has a rectangular divergence with a typical ratio $\frac{Horizontal\ size}{Vertical\ size} \approx 7$ and with a planar polarisation. Thanks to the IDs, the polarisation of the emitted beam can be controlled by changing the trajectory of the electrons when pass through the ID. The polarisation of the emitted beam depends on the trajectory of the electrons: if the trajectory is elliptical, an elliptical polarisation is obtained, if it is in a determinate plane, it produces a linear polarisation in that plane, etc.

6. Pulsed structure: The presence of electron bunches (controlled by the radiofrequency cavity) and not a continuous flow of electrons, produce a pulsed emission of light. This allows to obtain temporal analyses, in which each bunch emits a light pulse that can be use to one analysis. Then, in a second, hundreds of analyses can be performed, resolving a temporal structure limited by the detector and computing system. For other cases, a continuous beam generation is considered.

All of the above mentioned properties, among others, make synchrotron facility as a necessary STSI to perform advanced analysis which develop the knowledge of science.

Do not forget that the electromagnetic radiation produced by a synchrotron has to be profited to perform the desired specific analysis. Hence, a control of this X-ray beam is needed in order to select their properties to carry out the experiment at the beamline.

iv Beamlines

Beamlines are situated outside and tangentially to the storage ring in the points where synchrotron radiation is produced (after a bending magnet or ID). They consist of an ensemble of optics to prepare the beam, the experimental part where the sample

is mounted and conditioned, and the control section. These parts are differentiated in three physical spaces, where typically each section correspond to a hutch: optical hutch, experimental hutch and control hutch. The presence of the hutches in the case of the optical and experimental part is due to protect the exterior working space from the electromagnetic radiation beam that, if the energy is elevated, is biohazardous. These hutches are a metal blinded space where the emitted radiation is stopped before irradiate the working public space.

Below, a short explanation about the three hutches can be found:

1. Optical Hutch: In this section, the generated polychromatic beam is prepared to irradiate the sample in the experimental hutch. First, the enter slits delimit the beam size which will be monochromate by the mirrors of the monochromator. Then, the focusing mirrors and other slits prepare the beam to irradiate the sample in the contiguous experimental space. In addition, other systems can be installed to control the beam position or their properties.

2. Experimental Hutch: Is in this specific part where the sample and the instrumentation needed to perform the analysis are installed. Sample environment (cryocooler, furnace, diamond press, etc.), experimental conditions (vacuum chamber, magnets, diffractometer, etc.), detection systems, etc. can be found in this experimental hutch.

3. Control Hutch: Working space where the scientist control and supervise all the systems of the beamline using a computer control. Control the optics of the beamline, the sample conditions and data acquisition are three of the main purposes of the control hutch.

Beamlines belong to the scientific part of the synchrotron radiation generation. It provides the tools to perform the adequate analysis to the sample. Each beamline is specifically designed to a specific purpose, following the scientific requirements. Several instrumental parameters has to be taken into account when the beamline is designed: energy range (select between a BM or ID), precise optics (monochromator for high, medium or low energies), sample environment (sample positioning, magnetic fields, temperature control, pressure...), detection systems (fluorescence, total electron yield, CCD camera...) and other systems like automatic sampler exchanger, vacuum, pre-chambers, etc.

6.3.3 Applications

Here, few scientific fields where the synchrotron radiation can be applied to obtain significant results are presented:

1. Medicine: From study the basis of the chemistry involving biological and nanostructures,[47] to cancer therapy[48] with X-ray beam due to their controlled size and energy perfectly controlled dose and depth, reducing the collateral effects of the radiotherapy.

2. Cultural heritage: Study the composition, origin or to authenticate the cultural heritage[49] can be performed with non destructive techniques with synchrotron radiation (structural or compositional analysis). Also, to study the internal composition and make a tridimensional map of a sample without destroy it is possible thanks to the computed imaging techniques.[50]

3. Chemistry: Thanks to the high brilliance and control of the beam, low quantity samples can be analysed and also in real time (time resolved experiments). One social example is the analysis of samples of crime scenes when the sample availability is limited.[51]

4. Materials: Study the composition, structure and behaviour of novel materials can help to understand and improve these materials which can have a potential impact in the society.[52, 53]

These are some of the practically infinite possibilities to use synchrotron radiation. Actually, research to develop new analysis systems and techniques are being addressed.

6.4 Neutron versus synchrotron

At this point, synchrotron and neutron facilities have been introduced. Table 6.2 shows the most important differences between these two STSI:[54]

Changes in atomic scattering cross section for neutron and X-ray diffraction make that both techniques can be complementary in results. The cross section can also be likened to the atomic visibility by neutrons or X-rays, in the sense that some atoms are more visible for neutrons than for X-rays and vice-verse. Figure 6.9

Neutron	Synchrotron
Particle beam	Electromagnetic radiation beam
Nuclei and unpaired e interaction	Electronic wave interaction
Scatter by all elements (even lighter ones)	Scatter by heavy atoms
Deep penetration	Super cial analysis
Less intensity (large samples)	High intensity (small samples)

Table 6.2: Neutron and synchrotron radiation beam comparison. Note the neutron beam is for large samples while synchrotron is focused in small size samples.

presented below expresses this fact in a graphical form.

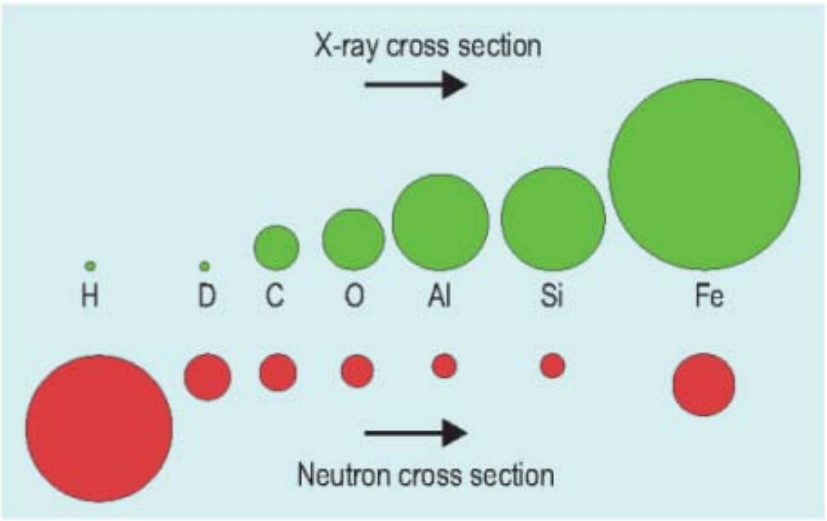

Figure 6.9: Schematic vision of the di erence of the atomic cross section for neutrons and X-rays.[55] Note that for X-rays there is an increasing tend with Z, while neutron is more random.

While X-ray interaction with the atom depends on the number of electrons, an as consequence of the atomic number, the neutron interaction with the nucleus depends on the *Fermi length*, which is a measure for the interaction. Neutrons have a random dependence with the atomic Z number, being possible to interact in a diverse form with two atomic species close in the periodic table. Table 6.3 shows these Fermi lengths[23] compared with the atomic number Z for the rst row of transition elements and the common elements of organic matter.

Atom	Atomic number	Fermi length	Atom	Atomic number	Fermi length
Sc	21	12.1	Ni	28	10.3(1)
Ti	22	-3.370(13)	Cu	29	7.718(4)
V	23	-0.443(14)	Zn	30	5.680(5)
Cr	24	3.635(7)	H	1	-3.74
Mn	25	-3.750(18)	C	6	5.805(11)
Fe	26	9.45(2)	O	8	6.6484(13)
Co	27	2.49 (2)			

Table 6.3: Fermi lengths for different atoms with similar Z number and for the principal atoms of the organic matter.

In general trends, neutron diffraction (high penetration deep, low flux) is used with scattering techniques to analyse large samples, samples containing lighter atoms (such as H, C, O) or samples where a similar Z atoms identification is needed. X-ray synchrotron radiation (high flux, small penetration) is focused more in investigating small samples via scattering to structural analyses and using spectroscopic techniques to atomic characterisation.

Each technique (X-ray or neutron) have their correspondent advantages and disadvantages, and the work of the scientist is to select the proper methodology and specific technique to fix the problems or looking for solutions. A combination of a few methods is also very useful, as it is going to be showing later in this work.

Bibliography Chapter 6

[1] "European portal on research infrastructures services." `http://www.riportal.eu`. Access July, 2013. (cited on page(s) 114)

[2] J. M. Hollas, *Modern spectroscopy.* John Wiley & Sons, 2004. (cited on page(s) 114)

[3] J. Yarwood, R. Douthwaite, and S. Duckett, eds., *Spectroscopic properties of inorganic and organometallic compounds: techniques, materials and applications.* The royal society of chemistry, 2012. (cited on page(s) 114)

[4] T.-K. Sham, ed., *Chemical applications of synchrotron radiation*, vol. 2. World scientific publishing, 2002. (cited on page(s) 114, 146)

[5] S. Limpijumnong, S. Rujirawat, A. Boonchun, M. F. Smith, and B. Cherdhirunkorn, "Identification of Mn site in Pb(Zr,Ti)O_3 by synchrotron x-ray absorption near-edge structure: Theory and experiment," *Applied Physics Letters*, vol. 90, no. 10, p. 103113, 2007. (cited on page(s) 115)

[6] A. Espinosa, A. Serrano, A. Llavona, J. Jimenez de la Morena, M. Abuin, A. Figuerola, T. Pellegrino, J. F. Fernandez, M. Garcia-Hernandez, G. R. Castro, and M. A. Garcia, "On the discrimination between magnetite and maghemite by XANES measurements in fluorescence mode," *Measurement Science and Technology*, vol. 23, no. 1, p. 15602, 2012. (cited on page(s) 115)

[7] R. K. Hocking, E. C. Wasinger, F. M. F. de Groot, K. O. Hodgson, B. Hedman, and E. I. Solomon, "Fe L-edge XAS studies of $K_4[Fe(CN)_6]$ and $K_3[Fe(CN)_6]$: a direct probe of back-bonding," *Journal of the American Chemical Society*, vol. 128, no. 32, pp. 10442–51, 2006. (cited on page(s) 115)

[8] D. J. Huang, C. F. Chang, H.-T. Jeng, G. Y. Guo, H.-J. Lin, W. B. Wu, H. C. Ku, A. Fujimori, Y. Takahashi, and C. T. Chen, "Spin and orbital magnetic moments of Fe_3O_4," *Physical Review Letters*, vol. 93, no. 7, pp. 2–5, 2004. (cited on page(s) 115, 209, 210)

[9] J. Als-Nielsen and D. McMorrow, *Elements of modern X-ray physics*. John Wiley & Sons, 2011. (cited on page(s) 115, 146, 158, 165)

[10] C.-S. Yoo, H. Wei, R. Dias, G. Shen, J. Smith, J.-Y. Chen, and W. Evans, "Time-resolved synchrotron X-ray diffraction on pulse laser heated iron in diamond anvil cell," *Journal of Physics: Conference Series*, vol. 377, p. 12108, 2012. (cited on page(s) 115)

[11] J. Kim, D. Casa, M. Upton, T. Gog, Y.-J. Kim, J. Mitchell, M. van Veenendaal, M. Daghofer, J. van den Brink, G. Khaliullin, and B. Kim, "Magnetic excitation spectra of Sr_2IrO_4 probed by resonant inelastic X-ray scattering: establishing links to cuprate cuperconductors," *Physical Review Letters*, vol. 108, no. 17, pp. 1–5, 2012. (cited on page(s) 115)

[12] E. Beaurepaire, H. Bulou, F. Scheurer, and J.-P. Kappler, eds., *Magnetism and synchrotron radiation: New trends*. Springer, 2010. (cited on page(s) 115, 146)

[13] C. Chappard, S. Bensalah, C. Olivier, P. J. Gouttenoire, A. Marchadier, C. Benhamou, and F. Peyrin, "3D characterization of pores in the cortical bone of human femur in the elderly at different locations as determined by synchrotron micro-computed tomography images," *Osteoporosis international*, 2012. (cited on page(s) 115)

[14] R. Robert, D. Zeng, A. Lanzirotti, P. Adamson, S. J. Clarke, and C. P. Grey, "Scanning X-ray fluorescence imaging study of lithium insertion into copper based oxysulfides for Li-ion batteries," *Chemistry of Materials*, vol. 24, no. 14, pp. 2684–2691, 2012. (cited on page(s) 115)

[15] F. Carroll, "Tunable, monochromatic X-rays: an enabling technology for molecular/cellular imaging and therapy," *Journal of Cellular Biochemistry*, vol. 90, no. 3, pp. 502–8, 2003. (cited on page(s) 115)

[16] P. Willmott, *An introduction to synchrotron radiation: techniques and applications*. John William & Sons, 2011. (cited on page(s) 115, 122, 123, 126, 127,

146, 163)

[17] Q. Wang, J. C. Hanson, and A. I. Frenkel, "Solving the structure of reaction intermediates by time-resolved synchrotron x-ray absorption spectroscopy," *The Journal of Chemical Physics*, vol. 129, no. 23, p. 234502, 2008. (cited on page(s) 115)

[18] N. Huse, T. K. Kim, L. Jamula, J. K. McCusker, F. M. F. de Groot, and R. W. Schoenlein, "Photo-induced spin-state conversion in solvated transition metal complexes probed via time-resolved soft X-ray spectroscopy," *Journal of the American Chemical Society*, vol. 132, no. 19, pp. 6809–16, 2010. (cited on page(s) 115)

[19] J. P. Abrahams, A. G. W. Leslie, R. Lutter, and J. E. Walker, "Structure at 2.8 Å resolution of F_1-ATPase from bovine heart mitochondria," *Nature*, vol. 370, pp. 621–628, 1994. (cited on page(s) 115)

[20] J. Byrne, *Neutrons, nuclei and matter: An exploration of the physics of slow neutrons*. IOP publishing, 1994. (cited on page(s) 116, 117)

[21] Image taken from `http://goo.gl/0CS94`. Access Dec. 2012. (cited on page(s) 116)

[22] H.-R. Wenk, *Neutrons in soft matter*, vol. 63. Geochemical society mineralogical society of America, 2006. (cited on page(s) 116, 146)

[23] A.-J. Dianoux and G. Lander, eds., *Neutron data booklet*. OCP science, 2003. (cited on page(s) 116, 118, 134)

[24] W. Mampe, P. Ageron, C. Bates, J. Pendlebury, and A. Steyerl, "Neutron lifetime measured with stored ultracold neutrons," *Physical review letters*, vol. 63, no. 6, pp. 593–596, 1989. (cited on page(s) 116)

[25] T. Imae, T. Kanaya, M. Furusaka, and N. Torikai, *Neutrons in soft matter*. John Wiley & Sons, 2011. (cited on page(s) 116, 146)

[26] C. G. Shull, W. A. Strauser, and E. O. Wollan, "Neutron diffraction by paramagnetic and antiferromagnetic substances," *Physical Review*, vol. 83, no. 2, pp. 333–345, 1951. (cited on page(s) 117)

[27] A. Filhol, C. Zeyen, P. Chenavas, J. Gaultier, and P. Delhaes, "Neutron structure at 40 K of an organic semiconductor, the ion radical salt of triethylammonium with 7,7,8,8-tetracyano-p-quinodimethane: $TEA^+ \cdot (TCNQ)_2^-$," *Acta Crystallographica*, vol. 36, no. 1980, pp. 2719–2726, 1980. (cited on page(s) 117)

[28] M. J. Cooper and R. Nathans, "The resolution function in neutron diffractometry. I. The resolution function of a neutron diffractometer and its application to phonon measurements," *Acta Crystallographica*, vol. 23, no. 3, pp. 357–367, 967. (cited on page(s) 117)

[29] H. F. Fong, B. Keimer, and P. Anderson, "Phonon and magnetic neutron scattering at 41 meV in $YBa_2Cu_3O_7$," *Physical Review Letters*, vol. 75, no. 2, pp. 316–319, 1995. (cited on page(s) 117)

[30] M. Hutchings, M. Thorpe, R. Birgeneau, P. Fleury, and H. Guggenheim, "Neutron and optical investigation of magnons and magnon-magnon interaction effects in NiF_2," *Physical Review B*, vol. 2, no. 5, pp. 1362–1373, 1970. (cited on page(s) 117)

[31] H.-R. Wenk, *Neutron scattering in earth sciences*, vol. 63. Geochemical society mineralogical society of America, 2006. (cited on page(s) 119)

[32] "Chernobyl disaster effects." `http://en.wikipedia.org/wiki/Chernobyl_disaster_effects`. Access Nov. 2012. (cited on page(s) 119)

[33] "Fukushima daiichi nuclear disaster." `http://en.wikipedia.org/wiki/Fukushima_Daiichi_nuclear_disaster`. Access Nov. 2012. (cited on page(s) 119)

[34] W. Woo, V. Em, E.-Y. Kim, S. Han, Y. Han, and S.-H. Choi, "Stress-strain relationship between ferrite and martensite in a dual-phase steel studied by in situ neutron diffraction and crystal plasticity theories," *Acta Materialia*, vol. 60, no. 20, pp. 6972–6981, 2012. (cited on page(s) 121)

[35] J. A. Wollmershauser, B. Clausen, and S. Agnew, "A slip system-based kinematic hardening model application to in situ neutron diffraction of cyclic deformation of austenitic stainless steel," *International Journal of Fatigue*, vol. 36, no. 1, pp. 181–193, 2012. (cited on page(s) 121)

[36] J. Hampel, F. M. Boldt, H. Gerstenberg, G. Hampel, J. V. Kratz, S. Reber, and N. Wiehl, "Fast determination of impurities in metallurgical grade silicon for photovoltaics by instrumental neutron activation analysis," *Applied radiation and isotopes*, vol. 69, no. 10, pp. 1365–8, 2011. (cited on page(s) 121)

[37] J. C.-H. Chen, B. L. Hanson, S. Z. Fisher, P. Langan, and A. Y. Kovalevsky, "Direct observation of hydrogen atom dynamics and interactions by ultrahigh resolution neutron protein crystallography," *Proceedings of the National Academy of Sciences of the United States of America*, vol. 109, no. 38, pp. 15301–6, 2012. (cited on page(s) 121)

[38] D. Chaney, T. Ferbel, W. Mollet, P. Slattery, D. Underwoord, E. Bleser, D. Johnson, B. Gobbo, J. Keren, R. Lipton, J. Rosen, R. Ruchti, and D. Spelbring, "Inclusive charged-particle production in neutron-nucleus collisions," *Physical Review Letters*, vol. 40, no. 2, pp. 71–74, 1978. (cited on page(s) 121)

[39] A. Saadat-Monfared, M. Mohseni, and M. H. Tabatabaei, "Polyurethane nanocomposite films containing nano-cerium oxide as UV absorber. Part 1. Static and dynamic light scattering, small angle neutron scattering and optical studies," *Colloids and Surfaces A: Physicochemical and Engineering Aspects*, vol. 408, pp. 64–70, 2012. (cited on page(s) 122)

[40] N. Sharma and V. K. Peterson, "In situ neutron powder diffraction studies of lithium-ion batteries," *Journal of Solid State Electrochemistry*, vol. 16, no. 5, pp. 1849–1856, 2011. (cited on page(s) 122)

[41] "Fel: Free electron laser." `https://www.xfel.eu/`. Access July, 2013. (cited on page(s) 122)

[42] P. J. Duke, *Synchrotron radiation: Production and properties*. Oxford University Press, 2009. (cited on page(s) 123)

[43] G. Henderson and D. R. Baker, *Synchrotron radiation: earth, environmental and material sciences applications*, vol. 30. Mineralogical association of Canada, 2002. (cited on page(s) 123)

[44] Image taken from `http://goo.gl/xDzNM`. Access Nov. 2012. (cited on page(s) 125)

[45] Image modified from `http://goo.gl/FbLsQ`. Access Apr. 2012. (cited on page(s) 128)

[46] Image modified from `http://goo.gl/5Fypu`. Access Dec. 2012. (cited on page(s) 130)

[47] S. Laera, G. Ceccone, F. Rossi, D. Gilliland, R. Hussain, G. Siligardi, and L. Calzolai, "Measuring protein structure and stability of protein-nanoparticle systems with synchrotron radiation circular dichroism," *Nano letters*, vol. 11, no. 10, pp. 4480–4, 2011. (cited on page(s) 133)

[48] S. Gil, S. Sarun, A. Biete, Y. Prezado, and M. Sabes, "Survival analysis of F98 glioma rat cells following minibeam or broad-beam synchrotron radiation therapy," *Radiation oncology (London, England)*, vol. 6, no. 1, p. 37, 2011. (cited on page(s) 133)

[49] L. Bertrand, L. Robinet, M. Thoury, K. Janssens, S. X. Cohen, and S. Schöder, "Cultural heritage and archaeology materials studied by synchrotron spectroscopy and imaging," *Applied Physics A*, vol. 106, no. 2, pp. 377–396, 2011. (cited on page(s) 133)

[50] M. E. Eriksson and F. Terfelt, "Exceptionally preserved Cambrian trilobite digestive system revealed in 3D by synchrotron-radiation X-ray tomographic microscopy," *PloS one*, vol. 7, no. 4, p. e35625, 2012. (cited on page(s) 133)

[51] A. Banas, K. Banas, M. B. H. Breese, J. Loke, B. Heng Teo, and S. K. Lim, "Detection of microscopic particles present as contaminants in latent fingerprints by means of synchrotron radiation-based Fourier transform infra-red micro-imaging," *The Analyst*, vol. 137, no. 15, pp. 3459–65, 2012. (cited on page(s) 133)

[52] Y. Zhao, J. Grivel, D. He, P. Pallewatta, A. Abrahamsen, J. Bednarčâk, and M. V. Zimmermann, "In-situ synchrotron X-ray study of the phase and texture evolution of Ceria and Superconductor films deposited by chemical solution method," *Physics Procedia*, vol. 36, pp. 497–502, 2012. (cited on page(s) 133)

[53] I. Lauermann, M. Bär, and C.-H. Fischer, "Synchrotron-based spectroscopy for the characterization of surfaces and interfaces in chalcopyrite thin-film solar cells," *Solar Energy Materials and Solar Cells*, vol. 95, no. 6, pp. 1495–1508, 2011. (cited on page(s) 133)

[54] "Ill: Neutrons for science." `www.ill.eu`. Access July, 2013. (cited on page(s) 133, 153, 178)

[55] Image modified from `http://goo.gl/kWlRV`. Access Dec. 2012. (cited on page(s) 134)

Chapter 7

Characterisation Techniques

Contents

Chapter 7 explains the fundamental basis of the principal techniques used during this research: Neutron & X-ray diffraction[1–5] and X-ray Magnetic Circular Dichroism (XMCD).[6–8] In addition, due to the high specialised instrumentation used, a general vision of the specific synchrotron and neutron beamlines components are also explained.

7.1 Neutron and X-ray diffraction

A diffracted beam is produced by the individual atomic elastic scattering of the incident radiation whose wavelength is close to the atomic planes interspace. When the beam is scattered in all directions by the electronic atomic wave (for X-rays) or the atomic nucleus and unpaired electrons (for neutrons), it occurs in some spatial directions a constructive phenomena of the scattered radiation where the diffracted beam is produced.[9] The law which governs the spatial directions where a diffracted beam is produced is the Bragg's Law (equation 7.1).

The analysis of the produced diffracted beams allows to infer crystallographic information about the crystal which has produce the phenomenon. Below at the point 7.1.1, the crystallographic basis and diffraction conditions are explained to understand the future analysis and conclusions obtained through neutron and X-ray diffraction.

7.1.1 Fundamentals

In this section, a short explanation about the diffraction techniques (neutron and X-ray) is presented:

i Crystal structure

The unit cell is the minimum package of atoms which, repeated infinitely in the three space directions, generates a crystal structure. A perfect crystal structure should be infinite in the space so it does not exit in real. It is considered as a mathematical approximation to understand the scattering effects (among others) of the matter.

A unit cell of a crystal is de ned by 6 cell parameters: 3 angles , , σ and 3 lattice parameters a, b and c (g. 7.1). Each atom in the cell is de ned in the space in reference to the three axis a, b, c which are considered as unitary vectors. For example, an atom situated in the position (0 0 0), which correspond to the three a, b and c lattice parameters is located in the origin of coordinates, while an other in the position (1/2 1/2. 1/2) is in the middle of the unit cell.

Depending on the relationship of the cell parameters, seven crystal cells can be described:

1. cubic = =σ=90^o & a=b=c
2. tetragonal = =σ=90^o & $a = b = c$
3. orthorhombic = =σ=90^o & $a = b = c$
4. rhombohedral = =σ= 90^o & $a = b = c$
5. monoclinic = = 90^o,σ= 90^o
6. triclinic = =σ= 90^o
7. hexagonal $a = c$ & = 90^o, σ = 120^o

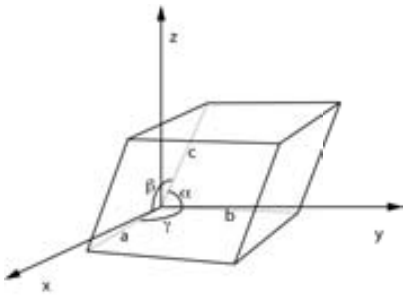

Figure 7.1: Representation of a unit cell parameters in the real space.

These crystal units are Bravais lattices that consist of crystal cells which repeated in the space by translation of the unit cell in one unit along the space generate a perfect crystal. Bravais lattices describe the structure of all real crystal.

Di erent atoms (three as minimum) de ne an atomic plane in the space. This plane is identi ed through the Miller Index (h k l) which are three lattice parameters. Take a plane cutting the unitary vectors a, b and c (which correspond to the lattice parameters) of the unit cell in the points a , b and c (positive or negative) then, the Miller Index are calculated as the reciprocal of this intersection:

$h = \frac{1}{a}$ $k = \frac{1}{b}$ $l = \frac{1}{c}$

An important parameter to consider in the de nition of the crystal structure is the interplanar space $d_{h\,k\,l}$ between two crystallographic planes (see gure 7.2).

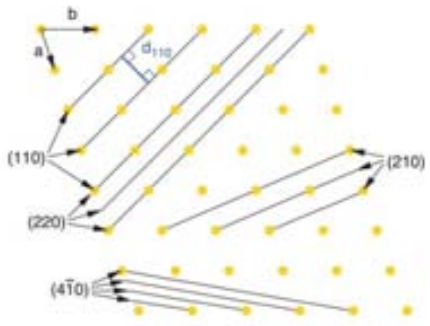

Figure 7.2: Schematic representation of some planes with their corresponding Miller index. The distance between two planes is also represented.

ii Bragg law

X-ray diffraction phenomenon can be understood by the Bragg law formula 7.1:

$$N\lambda = 2dsin\theta \tag{7.1}$$

where, N is an integer number, λ is the wavelength of the incident radiation, d is the interplanar distance between two (h k l) atomic planes, and θ the angle of incidence.

In case of Bragg law conditions are achieved (for a determinate λ and θ depending on the interplanar distance d), a constructive phenomenon of the diffracted beam occurs in the angle 2θ respect to the incident beam direction. Then, at this angle 2θ the diffracted beam can be detected (and not in other spatial directions due to there is no interaction phenomenon) as can be shown in the figure 7.3.

This Bragg law describes, in a brief form, the spatial direction where the maximum of the diffracted beam can be found. Reciprocally, scanning the space in order to find the diffracted beam, and knowing also the angle of incidence, many information about the atomic planar spacing can be deduced.

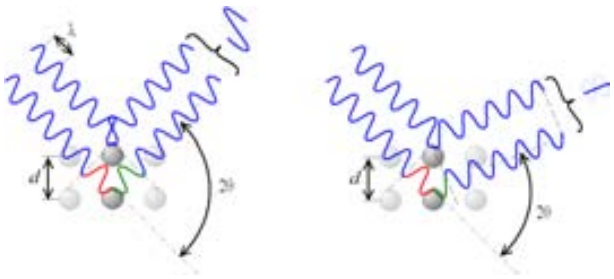

Figure 7.3: Representation of the Bragg law conditions to produce a diffraction phenomenon. Left: a constructive interference is produced, then a diffracted beam can be detected; Right: conditions does not obey the Bragg law, and as consequence, no interference is generated.

iii Ewald sphere

The Bragg law can be reformulated as:

$$sin\theta = \frac{\frac{1}{d_{hkl}}}{\frac{2}{\lambda}} \tag{7.2}$$

and the geometric solutions to the equation could be any right triangle inscribed in a sphere with diameter $\frac{2}{\lambda}$. This sphere is the Ewald's Sphere.

Now, considering the drawing of the planes (h k l) in the reciprocal space forming a network of points, it is possible to relate the planes which produce diffraction with the Ewald sphere. To do this, several conditions must to be followed:

1. Centre: In the centre of the sphere will be situated the crystal which produces the diffraction.
2. Origin of coordinates: The point (0 0 0) will be the surface point where the non-diffracted beam is located.
3. Incident beam: K_i, that ends at the centre of the sphere and has a modulus of $\frac{1}{\lambda}$. Generally this vector is also represented ending at the origin.
4. Diffracted beam: K_d, which starts in the centre of the sphere and ends in their surface due to their modulus is also $\frac{1}{\lambda}$.

In addition, to define properly the crystal cell in the reciprocal space, a conversion of the lattice parameters *a, b* and *c* into the reciprocal ones *a*, b** and *c** is needed. This mathematical relationship is described by the formula 7.3:

$$\begin{aligned} a^* &= 2\pi \frac{b \times c}{a \cdot (b \times c)} \\ b^* &= 2\pi \frac{c \times a}{b \cdot (c \times a)} \\ c^* &= 2\pi \frac{a \times b}{c \cdot (a \times b)} \end{aligned} \tag{7.3}$$

Following these rules, a third vector Q can be described to related both vectors K_i and K_f, a vector that close the right triangle of diffraction.

$$Q = 2|k|sin\theta = \frac{4\pi}{\lambda} sin\theta \tag{7.4}$$

It can be understand from this explanation that only a plane whose point in the reciprocal space is situated on the surface of the Ewald's sphere achieving the conditions explained before, will produce a diffracted beam.

When a sample has to be analysed and multiple planes need to be studied trough diffraction, a rotation of the sample with a goniometer is carried out, in order to change the conditions to produce diffraction of other crystallographic planes.

In the figure 7.4, the Ewald sphere jointly with some diffracting planes can be seen.

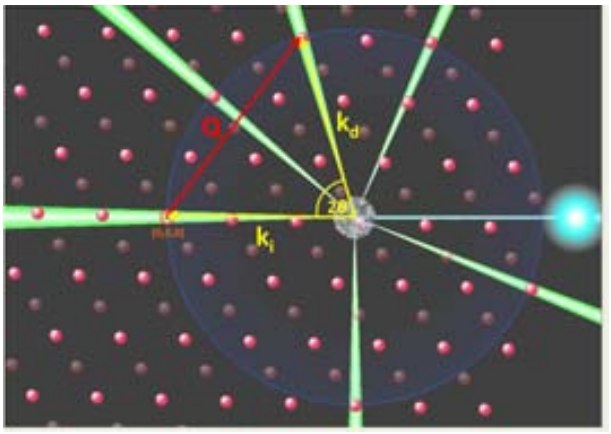

Figure 7.4: Schematic vision of the Ewald sphere jointly to the k_i, k_d and Q vectors.[10] Note that only the points on the surface of the sphere produces a diffraction phenomena.

iv Powder diffraction

Since this point, the explanation of a perfect single crystal diffraction has been summarised: a diffraction spot can be detected for determinate d_{hkl} planes, producing a set of diffraction spots that can be analysed to know crystal information. But in the case that a sample is formed by infinite quantity of single crystals randomly oriented, a X-ray powder diffraction (XRPD) or neutron powder diffraction (NPD) measurement is performed.

This technique is based on the fact that the same crystallographic plane is randomly oriented among the disoriented crystals, producing no single point of diffraction, but a cone of diffraction (also denominated as Debye-Scherrer rings when are represented on the detector plane). Between the total randlomly orientation and a perfect crystal system, they exit several intermediate cases where the sample can has preferred orientations. The fact that exist different preferential orientations can be achieved by the XRD pattern, as the following figure 7.5 demonstrates:

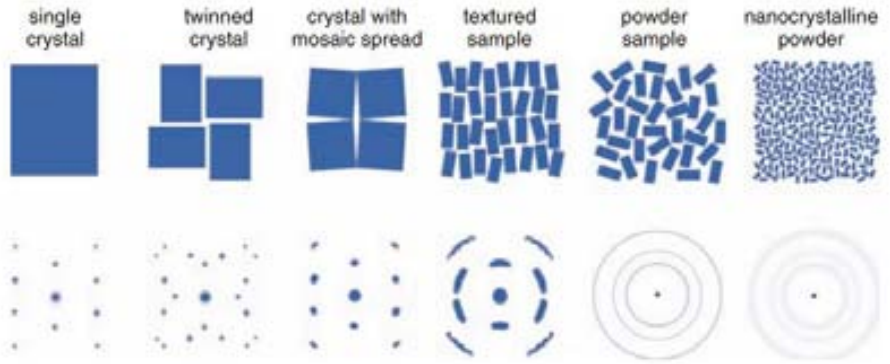

Figure 7.5: Representation of the diffraction patterns from different samples and orientations.

Powder samples are generally analysed in one dimensional direction due to their equal contribution in intensity to the Debye-Scherrer rings. The transformation between the Debye-Scherrer rings to the powder diffraction common spectra is shown in the figure 7.6.

As result, the common powder diffractogram is obtained, where the signal intensity is represented in front of the angle 2θ. By its part, when analysing single crystals, the sample has to be measured in all spatial directions to extract

information about all the atomic crystallographic planes. This is achieved by oriented adequately the crystal with a goniometer and/or orienting the detection system.

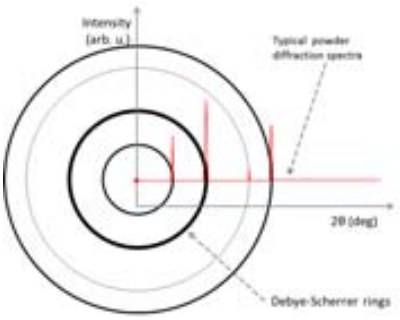

Figure 7.6: Generation of the powder di raction pattern through the di raction cones.

Returning to the properties of the neutron explained at the point 6.2.1, the interaction with unpaired electrons of paramagnetic atoms can occur due to the magnetic moment of the neutron. If the magnetic atoms show a repetitive ordering in the spin orientation, a new magnetic cell can be de ned. Then, in a magnetic sample two possible cells can be found: the crystalline and the magnetic one, that they do not necessary match (see gure 7.7). As consequence, a neutron beam can be di racted by atomic planes or by ordered magnetic atoms, generating a di raction pattern with signals from the crystal and the magnetic cell.

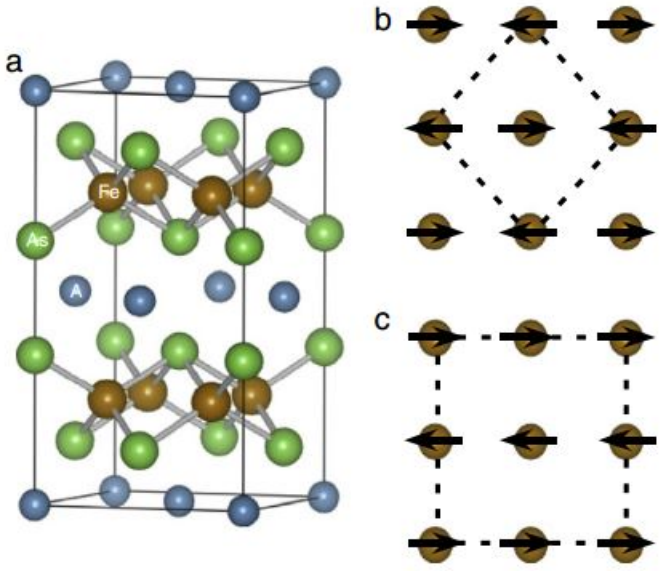

Figure 7.7: (a) Crystal structure of AFe_2As_2 (A=Ca, Ba). (b) and (c) are the representation of two possible spin magnetic ordering of the Fe atomic planes.[11] Note that in any of the two magnetic possible con gurations, the magnetic unit cell is larger than the crystalline unit cell.

De nitely, the X-ray and neutron di raction pattern is unique and sing of a

particular crystallographic cell. Magnetic structures are better to be studied by neutron diffraction due to the distinct contribution of the crystallographic and magnetic structure to the diffraction pattern, deducing besides structural and magnetic information.

7.1.2 Instrumentation

Neutron and synchrotron X-ray diffraction needs, apart from the neutron and X-rays generation explained at the point 6, a set of instrumentation to perform the analysis desired correctly. In this work, neutron powder diffraction to magnetic ferrite nanoparticles and X-ray powder and monocrystal diffraction to magnetic ferrite nanoparticles and nanocomposite superconducting layers have been performed respectively. Next, a brief explanation of the conditions of measurement are explained.

i Neutron beamline

Neutron powder diffraction analyses were performed in D1B neutron beamline at ILL (Institute Laue-Langevin) at Grenoble, France.[12]

ILL is the biggest thermal neutron generator built, and it is supported by several European Union members and private scientific partners. Their reactor and instrumentation generate the adequate conditions to perform high sophisticated analyses with neutron scattering or absorption techniques. With a neutron reactor of 58.3 MW, the ILL produce at the moderator level, 1.5×10^{15} $\frac{neutrons}{cm^2}$. It provides also around 50 neutron beamlines divided in 5 subcategories:[13] Diffraction (where D1B is located), Large Scale Structures, Time of Flight, Triple Axis and Nuclear & Particle Physics.

D1B specifications[14] makes the beamline as the adequate one to perform the desired neutron powder diffraction measurements. Below, the principal characteristics of the beamline are resumed (table 7.1).

Figure 7.8 shows by its part a scheme of the D1B neutron beamline signalling the principal components for measurements. Cryostat is coupled centred on the sample.

For sample measurements, $\sim$ 0.5 g of ferrite magnetic nanoparticles powder were

D1B technical specifications	
Monochromator	Pyrolytic graphite (0 0 2)
Neutron wavelength	2.52 Å
$\lambda/2$ ratio	0.0052
Collimator	Radial
Detector	$^3He/CF_4$ multidetector
Angle, resolution and efficiency	128^o, 0.2 Å, 86 %
Sample environment	Cryostat (from 1.7 K to 300 K)

Table 7.1: Principal technical specifications of D1B, neutron beamline at the ILL used for neutron powder diffraction analyses.

introduced in a vanadium cylindrical can which is supported by a metal shank and introduced into the cryostat system at room temperature.

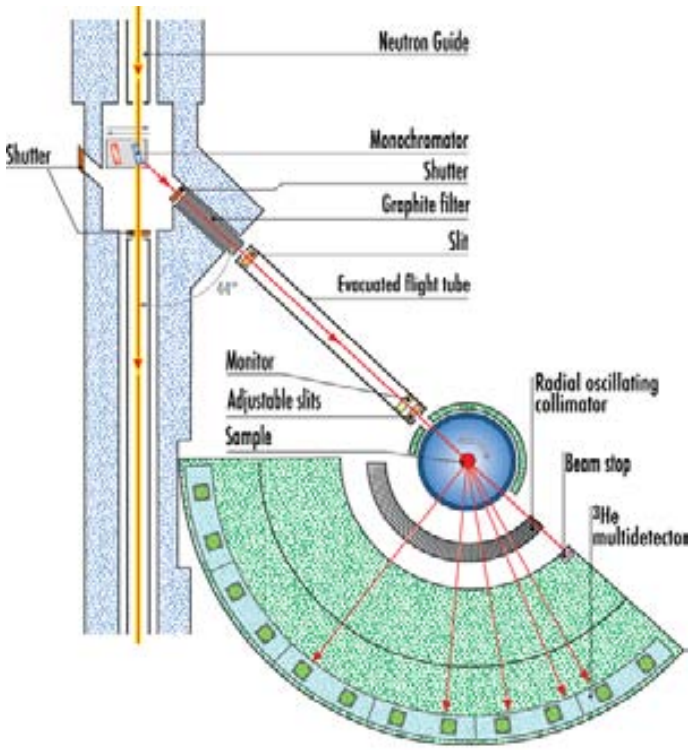

Figure 7.8: Layout of D1B powder diffraction beamline at the ILL neutron reactor. The principal components used (except the cryostat) are signalised.

ii Synchrotron X-ray beamline

X-ray synchrotron diffraction measurement were performed at Synchrotron Soleil (Gif-sur-Yvette, France), at the DiffAbs (Diffraction & Absorption) beamline.

Synchrotron Soleil is a 3^{rd} generation source where the first users come in 2008. Nowadays, the demand of beam time exceeds the available time for users. The principal characteristics are exposed in the table 7.2.[15, 16]

One of the beamlines at synchrotron Soleil is DiffAbs, devoted to the diffraction and absorption of hard X-rays (from 3 KeV) with a specialised instrumentation. The most significant specifications for synchrotron users are resumed below:[17]

This beamline has at the disposal of the users a 6+2 axis diffractometer is for measurement. In addition, a laser can be used jointly with a levitation chamber in order to make experiments at high temperatures (up to 3200 ^{o}C). In addition, multiple detectors: 0D point, 2D CCD and fluorescence detector are also available for the possible experiments. In brief, diverse experimental set-up and sample environments

Synchrotron Soleil	
Energy	2.75 GeV
LinAc	100 MeV
Storage Ring	254 m
Intensity	400 mA
Beamlines	24
Stations	35

Table 7.2: Principal technical characteristics of the Synchrotron Soleil

DiffAbs beamline	
Source	Bending magnet
Accessible energy range	from 3 to 23 KeV
Energy resolution ($\frac{\Delta E}{E}$)	10^{-4}
Flux	10^{14} $\frac{ph}{s \cdot 0.1\% BW}$ (8KeV, 500 mA)
Flux on sample	10^{11} to 10^{12} $\frac{ph}{s}$ (8KeV, 500 mA)
Divergence	0.24 x 3.5 $mrad^2$ (vertical x horizontal)
Beamsize (at the sample)	300 μm^2 (FWHM)

Table 7.3: Principal characteristics of DiffAbs beamline

can be installed in this beamline depending on the experimental requirements. In this case, point detector and diffractometer have been used to perform the desired experiments.

The diffractometer has all the required motorised movements (with a precision even until thousandth of degree) in order to rotate the sample in all directions around a central rotation point. The sample angles will be denominated as ϕ, ω, and χ. The detector used for the analysis can move in the vertical (angle δ) or in the horizontal plane (angle γ) with respect to the synchrotron plane. Figure 7.9 and figure 7.10 show the principal parts of the diffractometer and the movement angles.

Special qualities of the synchrotron X-ray beam, together with the high precision instrumentation at DiffAbs beamline, make possible to perform sophisticated analysis that, with a laboratory common source, would not be feasible. Two principal

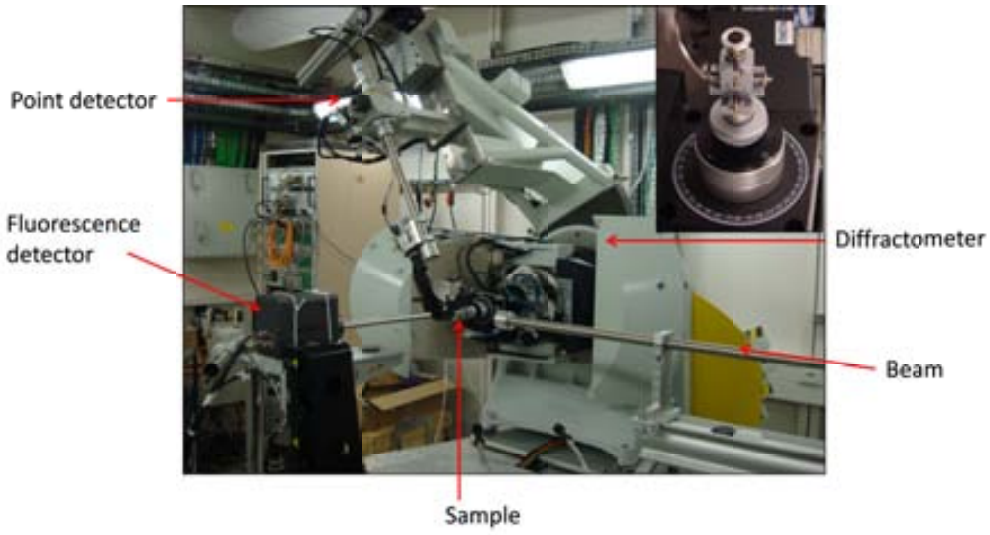

Figure 7.9: Experimental station: the di ractometer and the detector are signalled. The inset shows a detailed view of the sample region with a superconducting YBCO layer mounted.

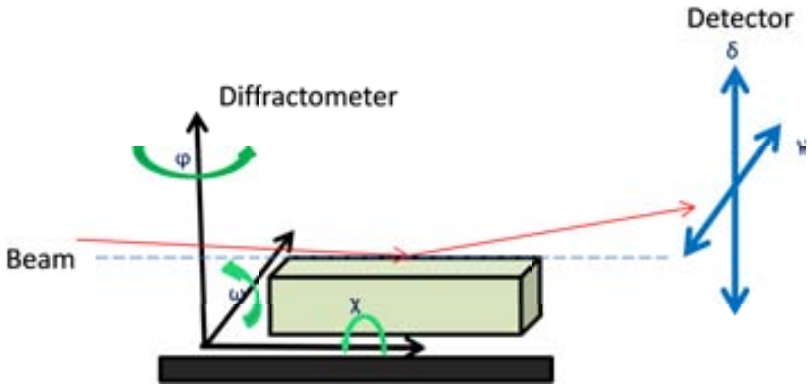

Figure 7.10: Scheme of the three angles of the di ractometer (, π, and) for out of plane con guration (=90°) and the two scan direction of the detector (σ horizontal, χ vertical). For in plane analysis (=0°), the sample was rotated by 90° resulting in a vertical surface geometry.

diffraction configuration (and one combination) have been applied in order to perform the desired experiments: Bragg-Brentano and grazing incidence analysis.

1. Bragg-Brentano: Denominated also ω/δ scan (or $\theta/2\theta$ for common laboratory sources nomenclature) is based on the variation of the angle of incidence ω, analysing the diffracted signal (if any) at δ angle. This configuration is commonly used to powder samples (because there is no preferred orientation), but it is also utilised to study preferential orientation of the sample, because only the planes parallel to the diffraction plane can achieve the Bragg diffraction conditions. This last point is important for monocrystalline or epitaxial growth samples (as YBCO layers ones).

2. Grazing incidence: Technique used to study thin layers (few nanometers) where it is important to achieve a good signal/noise ratio. If Bragg-Brentano configuration is used, the penetration deep of the beam generates a huge signal of the substrate, hiding possible diffraction signals of the sample of interest. To improve the signal/noise ratio, it is needed to decrease the penetration deep at the same time that a bigger area of the sample is illuminates. Both requisites are achieved by a grazing angle incidence.

   When the X-rays impact on the sample, their penetration deep is related with the incident angle. Smaller angles, larger area illuminated and smaller penetration until the critical angle (between 0.1^o and 0.5^o depending on the surface roughness, composition, etc.). Below this critical angle α_c, a phenomenon denominated "total external reflexion" is produced, making that the X-ray beam only penetrates the first atomic layers and is completely reflected. With this configuration, an study of the sample surface can be performed, avoiding as much as possible the signal of the substrate.[3]

3. Pole figures: Pole configuration to produce pole figures is a mixing between the Bragg-Brentano and grazing incidence. It consist of study the orientation in the space of a crystallographic plane by fix the detector in the δ angle characteristic of the plane, and angulary move the sample in all directions by the angles φ and χ. When a plane is oriented in diffraction conditions it produces a signal in the detector, and studying the position of the angles and the intensity of the signal, it is possible to determine the orientation of the planes (and crystal) in the sample.

YBCO nanocomposite nanostructured superconducting layers were measured in both con gurations. If a perfect epitaxial growth is considered, three oriented planes have to be studied: (h 0 0), (0 k 0) and (0 0 l). Bragg-Brentano con guration was used to perform out of plane measurements for the (0 0 l) planes, while (h 0 0) and (0 k 0) planes were measured with grazing incidence (0.3^o) to minimise the substrate contribution. The di ractometer geometry is explained in the gure below.

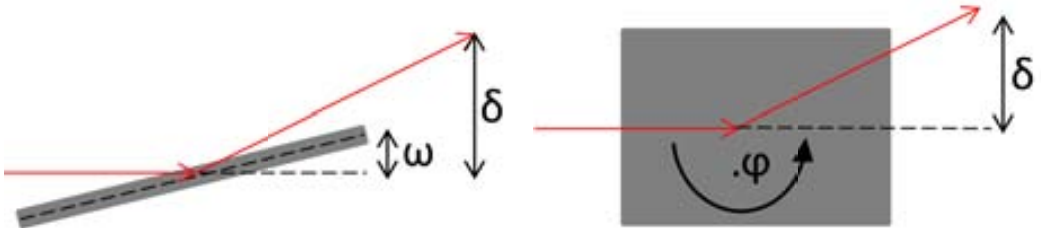

Figure 7.11: Side view of the geometries used for out of plane (left) and in plane (right) at 0.3° grazing analysis of YBCO layer. The angles used for the di erent scans are shown.

$BaZrO_3$ nanotracks on $LaAlO_3$ single crystal were mostly studied by grazing incidence due to their low size (arround 60 nm) but also by Bragg-Brentano con guration measurements to make an out of plane analysis.

7.2 X-ray magnetic circular dichroism

X-ray Magnetic Circular Dichroism (XMCD), which is based on X-ray Absorption Spectroscopy (XAS), is a characterisation technique to study the composition and magnetic behaviour of principally magnetic samples. In this work, XMCD has been applied to study the composition and magnetic behaviour of the ferrite magnetic nanoparticles as synthesised and when embedded within the YBCO superconducting matrix.

7.2.1 Fundamentals

Dichroism is a term which means two-coloured . A material which present di erent light absorption depending on the light polarisation is denominated as a dichroic material. In the case of magnetic atoms, their dichroic absorption depends also on the

magnetisation intensity and orientation caused by an external magnetic field. Then, by measuring the XAS spectra for both circular polarisation senses (right-handed & left-handed), and after subtract one respect to the other, the subtraction obtained is denominated as the XMCD spectrum. XMCD occurs only in magnetic samples, and more precisely, is caused by the magnetic atoms of the sample.

Magnetic materials are hardly studied due to their important applications[18–20] with XMCD technique. It is also remarkable that the interest of know the origin of the magnetism in magnetic nanostructured samples is quickly growing last years.[21, 22] To understand the origin and evaluate the magnetism of magnetic atoms, first, a briefly introduction to the atomic structure is needed.

i Atomic orbitals and electronic terms

The Schröndinger equation for an hydrogen-like atom (7.5) defines in their solutions the atomic orbitals with n_p, l, and m_l as their quantum numbers.

$$H\ E\ =\ \psi\ E \tag{7.5}$$

being H the Hamiltonian (equation 7.6), ψ the wave function and E the energy of the state ψ.

$$H = \frac{-\hbar^2}{2m}\nabla^2 - \frac{Ze^2}{r} \tag{7.6}$$

m is the mass of the e^-, Z, the atomic number, e the charge of the e^- and r the atomic radius.

Atomic numbers define exactly an electron in a determinate atomic orbital. n is the principal quantum number, and it defines the energy level of the orbital (n=1, 2, 3...); l is the second quantum number correspond to the magnetic moment of the orbital (l=0, 1, 2... n-1); and m_l indicates the orientation of the magnetic moment (m_l=-l, -l +1... l-1, l). Finally, the spin projection number of the electron m_s is related with the two possible spin states of the e^-in an atomic orbital (m_s= -1/2 or 1/2).

Pauli's exclusion principle is a quantum mechanical condition that explains that two electrons cannot have exactly the same quantum numbers, and it signifies that

two electrons cannot occupy the same atomic orbital. This means that an electron can be located in an specific atomic orbital thanks to their quantum numbers. If a fundamental state of the atom is considered, their electronic configuration can be defined by the quantum numbers of the last valence electron.

ii Term symbols

Term symbols[23] are an abbreviated resume of the atomic quantum numbers for a precise n. In other words, is the description of the angular moments of an atomic orbital n.

$$^{2S+1}L_J \tag{7.7}$$

S is the spin multiplicity (number of unpaired e^- divided by 2); L, the orbital quantum number, which depends on the sum of m_l (L: S for m_l=0, P for m_l=1, D for m_l=2, F for m_l=3, G, H...), and J, the angular momentum quantum number is from | L-S | to L+S by step of 1.

To determinate the term symbol of the ground level of a $3d^n$ atom, Hund determined three laws:

1. Maximum spin S are lowest in energy
2. Lowest energy is achieved with maximum orbital moment L
3. If spin-orbit coupling happens, the lowest term has J=| L-S| if the atomic orbital is less than half full and J=L+S if the shell is more than half full.

For example: to a Fe^{3+} atom (d^5), the term symbol of the ground state is $^6S_{5/2}$, while for a Cu^{2+} (d^9) is $^2D_{5/2}$.

Dipole selection rules determine the final state of an excited atom: ΔJ= +1, 0, -1 (but not for J=J'=0), ΔS=0 and ΔL=1. Then, because it is interesting to study the magnetic properties of transition atoms, which is related with the 3d orbital occupancy and energy, a promotion of an internal electron (generally from the orbital 2p) to the 3d valence band is produced. For a transition metal with ground state $2p^6 3d^n$, the excited level is produced by exciting an electron of the 2p level to a hole of the 3d atomic shell with a determinate energy from the X-rays, having $2p^5 3d^{n+1}$ as

final state configuration. This transition can introduce multiple final states following the selection rules, depending on the final m_l configuration. Table 7.4 shows the possible transitions of the $3d^n$ atoms and the number of term symbols of the final states.

$2p \rightarrow 3d^n$ transitions and final term symbols

Fundamental term	Transition	n^o of transitions	n^o of final term symbols
$^1S_0$	$3d^0 \rightarrow 2p^5 3d^1$	3	12
$^2D_{3/2}$	$3d^1 \rightarrow 2p^5 3d^2$	29	45
$^3F_2$	$3d^2 \rightarrow 2p^5 3d^3$	68	110
$^4F_{3/2}$	$3d^3 \rightarrow 2p^5 3d^4$	95	180
$^5D_0$	$3d^4 \rightarrow 2p^5 3d^5$	32	205
$^6S_{5/2}$	$3d^5 \rightarrow 2p^5 3d^6$	110	180
$^5D_2$	$3d^6 \rightarrow 2p^5 3d^7$	68	110
$^4F_{9/2}$	$3d^7 \rightarrow 2p^5 3d^8$	16	45
$^3F_4$	$3d^8 \rightarrow 2p^5 3d^9$	4	12
$^2D_{5/2}$	$3d^9 \rightarrow 2p^5 3d^{10}$	1	2

Table 7.4: X-ray absorption transitions for $3d^n$ atoms.[23]

The energy of a precise atomic orbital is defined by the principal atomic quantum number n and the second one l. Without presence of an electric or magnetic field, the atomic sublevels defined by l have the same energy (degenerated levels). But, if the degeneration is broken by applying a magnetic (or electric) field, an energy splitting of the m_l sublevels occurs (see figure 7.12). Remembering the electronic configuration, different values of J can be described depending on the m_j and spin values, splitting each m_j subshell into two energetic levels, obtaining $2m_j$ electronic states. This is crucial to understand the initial and final possible electronic states when an electronic transition occurs between two atomic orbitals. Practical applications of this fact can be used to conclude structural and electronic information about the atoms composing the sample.

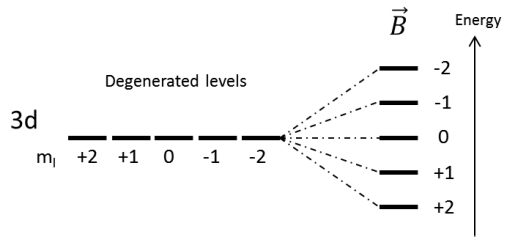

Figure 7.12: Energy of atomic orbitals. Left, degenerated levels; Right, the degeneration is broken by e ect of the magnetic eld.

iii XAS and XMCD

XMCD has been recently optimised to study magnetic materials by measuring the absorption of a X-ray circular polarised beam under an external magnetic eld, which is applied to broke the orbital degeneration.[4] XMCD technique is used to analyse small amounts of magnetic samples with atomic selectivity depending on the 2p 3d transition energy (last occupied electronic levels).

Photons are a particle and a wave at the same time following the wave-particle duality. Focusing on the wave component, photons are electromagnetic wave which is formed by a magnetic and electric perpendicular elds. These elds propagate along the space following the Maxwell equations:

$$E^{(\ )} = [E_x^{(\ )}\ E_y^{(\ )}\ E_z^{(\ )}] \tag{7.8}$$

being

$$\begin{aligned} E_x^{(\ )}(r\ t) &= E_x^{(\ max)}\ cos(\pi t\quad k^{(\ )}\ r\quad \chi_x^{(\ )}) \\ E_y^{(\ )}(r\ t) &= E_y^{(\ max)}\ cos(\pi t\quad k^{(\ )}\ r\quad \chi_y^{(\ )}) \\ E_z^{(\ )}(r\ t) &= E_z^{(\ max)}\ cos(\pi t\quad k^{(\ )}\ r\quad \chi_z^{(\ )}) \end{aligned} \tag{7.9}$$

where $E^{(\ max)}$ is the maximum value for the electric eld; π is the frequency of the wave; k, their propagation vector (wave vector); r is the spacial coordinate and t the temporal one; and χ is the initial phase di erence in the time-space origin.

To generate a circular polarised photons, the phase di erence between the magnetic and electric eld has to be $\nu\ 2\quad n\nu$ and the same amplitude. In synchrotron lightsources, polarised light is generated by an insertion device (see chapter 6, subsection ii and iii). Circular polarisation can be right-handed (RCP) or left-handed (LCP) considering the k propagation vector as the reference sense.

The interaction of circular polarised light with 2p electrons of the atoms comes determinate by the selection rules. A photon carries an angular momentum that can be transfer to the e , varying its m_l in one unit depending on the polarisation direction: +1 for RCP photons and -1 for LCP photons (taken as convention). This means that for an atom which absorbs RCP light, only m=+1 transition occurs; while if the light is LCP, the transition with m=-1 can happen.

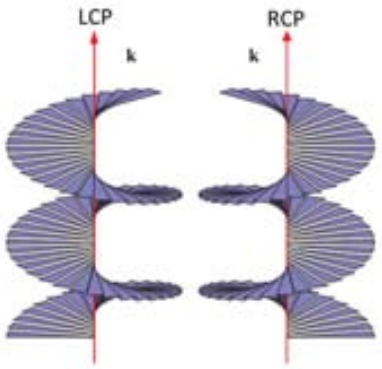

Figure 7.13: Left, left-handed polarised beam; right, right-handed polarised beam

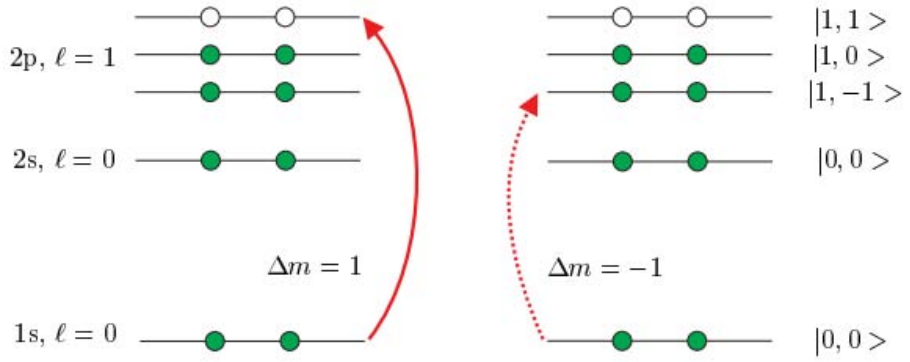

Figure 7.14: Simpli ed vision of electronic transitions for absorption of RCP photons (left) and LCP (right) with no degenerated levels. Note that the LCP transition (m=-1) can not occur because the nal orbital is already complete.

Magnetic atoms have at least one unpaired electron, generating that the number of spin up and spin down electrons was not the same. This in uences in the absorption of RCP and LCP light. In the case of $3d^n$ atoms, the probability to excite a 2p level electron to a 3d orbital, depends on the occupancy of the nal state (see gure 7.14). With this fact, and knowing that the nal electronic states could be multiples, some electronic and magnetic information can be gathered by using XMCD analysis. To evaluate this information, the RCP and LCP spectra are collected by measuring the proportion of absorbed photons in function of the energy, because for a precise energy, only an atomic transition can occurs.

In brief, XMCD is a technique which uses circular polarised light to produce a

$L_{II}(L_2)$ $(2p_{1/2} \rightarrow 3d)$ and $L_{III}(L_3)$ $(2p_{3/2} \rightarrow 3d)$ transitions to study the magnetic behaviour of an specific magnetic atom. Energetic levels of these atoms do not present degeneration because a magnetic external field is applied until saturate the magnetic sample. RCP and LCP X-ray absorption is measured separately in function of the photon energy (range lower the KeV) and under the same magnetic field (with the same direction that the k vector propagation). XMCD spectrum results from the subtraction of RCP and LCP spectra.

Figure 7.15 shows the RCP and LCP absorption in function of the energy (eV) and the XMCD signal ($I_{RCP} - I_{LCP}$) and their corresponding mathematical integration.

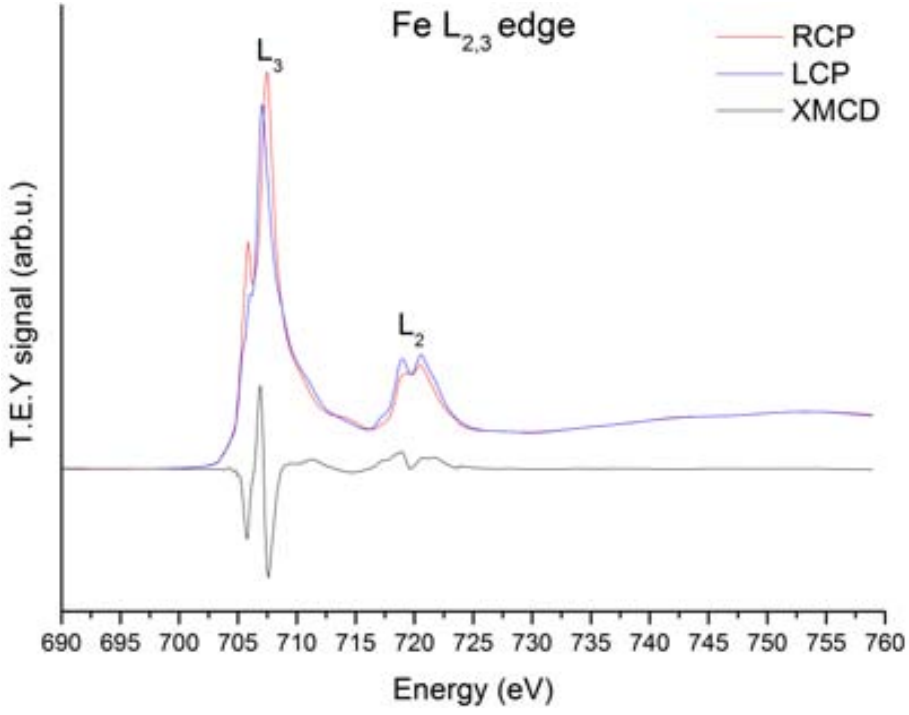

Figure 7.15: Figure with shows the $L_{II,III}$ absorption edge of Fe, the XMCD signal and their integration.[3]

As it can be seen in the figure, the XAS and XMCD spectra depends on the energy, which is related with the energy gap between the 2p and 3d electronic sublevels. The maximum absorption and the shape of the peak depends on the atom (chemical specificity) and more precisely on the oxidation state and chemical environment (different atomic energy implies different transition energy). Knowing this, and with the adequate tools and analyses, structural and chemical information can be extracted from the XAS spectrum. XMCD shows, by its part, the magnetic

behaviour of the studied atom. A null signal indicates a no magnetic atom, while peaks demonstrate that a deviation between the RCP and LCP absorption, meaning that exist a magnetic moment in the atom. XMCD signal is sensitive to detect even a 0.001 μ_B.

The importance to study compounds of the first row of transition is due to the magnetic moment of the corresponding atoms can be separated in the spin and orbital moment, knowing the percentage of each one in the final magnetism. It occurs that, for these elements, the magnetic moment generated by the intrinsic spin of unpaired electrons (spin moment) can coupled with the magnetic moment generated by the displacement of the e around the nucleus. If a spin-orbit coupling exists, the 2p level is split, while 3d level is also split by exchange interaction . To see graphically the spin-orbit effects, see the figure below 7.16.

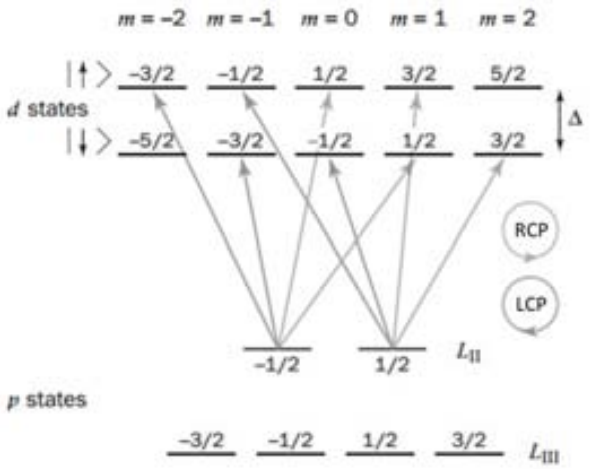

Figure 7.16: Example of L_2 transitions to 3d level following the selection rules: m_l=+1 for RCP and -1 for LCP. p states are split by action of the spin-orbit magnetic coupling and d states by the exchange energy.

iv Sum rules

Sum rules were described by Thole et al.[24] with the aim to separate the different contribution to the global magnetic moment of the spin and orbital moment. Specifically, they have been applied for the $2p \rightarrow 3d$ transitions of 3d transition metals studied trough XAS and XMCD measurements. The equations which describe the sum rules are the following (7.10 & 7.11).

Orbital moment:

$$\langle L_z \rangle = -\frac{\int(\mu_+ - \mu_-)}{\int \mu} \cdot 2n_h \tag{7.10}$$

Spin moment:

$$\langle S_z \rangle = -\frac{\int_{L_3}(\mu_+ - \mu_-) - \int_{L_2}(\mu_+ - \mu_-)}{\int \mu} \cdot \frac{3}{2} \cdot n_h \tag{7.11}$$

being, μ_+ (μ_-) the absorption for the right-handed (left-handed) polarised light, and μ the sum of the the two polarised signals. In order to realise a correct calculation, it is necessary to normalise the XAS spectrum between 0 and 1 as absorption values (0 intensity before the L_3 edge, and 1 after the L_2 absorption edge). Then the equations can be rewritten as:

Orbital moment:

$$\langle L_z \rangle = -\frac{4\int_{L_3+L_2}(\mu_+ - \mu_-)}{3\int_{L_3+L_2}(\mu_+ + \mu_-)} n_h \mu_B \tag{7.12}$$

Spin moment:

$$\langle S_z \rangle = -\frac{6\int_{L_3}(\mu_+ - \mu_-) - 4\int_{L_3+L_2}(\mu_+ - \mu_-)}{\int_{L_3+L_2}(\mu_+ + \mu_-)} n_h \mu_B \left(1 + \frac{7\langle T_z \rangle}{2\langle S_z \rangle}\right)^{-1} \tag{7.13}$$

considering T_z as the spin quadrupole moment, factor that can be neglected because the calculus $\frac{\langle T_z \rangle}{\langle S_z \rangle}$ has a low contribution to the final result (less than 1 % which is less than the calculation error bar).

Several integral values are needed to carried out the calculations, and for it, the net absorption value (signal minus background) is required. To do this, in the first studies on a Fe thin film, the net signal was calculated by measuring only the support and making the difference. But in the case showed here, the magnetic Nps sample is surrounded by other unquantifiable materials, and then, an approximation to calculate the background is taken: a *tanh* two step function between 0 and 1 (as the normalised XAS spectrum) with a step value of 2/3 of the total corresponding

to the L_3 absorption edge and 1/3 to the L_2 edge-jump (degenerated levels), and with the width of the absorption edge similar to the natural width of the atomic transition.[25]

The following gure 7.17 shows the XAS and XMCD signals, the background two step function and at the same time it identify the points where the integral values have to be taken (identi ed as *p, q* and *r*).

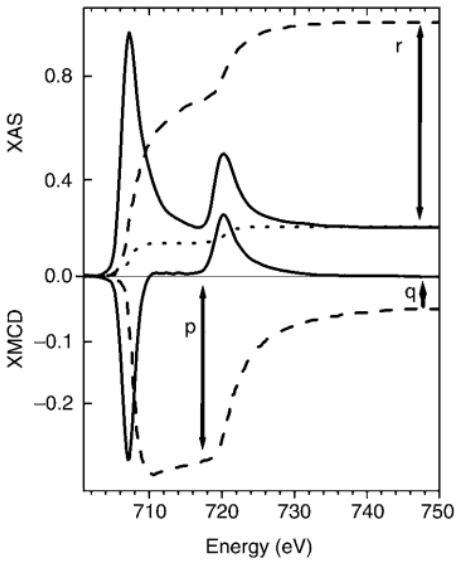

Figure 7.17: Representation of a typical XAS and XMCD spectra showing the integral values *p, q* and *r* needed for the sum rule calculations.[7]

Thus, simplifying the spin and orbital equations by substituting the integral values by the corresponding *p, q* and *r* values, the equations 7.14 & 7.15 can be written.

Orbital moment:

$$m_{orb} = \frac{4q}{3r} n_h \quad _B \tag{7.14}$$

Spin moment:

$$m_{spin} = \frac{6p \quad 4q}{r} n_h \quad _B \tag{7.15}$$

Sum rules calculations allows to separate with a certain degree of simplicity the orbital and magnetic moments of the transition metal analysed. Some difficult can be presented when the calculations are carried out, as it can be the signal quality, the differentiation between the L_3 and L_2 integrals, signal-noise ratio, non-measurable background, etc. Results obtained for the samples analysed during this work are showed in the section 9.4.

XAS and XMCD have been used as analyses methodology to study ferrite magnetic nanoparticles as synthesised and embedded into superconducting layers. This research has been performed in order to know the chemical and magnetic information concerning the synthesised ferrite nanoparticles as generated and after being embedded inside the YBCO superconducting layer.

7.2.2 Instrumentation

XAS/XMCD analyses have been realised at BOREAS beamline[26] at the Alba Spanish synchrotron.[27]

Alba is a recent 3^{th} generation source whose first users started at May 2012. The principal characteristics of the synchrotron are resumed in the table 7.5.

Synchrotron Alba	
Energy	3 GeV
LinAc	100 MeV
Storage Ring	270 m
Intensity	100 mA
Beamlines	7

Table 7.5: Principal properties of the Synchrotron Alba.[27] It is remarkable that nowadays the synchrotron Alba is in constant upgrading.

Because ALBA is being in their first steps, the intensity is not the final nominal current, and the number of beamlines will be increased in a close future with new specialised beamlines in order amplify the research possibilities.

The beamline used for this measurements was BOREAS (Beamline for resonant absorption and scattering), and more specifically the XMCD endstation with HECTOR magnet. It consists of an ultra high vacuum chamber with manifold superconducting magnets in several configurations to magnetise the sample and a cryostat to control the sample temperature. Most remarkable characteristics are presented below (table 7.6) jointly with the X-ray flux in function of the energy (figure 7.18), but it has to be taken into account that the beamline is also in constant upgrading.

BOREAS beamline	
Source	APPLE II Undulator
Accessible energy range	from 80 to 4000 eV
Resolving power	15000 for 80 $eV < E <$ 1500 eV
Flux	$8 \cdot 10^{12}$ ph/s at 700 eV
Beamsize (at the sample)	>100x20 (horizontal x vertical)µm
Magnet	±6 T oriented in beam direction
Range of temperature	from 1,5 to 370 K
Pressure (sample chamber)	$\sim 10^{-10}$ mbar
Detection system	Total Electron Yield (T.E.Y.) and Fluorescence

Table 7.6: Technical specifications of BOREAS beamline[26]

To end with the description of the BOREAS beamline, the following figure 7.19 shows different instrumental components of the BOREAS beamline as an example of the instrumentation required.

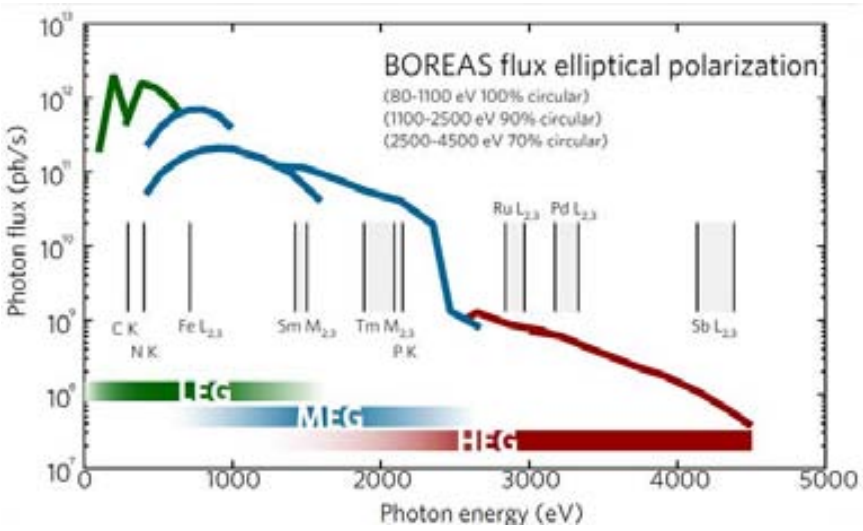

Figure 7.18: Analysis of the X-rays flux in function of the energy for a circular polarisation radiation. The three energy grating (low, medium and high) are needed to produce all the range available.

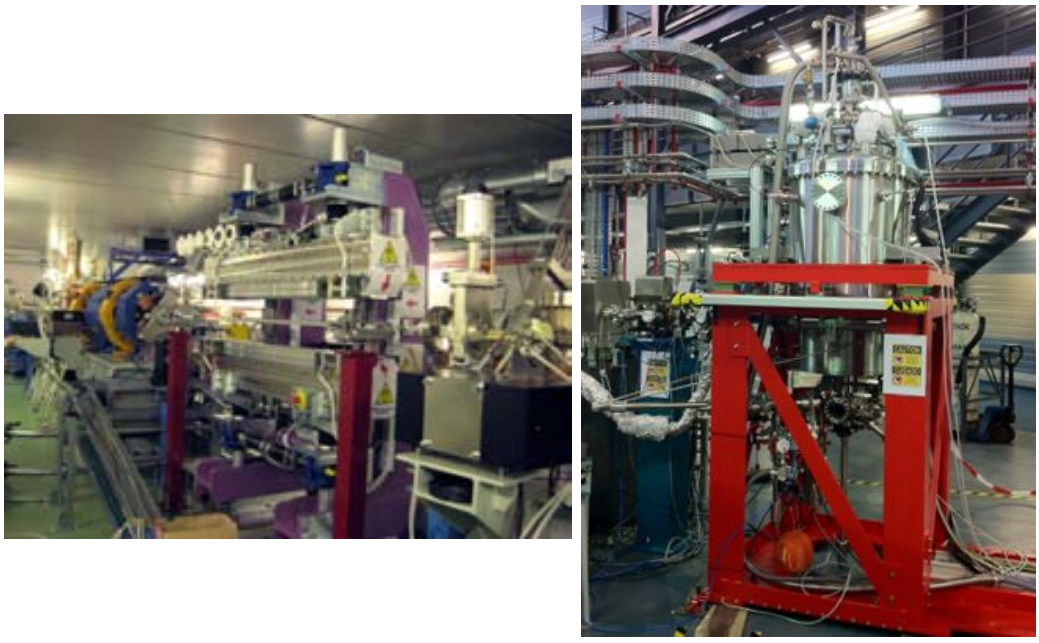

(a) Apple II undulator (b) XMCD enstation

Figure 7.19: Different parts forming the BOREAS beamline: (a) the insertion device, an Apple II undulator; (b) XMCD endstation with HECTOR magnet.

Bibliography Chapter 7

[1] T.-K. Sham, ed., *Chemical applications of synchrotron radiation*, vol. 2. World scientific publishing, 2002. (cited on page(s) 114, 146)

[2] H.-R. Wenk, *Neutrons in soft matter*, vol. 63. Geochemical society mineralogical society of America, 2006. (cited on page(s) 116, 146)

[3] J. Als-Nielsen and D. McMorrow, *Elements of modern X-ray physics*. John Wiley & Sons, 2011. (cited on page(s) 115, 146, 158, 165)

[4] P. Willmott, *An introduction to synchrotron radiation: techniques and applications*. John William & Sons, 2011. (cited on page(s) 115, 122, 123, 126, 127, 146, 163)

[5] T. Imae, T. Kanaya, M. Furusaka, and N. Torikai, *Neutrons in soft matter*. John Wiley & Sons, 2011. (cited on page(s) 116, 146)

[6] J. Stöhr and H. C. Siegmann, *Magnetism: from fundamentals to nanoscale dynamics*. Springer, 2006. (cited on page(s) 33, 146)

[7] F. de Groot and A. Kotani, *Core level spectroscopy of solids*. CRC Press, 2008. (cited on page(s) 146, 168)

[8] E. Beaurepaire, H. Bulou, F. Scheurer, and J.-P. Kappler, eds., *Magnetism and synchrotron radiation: New trends*. Springer, 2010. (cited on page(s) 115, 146)

[9] G. E. Bacon, *Neutron diffraction*. Clarendon Press - Oxford, 2009. (cited on page(s) 146)

[10] Image modified from `http://goo.gl/6XX0p`. Access Dec. 2012. (cited on page(s) 150)

[11] Y. Wang, Y. Ding, and J. Ni, "First-principles study of pressure effects on $CaFe_2As_2$ and $BaFe_2As_2$," *Solid State Communications*, vol. 149, no. 47-48, pp. 2125–2129, 2009. (cited on page(s) 152)

[12] "Ill: Neutrons for science." `www.ill.eu`. Access July, 2013. (cited on page(s) 133, 153, 178)

[13] "Ill neutron beamlines classification." `http://www.ill.eu/fr/instruments-support/instruments-groups/`. Access July, 2013. (cited on page(s) 153)

[14] "Specifications of d1b neutron beamline at ill." `http://www.ill.eu/fr/instruments-support/instruments-groups/instruments/d1b/description/instrument-layout/`. Access July, 2013. (cited on page(s) 153)

[15] "Synchrotron soleil general web." `http://www.synchrotron-soleil.fr`. Access July, 2013. (cited on page(s) 155, 219)

[16] "Synchrotron soleil beam characteristics." `http://www.synchrotron-soleil.fr/portal/page/portal/SourceAccelerateur/ParametresPrincipaux`. Access July, 2013. (cited on page(s) 155)

[17] "Diffabs beamline at synchrotron soleil." `http://www.synchrotron-soleil.fr/Recherche/LignesLumiere/DIFFABS`. Access July, 2013. (cited on page(s) 155, 219)

[18] M. Baibich, J. Broto, A. Fert, F. Nguyen Van Dau, F. Petroff, P. Eitenne, G. Creuzet, and F. A. (cited on page(s) 160)

[19] S. Ikeda, J. Hayakawa, Y. M. Lee, F. Matsukura, Y. Ohno, T. Hanyu, and H. Ohno, "Magnetic Tunnel Junctions for Spintronic Memories and Beyond," *IEEE Transactions on Electron Devices*, vol. 54, no. 5, pp. 991–1002, 2007. (cited on page(s) 160)

[20] M. Cao, Z. Li, J. Wang, W. Ge, T. Yue, R. Li, V. L. Colvin, and W. W. Yu, "Food related applications of magnetic iron oxide nanoparticles: Enzyme immobilization, protein purification, and food analysis," *Trends in Food Science & Technology*, vol. 27, no. 1, pp. 47–56, 2012. (cited on page(s) 51, 160)

[21] L. Li, S. Yang, X. Yang, X. Xu, and C. Tang, "Boron adsorption induced magnetism in zigzag boron nitride nanotubes," *Journal of Molecular Structure*, vol. 1020, pp. 183–187, 2012. (cited on page(s) 160)

[22] M. Valant, T. Kolodiazhnyi, I. Arčon, F. Aguesse, A.-K. Axelsson, and N. M. Alford, "The Origin of Magnetism in Mn-Doped $SrTiO_3$," *Advanced Functional Materials*, vol. 22, no. 10, pp. 2114–2122, 2012. (cited on page(s) 160)

[23] *Neutron and X-ray spectroscopy*. Springer. (cited on page(s) 161, 162)

[24] B. T. Thole, P. Carra, F. Sette, and G. V. D. Laan, "X-Ray circular dichroism as a probe of orbital magnetization," *Physical review letters*, vol. 68, no. 12, pp. 1943–1946, 1992. (cited on page(s) 166)

[25] M. O. Krause and J. H. Oliver, "Natural widths of atomic K and L levels, K_α X-ray lines and several KLL Auger lines," *Journal of Physical and Chemical Reference Data*, vol. 8, no. 2, pp. 229–338, 1979. (cited on page(s) 168)

[26] "Boreas beamline characteristics." `https://www.cells.es/Beamlines/VP/`. Access July, 2013. (cited on page(s) 169, 170, 196)

[27] "Alba spanish synchrotron web page." `http://www.cells.es`. Access July, 2013. (cited on page(s) 169, 196)

Chapter 8

Neutron Diffraction for MFe_2O_4

Contents

In this chapter, the results obtained through neutron powder diffraction (NPD) are presented. This characterisation technique has been profited in order to study the structure of the NPs prepared by the two optimised methodologies: thermal and microwave. Previous studies have demonstrated that MW radiation generates nanoparticles with higher internal defects than common thermal routes, principally because their lower temperature and reduction of the annealing time.[1, 2] Then, the goal of this study is to compare the internal structure of the diverse produced ferrites.

The nanocrystals analysed using NPD were: $MnFe_2O_4$, Fe_3O_4, $CoFe_2O_4$ and $ZnFe_2O_4$ synthesised by thermal and microwave routes, and also $NiFe_2O_4$ made only via thermal methodology because when the measures were carried out, the synthesis of nickel ferrite using microwave radiation was not yet established. Find below the measurements and data exploitation of this experiment.

8.1 Experimental details

Neutron powder diffraction experiments were performed at the neutron beamline *D1B* of the European neutron reactor, the *Institute Laue-Langevin (ILL)*, located at Grenoble, France.[3]

D1B is a neutron diffraction beamline exploited (and supported) by the general European council for the research development and the *Consejo Superior de Investigaciones Científicas* (the Spanish public research centres founded by the government) through a denominated *Collaborating Research Group* agreement. The resumed properties and parameters of the neutron reactor and the beamline have been explained at the chapter 7, section i.

8.1.1 Rietveld refinement

Rietveld method[4] is a mathematical methodology based on least squares minimisation used to find different structural details by making calculated pattern to match as better as possible measured diffraction pattern (neutron or X-ray). There are many parameters that can be refined during this process and these can be divided into three groups: overall parameters affecting the whole pattern (such as zero-error,

parameters describing background, ...); profile parameters that describe position and the shape of the diffraction peaks (this includes cell parameters); and purely structural parameters (atomic positions, atomic magnetic moments, occupancies, and temperature factors). By adjusting these parameters, the microstructure and the structural details, such as bond distances and bond angles, of the sample can be obtained. The refinements have been performed using *FullProf_Suite of Programs*.[5]

To apply the Rietveld method a prior knowledge of the structure (approximate atomic positions and composition) is needed. In our case, Rietveld refinement has been applied for a spinel structure with $Fd\bar{3}m$ (no. 227) space group, where $8a$ and $16d$ Wyckoff positions (named A and B respectively) are fully occupied by the M^{2+} and Fe^{3+} cations maintaining the general stoichiometry as MFe_2O_4. Because ferrite spinel has an ordered magnetic structure, it is needed to determine the magnitude and direction of the magnetic moment of each magnetic atom. The diffraction patterns show a limited number of magnetic reflexion (magnetic structure) limiting the calculation for the magnetic moment. After some trials, we decided to constrain the magnetic moment over one of the axis of the cubic cell and refine only the average magnetic moment of each sublattice (aforementioned A and B positions).

Final refinements have been performed with oxygen positions (1 degree of freedom), cationic distribution (1 degree of freedom) and magnetic structure (2 degrees of freedom) as free structural parameters which affect to the integrated intensity of the peaks. Below, the results of this analysis are presented and analysed.

8.2 Results

Rietveld refinement gives data about the structural details of the spinel ferrite magnetic nanoparticles, information that has to be exploited in order to deduce as much structural information as possible. Following sections show by category the conclusions reasoned via data exploitation.

8.2.1 Di raction patterns

NPD pattern di ers from the common X-ray one because the interaction of the neutrons with the matter is not the same, as it has been explained previously in the chapter 6. Figure 8.1 shows these NPD patterns, that at rst view, a variation between the ferrites can be observed, fact that with X-ray di raction is not possible.

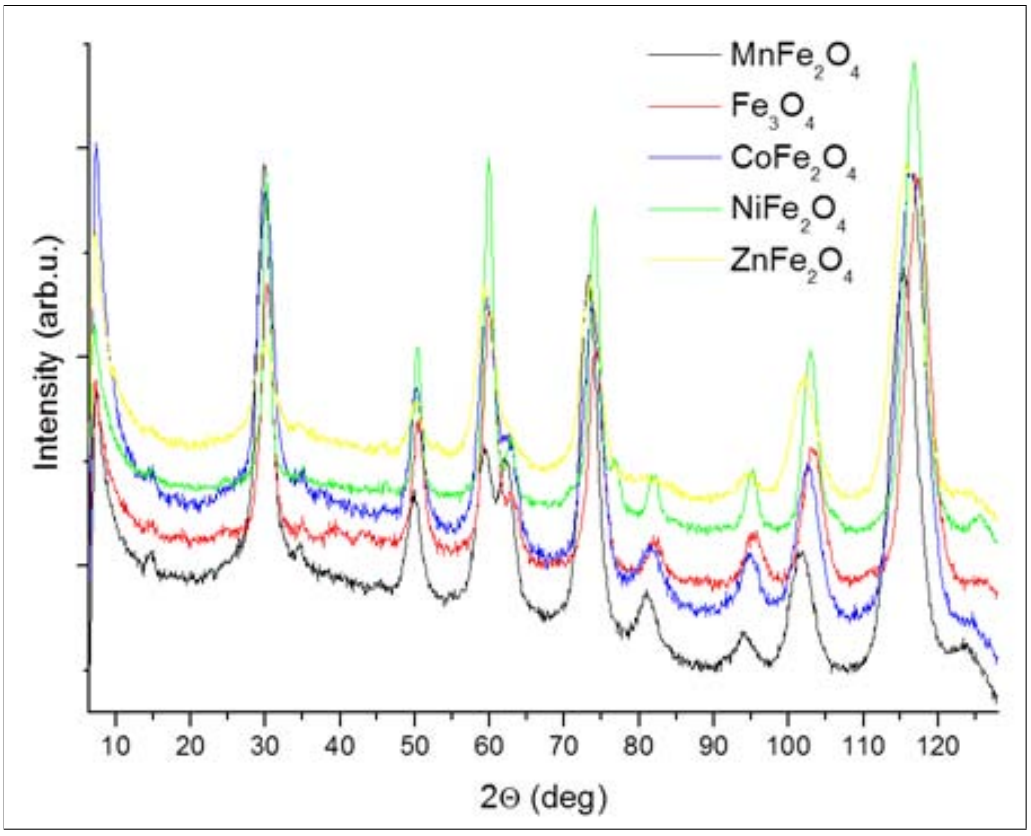

Figure 8.1: Neutron powder di raction patterns measured for the thermal synthesised nanoparticles.

The absence of non indexed peaks, together with high agreement parameters given by FullProf when Rietveld analysis is performed, make evident the phase purity of the spinel ferrites. In the case of the Fe_3O_4, at an angle 2μ of 40 degrees, some extra peaks that do not appear in the other cases indicates a secondary phase in the sample. The expected secondary phase can be maghemite (σ Fe_2O_3) or hematite (Fe_2O_3), because the NPs are synthesised without inert conditions, so an uncontrolled oxidation of the Fe_3O_4 can occur.[7] Magnetisation values of the iron oxide nanoparticles indicates the existence of σ Fe_2O_3 but not Fe_2O_3,

and due to this, Rietveld refinement has been performed taking the $\gamma - Fe_2O_3$ as a secondary phase.

In parallel, the decay of the background line is also informative. The presence of hydrogen atoms makes the background of NPD patterns to be very high at low angles and to decay to higher angles. This is due to the high incoherent scattering of hydrogen. Nanoparticles have been chemically cleaned exhaustively before measure at the ILL in order to eliminate the organic solvents and to reduce the noise in the neutron diffraction pattern. The low slope in the NPD patterns obtained denotes a low quantity of hydrogen atoms and, consequently, a low amount of organic molecules adsorbed on the nanoparticles (the higher the quantity of amorphous organic matter, the higher the amount of hydrogen, and the higher slope of the background of the diffraction patterns).

In the following example (figure 8.2), we plot from the Rietveld refinement of a X-ray diffraction pattern of the iron oxide nanoparticles, showing the observed and the calculated intensities, the discrepancies between them and the Bragg peaks position.

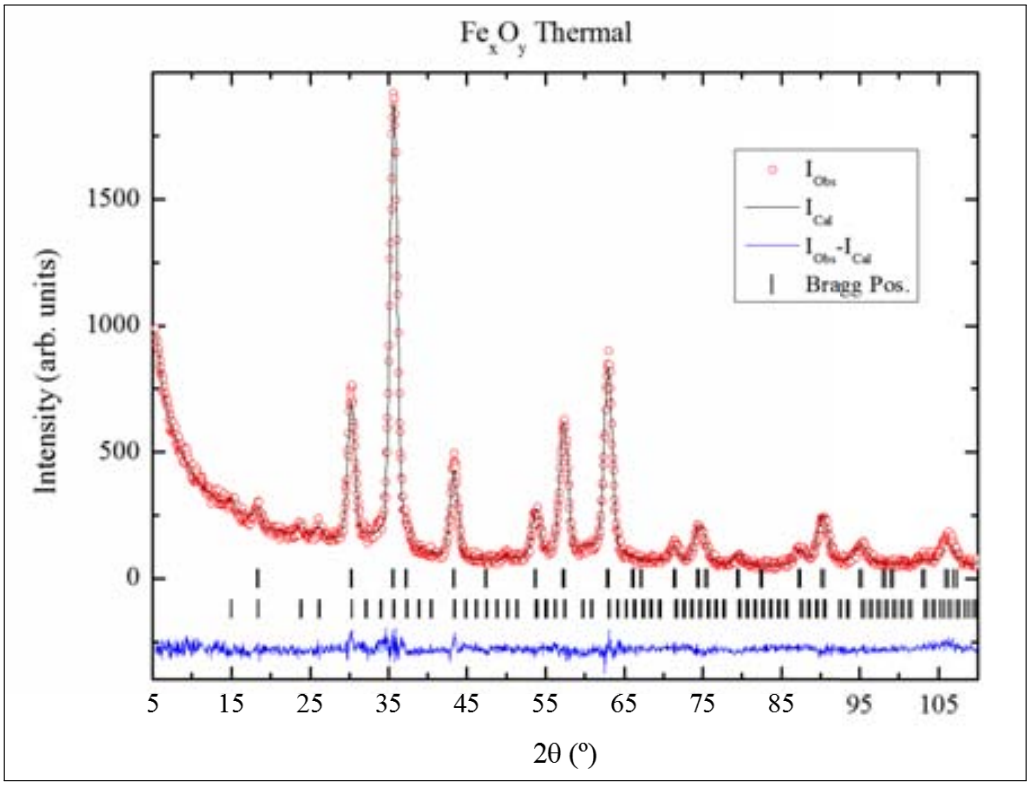

Figure 8.2: X-ray rietveld re nement generated by FullProf of the iron oxide nanoparticles, where two phases Fe_3O_4 and σ Fe_2O_3 are present.

8.2.2 Cell and crystal structure

Rietveld re nement provides diverse information about the crystal cell structure. This information comes conditioned by several parameters, such as the experimental conditions, re nement parameters, degrees of freedom, etc. They have been adjusted as better as possible in order to not over-exploit the data and obtain non real results.

i Cell parameters

Cell parameters of the di erent spinel ferrites are re ected in the table 8.1. These data are compared with those gathered through common laboratory XRPD in order to check the discrepancies between methods.

It can be seen that the cell parameters estimated with NPD and XRPD are similar, except for the case of the Zn ferrite, where exists some discrepancies which can come from the quality of the data acquired with the X-ray di ractometer. This

Spinel crystal & cell parameters

Compound	Route	Cell parameter (NPD) (Å)	Cell parameter (XRPD) (Å)	Crystal size (NPD) (nm)	Crystal size (XRPD) (nm)
$MnFe_2O_4$	T	8.433(3)	-	6.2	-
	M	8.383(3)	-	7.2	-
$CoFe_2O_4$	T	8.396(3)	8.395(1)	5.7	5.3
	M	8.391(3)	8.391(1)	5.2	4.1
$NiFe_2O_4$	T	8.375(3)	8.375(1)	11.5	13.7
$ZnFe_2O_4$	T	8.420(3)	8.440(1)	5.6	5.6
	M	8.321(3)	8.407(1)	4.7	4.1

Table 8.1: Crystal and cell parameters estimated via Rietveld refinement with Neutron Powder Diffraction (NPD) and X-ray powder diffraction (XRPD) for the ferrites produced via thermal (T) and microwave (M) routes. Some data have not been adjusted (signalled with a - symbol) because the quality of the experimental data collected.

case is similar to the $MnFe_2O_4$ one, whose size could not be calculated via XRPD. Cell parameters are the expected ones for a cubic ferrite spinel ∼8.4 Å. Scherrer equation (part II, equation 3.1) gives information about the crystal coherent size, which means the medium crystal size of the sample. In this case, the crystal size is similar to the TEM deduced ones with some divergences due to the calculation deviation. It is remarkable that the crystal size is constant even when the capping ligand has been eliminated from the surface (no signal of H and organic matter), being proof that the nanoparticles do not aggregate or coalesce. It is also interesting because the powder of nanoparticles produced can be redispersed in the desired solvent by adding a new coordinating ligand or by charging electrostatically the surface, as it has been experimentally verified.

For the iron oxide nanocrystals, an extra phase has been included in the Rietveld refinement in order to correctly reproduce the observed intensity. Thus, the iron oxide sample is treated as a mixture of magnetite (Fe_3O_4) and maghemite ($\gamma - Fe_2O_3$). Maghemite compound can be considered as a deficient cation iron (III) oxide structure,[8] so it is a product of a controlled oxidation of the magnetite.[7] Table

8.2, the crystal and cell parameters of these structure are revealed:

Fe_xO_y composition and crystallographic parameters					
Compound	Route	Composition (%)		Cell parameter (Å)	Crystal size (nm)
Fe_xO_y	T	Fe_3O_4	54	8.357(3)	7.2
		$\gamma - Fe_2O_3$	46	8.346(4)	
	M	Fe_3O_4	56	8.354(3)	7.2
		$\gamma - Fe_2O_3$	44	8.344(4)	

Table 8.2: Composition of the iron oxide nanoparticles generated by thermal (T) and microwave (M) route, together with the crystal and cell parameters.

These data indicate that the ferrites (MFe_2O_4, M = Mn, Co, Ni, Zn) are purely synthesised with the expected ferrite spinel crystal cell without secondary phases, while the iron oxide (Fe_xO_y) is a mixture of Fe_3O_4 and $\gamma - Fe_2O_3$. The phase distribution for these last NPs keeps constant for both synthetic routes, demonstrating that the heating method does not affect to their final composition. To prove that the solvent is a factor to take into account to control the oxidation degree of the compound, the same analyses where performed for magnetic nanoparticles thermally synthesised using Oleylamine as solvent and capping ligand.[9]

By comparing the results for phase composition when the nanoparticles were synthesised with the TREG or Oleylamine route, it is clearly seen that Oleylamine produces less ratio Magnetite:Maghemite (48:52), indicating a more oxidising medium for the TREG. The explanation of why the TREG is more oxidising than the Oleylamine is because during the thermal treatment, aldehyde groups are formed from the glycolic functional groups of the TREG.[10]

With this, it can be established that the ferrites produced are pure, while the Fe_3O_4 present a remarkable quantity of $\gamma - Fe_2O_3$, evidencing that the heating process does not affect to the final phase purity as the solvent of the reaction does.

ii Cation distribution

Remembering that the spinel structure is divided in two sublattices A (tetrahedral) and B (octahedral), with a cation distribution defined by the inversion degree i, the general formula of the spinel can be described as:

$$(M^{2+})^{A}_{1-i}(Fe^{3+})^{A}_{i}(M^{2+})^{B}_{i}(Fe^{3+})^{B}_{2-i}O_4$$

With Rietveld refinement of neutron powder diffraction, it is possible to evaluate with a good degree of reliability the cation distribution between the two sublattices, this could not be approximated with common laboratory techniques. For the calculations, a small number of approximations have been taken into account. It has been assumed that the total stoichiometry is the nominal one. This means the full occupancy of the corresponding crystallographic sites and with the total M/Fe ratio being 1:2. Results obtained allow to know the cation distribution, and then, write the exact formula with the atomic distribution. Below, in the table 8.3, the inversion degree for the NPs and their stoichiometry are attested.

Cationic distribution			
Compound	Route	Inversion degree	Stoichiometric formula
$MnFe_2O_4$	T	0.66	$[Mn_{0.34}Fe_{0.66}]^{A}[Mn_{0.66}Fe_{1.34}]^{B}O_4$
	M	0.68	$[Mn_{0.32}Fe_{0.68}]^{A}[Mn_{0.68}Fe_{1.32}]^{B}O_4$
$CoFe_2O_4$	T	0.64	$[Co_{0.36}Fe_{0.64}]^{A}[Co_{0.64}Fe_{1.36}]^{B}O_4$
	M	0.62	$[Co_{0.38}Fe_{0.62}]^{A}[Co_{0.62}Fe_{1.38}]^{B}O_4$
$NiFe_2O_4$	T	0.37	$[Ni_{0.63}Fe_{0.37}]^{A}[Ni_{0.38}Fe_{1.62}]^{B}O_4$
$ZnFe_2O_4$	T	0.36	$[Zn_{0.64}Fe_{0.36}]^{A}[Zn_{0.36}Fe_{1.64}]^{B}O_4$
	M	0.59	$[Zn_{0.41}Fe_{0.59}]^{A}[Zn_{0.58}Fe_{1.42}]^{B}O_4$

Table 8.3: Cation distribution (A, tetrahedral & B, octahedral sites) and stoichiometric formula of the nanocrystals analysed through NPD and Rietveld refinement.

Information concerning the inversion degree exposes that both methodologies make equal nanoparticles with similar inversion degree (considering the error bar of the calculation of the Rietveld refinement). It is also noteworthy that the inversion degree seems to keep constant around 60-70 %. In the case of the $NiFe_2O_4$, the inversion degree can not be obtained accurately because the scattering length of the Fe and the Ni are quite similar (9.45 vs 10.3 fm), doing that the error bar was bigger and then the calculation not conclusive. For the $ZnFe_2O_4$ NPs, a lower

inversion degree happens for the thermal synthesised nanoparticles, fact that can be related with the larger cell parameter (table 8.1). Larger cell parameter of the thermal synthesised zinc ferrite comes from a better cation order achieved with higher temperature and long time than in the case of the microwave generation.[11, 12] Also, this variation is more notable in the $ZnFe_2O_4$, because the difference between the atomic radius of the Fe and the Zn is bigger than in the case of the other ferrites,[13] facilitating the cation mobility and as consequence giving a more internal order.

iii Oxygen-metal distances

In this section, the oxygen-metal distances calculated with NPD refinement will be discussed. The importance of distance results is because information about the oxidation state of the metals in the spinel structure can be deduced. Computed data is compared with those calculated from the ionic distances tabulated by Shannon.[14] These tables report different sizes of the cations for their different oxidation states. From the experimental bond distances, and taking into account the inversion degree, a solid indication of the oxidation state of the cations is obtained.

Table 8.4 shows the cation-oxygen distances, calculated from Shannon, which fit better with the Rietveld data obtained. Trough this calculation, the oxidation states of the metals in the two crystallographic sites can be studied (table 8.5).

Oxidation states obtained by comparison with the Shannon distances reveal that the cationic oxidation state is the expected (M^{2+}, Fe^{3+}) for all the cases except for the $MnFe_2O_4$, where a mixture of Mn^{2+}, Mn^{3+}, Fe^{2+} and Fe^{3+} is present. The oxidation of Mn^{2+} in the ferrite magnetic nanoparticles (and the consequent reduction of the Fe (III) to Fe (II)) has been previously reported.[15] Then, having into account that the Mn^{3+} has a higher stabilisation energy in the B sites than the Fe^{2+}, the trivalent cation displaces the iron (II) to the tetrahedral holes. This oxidation seems to be related with the synthesis temperature: higher temperature, lower oxidation state for the Mn, which can be related with more anion vacancies at higher temperature.[16] For the others kind of ferrites, the expected oxidation state is found.

Cation-oxygen distances

Compound	Route	d(A-O) (Å)	d(B-O) (Å)	d(A-O) (Å) Shannon	d(B-O) (Å) Shannon
$MnFe_2O_4$	T	1.955(4)	2.036(4)	1.928	2.025
	M	1.933(2)	2.032(9)	1.924	2.025
$CoFe_2O_4$	T	1.898(6)	2.050(3)	1.902	2.057
	M	1.854(3)	2.071(3)	1.904	2.056
$NiFe_2O_4$	T	1.868(5)	2.062(5)	1.948	2.033
$ZnFe_2O_4$	T	1.924(5)	2.048(5)	1.940	2.042
	M	1.868(9)	2.069(9)	1.915	2.053

Table 8.4: Cation-oxygen distances for the tetrahedral (A) and octahedral (B) sites. Shannon distances determines the metallic oxidation state.

Cation oxidation state

Compound	Route	A sites	B sites
$MnFe_2O_4$	T	Mn^{2+}/Fe^{2+}	Mn^{3+}/Fe^{3+}
	M	Mn^{2+}/Fe^{2+}	Mn^{3+}/Fe^{3+}
$CoFe_2O_4$	T	Co^{2+}/Fe^{3+}	Co^{2+}/Fe^{3+}
	M	Co^{2+}/Fe^{3+}	Co^{2+}/Fe^{3+}
$NiFe_2O_4$	T	Ni^{2+}/Fe^{3+}	Ni^{2+}/Fe^{3+}
$ZnFe_2O_4$	T	Zn^{2+}/Fe^{3+}	Zn^{2+}/Fe^{3+}
	M	Zn^{2+}/Fe^{3+}	Zn^{2+}/Fe^{3+}

Table 8.5: Cation oxidation states in the tetrahedral (A) and octahedral (B) positions calculated via Shannon distances.

8.2.3 Microstructure

The position of the diffraction peaks in the powder patterns (X-ray and neutron) depends on the distance between crystallographic planes, allowing to obtain cell parameters. Besides, the shape of the diffraction peaks are determined by two contribution:one contribution is introduced by the diffractometer, and the other is the microstructure of the sample, mainly the crystal size and the microstrain (lattice deformations). The contribution of the diffractometer is determined by measuring a compound that can be considered as perfect (the contribution from its microstructure can be ignored in front of the contribution from the instrument), allowing to obtain the contribution from the sample. This has been done by measuring SiO_2 for XRPD and $Na_2Ca_3Al_2F_{14}$ for NPD. Profiting this fact, it has been reckon the microstrain of the nanoparticles produced by thermal and microwave synthetic procedures.

Microstructure			
Compound	Route	µstrain (‰) NPD	µstrain (‰) XRPD
$MnFe_2O_4$	T	23	-
	M	47	-
Fe_3O_4	T	7.7	-
	M	8.2	-
$CoFe_2O_4$	T	33	32
	M	25	29
$NiFe_2O_4$	T	16	15
$ZnFe_2O_4$	T	-	27
	M	-	12

Table 8.6: Microstructure of the different nanoparticles synthesised obtained by NPD and XRPD patterns. - symbol signifies that the refinement can not be performed with a reliable result.

Table 8.6 reflects the results for the microstructure calculation for the ferrite NPs. If these data are compared with those presented in the tables 8.1 and 8.2, it is possible to conclude that the microstrain has a dependence with the crystal size. For bigger nanoparticles, more stressed structure is generated, probably due to bigger structures need more time and temperature to relax the crystal. By the part of the synthetic methodology, no relevant conclusions can be extracted that relate the route

with the microstrain of the nanocrystals.

8.2.4 Magnetism

In the chapter 7, the interaction of the neutron with the magnetic atoms of the sample has been explained. Profiting this phenomena, an approximation of the magnetic moment for both sublattices of the spinel can be estimated with Rietveld refinement and compared with those obtained via SQUID magnetometry. Results are showed in the following table 8.7:

Magnetic moments					
Compound	Route	μ(μ_B) A sites	μ(μ_B) B sites	Total |μ| (μ_B)	M_s (μ_B/f.u.) (SQUID)
$MnFe_2O_4$	T	4.0	-3.4	2.8	3.9
	M	4.8	-1.7	2.6	3.3
Fe_3O_4	T	4.8	-3.5	2.2	3.4
	M	5.1	-3.4	1.7	3.1
$CoFe_2O_4$	T	4.4	-3.0	1.6	3.1
	M	4.3	-2.9	1.5	2.7
$NiFe_2O_4$	T	4.3	-3.5	2.7	2.7
	M	-	-	-	1.0
$ZnFe_2O_4$	T	1.0	-2.1	3.2	2.5
	M	2.6(7)	-2.6(3)	2.6	2.4

Table 8.7: Magnetic moment calculated for both sublattices, the tetrahedral (A) and the octahedral (B). Results are compared with the SQUID magnetometry information.

With this information, the relation between the magnetism of the nanoparticles provided by NPD and SQUID magnetrometry can be compared in global therms: higher total μ_B given by neutron diffraction implies higher magnetic saturation in the SQUID magnetometry. Nevertheless, in the case of the zinc ferrite, the error bar is larger than in the other cases, being the calculation for the global magnetic moment not conclusive.

Neutron diffraction is a technique which evaluates the ordered magnetic moment of each crystal sublattices (oriented along one crystallographic axis). Besides, the measurement in the SQUID magnetometer is done at different conditions: NPD is done at zero applied magnetic field and at room temperature, while for SQUID measures an strong magnetic field (7 T) is applied and the measure is done at 10 K. In addition, the eventual magnetic domains barely affect the result by NPD. Then, these two methodologies to evaluate the magnetism of the sample cannot be directly related.

8.3 Chapter summary

Neutron powder diffraction characterisation technique has been used combined with Rietveld refinement to obtain structural and magnetic information, but even an approximation to the cationic oxidation states and magnetic moments have been analysed.

As outcome, the comparative study between the structure of the nanoparticles generated by microwave and thermal synthetic route demonstrates that the microwave produces nanoparticles with similar structure, cationic distribution and magnetic moments than the thermal procedure, which are the expected one for the spinel ferrites. Only the $MnFe_2O_4$ presents a variation in the expected cationic oxidation states finding both, the iron and manganese cations, with an oxidation state of +2 and +3.

The case of the magnetite (Fe_3O_4) deserves an special treatment because maghemite ($\gamma - Fe_2O_3$) has been found in a 45 % as secondary phase in both synthetic procedures.

Bibliography Chapter 8

[1] J. A. Gerbec, D. Magana, A. Washington, and G. F. Strouse, "Microwave-enhanced reaction rates for nanoparticle synthesis," *Journal of the American Chemical Society*, vol. 127, no. 45, pp. 15791–800, 2005. (cited on page(s) 70, 178)

[2] N. G. Joivic, A. S. Masadeh, A. S. Kremenovic, B. V. Antic, N. D. Cvjetic, G. F. Goya, M. V. Antisari, and E. S. Boz, "Effects of thermal annealing on structural and magnetic properties of lithium ferrite," *Journal of Physical Chemistry C*, vol. 113, no. 48, pp. 20559–20567, 2009. (cited on page(s) 178)

[3] "Ill: Neutrons for science." `www.ill.eu`. Access July, 2013. (cited on page(s) 133, 153, 178)

[4] H. M. Rietveld, "A profile refinement method for nuclear and magnetic structures," *Journal of Applied Crystallography*, vol. 2, no. 2, pp. 65–71, 1969. (cited on page(s) 178)

[5] J. Rodriguez-Carvajal, "Recent advances in magnetic structure determination by neutron powder diffraction," *Physica B: Condensed Matter*, vol. 192, no. 1-2, pp. 55–69, 1993. (cited on page(s) 179)

[6] D. S. Mathew and R.-S. Juang, "An overview of the structure and magnetism of spinel ferrite nanoparticles and their synthesis in microemulsions," *Chemical Engineering Journal*, vol. 129, no. 1-3, pp. 51–65, 2007. (cited on page(s) 50)

[7] T. W. Swaddle and P. Oltmann, "Kinetics of the magnetite - maghemite - hematite transformation, with a special reference to hydrothermal systems," *Canadian Journal of Chemistry*, vol. 58, no. 17, pp. 1763–1772, 1980. (cited on page(s) 180, 183)

[8] R. Grau-Crespo, A. Y. Al-Baitai, I. Saadoune, and N. H. De Leeuw, "Vacancy ordering and electronic structure of $\gamma - Fe_2O_3$(maghemite): a theoretical investigation," *Journal of physics. Condensed matter.*, vol. 22, no. 25, pp. 255401–255408, 2010. (cited on page(s) 183)

[9] L. Perez-Mirabet, E. Solano, F. Martinez-Julian, R. Guzman, J. Arbiol, T. Puig, X. Obradors, A. Pomar, R. Yañez, J. Ros, and S. Ricart, "One-pot synthesis of stable colloidal solutions of MFe_2O_4 nanoparticles using oleylamine as solvent and stabilizer," *Materials Research Bulletin*, vol. 48, no. 3, pp. 966–972, 2013. (cited on page(s) 52, 85, 184)

[10] N. Miguel-Sancho, O. Bomati-Miguel, A. G. Roca, G. Martinez, M. Arruebo, and J. Santamaria, "Synthesis of magnetic nanocrystals by thermal decomposition in glycol media: Effect of process variables and mechanistic study," *Industrial & Engineering Chemistry Research*, vol. 51, no. 25, pp. 8348–8357, 2012. (cited on page(s) 73, 79, 184)

[11] M. Atif, S. Hasanain, and M. Nadeem, "Magnetization of sol-gel prepared zinc ferrite nanoparticles: Effects of inversion and particle size," *Solid State Communications*, vol. 138, no. 8, pp. 416–421, 2006. (cited on page(s) 186)

[12] C. N. Chinnasamy, A. Narayanasamy, N. Ponpandian, K. Chattopadhyay, H. Guerault, and J.-M. Greneche, "Magnetic properties of nanostructured ferrimagnetic zinc ferrite Magnetic properties of nanostructured ferrimagnetic zinc ferrite," *Journal of physics. Condensed matter*, vol. 12, pp. 7795–7805, 2000. (cited on page(s) 186)

[13] C.-K. Kim, J.-H. Lee, S. Katoh, and R. Murakami, "Synthesis of Co-, Co-Zn and Ni-Zn ferrite powders by the microwave-hydrothermal method," *Materials Research Bulletin*, vol. 36, pp. 2241–2250, 2001. (cited on page(s) 186)

[14] R. D. Shannon, "Revised effective ionic radii and systematic studies of interatomic distances in halides and chalcogenides," *Acta Crystallographica*, vol. 32, pp. 751–767, 1976. (cited on page(s) 186)

[15] G. Bonsdorf, M. A. Deneckeb, K. Schäfer, S. Christen, H. Langbein, and W. Gunber, "X-ray absorption spectroscopic and Mössbauer studies of redox and cation-ordering processes in manganese ferrite," *Solid State Ionics*, vol. 101-103, pp. 351–357, 1997. (cited on page(s) 186)

[16] Z. J. Zhang, Z. L. Wang, B. C. Chakoumakos, and J. S. Yin, "Temperature dependence of cation distribution and oxidation state in magnetic Mn-Fe ferrite nanocrystals," *Journal of American Chemical Society*, vol. 120, no. 8, pp. 1800–1804, 1998. (cited on page(s) 186, 200)

Chapter 9

Synchrotron XAS & XMCD

Contents

In this chapter, site-specific information on the atoms forming the magnetic ferrite nanoparticles under investigation ($MnFe_2O_4$, $CoFe_2O_4$ and Fe_3O_4) is obtained through X-ray Absorption Spectroscopy (XAS) and X-ray Magnetic Circular Dichroism (XMCD).

Structural and magnetic differences between the nanoparticles synthesised by both thermal and microwave activation processes are presented. In addition, a study of the properties of $MnFe_2O_4$ NPs when embedded in a YBCO layer are presented.

9.1 Experimental details

XAS (X-ray Absorption Spectroscopy) and XMCD (X-ray Magnetic Circular Dichroism) spectra have been acquired using the BOREAS beamline[1] at the ALBA[2] synchrotron light facility, whose characteristics were introduced in chapter 7.2.2.

Nanoparticle samples ($\sim$ 0.1 g or less) were fixed on a gold coated sample holder with double-side carbon adhesive tape as support. This sample holder was introduced into the HECTOR UHV (Ultra High Vacuum) chamber, where the sample was magnetized in a magnetic field up to 5 T parallel to the beam direction at room temperature. The almost incident circular polarised light was produced by an APPLE II undulator that allows controlling the polarisation handedness between the right circular polarisation (RCP) and left circular polarisation (LCP). The measurements were performed by monochromating the soft X-ray beam with a low-energy grating monochromator (<1200 eV) and passing through entrance and exit slits, typically using 15 micron vertical openings for high resolution and flux, and much wider in horizontal opening (1000 microns). TEY (Total Electron Yield) has been used as a detection mode, because unfortunately, fluorescence detection was not yet available at the endstation when the measurements were performed.

9.1.1 Samples measured

Samples measured were $MnFe_2O_4$, Fe_3O_4 and $CoFe_2O_4$ NPs synthesised by both methodologies, thermal and microwave. In addition, $MnFe_2O_4$ nanoparticles embedded in an YBCO SC layer were analysed in order to study their magnetic behaviour

after the thermal growth treatment. For comparison with the latter study, free $MnFe_2O_4$ nanoparticles subjected to the same thermal procedure than the YBCO layer were analysed as well. Below, the spectra taken together with an explanation concerning the different samples are displayed.

9.2 Ferrite magnetic nanoparticles

9.2.1 Fe_3O_4

The first measurements were done with magnetite obtained by both methodologies (thermal and microwave) and they were compared with the corresponding data from commercial magnetite (*Sigma-Aldrich*, size 50 nm) taken as a standard reference sample.

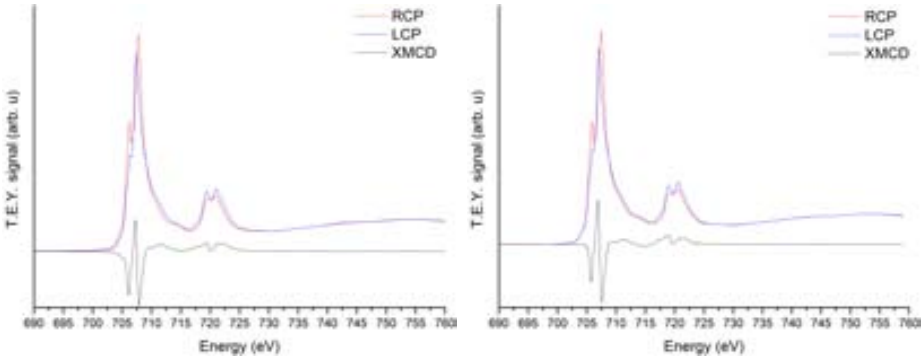

(a) Fe_3O_4 Thermal

(b) Fe_3O_4 Microwave

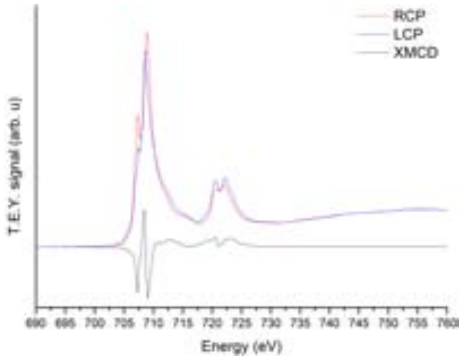

(c) Fe_3O_4 Standard

Figure 9.1: Spectra of the Fe edge of the Fe_3O_4 NPs studied: Fe_3O_4 Thermal (a), Fe_3O_4 MW (b) and the commercial sample (c).

Figure 9.1 shows the spectra for the Fe_3O_4 obtained by both, thermal and microwave methodologies as well as for the magnetite standard reference. The curves represent the XAS spectra for the RCP and LCP light, and the XMCD signal resulting from the subtraction of the RCP and LCP spectra. The results correspond to those previously described in the bibliography, concluding that samples can be identified as Fe_3O_4.[3] Having a closer look, it can be observed that the relative intensity of the XMCD peaks from the synthesised samples are different from those described for Fe_3O_4 in the literature. Knowing that the relative peak areas correspond to the number of atoms at the three inequivalent crystallographic sites (different stabilisation energy) and that the first XMCD low-energy peak corresponds to the Fe^{2+} in the Oh sites, while the second and third peaks can be assigned to the Fe^{3+} in Td and Oh holes, respectively,[4] it is possible to compare the cationic distribution between the studied samples.

Previous studies show that the relative signal intensity from the first peak in the prepared sample is larger than those described in the literature, concluding that the sample analysed here contains less iron (II) than the pure referenceFe_3O_4.[5, 6] This fact is in agreement with the presence of $\gamma - Fe_2O_3$ in the iron oxide nanoparticles, which corresponds to the fully oxidised form of the spinel[7, 8] that has been also detected using NPD (chapter 8).

9.2.2 $CoFe_2O_4$

Now the $CoFe_2O_4$ NPs are analysed, in this case for the Co and Fe $L_{2,3}$ edges and for both chemical routes for the synthesis. The resulting spectra can be seen in the following figures 9.2.

Thereby, the formation of $CoFe_2O_4$ is corroborated for both cases. The Co edge indicates an oxidation state of +2, but considering that the Fe edge should reflect only Fe (III) (which is apparently not the case) this indicates the possibility that there is a small proportion of Co^{3+} inside the structure, because some Fe^{2+} observed in the Fe edge. This phenomenon is common when a disorder inside the structure occurs, producing an exchange of the oxidation states between the Co and Fe atomic species. The presence of Co^{3+} has not been detected by the Shannon distances within the neutron diffraction data (chapter 8.2, section iii), probably due to the low

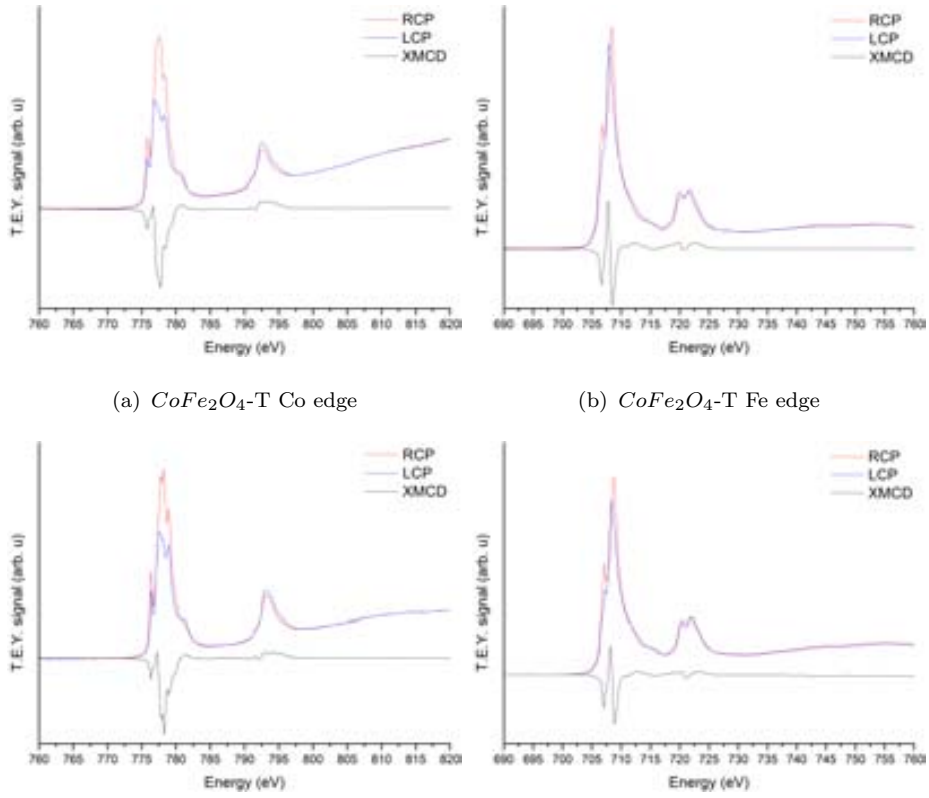

(a) $CoFe_2O_4$-T Co edge

(b) $CoFe_2O_4$-T Fe edge

(c) $CoFe_2O_4$-MW Co edge

(d) $CoFe_2O_4$-MW Fe edge

Figure 9.2: XMCD Spectra of the Co (a) and Fe (b) edge of thermal $CoFe_2O_4$, and the Co (c) and Fe (d) of the MW synthesised $CoFe_2O_4$.

concentration and the error bar of the refinement calculus.

Thus, it can be stated that the synthesis of $CoFe_2O_4$ leads to a mixture of oxidation states, which finally could result into variations regarding the final properties of the nanoparticles such as, e. g., the magnetic properties: Ferrimagnetism and superparamagnetic behavior with higher coercive field (as has been observed experimentally with SQUID magnetometry). As a matter of fact, both synthetic routes result into equal structures with (presumably) equal cationic distribution along the crystallographic lattice.

9.2.3 $MnFe_2O_4$

Manganese ferrite nanoparticles deserve a special analysis because this type of NP has been embedded into YBCO SC layers leading to interesting properties. First of

all, a comparison between the XMCD curves for nanoparticles originated via the two heating methods are analysed in the following figure 9.6.

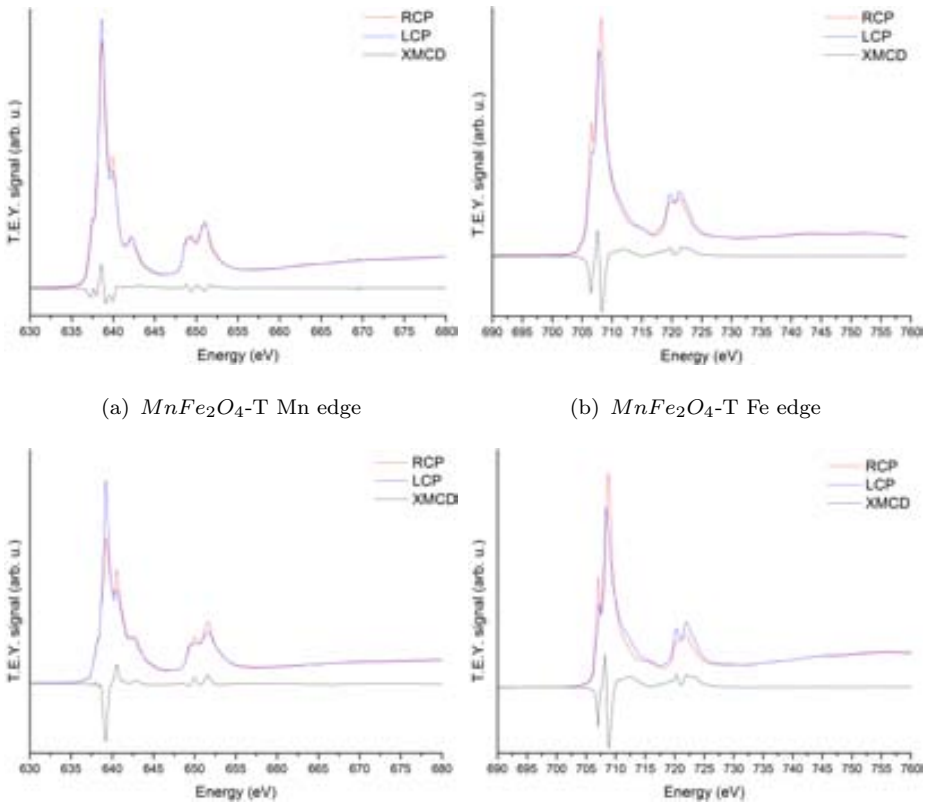

(a) $MnFe_2O_4$-T Mn edge

(b) $MnFe_2O_4$-T Fe edge

(c) $MnFe_2O_4$-MW Mn edge

(d) $MnFe_2O_4$-MW Fe edge

Figure 9.3: XMCD Spectra of the Mn (a) and Fe (b) edge of thermal $MnFe_2O_4$, and the Mn (c) and Fe (d) of the MW synthesised $MnFe_2O_4$.

At a first glance, it is possible to deduce the Mn oxidation state when correlating the present results with the previous bibliographic studies.[9] It can be found that the third peak of the XAS spectrum (around 643 eV) corresponds to the Mn^{3+}, while the two first peaks can be assigned to the expected Mn^{2+} of the spinel manganese ferrite. Correlated with this change in Mn oxidation state is the reduction of some Fe^{3+} to Fe^{2+} as has been deduced from the Shannon distances in chapter 8.2, section iii in order to maintain the charge balance of the structure. More Mn^{3+} is formed in the case of thermal NPs, as can be expected from the longer time and the higher temperature of the synthesis.[10]

Consequently, the existence of Mn^{3+} in the media can arise from two different phenomena: The generation of a mixed spinel or the formation of two phases. Both

hypothesis cannot be studied separately with the techniques used here, but the data obtained so far are in agreement with the formation of a mixed spinel since the presence of two crystalline phases should be detected by neutron diffraction measurements (chapter 8).

i Mn XAS simulation

With the aim to corroborate the latter hypothesis concerning the coexistence of Mn^{2+} and Mn^{3+}, a simulation of the XAS spectrum (RCP + LCP) has been realized. The program required to perform the calculations was *CTM4XAS*.[11] This software has been developed to calculate the XAS, XMCD and other spectra of different elements in different conditions (oxidation states, crystal field, charge transfer ...). For the case shown here, separate simulations of the XAS spectra for Mn^{2+} and for Mn^{3+} were required. Then, a linear combination of the different XAS patterns with adequate proportion in order to fit the experimental data was performed.

CTM4XAS requires as input several parameters, such as the atomic species and their oxidation state, crystal field and charge transfer parameters, etc. to calculate the pattern that will be plotted with the corresponding broadening and options (see figure 9.4).

After introducing the input data and extracting the numerical results, the linear combination of both the Mn^{2+} and Mn^{3+} spectra has been performed in order to generate an approximation to the experimental spectrum, resulting in the following figure 9.5.

Both spectra are presented after subtraction of the corresponding two-step functions. The simulation reproduces correctly the main features of the data. It can be observed that the main difference consists of the peak broadening due to the photon energy resolution of the beamline monochromator. In addition, some peaks are observed slightly higher energies that the simulation. These are likely related to crystal field effects. Based on this, it is expected that further simulation work should allow an even better fit, by tuning the crystal field parameters and peak broadening[a].

The important information that can be extracted for this simulation is that for the combination of both spectra, a value for the percentage of Mn^{2+} and Mn^{3+},

[a]Such analysis and results are out of the scope of the thesis work, and will be presented elsewhere

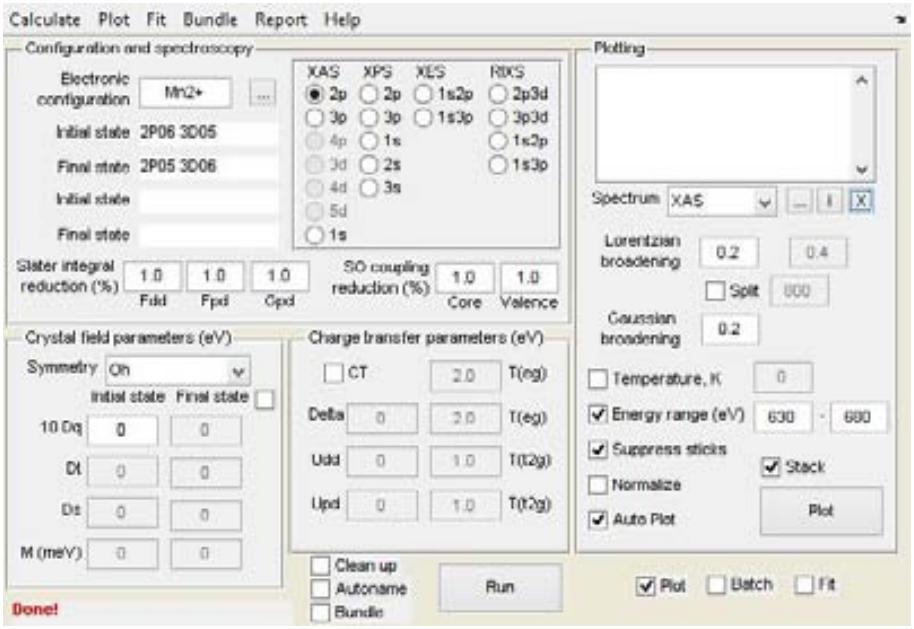

Figure 9.4: Screenshot showing the *CTM4XAS* interface where the input data has to be introduced.

respectively, has been estimated. As a result, around the 82 % is Mn^{2+}, while the Mn^{3+} is about the remaining 18 %.

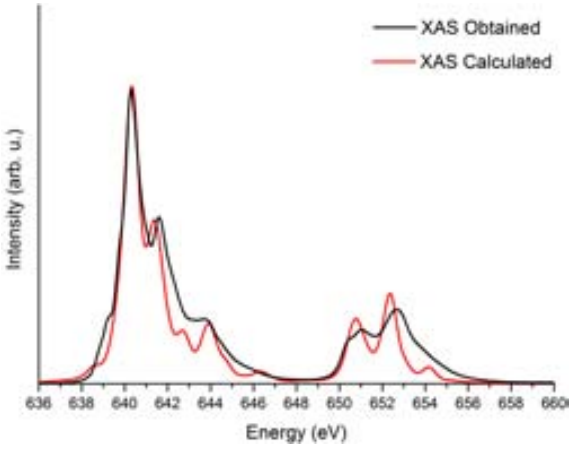

Figure 9.5: XAS simulation of the Mn edge of the $MnFe_2O_4$ NPs synthesised via microwave route.

ii $MnFe_2O_4$ NPs thermally treated

Once the $MnFe_2O_4$ NPs have been analysed, it is interesting to compare the results of the original as synthesised NPs, with those obtained after a thermal treatment equaling that to which the chemical solution of YBCO is subjected in order to yield the epitaxial YBCO. This means to subject the nanoparticles to a thermal procedure with a controlled atmosphere up to 810^{o}C (chapter 2.2.2). The next figure 9.6 shows the XAS and XMCD spectra of the Mn and Fe edges of the new thermally treated compound.

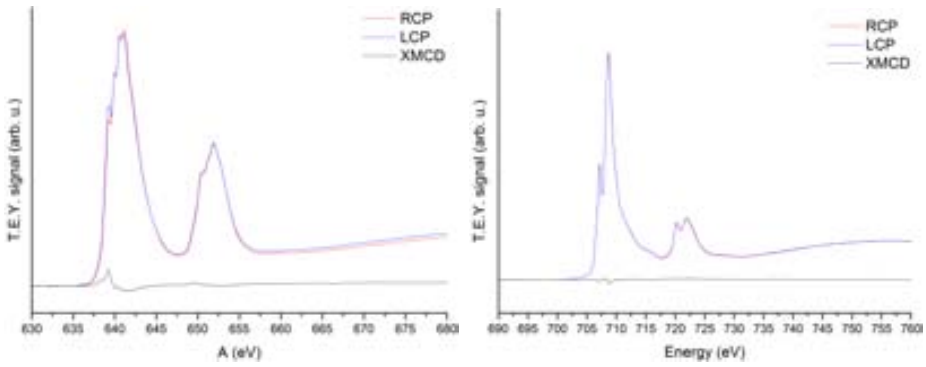

(a) Mn edge (b) Fe edge

Figure 9.6: $MnFe_2O_4$-MW XMCD spectra after the thermal treatment to YBCO crystal growth . (a) Mn edge and (b) Fe edge.

The analysing of XAS and RCP, LCP spectra indicate a reduced XMCD effect,

which agrees with the fact that the NPs have a lower magnetic moment when compared with the same compound as a bulk material. It is possible that this phenomenon comes from the presence of MnO_2, Mn_2O_3 and $\alpha - Fe_2O_3$ (hematite) structures, which probably have been formed under the applied harsh conditions. The metallic oxidation states of the Mn can be confirmed by comparing the XAS spectra with those obtained for a Mn with a mixture of +3 and +4 oxidation states, as it can be in the $La_{0.7}Sr_{0.3}MnO_3$,[12] but in this case, some remanences of Mn^{2+} can be found. Notwithstanding this oxidation process, some remains of the original ($MnFe_2O_4$) phase can be still detected. To prove the existence of a mixture of three phases a SQUID magnetometry analysis was performed where a mixed magnetic behaviour is expected: Antiferromagnetic for MnO_2 and $\alpha - Fe_2O_3$, and superparamagnetic from the remaining $MnFe_2O_4$. Figure 9.7 shows the corresponding SQUID measurements.

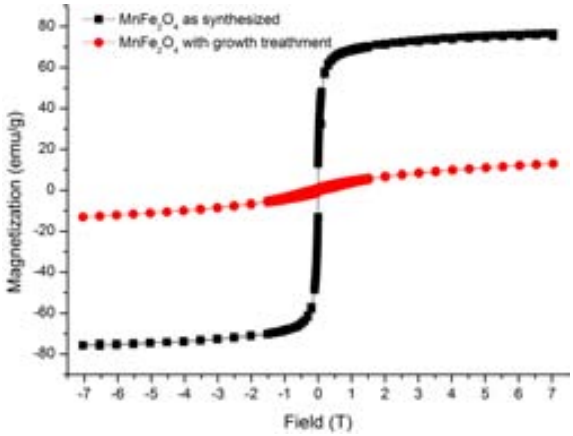

Figure 9.7: SQUID measurement comparing the magnetic behaviour of $MnFe_2O_4$ NPs before and after the thermal treatment.

The M(H) curve after the thermal treatment according to the YBCO growth conditions proves the presence of a superparamagnetic as well as an antiferromagnetic phase which should be expected to decrease the total M_s value. This conclusion does not imply that when the nanoparticles are embedded into the YBCO layer this would lead to exactly the same process since in the latter case the NPs are protected from the oxidation by the YBCO matrix. In fact, in the chapter 10 the $MnFe_2O_4$ spinel structure inside the YBCO is proved through synchrotron XRD.

9.3 YBCO nanocomposite nanostructured layers

To complete the XAS & XMCD analyses, a YBCO thin layer with embedded $MnFe_2O_4$ NPs has been analysed.[b]

The sample was mounted onto the sample holder with the help of a carbon tape and connected with the holder with silver paint in order to minimise parasitic effects of electric charging of the sample during measurements. The signal gain was also increased as compared to the other NP measurements to get a higher signal/noise ratio, but, as consequence, some electrical noise is recorded with the raw data. The reason for this is that, remembering the TEY basics, it is possible to measure only the first five nanometers of the sample (with 200 nm thickness) because the limited eectron scape depth and, knowing that within the sample there is a low concentration of NPs of 1.5 % (as free $MnFe_2O_4$), it is expected that only a few nanoparticles of the external part of the layer can be detected. Nevertheless, some signal was detected giving the possibility to study the atomic state of the transition metal atoms forming the NPs. The following figure 9.8 shows the XAS & XMCD spectra.

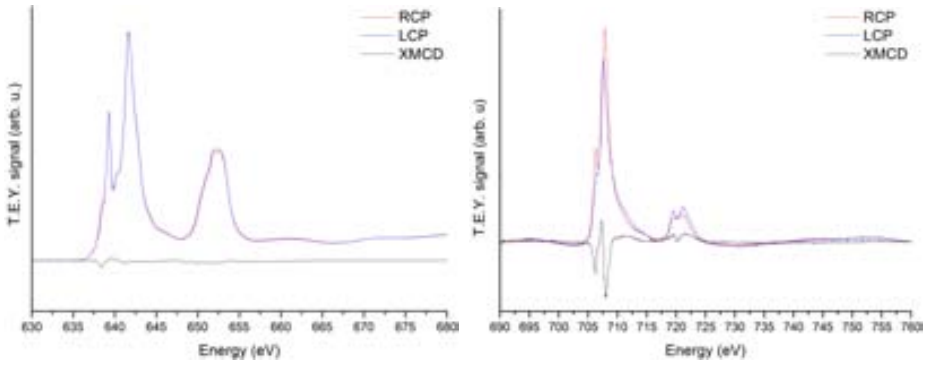

(a) Mn edge (b) Fe edge

Figure 9.8: $MnFe_2O_4$-MW XMCD spectra when embedded in a YBCO layer and after the thermal treatment according to crystal growth requirements: (a) Mn edge and (b) Fe edge.

[b]Different samples from the different steps of the YBCO thin layer generation (deposition and pyrolysis) have been analysed without results, because the sample substrates are insulators and only TEY detection system was installed at the beamline when the measurements were performed. It is planned to complete these measurements with further measurements, and use fluorescence detection to override the difficulties with insulating samples producing charging effects and low signals, and also to benefit from fluorescence larger probing depth. A related beam time proposal is under preparation.

The recorded absorption spectra can easily be compared with the previous ones from the free $MnFe_2O_4$ NPs as well as with the spectra from the samples after the thermal treatment. As a first hypothesis, it is possible to deduce that the last analysis is a mixture of the other two previously studied. The shape of the Mn absorption edge indicates the presence of Mn^{2+} with a considerable quantity of Mn^{3+}, meaning that the Mn atoms have been partially oxidised. On the other hand, the Fe edge shows the common spectra for a mixture of Fe^{2+} and Fe^{3+}, having a lower dichroism than the original NPs, but much larger than the NPs subjected to the thermal process. Thus, the similarity between the previous and present results indicate the presence of unaltered $MnFe_2O_4$ NPs inside the nanocomposite YBCO superconducting layer together with an oxidised fraction of NPs containing Mn^{3+}.

Considering that only the superficial NPs within the YBCO top layers have been analysed, it is possible that these NPs are more exposed to the oxidizing atmosphere, while the internal NPs within the bulk of the YBCO layer remain practically immutable, and therefore, a mixed absorption spectrum is obtained.

According to the above measurements, the presence of some $MnFe_2O_4$ NPs embedded inside the YBCO structure could be verified, as has been the objective of this work. The interest of these nanoparticles is not only their phase or oxidation state, but the presence of non-superconducting region with their specific magnetic behavior. Results and conclusions from this study will be applied to the research in the improvement of the superconducting (magnetic) pinning effect.

9.4 Sum rules

This section reviews the use of Sum Rules on the XAS and XMCD data, as an advanced analysis to provide information on the spin and orbital magnetic moments, i.e. the atomic magnetic state of the species forming the samples.The following steps are described in order to calculate separately the spin and orbital magnetic moments of the different magnetic atoms forming the samples. In this case, only the Fe_3O_4 and $MnFe_2O_4$ nanoparticles produced via microwave methodology are analysed[c].

Remembering the Sum Rules (equations 7.14 & 7.15) and their conditions

[c]Calculations for the rest of the NPs generated will be developed in later work.

explained within section 7.2.1, first of all it is needed to plot the XAS and XMCD spectra and their corresponding integrals. For XAS spectra (sum of RCP and LCP), it is needed to normalize it between 0 and 1 before and after the absorption edges, then the *tanh* baseline is subtract to calculate correctly the integral value. The following figure 9.9 shows the obtained graphical results.

By plotting the integrals, it is possible to calculate the *p, q* and *r* values required for the calculation of the spin and orbital moments. These values are taken in the flat part of the integral for all the cases, but maintaining always the exact selected energy value between the XAS and XMCD spectra; in other words, if the *q* value is selected at a specific photon energy E, the value of the *r* integral must be taken at the same photon energy E.

After that, the number of holes (i.e., unoccupied electronic states) within the 3d electronic states it is needed, but since it is not possible to know the exact value in the experimental conditions, the value is approximated by considering the ground state of the atom (i.e., not taking into account the excited state of the atom). In addition, it is worth to consider that the nanoparticles analysed so far are formed by a mixture of different oxidation states of the same atom, and even in the case of the Fe_xO_y, two different phases do coexist: Fe_3O_4 and $\gamma - Fe_2O_3$. Then, the number of holes (n_h) for each atom species and valence is calculated by using the neutron diffraction data (oxidation state and composition) as shown in chapter 8.

The following table 9.1 shows the data necessary for the n_h deduction.

		Number of holes			
Compound	Atom	Oxidation state	n_h/atom	atoms/f.u.	total n_h
$MnFe_2O_4$	Mn	2+	5	0.32	5.68
		3+	6	0.68	
	Fe	2+	4	0.68	9.32
		3+	5	1.32	
Fe_xO_y	Fe_3O_4 (56 %)	2+	4	1	12.24
		3+	5	2	
	$\gamma - Fe_2O_3$ (44 %)	3+	5	2	

Table 9.1: Resume of the calculations to obtain the n_h for the $MnFe_2O_4$ and Fe_3O_4. Note that the magnetite is formed by a mixture with maghemite.

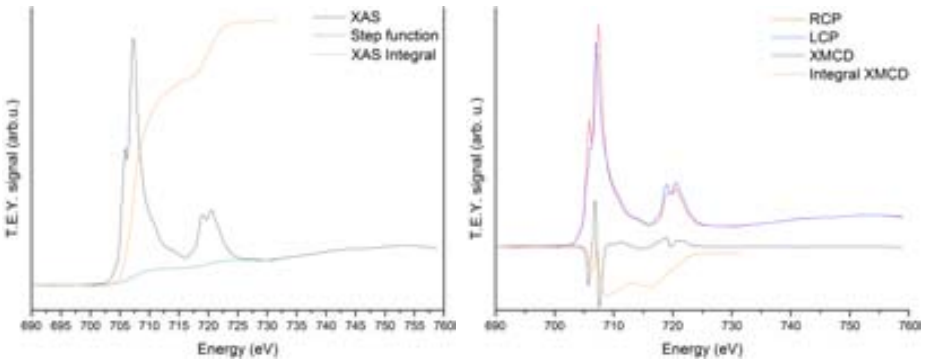

(a) Fe_3O_4 MW - Fe XAS

(b) Fe_3O_4 MW - Fe XMCD

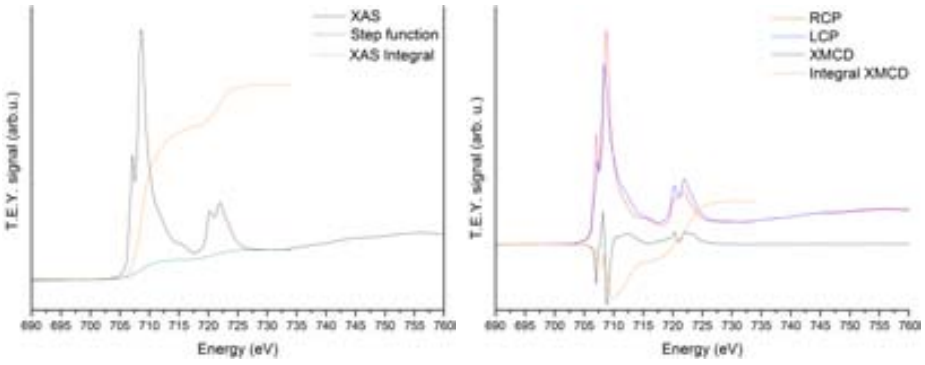

(c) $MnFe_2O_4$ MW - Fe XAS

(d) $MnFe_2O_4$ MW - Fe XMCD

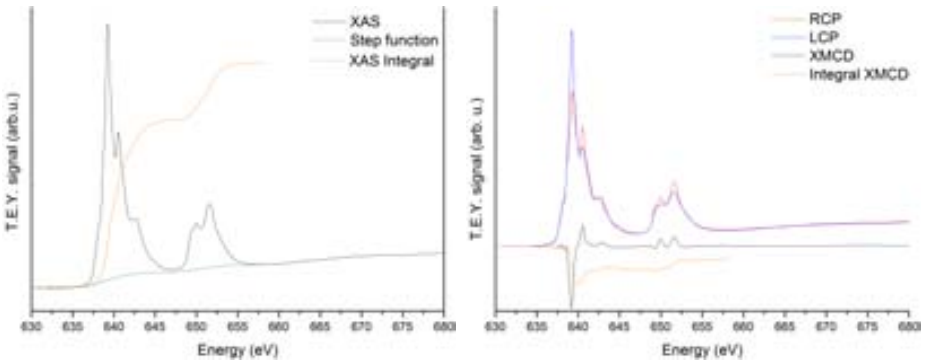

(e) $MnFe_2O_4$ MW - Mn XAS

(f) $MnFe_2O_4$ MW - Mn XMCD

Figure 9.9: Spectra of the Fe and Mn XAS & XMCD for the Sum Rules calculations. Note that the final of the integral is taken when the integral is flat.

Now that all the data have been collected and calculated, the spin and orbital moments can be calculated. Results are shown in table 9.2.

$\langle m_{orb} \rangle$ and $\langle m_{spin} \rangle$ calculations

Compound	Atom	n_h	p	q	r	$\langle m_{orb} \rangle$	$\langle m_{spin} \rangle$	$\langle m_{orb} \rangle / \langle m_{spin} \rangle$
$MnFe_2O_4$	Mn	5.68	- 0.110	-0.057	36.1	0.012	0.068	0.173
	Fe	9.32	- 0.082	0.254	31.6	-0.101	0.449	-0.224
Fe_xO_y	Fe	12.24	- 0.502	-0.084	42.8	0.032	0.763	0.04

Table 9.2: $\langle m_{orb} \rangle$ & $\langle m_{spin} \rangle$ in μ_B for the different atoms forming the nanoparticles studied at room temperature. The q and r values have been taken at a 658 and 730 eV for the Mn and Fe respectively.

The expected values founded in the bibliography for the orbital and spin moments of the different metals forming the samples are presented in the table 9.3.

$\langle m_{orb} \rangle$ and $\langle m_{spin} \rangle$ reference values

Compound	Atom	n_h	$\langle m_{orb} \rangle$	$\langle m_{spin} \rangle$	$\langle m_{orb} \rangle / \langle m_{spin} \rangle$
$MnFe_2O_4$	Mn	5.68	-0.01	4.08	0.002
	Fe	9.32	-0.05	-4.05	0.0123
Fe_xO_y	Fe	12.24	-0.06	-4	0.015

Table 9.3: $\langle m_{orb} \rangle$ & $\langle m_{spin} \rangle$ reference calculated values (μ_B) for the $MnFe_2O_4$[13] and for the Fe_3O_4[14] below the Verwey transition temperature.[15]

The numerical results obtained demonstrate the low Fe orbital moment for the case of the Fe_xO_y and also when it is forming part of the $MnFe_2O_4$ NPs, as it has been previously demonstrated in the literature (table 9.3 and Goering et al.[16] and Perez et al.[8]). Concerning the spin value, no clear result have been found, principally due to the different temperature when performing the measurements and, in addition, the difficulties encountered during the Sum Rule evaluation of the spectra, as it will be explained a below.

Sum Rules, which allows the calculation of the spin-orbit magnetic coupling of magnetic atoms, do not result in an absolute value without the accurate normalisation of good data. This is far from being straightforward due to several reasons:

1. The background subtraction carries difficulties to perform the Sum Rules.

2. Difficulty to get proper absolute values due to the normalisation choice.
3. Any heterogeneity in the NPs, specially in the outer region, which also may differ from one typo of nanoparticles to another.
4. Real differences between Fe_3O_4 NPs and the reference Fe_3O_4, such as differences in the measurements temperature.
5. The TEY detection mode is more complicated to analyse[17] than the transmission mode, because the influence of the electrical accumulation and the influence of different chemical compounds surrounding the sample can affect the final acquired data.

For those reasons, the applicability of sum rules to a complex non-uniform sample with different cationic sites and valences such as the MFe_2O_4 NPs is not straightforward and typical error bars for these samples should be larger than for uniform samples, possibly as large as 20 or 40 %. Still, the sum rule analysis has some quantitative interest, especially when discussing trends between samples. For this purpose and even more due to the difficulty to identify in the literature a clear reference for the compounds studied here regarding absolute orbital and spin values, it is essential to measure a standard sample for each compound analysed in conditions as close as possible to the experimental conditions for the NP samples of interest.

In order to represent the differences on the integral calculations depending on the data treatment, the following figure 9.10 shows how the XMCD integral changes depending on the normalization of the RCP and LCP curves.

It is clearly shown how the RCP and LCP data treatment influences in the final XMCD integral. For the data presented here, the last approach has been used. It consists of subtracting a straight base line from the RCP and LCP spectra calculated via a linear fit linear of the points before the first peak. With this demonstration, it would like to de demonstrated the difficulty to follow a standard procedure for performing the Sum Rule calculations. Because of that, the results can only be comparable between similar samples with equal data treatment. Even then, some discussion concerning data analysis can be found among the literature, such as Huang et al.[14] calculations and the answer by Goering et al.[18]

XAS & XMCD analysis allows to achieve deeper atomic and magnetic information than presented here. This pending work will be carried out in a close future, because it is out of time of this PhD. research.

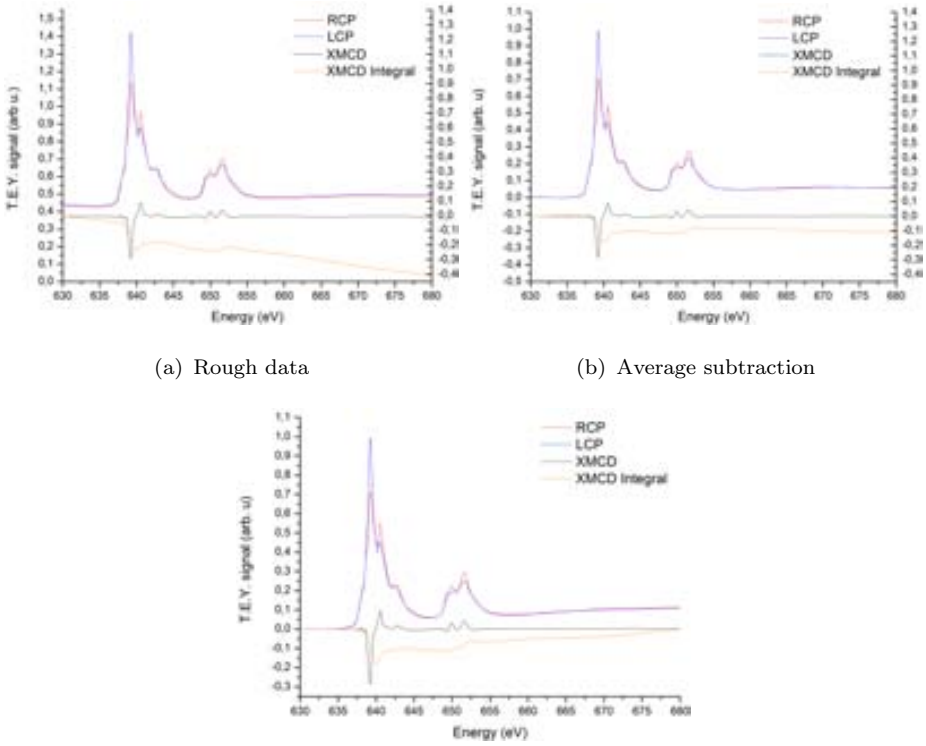

(a) Rough data

(b) Average subtraction

(c) Independent subtraction

Figure 9.10: Comparison of the XMCD integral depending on the XMCD data treatment. (a), without any modification, data as acquired; (b), after displace the curve to zero before the pre-edge region to zero without modify the slope (y-axis displacement); (c), after subtract a baseline calculated via a linear fit of the points before the L_3 edge.

9.5 Chapter summary

XAS & XMCD measurements have been performed with the aim to study the composition and magnetic behavior of the nanocrystals generated via the two optimized synthetic routes: Thermal and microwave.

Results agree with the previous neutron powder diffraction conclusions, because the presence of a mixture of oxidation states for the $MnFe_2O_4$, Fe_3O_4 and even $CoFe_2O_4$ is demonstrated. A verification of these results has been carried out by performing a simulation of the Mn XAS spectra, confirming that around the 18 % of the Mn atoms has a valence of Mn^{3+}.

$MnFe_2O_4$ nanoparticles have been also analysed as synthesised using the same

thermal treatment as the one for YBCO and finally were embedded in a *ex-situ* YBCO superconducting layer. These measurements have been performed with the aim to understand the changes occurring to the nanoparticles from their starting point (when synthesised) until their embedding inside the YBCO layer. Results prove that even these embedded nanoparticles have been partly oxidised, while some unaltered fraction of $MnFe_2O_4$ NPs still remains keeping their magnetic properties inside the YBCO layer, which has been one of the research goals of this work.

In addition, sum rules have been applied as a way to calculate approximately the orbital and spin magnetic moment, demonstrating that XAS and XMCD is an advisable tool to extract atomic and magnetic information of the atoms forming the sample.

Bibliography Chapter 9

[1] "Boreas beamline characteristics." `https://www.cells.es/Beamlines/VP/`. Access July, 2013. (cited on page(s) 169, 170, 196)

[2] "Alba spanish synchrotron web page." `http://www.cells.es`. Access July, 2013. (cited on page(s) 169, 196)

[3] C. I. Pearce, "Direct determination of cation site occupancies in natural ferrite spinels by $L_{2,3}$ X-ray absorption spectroscopy and X-ray magnetic circular dichroism," *American Mineralogist*, vol. 91, no. 5-6, pp. 880–893, 2006. (cited on page(s) 198)

[4] M. C. Richter, J.-M. Mariot, O. Heckmann, L. Kjeldgaard, B. S. Mun, C. S. Fadley, U. Lüders, J.-F. Bobo, P. de Padova, A. Taleb-Ibrahimi, and K. Hricovini, "$NiFe_2O4$ and Fe_3O_4 studied by XMCD and resonant photoemission," *The European Physical Journal Special Topics*, vol. 169, no. 1, pp. 175–180, 2009. (cited on page(s) 198)

[5] L. Signorini, L. Pasquini, F. Boscherini, E. Bonetti, I. Letard, S. Brice-Profeta, and P. Sainctavit, "Local magnetism in granular iron/iron oxide nanostructures by phase- and site-selective x-ray magnetic circular dichroism," *Physical Review B*, vol. 74, p. 014426, July 2006. (cited on page(s) 198)

[6] D. Kim, H. Lee, G. Kim, Y. Koo, J. Jung, H. Shin, J.-Y. Kim, and J.-S. Kang, "Interface electronic structures of $BaTiO_3$@X nanoparticles (X=$\gamma - Fe_2O_3$, Fe_3O_4, $\alpha - Fe_2O_3$, and Fe) investigated by XAS and XMCD," *Physical Review B*, vol. 79, no. 3, p. 033402, 2009. (cited on page(s) 198)

[7] S. Brice-Profeta, M.-A. Arrio, E. Tronc, N. Menguy, I. Letard, C. Cartier dit Moulin, M. Noguès, C. Chanéac, J.-P. Jolivet, and P. Sainctavit, "Magnetic

order in γ-nanoparticles: a XMCD study," *Journal of Magnetism and Magnetic Materials*, vol. 288, pp. 354–365, 2005. (cited on page(s) 198)

[8] N. Perez, F. Bartolome, L. M. Garcia, J. Bartolome, M. P. Morales, C. J. Serna, A. Labarta, and X. Batlle, "Nanostructural origin of the spin and orbital contribution to the magnetic moment in Fe_3O_4 magnetite nanoparticles," *Applied Physics Letters*, vol. 94, no. 9, p. 093108, 2009. (cited on page(s) 198, 209)

[9] S. Choudhury, *Spectroscopic study of transition metal compounds*. PhD thesis, University of Saskatchewan, 2010. (cited on page(s) 200)

[10] Z. J. Zhang, Z. L. Wang, B. C. Chakoumakos, and J. S. Yin, "Temperature dependence of cation distribution and oxidation state in magnetic Mn-Fe ferrite nanocrystals," *Journal of American Chemical Society*, vol. 120, no. 8, pp. 1800–1804, 1998. (cited on page(s) 186, 200)

[11] E. Stavitski and F. M. F. de Groot, "The CTM4XAS program for EELS and XAS spectral shape analysis of transition metal L edges.," *Micron*, vol. 41, pp. 687–94, Oct. 2010. (cited on page(s) 201)

[12] M. Richter, P. De Padova, C. Quaresima, P. Perfetti, R. Brochier, V. Ilakovac, O. Heckmann, L. Lechevallier, M. Zerrouki, C. Teodorescu, C. Fadley, N. Hamdan, and K. Hricovini, "Resonant photoemission and XMCD on Mn-based systems," *Journal of Alloys and Compounds*, vol. 362, no. 1-2, pp. 41–47, 2004. (cited on page(s) 204)

[13] V. Antonov, B. Harmon, and A. Yaresko, "Electronic structure and x-ray magnetic circular dichroism in Fe3O4 and Mn-, Co-, or Ni-substituted Fe3O4," *Physical Review B*, vol. 67, no. 2, p. 024417, 2003. (cited on page(s) 209)

[14] D. J. Huang, C. F. Chang, H.-T. Jeng, G. Y. Guo, H.-J. Lin, W. B. Wu, H. C. Ku, A. Fujimori, Y. Takahashi, and C. T. Chen, "Spin and orbital magnetic moments of Fe_3O_4," *Physical Review Letters*, vol. 93, no. 7, pp. 2–5, 2004. (cited on page(s) 115, 209, 210)

[15] G. Rozenberg, M. Pasternak, W. Xu, Y. Amiel, M. Hanfland, M. Amboage, R. Taylor, and R. Jeanloz, "Origin of the Verwey Transition in Magnetite," *Physical Review Letters*, vol. 96, no. 4, p. 045705, 2006. (cited on page(s) 209)

[16] E. Goering, S. Gold, L. M., and S. G., "Vanishing fe 3d orbital moments in single-crystalline magnetite," *Europhysics Letters*, vol. 73, no. 1, pp. 97–104, 2006. (cited on page(s) 209)

[17] R. Kurian, K. Kunnus, P. Wernet, S. M. Butorin, P. Glatzel, and F. M. F. de Groot, "Intrinsic deviations in fluorescence yield detected x-ray absorption spectroscopy: the case of the transition metal $L_{2,3}$ edges," *Journal of physics. Condensed matter : an Institute of Physics journal*, vol. 24, no. 45, p. 452201, 2012. (cited on page(s) 210)

[18] E. Goering, M. Lafkioti, and S. Gold, "Comment on "Spin and Orbital Magnetic Moments of Fe_3O_4"," *Physical Review Letters*, no. 3, p. 39701. (cited on page(s) 210)

Chapter 10

X-Ray Diffraction for $YBa_2Cu_3O_{7-\delta}$ Nanocomposites

Contents

10.1 Experimental details

X-ray synchrotron diffraction measurements were carried out at DiffAbs beamline[1] at the synchrotron Soleil.[2]

To perform the analyses, the 6-axis diffractometer has been operated, where the sample is mounted and irradiated with monochromatic radiation of 8.048 ± 0.001 KeV (Cu K_α), the same wavelength than common laboratory sources. The point detector slits were 0.3 x 4 mm (vertical x horizontal), with an acceptance of 0.02^o at 710 mm of distance between the sample and the detector.

Single crystal YBCO superconducting layer were measured with a configuration out of plane (δ/ω scan) and in plane (δ/φ scan, grazing incidence geometry; see chapter 7, section 7.1.2), in order to study the crystal composition, structure and microstructure. In addition, several nanocomposite YBCO layers have been studied:

1. Standard: YBCO standard sample that is taken as a reference system.
2. *In-situ* NPs-YBCO: two samples YBCO with $BaZrO_3$ and Ba_2YTaO_6 NPs embedded respectively
3. *Ex-situ* NPs-YBCO: YBCO with $MnFe_2O_4$ NPs and other sample with $BaCeO_3$ nanoparticles
4. BZO nanofibers: $BaZrO_3$ nanofibers generated by electrospinning on a LAO single crystal

Superconducting properties of the nanostructured layers studied are revealed in the table 10.1. These measurements have been performed in order to know the quality of the sample in superconducting terms.

With these results it is possible to deduce that the BZO sample is not optimal, because their critical current is low (under the standard sample). The opposite case is the standard YBCO layer, which has similar J_c value than the nanostructured layers. Previous works of the group have been developed a new optimised system which prepares high quality standard YBCO superconducting, process that will be applied to improve the generation of nanocomposite samples in order to improve their J_c value. In spite of this, other superconducting parameters not analysed here have demonstrated the importance of embed nanoparticles inside the YBCO layers,

Superconducting properties			
Sample	% of NPs	T_c (K)	J_c (MA/cm^2) at 77 K
Standard	-	91.0	3.9
$BaZrO_3$	6	90	1.5
Ba_2YTaO_6	10	90	4
$MnFe_2O_4$	1.5	89.2	4
$BaCeO_3$	6	90.6	4.3

Table 10.1: Resume of the SC properties T_c and J_c of the nanocomposite superconducting layers and the standard reference analysed by X-ray synchrotron diffraction. The quality of the BZO sample is not optimal.

as in example, the penetration of the external magnetic field in function of the temperature.

10.2 $YBa_2Cu_3O_{7-\delta}$ reference layer

Details obtained with XRD for a standard YBCO superconducting layers are presented and analysed. A YBCO standard (YBCOstd) with J_c^{77K}=3.9 MA/cm^2 and T_c=91 K has been measured. This can be considered as a good quality sample, and it is optimal for analysis, because it is expected that it does not contain secondary phases or impurities. For this sample, several measurements have been performed, such as reflectivity to study their thickness, and XRD out and in plane to check their phase composition and the microstrain (μstrain) of the specimen. Below, the analyses, calculation and outcomes are explained.

10.2.1 Thickness oscillations

At is has been explained in the chapter 7.1.1, when the incidence angle of X-rays becomes small, it exists an angle where a total external reflexion is achieved (critical angle), and all the incident photons are reflected by the sample. At an angle close to this critical one, and for multilayer samples, some interference events occur with the collimated X-ray beam causing reflectivity. The reflectivity phenomenon is based on the fact that two flat layers with different electron density reflect the

electromagnetic radiation in a different way. When the X-rays are reflected by both layers an interference pattern occurs, and if the intensity of the reflected beam is measured in function of the angle, an oscillating signal is produced.

By analysing the waves of the oscillating signal from reflectivity, information about the density, the thickness and the roughness of the analysed layer can be extracted. One of the characteristics that is needed to perform reflectivity measurements is a thin and flat sample (less than 200 nm approx.), because with thicker samples, the oscillating signal by the reflectivity has a small period that cannot be resolved by the detection system (not enough resolution).

In this case, the reflectivity pattern cannot be perceived, probably due to the inhomogeneity and the big roughness of the sample. Instead of this, the oscillating signal detected at the (0 0 1) YBCO Bragg peak of the sample generated by a phenomenon similar to the one mentioned above was studied. The periodicity of the signal is related to the thickness of the layer (epitaxial part only): higher frequency, thicker layer and conversely lower frequency oscillation, thinner layer. The relation that relates these two parameters is the following:

$$t = \frac{\lambda}{2 \cdot \Delta\theta \cdot cos\theta} \tag{10.1}$$

where t is the thickness of the layer, λ the wavelength of the radiation incidence, $\Delta\theta$ is the variation between two maximum (or minimum) of two contiguous oscillations, and θ is the average incident angle of the oscillation.

The thickness measured in this case corresponds only to the epitaxial part of the layer, contrarily to reflectivity measurements, where the full thickness of the layer (epitaxial and non-epitaxial part) can be deduced. Figure 10.1 shows the results for the first Bragg peak of the (001) YBCO plane.

By applying the equation 10.1 it is possible to estimate the thickness of the layer, that is expected to be found around 200 nm. Effectively, the value gather is 196±6 nm, indicating complementarily that the layer has a low roughness.

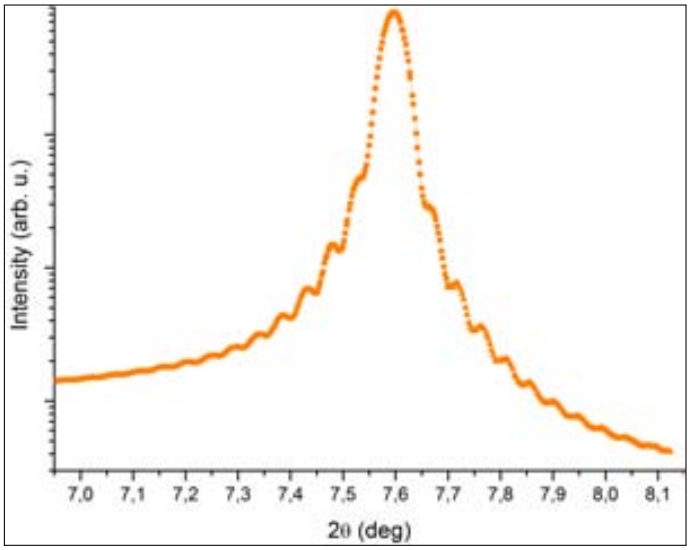

Figure 10.1: Thickness oscillations of YBCO standard.

10.2.2 Phase composition

To check the phases present and impurities (if any) of the generated YBCO layers, the diffraction pattern for the sample in both configurations, in and out of plane has been studied.

Figure 10.2 shows the diffraction patterns of the YBCO standard superconducting layer. In the 10.2(a) diffractogram, the out of plane oriented planes (0 0 l) can be observed, as expected for the epitaxial growth of the YBCO. By its part, in the 10.2(b) in plane diffraction pattern, both, the (h 0 0) and (0 k 0) Bragg planes from the YBCO crystal cell can be observed without azimuthal rotation of the sample, indicating that the orthorhombic YBCO grows without variation between the a and b directions. Previous studies have been demonstrated, for the case of the $SrTiO_3$ as substrate, that the YBCO grows also with a twined orientation. The reason has been justified by the tetragonal distortion of the neighbour terraces of the $SrTiO_3$.[3] This crystal twinning, confirmed by multiple rocking scans analyses, has been found for all the (nanocomposite) YBCO superconducting layers analysed.

Parallel to this, the LAO cubic cell can be also studied observing their correspondent Bragg peaks, assigned to the (0 0 1), (0 0 2) and (0 0 3) planes. The fact that for in plane measurements the substrate signal was low is due to the grazing incidence configuration used, illuminating a larger region of the sample surface, reducing the

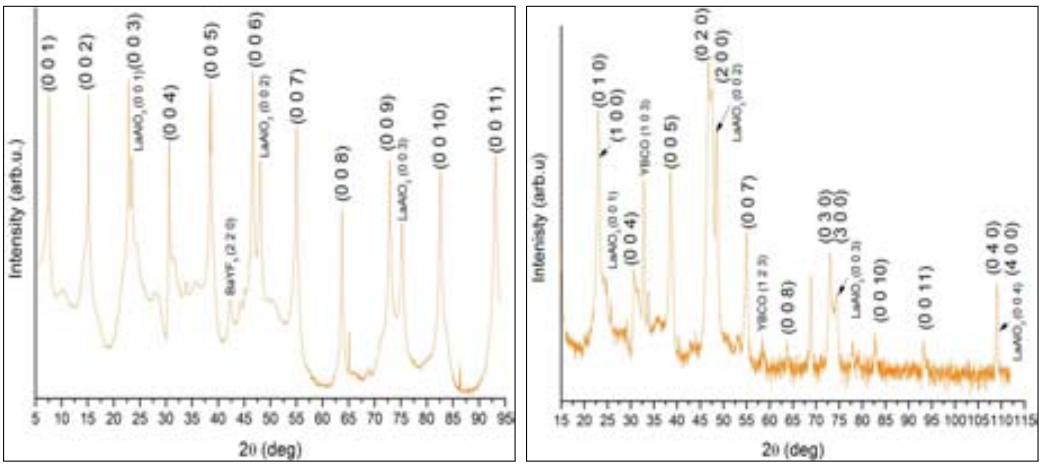

(a) Out of plane

(b) In plane

Figure 10.2: Synchrotron XRD for the YBCO standard sample: (a) out of plane and (b) in plane diffractogram. Note the decay in intensity of the in plane diffractogram due to the misalignment of the sample with respect to the calibrated substrate.

beam penetration in the sample, and then, giving a lower intensity of the LAO signal in the in plane diffractogram 10.2(b).

10.2.3 Rocking scans

Once the (h 0 0) and (0 k 0) peaks have been identified in the in plane measurement, now it is interesting to study their distribution by realising rocking scans, which is to maintain the δ position constant and turn the sample to know how h and k planes are oriented (φ scans). In turn, figure 10.3 shows the differences between the out of plane and in plane configuration, explaining the angles and directions in the reciprocal space.

Rocking scan configuration uses two angles φ and δ. In the first place, the rocking scan methodology consists of doing a δ/φ scan to found a Bragg peak and then, affix the detector (angle δ) in the angle which correspond to the maximum of the peak. Below, the rocking scan starts rotating only the angle φ in order to detect if the plane that has been found with the δ/φ measurement is oriented in other in plane direction. For example, for a single crystal orthorhombic structure, it is expected to recognise only two signals separated by 180^o, while for a cubic crystal cell, the signal

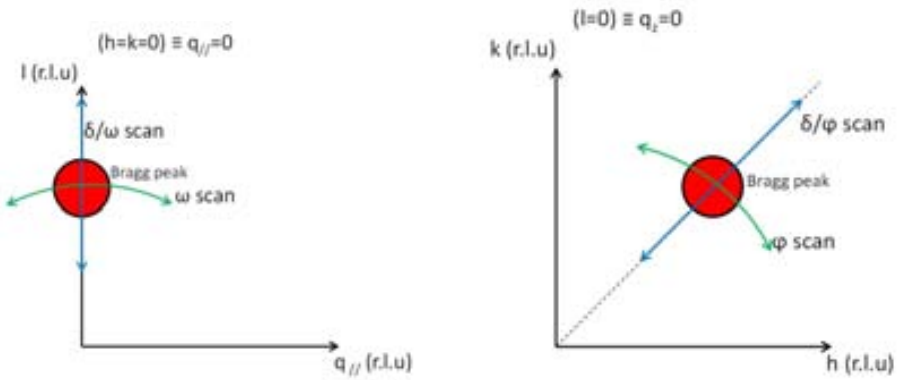

(a) Rocking scan out of plane (b) Rocking scan in plane

Figure 10.3: View in the reciprocal space in reciprocal lattice units (r.l.u) the measurements directions for out of plane (a) and in plane (b).

is repeated each 90^o due to the cell symmetry.

When the in plane Bragg peaks of the standard YBCO are analysed to found the (h 0 0) and (0 k 0) orientations, the signal is repeated (or split) in less than 1^o, indicating two preferential crystal grow directions with equal distribution. Figure 10.4 shows an example of the rocking scans for the reference YBCO sample.

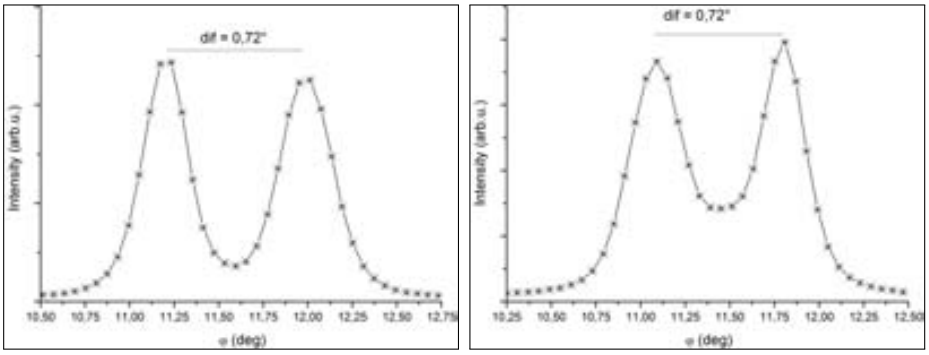

(a) Plane (1 0 0) (b) Plane (0 1 0)

Figure 10.4: Rocking scans of (1 0 0) (a) & (0 1 0) (b) planes of the standard YBCO.

This splitting, which has been found in all the samples except for the YBCO-Ba_2YTaO_6 specimen, is comprised between 0.7 - 0.8^o, which is a low distortion for the continuity of the YBCO single crystal. The presence of this aperture in two preferred orientation does not have imply an influence in the superconducting

capabilities, but it would be interesting to study it and determine their origin.

With the aim of understanding better this splitting of the peaks, a map of the reciprocal space region of the plane (4 0 0) and (0 4 0) of the sample YBCO-BZO was carried out. This representation is made by scanning (over a grid/mesh) the azimuth angle φ in function of the detector angle δ. The conversion to reciprocal space to the real one is done using the transformation of the equation 10.2.

$$\begin{pmatrix} q_x \\ q_y \\ q_z \end{pmatrix} = \frac{2\pi}{\lambda} \begin{pmatrix} cos\alpha_f cos\delta - cos\alpha_i cos\varphi \\ cos\alpha_f sin\delta - cos\alpha_i sin\varphi \\ sin\alpha_f + sin\alpha_f \end{pmatrix} \tag{10.2}$$

where α_i and α_i are the incident and reflected angle of the beam (in this case equal to 0.3^o for grazing incidence and approximate to 0^o). This yields immediately to $q_z \approx 0$ (as expected for an in plane measurement).

Finally, to settle the q_x and q_y axes in reciprocal lattice units (r.l.u.):

$$h(r.l.u.) = \frac{q_x}{\frac{2\pi}{a}} \quad \& \quad k(r.l.u.) = \frac{q_y}{\frac{2\pi}{b}} \tag{10.3}$$

being a and b the lattice parameters of the cell.

After applying these corrections, the following figure 10.5 is generated.

As it can be seen, the figure is centred around the k=4, meaning the plane (0 4 0) of the YBCO, being the other two signals at k=4.07 the Bragg peaks corresponding to the YBCO tetragonal distortion of the (4 0 0) plane. At the top of the figure, the intenser Bragg peak of the LAO can be observed.

When a in plane δ/φ measurement is performed, the scan pass trough h=0, (because the layer is centred with the LAO crystal), and the signal obtained for the YBCO planes are two local maximum (centre of the two peaks) and not the two real maximum for each Bragg plane. For this reason, when in plane measurements are performed, and if the sample is aligned with the LAO crystal parameters, a decay in the intensity at higher angles occurs, because the distance of the Bragg planes in the reciprocal space increase making that at h=0 r.l.u. the signal was lower.

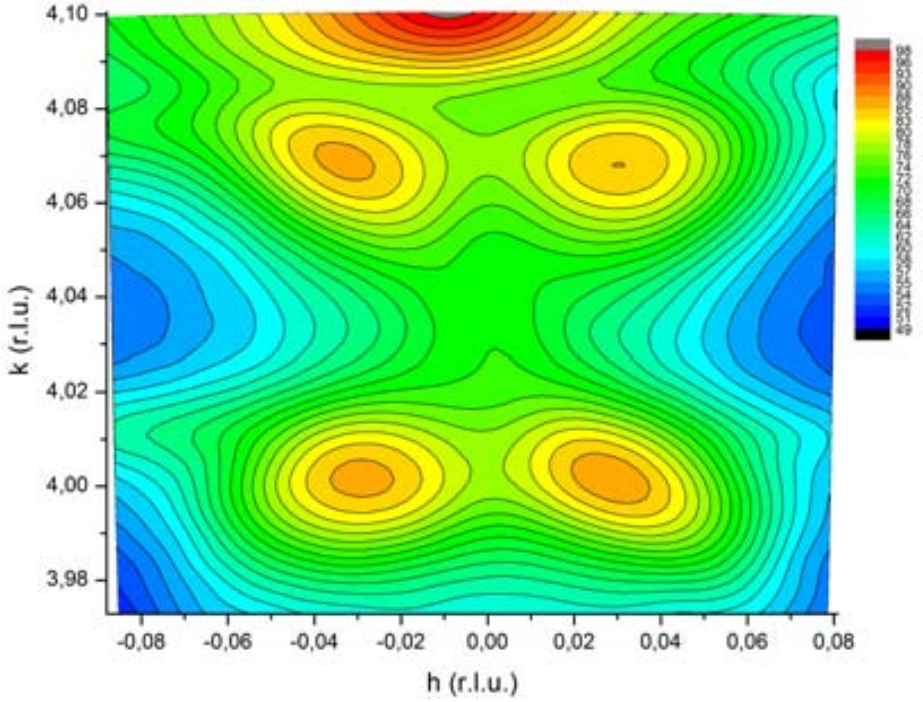

Figure 10.5: Map of the (4 0 0) and (0 4 0) planes in the reciprocal space. r.l.u = reciprocal lattice units. Consider $q_z \approx 0$.

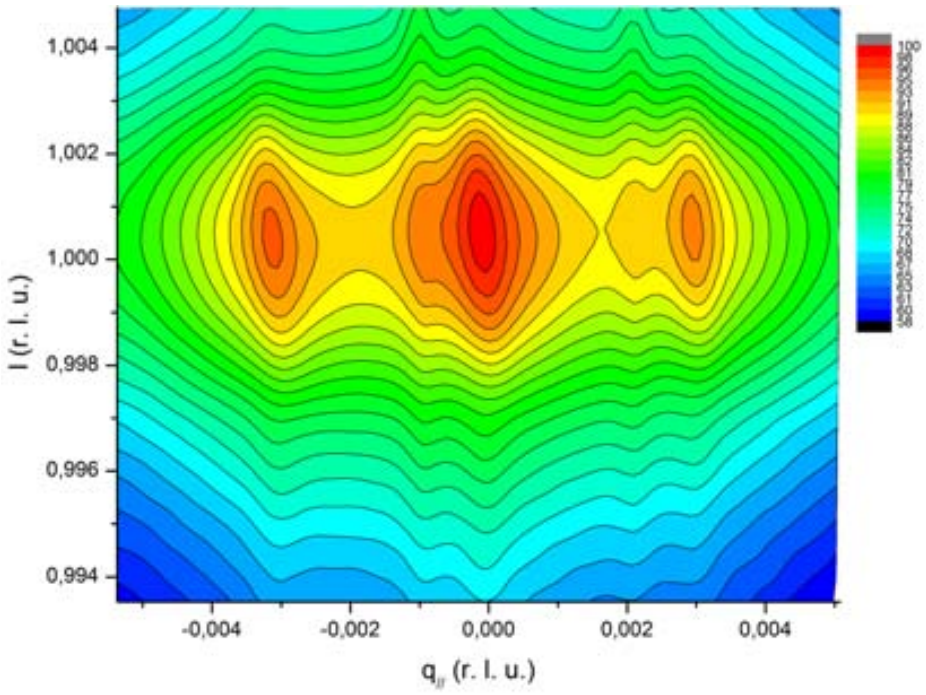

Figure 10.6: Map of (0 0 1) region YBCO-$MnFe_2O_4$ plane in the reciprocal space. r.l.u = reciprocal lattice units.

By its part, for out of plane planes, no splitting has been detected, but it occurs that for the YBCO-$MnFe_2O_4$ sample, generated by ink-jet printing, a disposition of the (0 0 l) planes as a elongated trunked pyramid was found (figure 10.6).

The observed form can be due to the ink-jet printing methodology, where several strips in the same direction are formed drop by drop on the LAO substrate. After this pattern draw, the layer is thermally treated to grow the YBCO. During this step, the drops of the chemical solution fusion, giving an homogeneous layer, but following this result, some signals of the strips still remains. To check this, a turn of 90^o in the azimuth angle was performed and measured, now across the strips, finding the inverse pattern. As conclusion, the presence of strips deposited when the pattern is draw influences in the final structure.

10.2.4 Microstrain

In this section, the methodology to deduce the microstrain of the YBCO crystal structure is explained. First of all, an analysis of the main peaks of the YBCO for the in and out of plane measurements are needed, because the Williamson-Hall (W-H) plot (equation 10.4) require it to perform the microstrain calculations.[4]

$$\beta \cdot cos\theta = \frac{\lambda}{D_v} + 4\varepsilon \cdot sin\theta \tag{10.4}$$

with β being the integral Breadth (area/height), λ the wavelength, D_v the thickness of crystal coherence length, θ the angle of incidence where the diffraction is detected and ε the microstrain.

From the W-H plot the crystal length coherence and the microstrain of the YBCO can be determined. Figure 10.7 shows the representation of the W-H plot for out of plane measurements, where the (0 0 l) planes of the YBCO are analysed.

With the linear fitting of the points coming from the (0 0 l) Bragg peaks of the YBCO, it is possible to deduce a thickness of the layer of 196 nm (exactly that one through via the thickness oscillations) and a microstrain of 0.067 % in the c axis of the superconducting thin layer. It is important to note that even if the error bar is big, it is smaller than the given one by the laboratory equipment. In laboratory

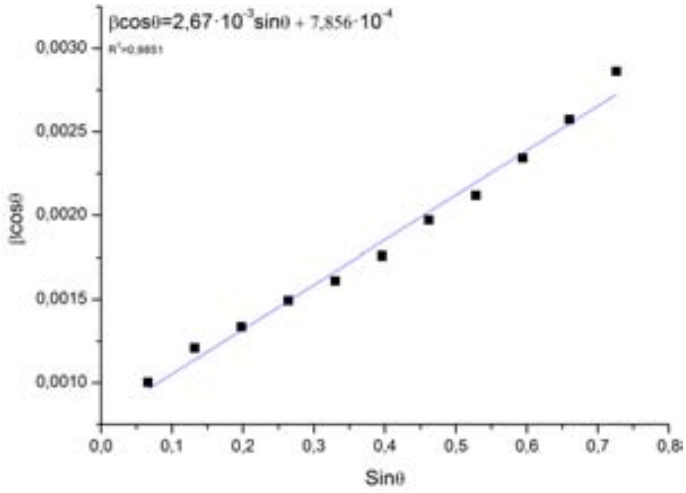

Figure 10.7: Out of plane Williamson-Hall Plot of a standard YBCO layer.

XRD, only 4 peaks can be used as maximum to compute the microstrain, because the resolution and the photon flux are not enough to observe so many peaks.

Knowing that it exists an splitting in the in plane planes, it is necessary to know a microstrain for each twinned crystal, and as consequence two data for the two h and k family planes will be measured. Then, microstrain for the h (and k) planes which correspond to the right-twinned crystal, and other for the left-twinned crystal, will be assigned.

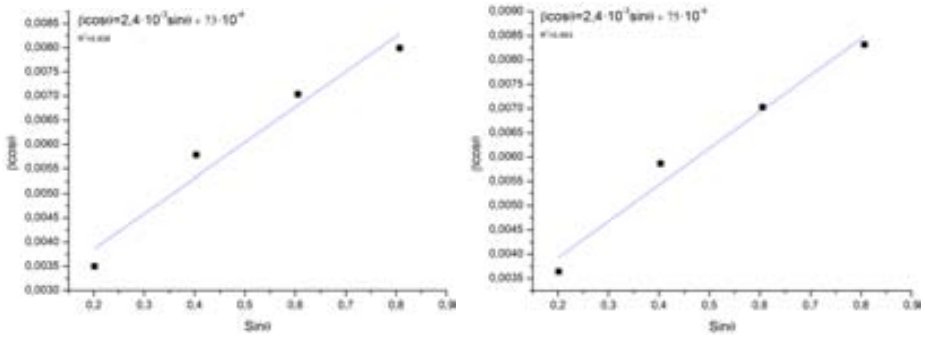

(a) L - h planes

(b) R - h planes

Figure 10.8: Microstrain of the h planes for the two twinned crystals: the left (a) and the right one (b).

Through these W-H plot (figure 10.8), a microstrain of 0.06 % established for both crystal directions in the planes (h 0 0). The following figure, 10.9 is the result for the (0 k 0) planes.

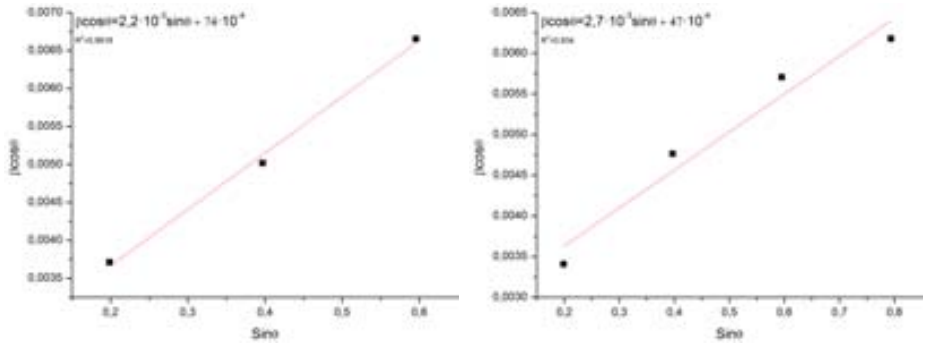

(a) L - k planes (b) R - k planes

Figure 10.9: Microstrain of the k planes for the two twinned crystals: the left (a) and the right one (b).

Now, the revealed microstrain for the (0 k 0) planes is 0.07 % for the right twinned crystal and 0.06 % for the left one.

After analyse all the microstrain for the YBCO reference sample, it is possible to conclude that the strain is isotopic for the three crystallographic directions with a value approximate of 0.06 %.

10.3 $YBa_2Cu_3O_{7-\delta}$ nanocomposites

Once the analytical methodology has been defined for the case of the standard YBCO, now the nanocomposite superconducting layers are going to be studied. Two SC layers generated via *in-situ* process with $BaZrO_3$ and Ba_2YTaO_6 NPs embedded, and two more produced by *ex-situ* spin coating and ink-jet printing with $BaCeO_3$ and $MnFe_2O_4$ NPs respectively are evaluated.

10.3.1 Phase purity

To study the purity of the YBCO layers studied, and to probe the presence of the nanoparticles phase inside the YBCO thin layers, out of plane XRD and in plane GIXRD have been performed. These measurements allows to identify the Bragg peaks of the compounds forming the specimen. The following figures 10.10 and 10.11 shows the diffraction patterns for out of plane and in plane configuration respectively.

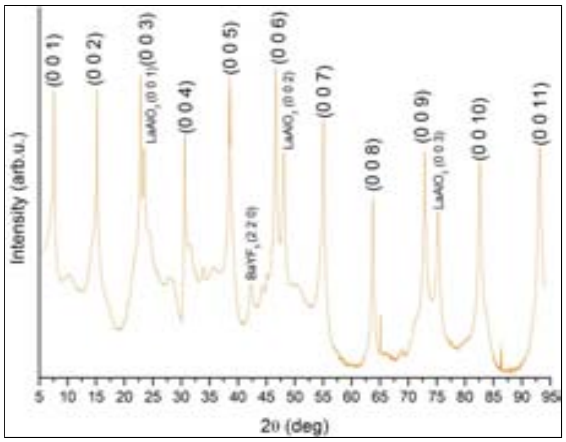

(a) YBCO standard

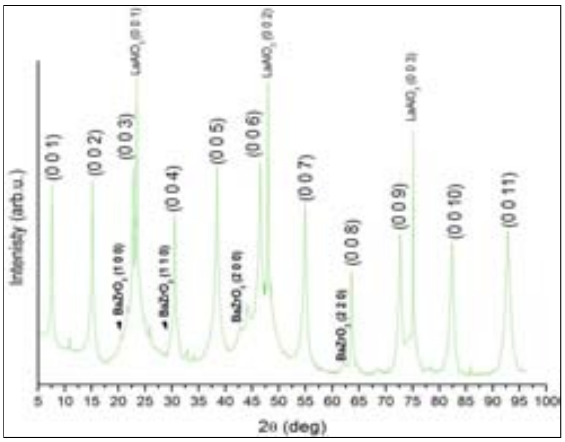

(b) YBCO $BaZrO_3$

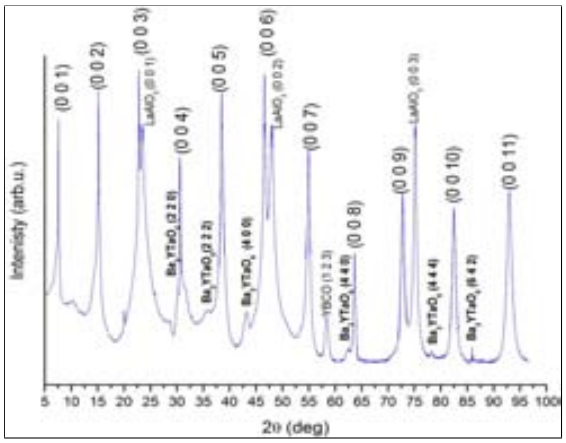

(c) YBCO Ba_2YTaO_6

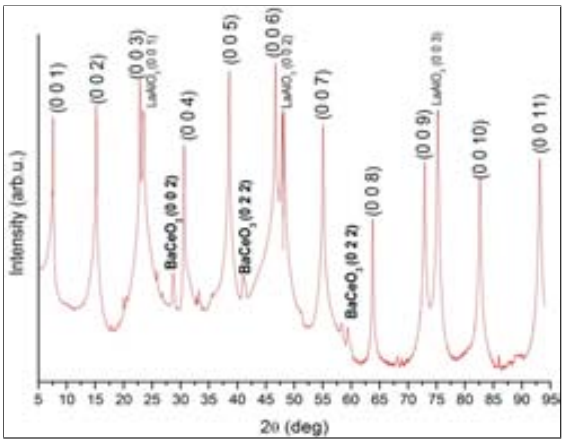

(d) YBCO $BaCeO_3$

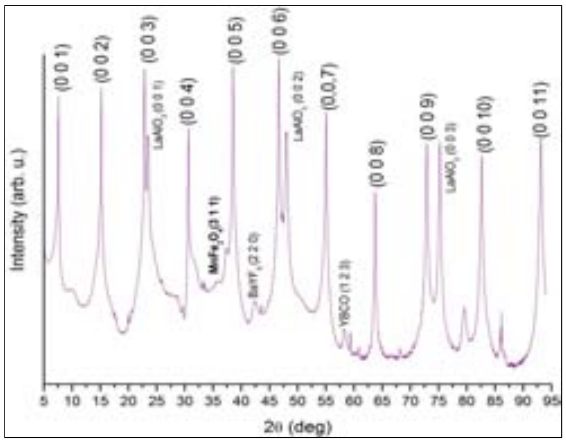

(e) YBCO $MnFe_2O_4$

Figure 10.10: Out of plane diffraction patterns for the different nanocomposite YBCO superconducting layers with NPs embedded

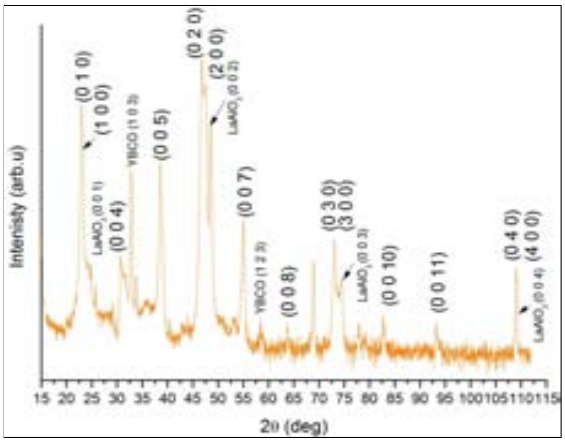

(a) YBCO standard

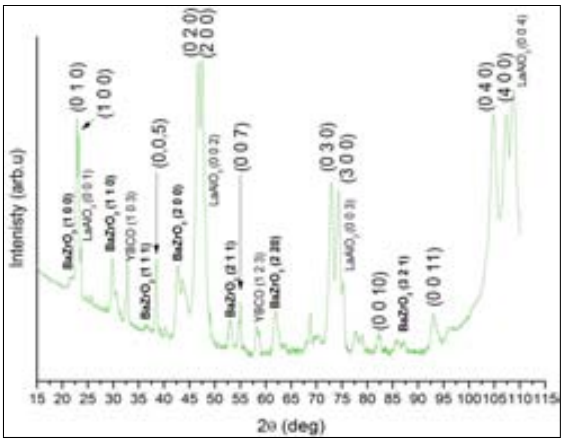

(b) YBCO $BaZrO_3$

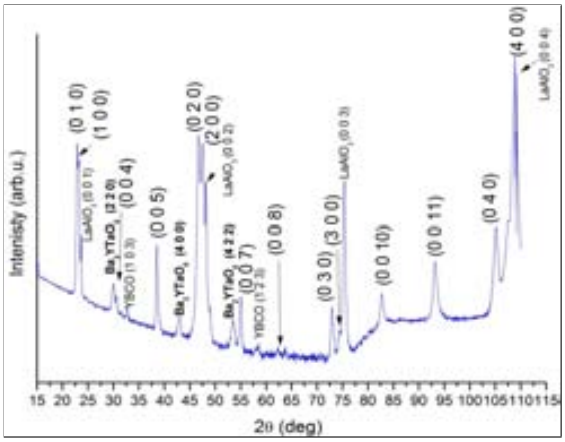

(c) YBCO Ba_2YTaO_6

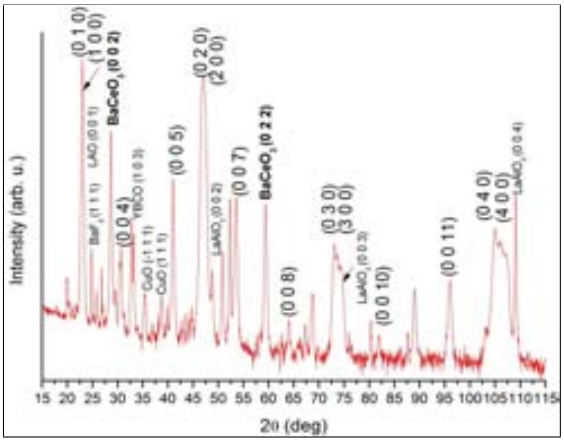

(d) YBCO $BaCeO_3$

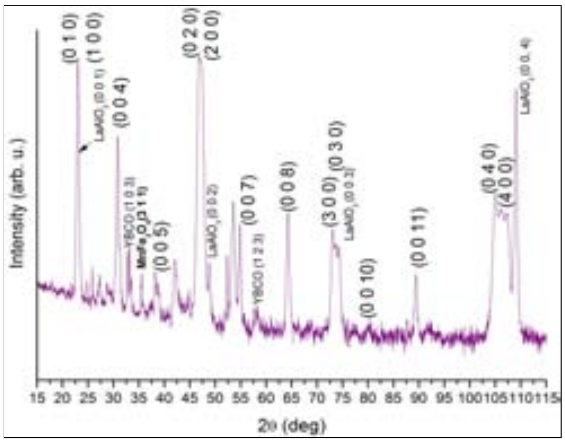

(e) YBCO $MnFe_2O_4$

Figure 10.11: In plane diffraction patterns for the different nanocomposite YBCO superconducting layers with NPs embedded

Out of plane diffraction patterns (fig. 10.10) confirm the (0 0 l) planes of the YBCO (as expected for a epitaxial growth), jointly with some secondary YBCO planes for the disoriented YBCO. In the case of the nanocomposite SC samples, some peaks identifying the phase of the nanoparticles, can be assigned. Complementarily, some extra peaks which correspond with undesired compounds (CuO, $Y_2Cu_3O_5$ ...) appear.

By its part,the in plane GIXRD diffractograms (fig. 10.11) show the (h 0 0) and (0 k 0) planes jointly, because of the orthorhombicity of the YBCO. In addition, some (0 0 l) planes are present coming from the YBCO that has grown with the c axis parallel to the LAO surface. In the case of the nanocomposite samples, the corresponding structure can be identified via the Bragg diffraction planes. Then, the existence of $BaZrO_3$, Ba_2YTaO_6, $BaCeO_3$ & $MnFe_2O_4$ nanoparticles inside the YBCO can be proved.

Several secondary peaks (apart from the expected one for the nanoparticles) can be found, and are byproducts of the YBCO generation and growth. These compounds are more easily identified in the in plane diffraction pattern because there are less intenser Bragg peaks with which they could be overlap.

With the diffraction patterns it is possible to determine the cell parameters of the YBCO and the LAO substrate of the studied samples, and make a comparison between them. The next table 10.2 contains the results obtained.

Cell parameters

	YBCO std	YBCO $BaZrO_3$	YBCO Ba_2YTaO_6	YBCO $MnFe_2O_4$	YBCO $BaCeO_3$
YBCO a	3.819	3.824	3.826	3.822	3.825
YBCO b	3.880	3.887	3.887	3.882	3.887
YBCO c	11.665	11.692	11.682	11.659	11.659
LAO	3.785	3.788	3.784	3.785	3.781

Table 10.2: Cell parameters calculated through diffraction patterns of the YBCO orthorhombic cell and the LAO cubic substrate.

Data prove the similar cell parameters for all the cases when consider the error bar of the measurement. Also, it can be checked again the similar cell parameters

for the LAO with the a and b axis of the YBCO, generating in the final structure, a 90^o twin of the YBCO cell, because both axis match with the LAO cell.

10.3.2 Microstrain

Following the same W-H plot used for the YBCO standard, here the results for the four nanocomposite superconducting layers are presented in the figure 10.12.

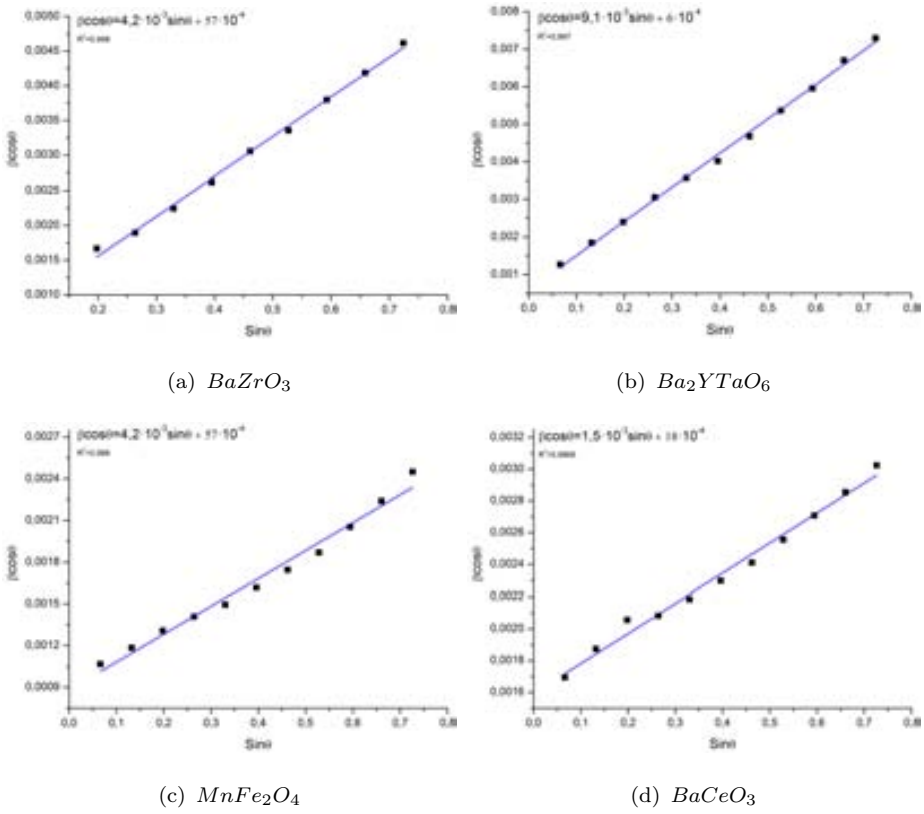

Figure 10.12: Microstrain out of plane for the different nanocomposite YBCO layers modified by *in-situ* (a) & (b) and *ex-situ* (c) & (d) methodologies.

It can be observed the good regression value of the straight line, confirming the good quality of the measurements. Only in the case of the BZO, the data correspondent to the two first planes had to be avoided. Therefore, the following table 10.3 resuming the microstrain for the crystallographic directions can be completed.

By analysing the table, some conclusions are extracted:

1. Thickness: The thickness of the layers are the expected one (arround 200

Calculated microstrain						
	l planes		microstrain h planes (%)		microstrain k planes (%)	
Layer	Thickness (nm)	Out microstain (%)	left	right	left	right
Std.	196	0.06	0.06	0.06	0.06	0.07
$BaZrO_3$	232	0.13	0.29	0.35	0.24	0.26
Ba_2YTaO_6	270	0.23	0.21		0.24	
$MnFe_2O_4$	175	0.05	0.09	0.09	0.07	0.07
$BaCeO_3$	102	0.05	0.15	0.16	0.08	0.06

Table 10.3: Data assess trough the Williamson-Hall plot to calculate the microstrain of the three crystallographic h, k, l planes. The BYTO crystal does not present the two twinned direction.

nm), and is bigger for the Std., BZO and BYTO than for the $MnFe_2O_4$ and $BaCeO_3$ due to the initial concentration of the chemical solution precursors. For *ex-situ* generated thin layers, the initial precursor solution has been diluted to the half (0.75 M in sum of metals), doing layers with 100 nm of thickness. It occurs that for the $MnFe_2O_4$-$YBa_2Cu_3O_{7-\delta}$ layer generation, the thickness could be corrected by the drop concentration on the substrate, because for a solution with the half of precursors, the double of drops should be deposited. With this correction, it has been possible to produce a layer with a thickness comparable with the standard samples.

2. Microstrain: The transport current capabilities of the manufactured layers seems to be directly related with a higher isotropic strain without be remarkable the strain degree. Higher isotropic microstrain correspond to the higher J_c, while for more anisotropic microstrain worse current transport efficiency.

10.3.3 $MnFe_2O_4$ in $YBa_2Cu_3O_{7-\delta}$ identification

In the case of the YBCO-$MnFe_2O_4$ sample, it is interesting to confirm that the spinel structure still exists inside the YBCO after the preparation procedure, because since this point, with the measurements done with laboratory common techniques (section 4.3), no direct proof of the nanoparticles along the layer had been carried

out.

It is known that the main Bragg peak of the spinel is at 35.5^o for radiation with 1.54 Å of wavelength, but at this same angle appears also a main peak of the CuO, together with other at 38.7^o. The fact is that doing a search of the spinel, it is not possible to assign correctly if the signal correspond to the $MnFe_2O_4$ or to the CuO phase. In order to discern between these two possible cases, first of all a δ/φ scan looking for the Bragg peak at 35.5^o has been done. Then through rocking scans (section 10.2.3) the orientation of (until now) unknown phase is analysed. Next, the same rocking scan at 38.7^o (CuO secondary Bragg peak) was realised.

Through this diffraction measurements is is possible to found if the spinel phase (which correspond to $MnFe_2O_4$) is in the sample. If the two rocking scans demonstrate exactly the same plane orientation, then the unknown phase is CuO, while if the orientations are not equal, it means that there are two phases in the YBCO matrix: CuO and $MnFe_2O_4$. The following figures 10.13 and 10.14 show the diffractograms for this study.

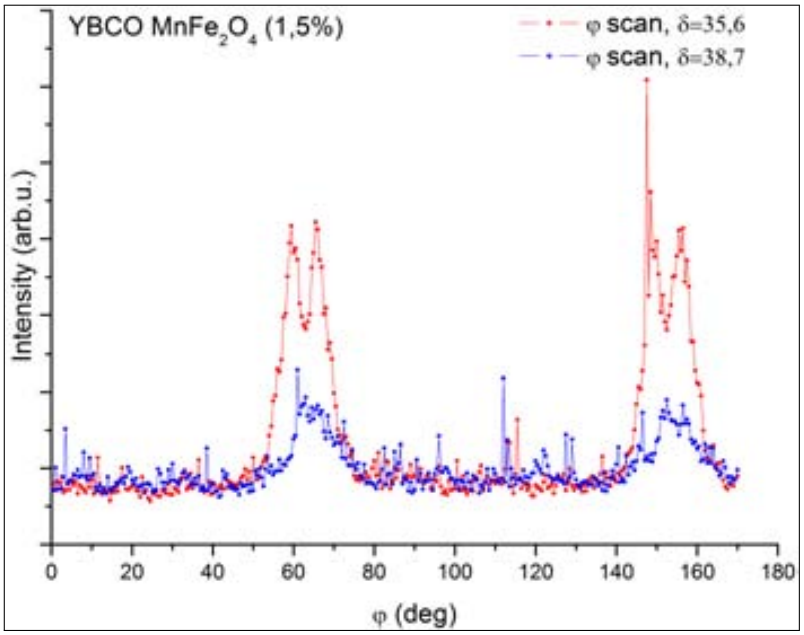

Figure 10.13: Rocking scan of at the two angles where the spinel and CuO can be found. The difference between them indicates the existence of the spinel structure. As expected for a cubic structure, the peaks signal is repeated each 90^o.

Then, the spinel structure coming from the $MnFe_2O_4$ inside the $YBa_2Cu_3O_{7-\delta}$

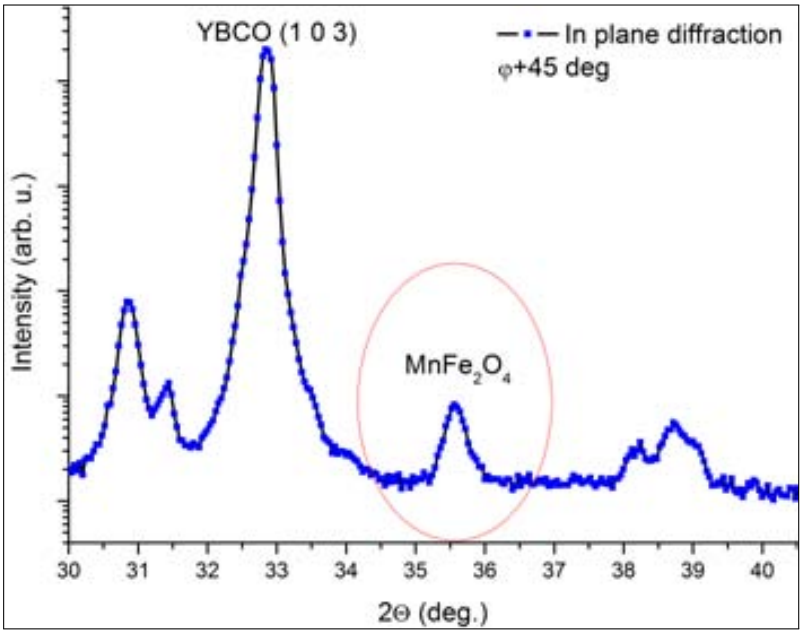

Figure 10.14: Evidence of the Bragg plane of the spinel structure of the $MnFe_2O_4$ oriented in a minimum of the CuO. The diffraction pattern was taken by orientating the sample respect to the $MnFe_2O_4$ maximum ($\varphi = 45^o$).

has been proved.

Complementary data concerning the preferred orientation of the nanoparticles can be analysed. Knowing that the peak contribution correspond only to the fraction of nanoparticles oriented in this direction, it is possible to know the percentage of nanoparticles which have this analysed plane orientation. The procedure consists of finding out the relation between the peak area (oriented nanoparticles) after subtracting the area which corresponds to the CuO contribution in this angle, and the background area (contribution of the random nanoparticles) extrapolating for a complete 360^o rocking scan. Realising this procedure, a 70 % of random disposition of the nanoparticles, being the 30 % remain with a preferred orientation. In addition, as it can be observed in the figure 10.13, the $MnFe_2O_4$ oriented nanoparticles have two preferential orientations with an splitting of 10^o.

10.3.4 Nanoparticles crystal size

Crystal size of the nanoparticles can be deduced through the diffraction patterns by applying the Scherrer formula (equation 3.1):

Size of NPs		
Nanoparticle	size (nm)	Original size (nm)
$BaZrO_3$	11.3	-
Ba_2YTaO_6	13.7	-
$MnFe_2O_4$	*	7.5
$BaCeO_3$	37.5	2.6

Table 10.4: Crystal size of the nanoparticles embedded inside the YBCO layer. $BaZrO_3$ and Ba_2YTaO_6 NPs are generated *in-situ*, an there is not an original size.

The crystal size (table 10.4) of NPs is bigger than the desired one (below 10 nm). $BaZrO_3$ and Ba_2YTaO_6 NPs are generated *in-situ*, and the liming factor to growth is the local absence of the chemical precursors. By its part, the $MnFe_2O_4$ and $BaCeO_3$ NPs size show a sintering process during the YBCO layer generation. During the high temperature needed for the $YBa_2Cu_3O_{7-\delta}$ growth, the NPs can coalesce and sinterise in larger nanoparticles. This undesirable phenomenon is unavoidable in the reaction conditions applied, due to the high temperatures required and long times used, which make easier the atomic mobility.

For the case of $MnFe_2O_4$ NPs, even HR-TEM demonstrates the increase in size of the NPs, the exact value can not be reckoned with the Scherrer formula due to the main peak of the spinel at 35.5^o is overlapped with the CuO, and both contributions cannot be separated to calculate the FWHM of the peak which corresponds to the $MnFe_2O_4$ nanoparticles.

10.3.5 Nanoparticles and $YBa_2Cu_3O_{7-\delta}$ orientation

i $YBa_2Cu_3O_{7-\delta}$ AB planes

The first study was performed with the YBCO which grows with the c axis of the YBCO parallel to the LAO surface (YBCO with planes ab or YBCO-AB) found in the YBCO-BYTO nanocomposite. The orientation of the plane (0 0 5) in the grazing incidence (in plane) was studied, because this peak is clearly identified. Thus, it is deduced that the YBCO-AB grows in only four preferred orientations (figure 10.15) in order to maximise the mismatching between the YBCO and LAO crystal cell.

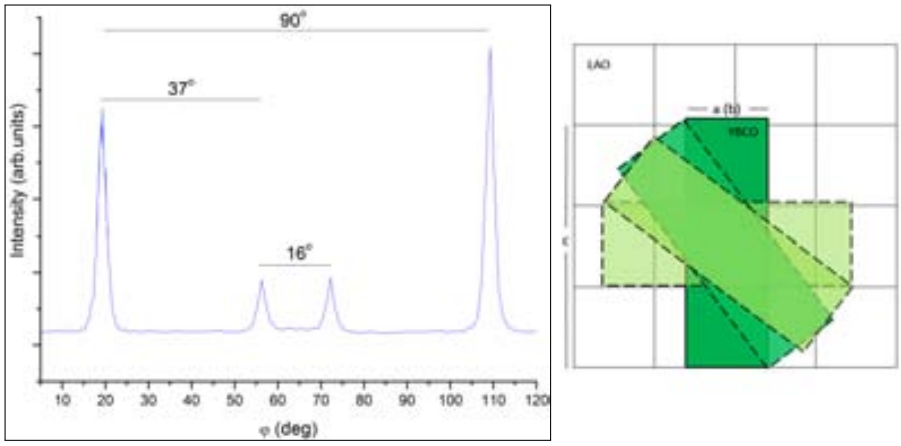

(a) scan (b) Orientations

Figure 10.15: λ scan of the plane (0 0 5) (a) of the YBCO-AB, which has grown parallel to the surface and their schematic representation (b).

Studying now the in plane a and b planes of the YBCO (now in the YBCO-BZO sample), it can be observed how these planes grow in two determined orientations separated by 90^o (10.16).

This means that the (2 0 0) plane grows on the LAO with two perpendicular directions, as expected from the 4-fold symmetry of the substrate. As it has been explained before, the YBCO grows with a orthorombic direction, and being the two intensities similar for the (h 0 0) and (0 k 0) planes, it can be deduced that there is no preference for any of the two possible orientations of the crystal cell. In fact, for a square (cubic) lattice, these 2 directions at 90^o are indistinguishable.

Via the two examples shown here, and other crystallographic planes studied, it can be prove the epitaxial growth of the YBCO on the LAO substrate. The YBCO-AB, which is present in low quantity, have also a preference in their orientation when grow.

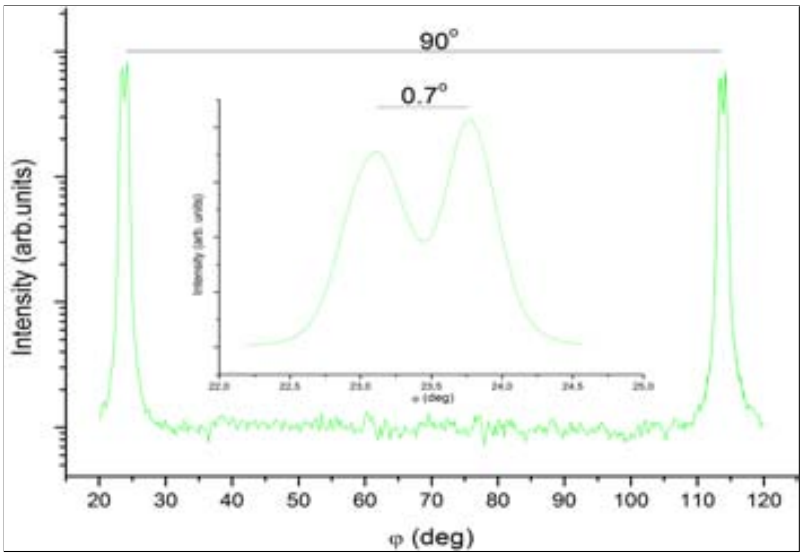

Figure 10.16: φ scan demonstrating the orientation of the a and b planes which grow on the LAO surface. The inset shows a zoom of the first peak, showing a double peak.

ii $BaZrO_3$ NPs

Now, the orientation of the BZO NPs was studied via the plane (1 1 0) in the YBCO-BZO nanocomposite.

In the figure 10.21 it can be clearly seen a preferential orientation of this plane at an angle φ of 45^o respect to the LAO crystal cell. Two other orientations (four peaks for a cubic symmetry) are also favoured. The determination of the oriented fraction respect to the random part (as in the case of $MnFe_2O_4$ case, 10.3.3), gives that around the 42 % of the BZO is oriented in any of these orientations, having the 58 % a random disposition.

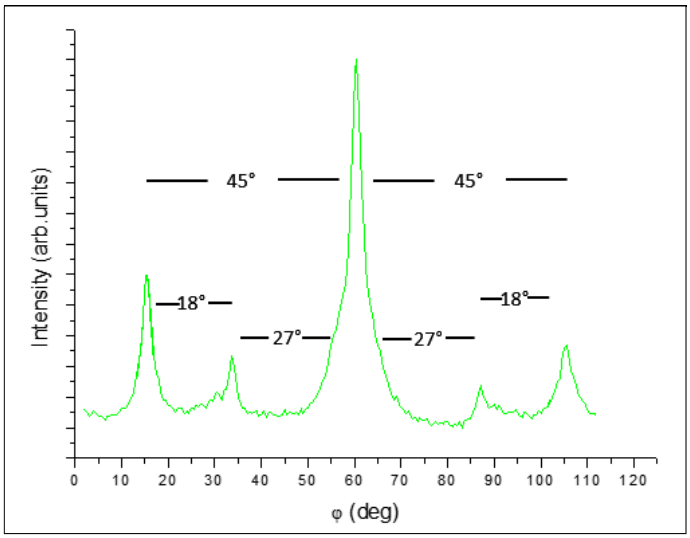

Figure 10.17: λ scan of the plane (1 1 0) of the BZO NPs.

iii Ba_2YTaO_6 NPs

In the case of the BYTO NPs in YBCO, their preferred orientations via pole gures has been studied. As explained in chapter 7, pole gures consist of x the detector in the maximum of a Bragg plane and move the sample in angular directions. Consequently, a three dimensional spectra can be represented, where each spot correspond to a preferred orientation 10.18).

In order to avoid the YBCO contribution for the pole gures, the same analyses were performed to the YBCO standard layer, and are represented in the gure 10.18 with the same colour scale.

For the plane (4 0 0), the favoured orientation is the epitaxial one (parallel to the LAO surface) but with one degree of misalignment in four directions (see gure 10.19 for a detailed view). In other words, the BYTO grows with one degree ($\lambda = 1^o$) between the plane (0 0 l) of the YBCO and the plane (4 0 0), and also in four direction (= 0, 90, 180 and 270^o), like 4 cubes. Other orientations can be found at $\lambda = 51^o$ and = 45^o, indicating other preferential crystal growth disposition of the Ba_2YTaO_6 nanoparticles.

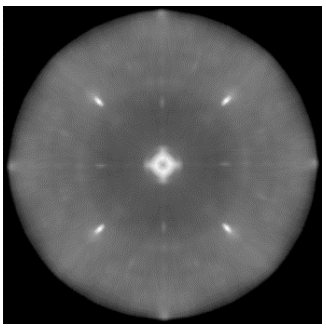

Figure 10.19: BYTO plane (4 0 0) pole gure

Finally, a plane orientation at λ=90^o, and repeated at

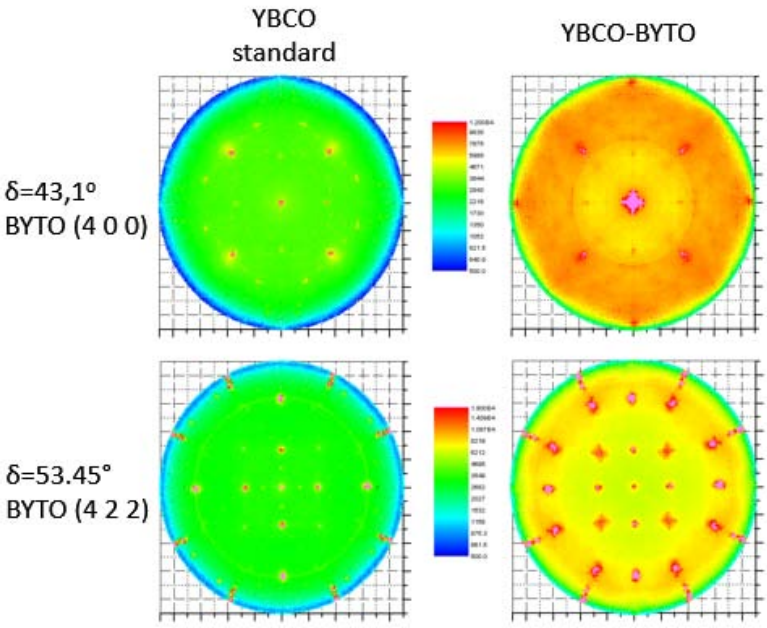

Figure 10.18: Pole gures of two planes of the BYTO (4 0 0) & (4 2 2) and the comparison with the same angle in a YBCO standard layer.

= 0, 90, 180 and 270^o can be observed, which is due to the family planes (4 0 0), that for a cubic cell is the same that (0 4 0) and (0 0 4) planes.

By its part, the plane (4 2 2) presents multiple preferred orientations related also between them for a cubic cell symmetry.

Concerning the percentage of random orientation, it can be concluded that the 33 % of the BYTO nanoparticles are disposed randomly inside the YBCO matrix, having the 66 % a favoured growth direction.

iv $MnFe_2O_4$ NPs

In this case, pro ting the λ scans performed to check the $MnFe_2O_4$ signal, the percentage of the random fraction has been obtained. For this case, two contributions have to be taken into account, the random part, and the contribution of the CuO to the main (3 1 1) Bragg peak of the ferrite (gure 10.13).

As a previous demonstrated result, for the 1.5 % of the externally synthesised ferrite magnetic nanoparticles embedded inside the YBCO, the 70 % is disposed

randomly. [a]

v $BaCeO_3$ NPs

The last sample to analyse the grain orientations was the $BaCeO_3$. In this case, the analyses through pole figures of the plane (1 1 0) (figure 10.20) at angle $\delta = 28.70^o$, and the plane (2 0 0) at angle $\delta = 41.05^o$ have been acquired.

The unexpected conclusion of this experiment makes the pole figures of these planes interesting to study due to the multiple growth directions of the $BaCeO_3$ embedded in the YBCO. The data emanated from pole figures (figure 10.20) give the multiple crystal favoured orientations for the $BaCeO_3$ NPs and their corresponding random orientation Debye-Scherrer rings. [b]

[a] Because the lack of measurement time, no plane orientation were measured for this sample.

[b] The calculus of the preferential orientations (and the complementary random part) has not been realised yet, because a long time crystallographic study is needed. The $BaCeO_3$ orientation study, and the other pole figures need a detailed study to interpret the crystal grow direction, research that is out of time of this thesis, and will be studied later.

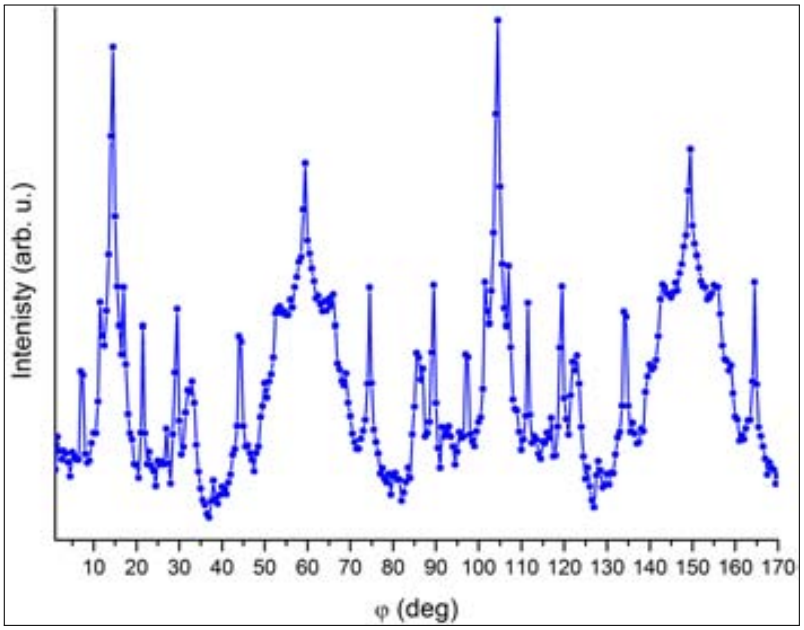

(a) Rocking Scan (1 1 0) =28.7^o

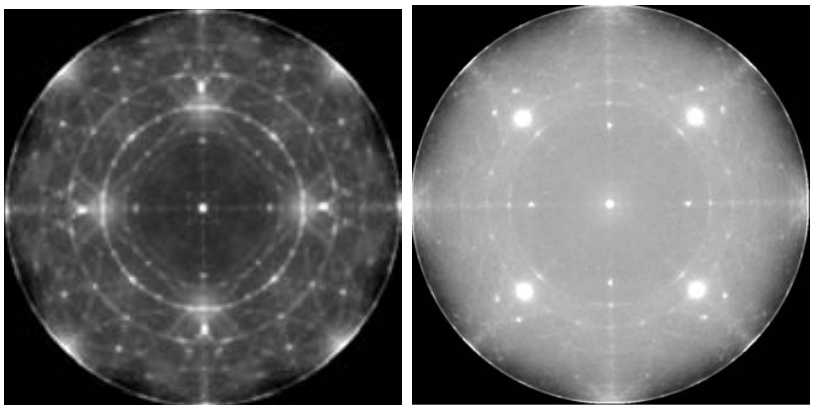

(b) (1 1 0) =28.7^o (c) (2 0 0) =41.05^o

Figure 10.20: $BaCeO_3$ NPs orientation: Plane (1 1 0) rocking scan (a) & pole gure (b) and (2 0 0) pole gure (c). The planes analysed indicates multiple preferred orientations of the $BaCeO_3$ nanocrystals.

10.4 $BaZrO_3$ nanotracks

$BaZrO_3$ nanotracks generated on a LAO single (0 0 1) crystal has been studied in order to verify their structure, composition and growth direction. The synthesis of these nanostructures is produced with the aim to modify the LAO substrate to fabricate *ex-situ* YBCO superconducting layer.

BZO nanotracks have been synthesised by electrospinning[5] with an epitaxial structure. After growth the BZO, several laboratory techniques were applied with the finality to verify the phase and growth of the fibers, but no clarify conclusions were obtained. These tracks have a size around 150 nm width and 10 nm height, measured by AFM (atomic force microscopy), and this is the main reason that common laboratory techniques do not identify this structure, because their low resolution. Figure 10.21 shows the TEM image of the nanofibers on LAO to study.

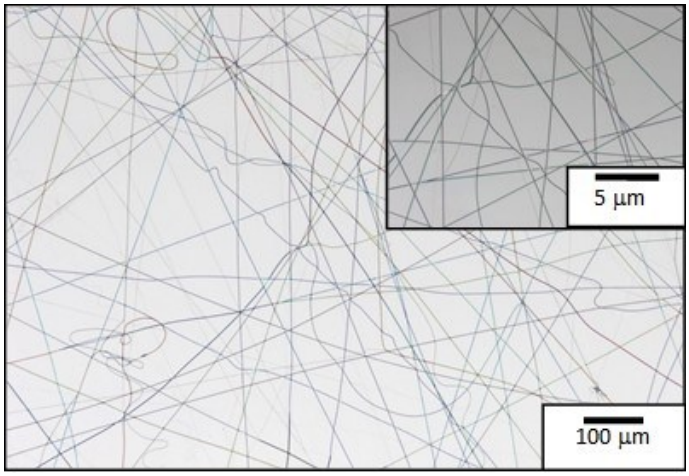

Figure 10.21: TEM image of BZO nanotracks generated by electrospinning.[5]

Synchrotron XRD with grazing incidence (GIXRD) has been applied to study these nanostructures on the LAO single crystal. GIXRD (δ/φ scan) is needed instead the Brag-Brentano configuration because the illuminated area is larger and the penetration deep is reduced to the minimum, avoiding the substrate signal (that in this case is clearly larger). But, in order to known the planes which have grown parallels to the LAO surface, an analysis with a δ/ω configuration has been performed.

GIXRD was done, and the Bragg peaks identified as $BaZrO_3$ structure, as it can

be seen in the following figure 10.22. The presence of non react precursors, which form the barium an zirconium oxides can be also detected with in a low quantity.

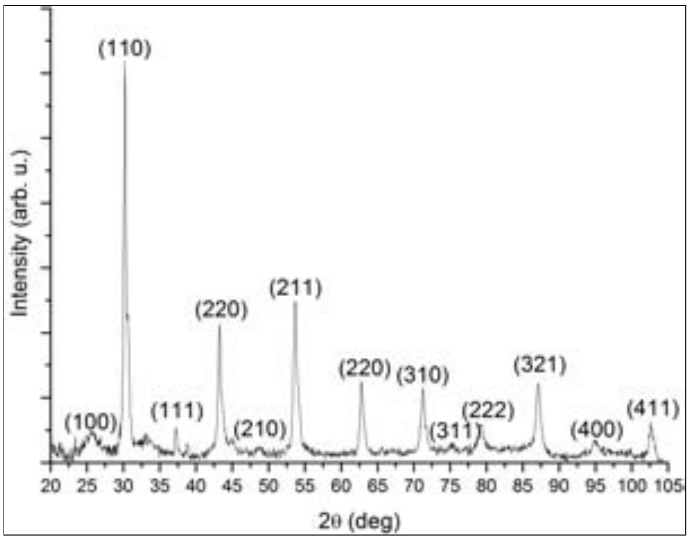

Figure 10.22: GIXRD of the BZO nanofibers. The Bragg diffraction peaks correspond clearly to the $BaZrO_3$ phase. Some peaks with low relative intensity can be identified, confirming the BaO and ZrO_2 as low quantity secondary phases.

After measure the GIXRD, out of plane geometry was disposed to measure the planes which grow epitaxially with the LAO surface. Results are presented in the figure 10.23.

The LAO Bragg planes are identified without doubt because they are more intense than those of the BZO which is due to the deeper penetration of the X-rays in this configuration. Anyway, two Bragg peaks can be identified from the BZO, the planes (200) and (220).

If these Bragg signals have been detected in this configuration, it indicates that both planes grow parallels to the LAO surface, in other words, they grow cube on cube respect to the LAO: BZO (200) & (220) // LAO (100). By analysing the (200) Bragg plane in a φ scan configuration (maintaining δ fixed) (figure 10.24), it is possible to study the percentage of epitaxial structure with the (200) plane parallel to the surface. This can be achieved by integrating the peak obtained and compared

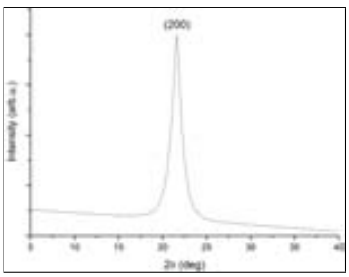

Figure 10.24: φ scan of the plane (200) of the BZO nanotraks.

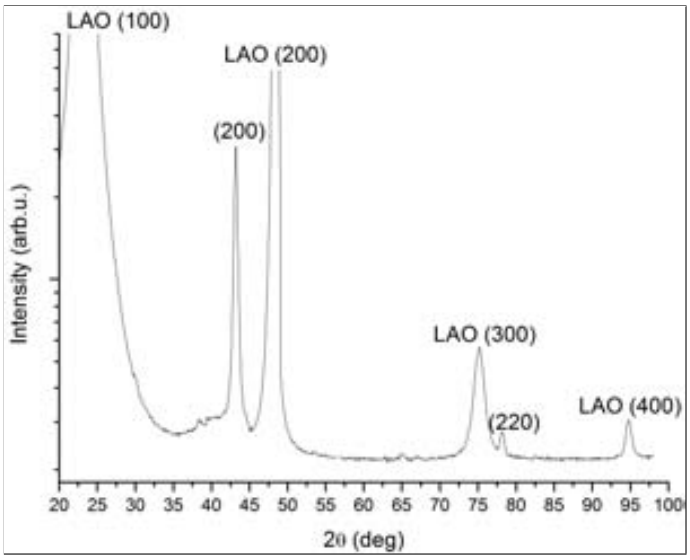

Figure 10.23: Out of plane XRD of the BZO nanofibers. The Bragg planes of the substract can be observed as a much larger intensity, but some (00l) peaks of the BZO are detected.

with the baseline (which is due to the not oriented (200)
planes). In such a way, the 15% of the BZO nanotracks growth with the plane (200) parallel to the surface.

Following the Scherrer formula (equation 3.1), the crystal domain size out of plane (height of the fibers) can be determined with a value of 17 nm. This data is in agreement with those deduced with the AFM, because the discrepancy between the values could come from the fact that with GIXRD more fibers have been measured, while AFM only measures a few of them.

As conclusion of this part, it has been demonstrated the high purity $BaZrO_3$ nanofibers generated via electrospinning on a $LaAlO_3$ single crystal. In addition their preferred epitaxial orientation has been studied, giving a 15 % of epitaxy with the plane (200). By its part, Scherrer formula confirm the height around 17 nm.

10.5 Chapter summary

XRD and GIXRD are powerful diffraction techniques which allows to study the structure, microstructure and orientations of the YBCO and the nanoparticles

embedded inside the SC layer. Results demonstrate the high phase quality of the standard and nanocomposite nanostructures, and allows to rely the microstructure with the superconducting capabilities.

In addition, the high sensitive technique demonstrates that the *ex-situ* methodology via ink-jet printing is possible to embed preformed nanoparticles (in this case $MnFe_2O_4$) inside the YBCO with the chemical solution deposition procedure.

Other *ex-situ* approaches, as the generation of BZO nanofibers on a LAO single crystal (where the YBCO will be grown), has been analysed to demonstrate the phase purity and orientation of the nanotracks.

Bibliography Chapter 10

[1] "Diffabs beamline at synchrotron soleil." `http://www.synchrotron-soleil.fr/Recherche/LignesLumiere/DIFFABS`. Access July, 2013. (cited on page(s) 155, 219)

[2] "Synchrotron soleil general web." `http://www.synchrotron-soleil.fr`. Access July, 2013. (cited on page(s) 155, 219)

[3] J. Brötz and H. Fuess, "Detwinning in $YBa_2Cu_3O_{7-\delta}$ films on vicinal $SrTiO_3$ (0 0 1) due to anisotropic strain at the interface," *Physica C: Superconductivity*, vol. 339, pp. 75–78, 2000. (cited on page(s) 222)

[4] G. K. Williamson and W. H. Hall, "X-ray line broadening from filed aluminium and wolfram," *Acta Metallurgica*, vol. 1, no. 1, pp. 22–31, 1953. (cited on page(s) 227)

[5] A. Calleja, S. Ricart, X. Granados, X. Palmer, E. Solano, J. A. Tornero, F. Cano, T. Puig, and X. Obradors, "Epitaxial $BaZrO_3$ tracks by electrospinning of metalorganic fibers on single crystals," *Crystal Engineering Communication*, vol. 14, no. 14, pp. 4686–4691, 2012. (cited on page(s) 244)

Chapter 11

Conclusions Part III

Large Scientific Facilities have been profited to perform complementary analyses to the magnetic ferrite nanoparticles and nanocomposite (*in-situ* & *ex-situ*) YBCO superconducting layers:

Rietveld refinement of the neutron powder diffraction measurements has been used to calculate different parameters of the crystal structure of the ferrite nanoparticles:

Results show how thermal and microwave route generate similar nanoparticles in composition and structure. A similar inversion degree can be found for the same kind of nanoparticles generated by the two methods, except for the case of the $ZnFe_2O_4$, where the cationic radius difference allows to an easier cationic mobility, producing a higher order in the thermal synthesised nanocrystals. This relays with the magnetic measurements, which tally with the SQUID magnetometry.

By its part, the oxidation states of the different atoms conforming the sample keep constant for both methodologies, even for the case of the Fe_3O_4, where a secondary phase, the maghemite ($\gamma - Fe_2O_3$) has been found in a 45 %. This expected result comes from an oxidising synthesis media, the TREG.

XAS & XMCD techniques results agree with the neutron powder diffraction measurements. When comparing the experimental results with previous bibliographic works, the same results when compared with neutron diffraction are obtained:

similar structure and behaviour for the nanoparticles generated via the two studied methodologies. The $CoFe_2O_4$ and $MnFe_2O_4$ present a mixture of +2 and +3 as oxidation states, being compensated by the presence of Fe^{2+}.

The $MnFe_2O_4$ was studied deeply because it has been also analysed when it is embedded inside the YBCO SC layer. Data collected after the insertion of NPs inside the YBCO, shows a partial oxidation of the nanoparticles to manganese oxide (Mn_2O_3 confirmed by theoretical calculations) and the corresponding iron (III) oxide. The remarkable result is that is only a partial oxidation, existing the original spinel structure inside the layer with their intrinsic magnetic properties.

Neutron powder diffraction, jointly with XAS & XMCD results, confirm the hypothesis that microwave generate similar nanoparticles than the thermal route in the most of the cases. This conclusion has to be remarked, because with it the microwave is promoted as a more efficient synthetic route for nanostructures, obtaining similar results than thermal procedures.

Synchrotron XRD for nanocomposite YBCO superconducting layers has allowed to calculate different parameters, such as: composition, microstrain, orientation etc. of the different YBCO layers with different nanoparticles embedded. In spite of the results have to be related with the superconducting capabilities, the crystallographic results demonstrates the high purity nanostructured layer when nanoparticles are embedded via *in-situ* or *ex-situ* approach. The YBCO-$MnFe_2O_4$ layer studied, shows the possibility to embedded preformed nanoparticles inside the YBCO structure via ink-jet printing technology. The influence of the nanocrystals in the strain of the YBCO layer has been analysed, demonstrating that isotropic strain implies higher J_c.

Plane orientation of the proper YBCO and the different nanoparticles embedded was investigated via rocking scans, mapping the reciprocal space or making pole figures. The ortorhomboicity of the YBCO, and the AB planes have been analysed jointly with the NPs preferential orientations. In the case of nanoparticles, they present a high random fraction, and among them, the $MnFe_2O_4$ NPs with a 70 %. $BaCeO_3$ nanocrystals deserves by its part, a remarkable case to study due to their multiple preferred disposition.

Complementarily, GIXRD configuration was used to analyse the BZO nanotracks generated by electrospinning on a LAO single crystal. The phase purity, and the random disposed fraction were analysed, confirming that the presence of $BaZrO_3$ forming the nanostructures with a high random part (85 %).

Part IV

General Conclusions

Chapter 12

General Conclusions

The work developed during this PhD project allows to extract several conclusions summarised below:

First The synthesis of a family of MFe_2O_4 (M= Mn, Fe, Co, Ni, Cu, Zn) NPs has been developed by two synthetic approaches: thermal and microwave, based on the polyol route, which produces NPs with a selectable concentration up to 256 mM and dispersible in polar media.

Second Properties of the NPs demonstrate that thermal and microwave methodologies produce similar NPs in structure and behaviour: constant size independently of the route required (below 10 nm), pure spinel structure without secondary phases, superparamagnetism with high saturation magnetisation, etc.

Third Neutron powder diffraction and Rietveld refinement confirm the high phase purity, except in the case of the Fe_3O_4, where a mixture with $\gamma - Fe_2O_3$ has been found with a constant ration for both routes (55:45 Fe_3O_4 : $\gamma - Fe_2O_3$).

Fourth XMCD measurements of the MFe_2O_4 (M=Mn, Co) NPs indicate a mixture of oxidation states of the Mn and Co inside the NPs (+2 & +3), being compensated by the iron (III) to iron (II) reduction.

Fifth Despite microwave and thermal procedures generate similar nanostructures, better dispersions have been obtained via microwave approach. Moreover, time and temperature reduction are required to produce microwave NPs.

Sixth Profiting the high stability of the solution obtained in high ionic force YBCO precursor solution, a new *ex-situ* methodology to prepare YBCO thin layers was developed.

Seventh The stable solution containing 1.5 or 3 % of $MnFe_2O_4$ NPs in the $YBa_2Cu_3O_{7-\delta}$ chemical precursor solution has been deposited by CSD ink-jet printing technique, fabricating nanocomposite superconducting layers.

Eight New produced $MnFe_2O_4$ - $YBa_2Cu_3O_{7-\delta}$ nanocomposite layers have been analysed, finding the NPs inside the YBCO matrix by HRTEM with some coalescence, and demonstrating the constant metal (Mn and Fe) distribution along the deep of the layer through XPS. In addition, superconducting capabilities (J_c and T_c) are maintained in the presence of the 1.5 % of NPs in the structure.

Ninth Synchrotron measurements (XAS-XMCD and XRD) demonstrate clearly the presence of the spinel structure of the $MnFe_2O_4$ embedded in the YBCO thin layer. Due to the harsh conditions of the YBCO growth, a partial oxidation of these NPs occurs, but only for those situated in the external part of the layer, generating a mixture of Mn_2O_3, MnO_2 and $\alpha - Fe_2O_3$ antiferromagnetic compounds, jointly with the remaining part of the superparamagnetic $MnFe_2O_4$.

Tenth The study with synchrotron XRD of *in-situ* & *ex-situ* superconducting nanocomposite layers has allowed to relate the YBCO microstrain (in plane and out of plane directions) with the superconducting capabilities. Isotropic microstrain has been proved to be better for the critical current improvement.

Eleventh X-ray synchrotron diffraction to study the crystal structure has been extended to other *ex-situ* and *in-situ* YBCO nanocomposites with $BaZrO_3$, Ba_2YTaO_6, CeO_2 and $MnFe_2O_4$ NPs embedded. It has been demonstrated their phase purity when compared with the standard one. Besides, the analysis of the crystal plane orientations of the YBCO and the NPs enable the possibility to study the YBCO orientation growth, twined crystals, direction splitting, misalignment and AB planes; the NPs disposition as their preferential orientations and random part, demonstrate the high random fraction orientation of the *ex-situ* $MnFe_2O_4$ and $BaCeO_3$ in the YBCO.

As general conclusion, a new approach to produce high quality ferrite magnetic nanoparticles and their inclusion inside the $YBa_2Cu_3O_{7-\delta}$ superconducting matrix trough *ex-situ* methodology has been achieved. Properties of the nanoparticles, YBCO and the new nanostructures have been studied with neutron and synchrotron radiation, obtaining a deep knowledge of their structure and behaviour.

Part V

Annexes

List of Figures

Page

List of Tables

Page

Publications

During this thesis, the following papers have been published:

1. L. Perez-Mirabet, E. Solano, F. Martinez-Julian, R. Guzman, J. Arbiol, T. Puig, X. Obradors, A. Pomar, R. Yañez, J. Ros, and S. Ricart, "One-pot synthesis of stable colloidal solutions of MFe_2O_4 nanoparticles using oleylamine as solvent and stabilizer", Materials Research Bulletin, vol. 48, no. 3, pp. 966-972, 2013.

2. E. Solano, L. Perez-Mirabet, F. Martinez-Julian, R. Guzman, J. Arbiol, T. Puig, X. Obradors, R. Yañez, A. Pomar, S. Ricart, and J. Ros, "Facile and efficient one-pot solvothermal and microwave-assisted synthesis of stable colloidal solutions of MFe_2O_4 spinel magnetic nanoparticles", Journal of Nanoparticle Research, vol. 14, no. 8, pp. 1034-1048, 2012.

3. A. Calleja, S. Ricart, X. Granados, X. Palmer, E. Solano, J. A. Tornero, F. Cano, T. Puig, and X. Obradors, "Epitaxial $BaZrO_3$ tracks by electrospinning of metalorganic fibers on single crystals", Crystal Engineering Communication, vol. 14, no. 14, pp. 4686-4691, 2012.

—

4. E. Solano, C. Frontera, T. Puig, X. Obradors, S. Ricart and J. Ros, "Study of microwave ferrite nanocrystals by neutron and X-ray diffraction. A structural comparison with thermal synthetic route", Journal of Applied Crystallography. *Accepted*

In addition, this work has been also presented in several national & international congress:

Oral communications: 10 presentations

Posters: 11 presentations

Notes